IUTAM Bookseries

Jinjun Wang
Ivan Marusic *Editors*

IUTAM Proceedings of the IUTAM Symposium on Turbulent/Non-Turbulent Interface in Turbulent Shear Flows

Springer

IUTAM Bookseries **45**

The IUTAM Bookseries publishes the refereed proceedings of symposia organised by the International Union of Theoretical and Applied Mechanics (IUTAM).

Every two years the IUTAM General Assembly decides on the list of IUTAM Symposia. The Assembly calls upon the advice of the Symposia panels. Proposals for Symposia are made through the Assembly members, the Adhering Organizations, and the Affiliated Organizations, and are submitted online when a call is launched on the IUTAM website.

The IUTAM Symposia are reserved to invited participants. Those wishing to participate in an IUTAM Symposium are therefore advised to contact the Chairman of the Scientific Committee in due time in advance of the meeting. From 1996 to 2010, Kluwer Academic Publishers, now Springer, was the preferred publisher of the refereed proceedings of the IUTAM Symposia. Proceedings have also been published as special issues of appropriate journals. From 2018, this bookseries is again recommended by IUTAM for publication of Symposia proceedings.

Indexed in Ei Compendex and Scopus.

Jinjun Wang · Ivan Marusic
Editors

Proceedings of the IUTAM Symposium on Turbulent/Non-Turbulent Interface in Turbulent Shear Flows

Springer

Editors
Jinjun Wang
Institute of Fluid Mechanics
Beihang University
Beijing, China

Ivan Marusic
Mechanical Engineering
University of Melbourne
Parkville, VIC, Australia

ISSN 1875-3507 ISSN 1875-3493 (electronic)
IUTAM Bookseries
ISBN 978-3-031-78150-6 ISBN 978-3-031-78151-3 (eBook)
https://doi.org/10.1007/978-3-031-78151-3

© The Editor(s) (if applicable) and The Author(s) 2025. This book is an open access publication.

Open Access This book is licensed under the terms of the Creative Commons Attribution 4.0 International License (http://creativecommons.org/licenses/by/4.0/), which permits use, sharing, adaptation, distribution and reproduction in any medium or format, as long as you give appropriate credit to the original author(s) and the source, provide a link to the Creative Commons license and indicate if changes were made.
The images or other third party material in this book are included in the book's Creative Commons license, unless indicated otherwise in a credit line to the material. If material is not included in the book's Creative Commons license and your intended use is not permitted by statutory regulation or exceeds the permitted use, you will need to obtain permission directly from the copyright holder.
The use of general descriptive names, registered names, trademarks, service marks, etc. in this publication does not imply, even in the absence of a specific statement, that such names are exempt from the relevant protective laws and regulations and therefore free for general use.
The publisher, the authors and the editors are safe to assume that the advice and information in this book are believed to be true and accurate at the date of publication. Neither the publisher nor the authors or the editors give a warranty, expressed or implied, with respect to the material contained herein or for any errors or omissions that may have been made. The publisher remains neutral with regard to jurisdictional claims in published maps and institutional affiliations.

This Springer imprint is published by the registered company Springer Nature Switzerland AG
The registered company address is: Gewerbestrasse 11, 6330 Cham, Switzerland

If disposing of this product, please recycle the paper.

Preface

The International Union of Theoretical and Applied Mechanics (IUTAM) symposium on Turbulence and Non-Turbulence Interface (TNTI) was held from October 8–11, 2024, in Beijing, China. This symposium is the first IUTAM Symposium on TNTI, reflecting the growing size and increasing popularity of the TNTI research community.

The objective of the symposium is to bring together leading researchers to discuss the latest developments and challenges in the study of TNTI. The TNTI is an irregular boundary between turbulent and irrotational flow, found in various flow types such as turbulent boundary layers, combustion flame fronts, atmospheric and oceanic turbulent patches, and pollutant dispersion. TNTI plays a crucial role in various turbulent flow scenarios, including intermittency, mixing, and entrainment processes, thus making it a significant area of research in turbulence studies.

Despite the progress made in recent decades, the scientific community still faces several challenges in fully characterizing and modeling TNTI. These challenges include the lack of a universally accepted definition of TNTI and the complex fractal multi-scale nature of the interface. Understanding the dynamics of TNTI is key to elucidating the mechanisms behind the exchange of mass, momentum, and energy between turbulence and irrotational outflows, and this remains an area requiring further exploration.

The symposium provided a platform for active researchers to consolidate current knowledge and envision future directions in TNTI research. Key topics included the scaling of TNTI geometries, kinematics, and dynamics; the role of turbulent structures in the entrainment process; multiphase flows involving TNTI; high-fidelity turbulence models accounting for TNTI intermittency; and reduced-order models for engineering applications. The symposium also aimed to synthesize insights and foster collaboration across multiple disciplines, such as aerospace science, chemical engineering, geophysics, and environmental science, to establish a global cooperation network benefiting the entire community.

The symposium program was planned, and the invited presentations were selected by the Scientific Committee of the symposium, nominated by IUTAM. The members of the Scientific Committee are Jinjun Wang (Chairman), Beihang University, China; Ivan Marusic (Co-Chair), The University of Melbourne, Australia; Atila Freire (IUTAM representative), Universidade Federal do Rio de Janeiro, Brazil; Guowei He, Chinese Academy of Sciences, China; Javier Jimenez, Universidad Politécnica de Madrid, Spain; Charles Meneveau, Johns Hopkins University, USA; Hyung Jin Sung, Korea Advanced Institute of Science and Technology, South Korea; Jerry Westerweel, Delft University of Technology, the Netherlands. The arrangements of the symposium were conducted by the local organizing committee: Pan Chong, Xiong Yuan, Xu Yang, and Wang Jiangsheng from Beihang University.

The symposium had more than 24 presentations, 19 of which were included in this book. More than 80 participants from over 10 countries and regions participated in the symposium. The speakers represented Australia, Canada, China, France, Germany, Japan, the Netherlands, Portugal, South Korea and the United Kingdom. The symposium attracted a diverse group of participants, fostering discussions and collaborations to address the unresolved issues in TNTI research. The contributions and insights shared during this event are expected to drive future advancements and promote a deeper understanding of the turbulent/non-turbulent interface. The symposium was organized by IUTAM, hosted by Beihang University, and co-organized by the Chinese Society of Theoretical and Applied Mechanics, the Beijing Association for Science and Technology, and the Beijing Society of Theoretical and Applied Mechanics. All the supports are gratefully acknowledged.

Jinjun Wang
Ivan Marusic

Organization

Scientific Committee

Atila Freire (IUTAM Representative)	Universidade Federal do Rio de Janeiro, Brazil
Guowei He	Chinese Academy of Sciences, China
Javier Jimenez	Universidad Politécnica de Madrid, Spain
Ivan Marusic	The University of Melbourne, Australia
Charles Meneveau	Johns Hopkins University, USA
Hyung Jin Sung	Korea Advanced Institute of Science and Technology, South Korea
Jinjun Wang	Beihang University, China
Jerry Westerweel	Delft University of Technology, The Netherlands

Contents

Invited Papers

Regular Papers

Invited Papers

Turbulent/Non-turbulent Interface in High Reynolds Number Pressure Gradient Boundary Layers

Ivan Marusic(✉), Wagih Abu Rowin, Mitchell Lozier, Luka Lindić, Ahmad Zarei, and Rahul Deshpande

Department of Mechanical Engineering, University of Melbourne,
Parkville, VIC 3010, Australia
imarusic@unimelb.edu.au
https://findanexpert.unimelb.edu.au/profile/29811-ivan-marusic

Abstract. We report two-dimensional particle image velocimetry experiments in high Reynolds number turbulent boundary layers imposed with a moderately strong streamwise pressure gradient. The unique aspect of these data are the highly resolved measurements across the outer region of a physically thick boundary layer, enabling accurate detection of turbulent/non-turbulent interfaces (TNTI). The present dataset is used to detect the TNTI of an adverse pressure gradient turbulent boundary layer and compare its characteristics with that for a zero-pressure gradient boundary layer, at a nominally similar friction Reynolds number. It is found that the TNTI exists across a broader range of wall-normal distance in presence of an adverse pressure gradient, as compared to the zero-pressure gradient case. Implications on conditionally averaged turbulence statistics are discussed based on detection of the TNTI.

Keywords: Experimental Fluid Mechanics · Wall-bounded turbulence · Adverse Pressure Gradient

1 Introduction

A characteristic feature of any turbulent flow is a broad spectrum of turbulent scales of motion, or eddies, whose dynamics are governed by the viscous and inertial forces acting on the flow. In turbulent flows, the relationship between these viscous and inertial forces has traditionally been described by the Reynolds number, a parameter which is non-dimensionalized using a characteristic length scale, velocity scale and viscosity, which are specific to each flow. These forces, and consequently the dynamics of the turbulent eddies, are confined within and regulated by the boundaries of the turbulent fluid flow. In this study, we will limit our focus to wall-bounded turbulent flows, specifically the turbulent boundary layer (TBL), which is technologically relevant to many engineering applications such as over aircraft wings and ship hulls.

J. Wang and I. Marusic (Eds.): IUTAM-TNTI 2024, IUTAM Bookseries 45, pp. 3–17, 2025.
https://doi.org/10.1007/978-3-031-78151-3_1

In the case of the TBL, one boundary is a solid wall (with discussion here limited to smooth walls only), while the second boundary is a complex and freely developing interface between the turbulent eddies within the TBL (turbulent region) and the external freestream flow (non-turbulent region). This interface will be referred to as the turbulent/non-turbulent interface (TNTI) henceforth [1]. In the case of the TBL, we will refer to the friction Reynolds number $Re_\tau = U_\tau \delta / \nu$, where U_τ and ν denote the mean friction velocity and kinematic viscosity respectively. We limit our discussion here to nominally high-Re_τ ($\gtrsim 7000$) TBLs, which have only been investigated experimentally to date. There are several methodologies reported in the literature on estimating the boundary layer thickness, δ; all of them essentially indicate the local wall-normal distance demarcating the freestream flow from the turbulent region, in a time-averaged sense. The freestream flow is considered to be irrotational and non-turbulent, although in practice there is almost always some measurable turbulence in the freestream flow. This freestream turbulence intensity varies depending on the experimental facility, but is typically orders of magnitude lower than the intensity of turbulent eddies within the TBL, such that the two regions are distinguishable. In addition to spatially identifying the turbulent and non-turbulent regions, the dynamics of this bounding TNTI also regulates the transport of important quantities such as mass, momentum, and energy between the turbulent and non-turbulent regions of the flow [21]. As such the mixing and entrainment processes associated with the TNTI are not only interesting, but also pertinent to many engineering applications, and are an active area of research for a variety of turbulent flows.

Many methods and measurement techniques have been used to locate or describe the TNTI of the TBL. Early methods utilized time-resolved measurements of the streamwise velocity from hot-wires to generate a statistical description of the TNTI. In the wake region of the TBL, large-scale pockets or bulges containing turbulent eddies which passed the hot-wire were highly contrasted with the relatively quiescent freestream flow creating a highly intermittent velocity signal. The turbulent parts of the signal were distinct due to the presence of high frequency and high amplitude turbulent fluctuations. This aspect of the velocity signal can be enhanced by differentiating [20] or high-pass filtering [19] the velocity signal, creating a so-called detector function. By applying a threshold to this detector function the turbulent portions of the signal can be identified and used to quantify the wake-region intermittency or compute conditionally averaged statistics for example [22]. More recently, spectral methods such as wavelet analysis [17], have also been employed to achieve similar outcomes. The spectral signature of the high frequency and high amplitude fluctuations, associated with the turbulent regions of the flow, are easy to identify and a detector type function can be created by averaging the spectral energy of relevant eddies. Each of these methods has some inherent subjectivity stemming from the use of thresholds and/or filtering/smoothing techniques which are applied to the velocity signals and/or detector functions [17, 20]. With the rise of spatially resolved two-dimensional velocity measurement techniques (e.g. particle imaging velocimetry, PIV), new methods were used to find a two-dimensional instantaneous representation of the TNTI. One method is introducing passive tracer particles into the turbulent and/or non-turbulent regions of the flow in order to make them distinguishable during imaging. However, quantities such as the vorticity [18] or local kinetic energy [16] have also been used successfully to delineate the turbulent and non-turbulent regions of the TBL without additional tracers. With these methods, once the TNTI is identified, various properties associated with the instantaneous TNTI can be investigated such as mass/energy flux, multi-scale dynamics, or conditional statistics [16]. Similar methods have also been applied with three-dimensional measurement techniques.

A majority of the previous research effort regarding TBL TNTI characteristics has been focused on canonical (i.e. smooth-wall, zero-pressure gradient (ZPG)) TBLs. However, TBLs encountered in engineering applications are typically exposed to non-canonical effects such as pressure-gradients. In particular, adverse-pressure gradients (APG) have been shown to affect the dynamics of large-scale eddies, one consequence of which is an increase in the growth rate of the boundary layer thickness [3]. It would follow that APG conditions can have an affect on the characteristics and dynamics of the TNTI as well [15]. In order to study TNTI dynamics of an APG TBL at high Re_τ, we will follow the technique described by Chauhan et al. [16] utilizing the local kinetic energy (LKE), measured using well-resolved planar PIV in the wall-normal direction, to locate the instantaneous TNTI bounding the TBL. To the best of the author's knowledge, this work represents the first analysis of TNTI employing the LKE methodology for a high-Re_τ turbulent boundary layer with an adverse-pressure gradient.

As per Chauhan et al. [16], the local kinetic energy, $\tilde{k}$, over a 3×3 spatial grid can be computed via Eq. 1.

$$\tilde{k} = 100 \times \frac{1}{9U_\infty^2} \sum_{m,n=-1}^{1} \left[\left(\tilde{U}_{m,n} - U_\infty \right)^2 + \left(\tilde{W}_{m,n} \right)^2 \right] \tag{1}$$

Here the instantaneous streamwise and wall-normal velocity components are denoted by $\tilde{U}$ and $\tilde{W}$ respectively, with U_∞ representing the mean freestream velocity. The corresponding streamwise and wall-normal axes will be represented by x and z respectively. In the region above the TNTI, it is expected that $\tilde{k}$ will be equal to the freestream turbulence intensity ($\overline{u^2}/U_\infty^2$ which is facility dependent), while below the interface $\tilde{k}$ will increase significantly approaching the wall. As such an LKE threshold, k_{th}, is chosen which corresponds to the known freestream turbulence intensity of the facility. A binary representation of the instantaneous flow field can then be obtained where non-turbulent regions ($\tilde{k} < k_{th}$) are assigned a value of 1 and turbulent regions ($\tilde{k} \gtrsim k_{th}$) are assigned a value of 0. The local interface position is then extracted using a contour algorithm to generate a contour line at a level of 0.5 which demarcates the turbulent and non-turbulent regions. With the instantaneous TNTI identified, a range of statistical calculations can then be undertaken to study the TNTI dynamics.

This paper reports preliminary analysis of the conditional statistics based on TNTI detection, for both ZPG and APG TBLs.

2 Experimental Setup

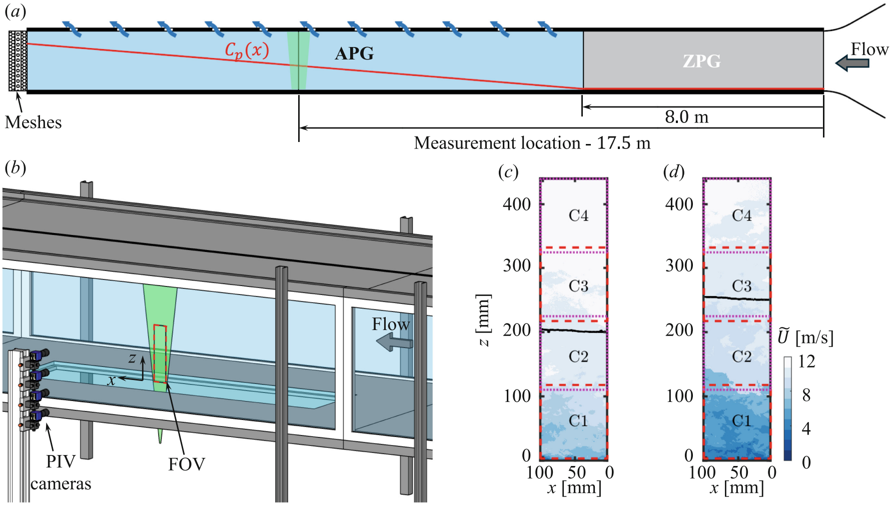

Fig. 1. (a) Schematic of the Melbourne wind tunnel modified to adjust the static-pressure coefficient (C_p) as a function of the streamwise distance, x. The arrows on the test section ceiling represent air bleeding on introduction of the blockage at the tunnel outlet (via meshes/screens). (b) Schematic illustrating the planar PIV setup, featuring the tower configuration of four cameras and the laser sheet passing through the glass tunnel floor. Instantaneous streamwise velocity, $\tilde{U}$-field for the (c) ZPG and (d) APG cases in the $xz-$plane. In (c) and (d), the flow direction is from right to left, and the boundary layer thickness (δ_{99}) is estimated based on the methodology used by Bobke et al. [12] and is indicated by black lines. The red and magenta rectangles in (c) and (d) represent the captured field-of-view by each camera, with each view labelled with the respective camera number, e.g., C1, C2.

2.1 Facility and APG Setup

Both the ZPG and APG flow scenarios were established in the large Melbourne wind tunnel facility (HRNBLWT; [5,13]), which permits precise control of the pressure gradient via air bleeds. The air bleeds are essentially spanwise slots existing on the tunnel ceiling, that are strategically spaced every 1.2 m along the 27 m long working section of the HRNBLWT. Figure 1(a) shows a schematic of the experimental setup, which includes a custom-designed frame installed at the test section outlet (inspired from Clauser [2]), that holds multiple screens/wire meshes to enforce the pressure gradient in the test section. These screens are made out of perforated steel, with a porosity of 51%. The magnitude of the adverse pressure gradient can be easily changed by varying the number of screens [13]. A ZPG condition is imposed across the test section by removing all the low porosity (∼51%) screens and installing a single high porosity screen at the outlet, similar to the original configuration of the HRNBLWT reported in Marusic et al. [5].

The unique aspect of the present wind tunnel setup is its ability to impose an APG at a sufficiently downstream location, after the TBL has grown under a nominally ZPG condition upstream (*i.e.*, a canonical condition). This is schematically indicated in Fig. 1(a), which shows a well-established canonical inflow ZPG up to $x \approx 8m$, maintained via choking the air bleeding from the tunnel ceiling. The APG is only enforced in the downstream section of the tunnel by permitting air bleeding from the ceiling, which leads to a quasi-linear growth in the tunnel static pressure (indicated by non-dimensional pressure coefficient, $C_p(x)$ in Fig. 1a). Here, the definiton of $C_p(x)$ is based on the freestream velocity variation along x (*i.e.*, $U_\infty(\mathrm{x})$), given by:

$$C_p(\mathrm{x}) = 1 - \mathrm{U}_\infty^2(\mathrm{x})/\mathrm{U}_\infty^2(\mathrm{x}=0) \tag{2}$$

The C_p variation obtained in this facility is unique with respect to the vast majority of past studies on APG TBL flows, which have predominantly relied on working-section inserts to produce a varying cross-sectional area to establish the adverse pressure gradient [4,6,7]. These working section inserts usually involve a constriction, leading to a favourable-pressure gradient, followed by a limited straight section for a zero-pressure gradient, before finally leading to the APG region. While each of these previous studies is in itself interesting, every change/perturbation in the upstream PG condition is known to result in unique history effects that affect the flow downstream [12,13]. In the select few past experiments without inserts [3,8,9], a canonical ZPG boundary layer led into an APG region, which was found to minimize the upstream history effects. However, all these experiments were conducted at $Re_\tau \lesssim 3\,000$, and thus restricted to low-moderate Reynolds numbers. For this purpose, the present study will investigate APG TBL flow at high Re_τ (∼7000), which will be compared with ZPG case at nominally matched Re_τ. Interested readers can find more details on this experimental setup in Deshpande et al. [13].

This study quantifies the intensity of the pressure gradient by defining the Clauser pressure gradient parameter, β [2] defined as:

$$\beta = (\delta^*/\rho U_\tau^2)\,(\mathrm{d}P/\mathrm{d}x)\,, \tag{3}$$

where $\delta^* = \int_0^{\delta_{99}}(1-\overline{U}(z)/U_e)\ \mathrm{d}z$ is the displacement thickness, $U_e = \overline{U}(z = \delta_{99})$, *i.e.* the mean streamwise velocity at the edge of the TBL, ρ is the fluid density and $\mathrm{d}P/\mathrm{d}x$ is the mean streamwise pressure-gradient at the x-location where β is estimated. All the experimental cases considered in this study, and their associated measurement conditions, have been documented in Table 1.

Here, δ_{99} is quantified using the same definition as used by Bobke et al. [12] and Deshpande et al. [13], based on the diagnostic plot method. Both δ_{99} and δ^* are quantified for the ZPG and APG cases via the PIV data, which will be described next (§2.2). Friction velocity, U_τ has been estimated directly via oil-film interferometry (OFI), which will be described in §2.3.

2.2 Planar PIV Setup

To acquire detailed measurements across the entire boundary layer, we employed four high-resolution Imager CX-25 12-bit resolution cameras staggered vertically to capture a narrow vertical column spanning the entire boundary layer height, as shown in Fig. 1(*b*). Each camera features a complementary metal oxide semiconductor (CMOS) sensor with dimensions of 5312 × 4608 pixels. The CMOS sensor possesses pixels measuring $2.7 \times 2.7\ \mu$ m^2. Equipped with Tamron SP AF 180 mm macro photography lenses set at an aperture size of $f/11$, each camera achieved a digital resolution of 22 μ m/pixel. Illumination was provided by an InnoLas SpitLight Compact PIV 400 dual pulse Nd:YAG laser, with typical spherical and cylindrical lenses configuration. To illuminate the boundary layer with minimum reflection in the vicinity of the wall, a laser sheet with an estimated thickness of 2 mm was directed from the bottom glass as illustrated in Fig. 1(*b*). Both the PIV measurements, in a high Re_τ ZPG and APG TBL, were conducted at the same streamwise location, $x \sim 17.5$ m (Fig. 1a). The flow was seeded with polyamide particles ranging from 1–2 μm in diameter. The final stitched field-of-view (FOV) measured 104 × 441 mm^2 (in $x \times z$).

Table 1. Details of the PIV data sets acquired for ZPG and APG scenarios

Case	Symbol	x (m)	$U_\infty(x=0)$ (m/s)	$U_\infty(x)$ (m/s)	Re_τ	$\frac{\nu}{u_\tau}$ (μ m)	δ_{99} (mm)	$\beta(x)$	#PIV Images
ZPG	◇	17.5	12.6	12.6	7500	36	270	0	2000
APG	◇	17.5	12.6	11.2	7100	46	328	1.4	2000

The synchronization of laser pulses and the four high-speed cameras was achieved using a programmable timing unit (PTU X, LaVision GmbH) controlled by DaVis 10.1. An ensemble of 2000 pairs of double-frame images with a laser pulse separation of 50 μ s was recorded. This pulse separation resulted in a maximum particle displacement of 10 pixels in the freestream region of $U_\infty = 12.6$ m s^{-1}. For camera calibration, a 2-D target comprising of 1 mm diameter dots, evenly spaced 5 mm apart, was utilised. The signal-to-noise ratio of the images was enhanced by subtracting the minimum intensity from the ensemble and subsequently normalizing them using the average intensity. Multi-pass cross-correlation was then applied with a final interrogation window size of 24×24 pixels (0.53×0.53 mm^2) with 50% overlap. The final window sizes, along with the laser sheet thickness, correspond to viscous-scaled spatial resolutions in the $x^+ \times y^+ \times z^+$ directions of $18 \times 55 \times 18$ and $11 \times 43 \times 11$ for the ZPG and APG cases, respectively, where the spanwise spatial average is associated with the 2 mm thick laser sheet. Here the superscript '+' denotes normalisation with the friction velocity U_τ and kinematic viscosity ν.

As can be noted above, the unique aspect of current PIV data set is its excellent wall-normal resolution ∼10–20 viscous units across the entire TBL, making it ideal for detecting and analyzing TNTI interfaces. Representative snapshots of the instantaneous streamwise velocity U in the $x \times z$ plane are depicted in Figs. 1(c) and (d) for the ZPG and APG TBLs, respectively. The annotated FOVs for each camera demonstrate the advantageous positioning of the current camera setup. In the ZPG case, the BL thickness, estimated based on δ_{99} lies in the FOV of camera 2. On the other hand, δ_{99} for APG TBL is situated close to the center of camera 3. This arrangement of cameras ensures high-resolution velocity measurement coverage of the entire BL for both the ZPG and APG experiments.

2.3 Oil-Film Interferometry

Oil film interferometry (OFI) is a direct and independent method for obtaining exact measurement of U_τ in turbulent boundary layers, especially at high Reynolds number where near-wall measurements are often inaccessible [10]. This friction velocity measurement technique has emerged as an important requirement for testing of scaling arguments in high Reynolds number TBLs, such as the validity of the inner-scaling, log-region, etc.

During an OFI experiment, a silicone oil (50 cSt) droplet is spread onto a smooth clean surface of the wind tunnel. As the droplet spreads into a thin film during 'wind on' condition, it is illuminated by a monochromatic light source, creating visible fringes captured by a DSLR camera (depicted in Fig. 2a). The rate of change of these fringes correlates with the thinning of the oil film, which relates to the local wall shear stress. Using a Nikon D800 DSLR camera in time-lapse mode, over 100 images are taken in a 5-second interval for each OFI database. These images are processed using a fast-Fourier-transform algorithm to extract fringe spacing from interferograms. As explored by Fernholz et al. [11], the wall shear stress can be expressed as the distance between fringes (Δx) over a period of time (Δt) as:

$$\tau_w = \mu_{oil} \frac{\Delta x}{\Delta t} \frac{\sqrt{n_{oil}^2 - -n_{air}^2 sin\theta}}{\lambda} \tag{4}$$

where n_{air} and n_{oil} denote the refractive indices of air and oil, respectively. The θ and λ respectively represent the illumination incident angle and wavelength of the light source (equal to 589.9 nm for the sodium lamp utilized). An example of oil droplet fringe patterns and evolution of the fringe spacing across an OFI test are shown on the left and right side of Fig. 2. The linear fringe spacing over time shows the quality of fringe patterns, and consequently the OFI results. Considering uncertainties associated with oil viscosity calibration, fringe extraction, and

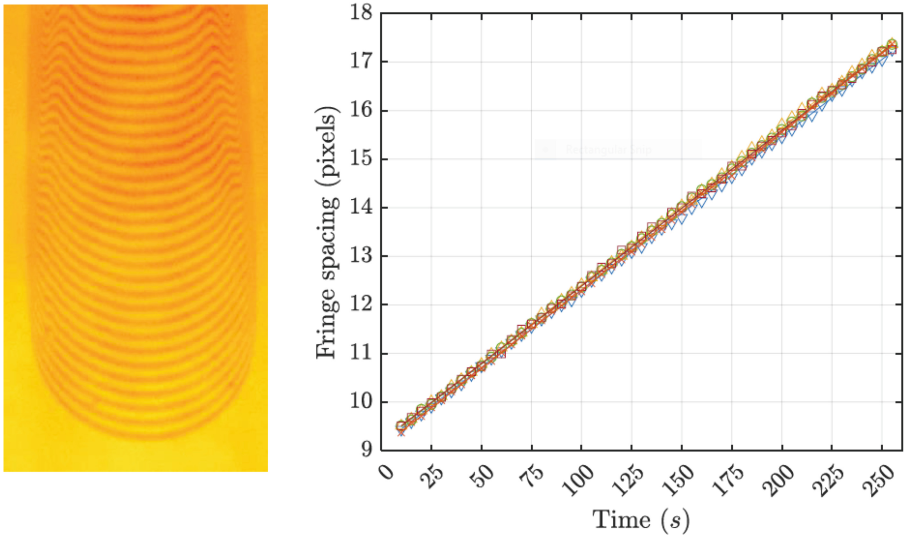

Fig. 2. Sample interferogram pattern and oil film fringe spacing for APG case

potential dust contamination of the oil film, the uncertainty obtained by OFI in this study is estimated to be within ±1.5%. The OFI experiment is conducted at $x \sim 17.5\,\mathrm{m}$ of the test section, for both ZPG and APG TBL experiments, to obtain their respective U_τ estimates at the exact same location as the PIV.

3 Results

This section presents and discusses results from our high-resolution PIV measurements for both the ZPG and APG cases, with a particular focus on estimating and comparing the TNTI characteristics for the two cases. Initially in §3.1, the mean statistics obtained from the PIV measurements will be validated by comparing them with the hot-wire data of Deshpande *et al.* [13], which were obtained under identical flow conditions as the present data (i.e. Re_τ, β and x-location). Next, in §3.2, we deploy the methodology proposed by Chauhan et al. [16] to detect the TNTI for both ZPG and APG cases. Finally in §3.3, we will compare and contrast the conditional statistics in the outer region, obtained based on detection of the TNTI, between the ZPG and APG TBL cases.

3.1 Measurement Validation

Viscous-scaled mean streamwise velocity profiles $\overline{U}^{+} = \overline{U}/U_\tau$ for the ZPG and APG experiments are plotted in Fig. 3(a). Here, the over-line denotes averaging in time (for profiles from hotwire data) and ensemble averaging (for PIV). In our current narrow streamwise FOV PIV measurement, we observed negligible

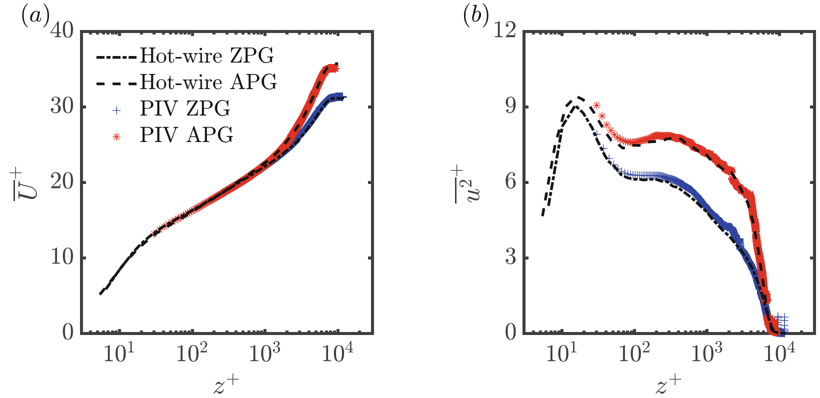

Fig. 3. Mean viscous scaled (a) streamwise velocity U^+ and (b) streamwise velocity fluctuations $\overline{u^2}^+$ for the ZPG and APG cases. The dash-dotted and dashed lines lines in (a) and (b) are data for ZPG and APG cases obtained from the hot-wire performed in Deshpande *et al.* [13] at comparable Reynolds number and pressure gradient of the current PIV measurement.

development of the TBL along the streamwise (x) direction, owing to which there were negligible changes in the turbulent statistics. Hence, all the PIV profiles plotted henceforth have been obtained based on averaging across the $x-$direction as well as across the number of images. Profiles of the hot-wire measurements by Deshpande *et al.* [13], for ZPG and APG under comparable conditions to the current PIV data, are included in Fig. 3(a) for comparison purposes. It is noteworthy that the friction velocity U_τ for each case is determined from the OFI measurement conducted at the same $x-$location as the PIV measurement, which has been discussed previously in §2.3.

Figure 3(a) illustrates that both the ZPG and APG experiment profiles exhibit good agreement with the hot-wire results. The first reliable data point of the current PIV measurement in the vicinity of the wall is at $z^+ \approx 30$ ($z \approx 1100\ \mu$ m for the ZPG and 1400 μ m for the APG cases), below which the reflection from the wall hinders accurate estimation. Additionally, Fig. 3(a) demonstrates that $\overline{U}^+$ for both ZPG and APG overlap reasonably well up to $z^+ \lesssim 750$, beyond which the $\overline{U}^+$ of the APG becomes greater than that of the ZPG in the wake region [3, 4, 8, 13].

The non-dimensionalized mean streamwise velocity fluctuations $\overline{u^2}^+ = \overline{u^2}/U_\tau^2$ for both the ZPG and APG, along with the hot-wire measurements, are shown in Fig. 3(b). This plot demonstrates favorable agreement between the current PIV data and the hot-wire results. As anticipated based on the literature [3, 8, 13], the $\overline{u^2}^+$ profile of the APG case exceeds that of the ZPG in the outer region of the TBL, despite the nominally similar Re_τ for the two cases. This is physical and is attributed to the energization of the inertial scales/eddies on imposition of the APG, and is not an artefact of U_τ-scaling [3].

This comparison between PIV and hotwire validates the former and paves the way for deeper analysis into the TNTI flow physics in the next subsections.

3.2 TNTI Detection

As discussed in the introduction, various methods have been proposed in the literature for detecting the TNTI. Given the high resolution of our current PIV data, we opted to employ the local kinetic energy (LKE) method, as previously demonstrated by Chauhan et al. [16] and discussed in the context of Eq. (1). This method relies on a threshold parameter k_{th}, where turbulent regions are identified when $\tilde{k} \gtrsim k_{th}$ and non-turbulent regions are labelled when $\tilde{k} < k_{th}$. To choose the threshold value for the present investigation, we followed the same procedure as done by Chauhan et al. [16], of selecting k_{th} based on comparison with the intermittency profiles obtained from reference hotwire measurement. We found $k_{th} = 0.2$ to yield satisfactory agreement between the intermittency profiles derived from the PIV data and those obtained from independent hot-wire data, although the comparison is not presented here.

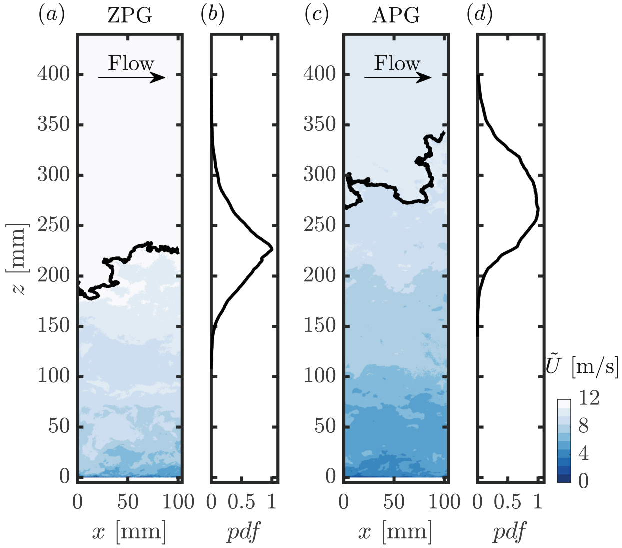

Fig. 4. Instantaneous streamwise velocity $\tilde{U}$ in an $xz-$plane for (a) ZPG and (c) APG cases. (b) and (d) display the probability density function (*pdf*) of the detected TNTI for ZPG and APG cases, respectively. The black lines in (a) and (c) represent the instantaneous TNTI detected for each corresponding case. In these plots, the flow direction is from left to right, as indicated by the arrow in (a) and (c).

Next, we use this criterion to determine the local interface position for both the ZPG and APG cases. Samples of the interface are illustrated in Fig. 4(a)

and (c) for the ZPG and APG experiments, respectively. The instantaneous streamwise velocity ($\tilde{U}$) associated with the detected interface are also provided in these figures. For the ZPG case in Fig. 4(a), the interface appears to vary within the range of 180 mm $\lesssim z \lesssim$ 230 mm for this particular flow realization. On the other hand, the interface appears to vary within 270 mm $\lesssim z \lesssim$ 350 mm in case of the APG, clearly indicating greater thickness of the TBL in case of the APG (which is also expected).

The above discussion (and Fig. 4) not only suggest a greater TBL thickness for APG TBLs but also a greater wall-normal extent of the TNTI region, as compared to the ZPG TBL case. To investigate this further, we analyze the probability density function (*pdf*) of the TNTI across the 2000 PIV fields acquired for both TBL cases. Figures 4(b,d) depict this TNTI for the ZPG and APG TBL, respectively. In case of the ZPG TBL, the *pdf* peaks at approximately $z \approx 227$ mm ($z^+ \approx 6300$) and exhibits a relatively narrow distribution. In contrast, the *pdf* for the APG case peaks at $z \sim 270\,\text{mm}$ and clearly exhibits a broader variation compared to the ZPG TBL. This analysis makes it imperative to investigate whether the conditional statistics based on the TNTI detection affect the APG TBL statistics more significantly than that in case of ZPG TBLs. We use this as a motivation to investigate the conditionally averaged turbulence statistics in the next subsection.

3.3 Conditional Statistics Based on Detection of TNTI

To illustrate the bias in mean turbulence quantities obtained based on the conventional Reynolds decomposition (*i.e.*, when both turbulent and non-turbulent regions are included), we estimate turbulence statistics obtained through conditional averaging below the detected TNTI interface, *i.e.* solely based on the turbulent region. The comparison between these two statistics is shown in Fig. 5, where conditional averaging within the turbulent region is denoted by angle brackets as $\langle . \rangle_{\mathrm{TR}}$, with the subscript 'TR' indicating turbulent region.

The mean viscous-scaled streamwise $\overline{u^2}^+$, wall-normal $\overline{w^2}^+$ velocity fluctuations, and Reynolds shear stresses $\overline{uw}^+$ for both the ZPG and APG cases are presented in Fig. 5. It is evident that the conditionally averaged mean streamwise velocity fluctuations $\overline{\langle u^2 \rangle}^+_{\mathrm{TR}}$ for the ZPG measurements in Fig. 5(a) overlap with the mean variance in the region close to the wall ($z^+ \lesssim 3000$), where the interface is not expected (refer *pdf* plot in Fig. 4b). However, beyond this region ($z^+ > 3000$), $\overline{\langle u^2 \rangle}^+_{\mathrm{TR}}$ appears to be reduced compared to the mean statistics, $\overline{u^2}^+$. This observation aligns with previous findings by Reuther & Kähler [14], who attributed the higher magnitude of $\overline{u^2}^+$ away from the wall, to the bias introduced by including non-turbulent regions in the averaging process. A similar trend can also be observed for $\overline{w^2}^+$ and $\overline{uw}^+$ in Figs. 5(b) and 5(c) for the ZPG case, where the conditionally averaged statistics are smaller than those of the mean statistics away from the wall.

Figure 5 also illustrates that the same observation holds true for the APG case as for the ZPG case, with the conditionally averaged statistics appearing unaf-

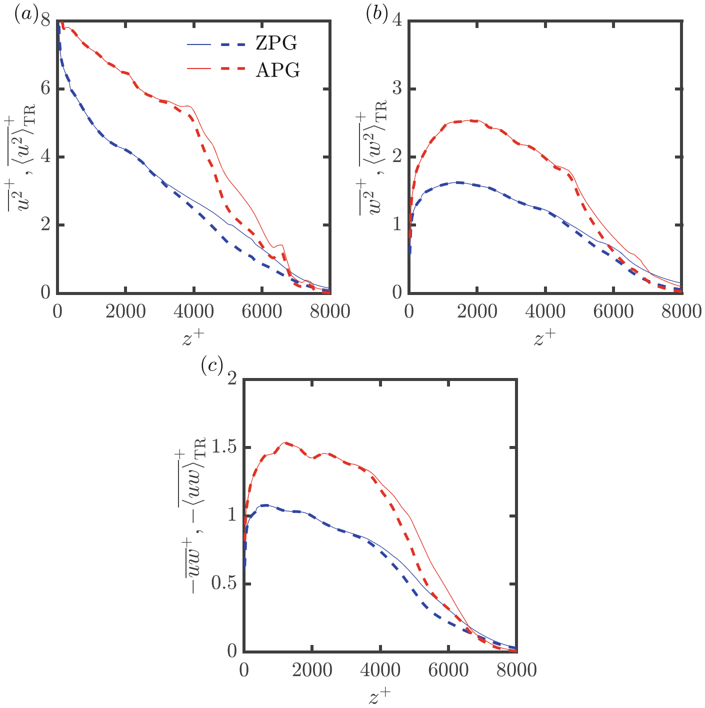

Fig. 5. Viscous-scaled (a) streamwise ($\overline{u^2}^+$), and (b) wall-normal variances ($\overline{w^2}^+$), and (c) Reynolds shear stresses ($\overline{uw}^+$) for the ZPG (blue lines) and APG cases (red lines). The solid lines represent ensemble-averaged data in space and across samples, with fluctuations estimated based on the conventional Reynolds decomposition (*i.e.*, accounting for both the turbulent region and the external freestream flow). While the dashed lines depict conditionally averaged data after identification of the turbulent region. The latter is denoted as, for example, $\overline{\langle u^2 \rangle}^+_{\mathrm{TR}}$.

fected close to the wall and reduced compared to the mean statistics away from the wall. However, owing to the larger magnitude of turbulence statistics in the APG case, the reduction in magnitude of the conditional statistics is much more pronounced compared to the ZPG case. Interestingly, the wall-normal height at which the interface begins to influence the conditionally averaged statistics (in case of APG TBL) is comparable to that observed for the ZPG case, when compared in viscous units (at $z^+ \gtrsim 3000$). This is despite the broader variations of the interface seen in the APG case, as shown previously in Fig. 4(d). Further investigations are needed to comprehensively quantify the influence of the interface on higher-order turbulence statistics in an APG TBL, and compare them with ZPG TBL.

4 Concluding Remarks and Future Work

The present study reports well-resolved 2-D PIV experiments in high Reynolds number ($Re_\tau \gtrsim 7000$) turbulent boundary layers. High resolution is obtained in the wall-normal direction by vertically stacking PIV cameras in a 'tower' configuration, to resolve the wall-normal variation of the turbulence statistics for comparison between a ZPG and APG TBL scenario. The turbulence statistics from PIV are validated against previously published hot-wire measurements, which were acquired at similar flow conditions to those considered for the PIV.

The high wall-normal resolution of the PIV measurements makes them ideally suited for analysis of the turbulent/non-turbulent interface (TNTI) in a high Re_τ TBL. To this end, the previously established methodology of Chauhan et al. [16] is deployed to compare the TNTI for a high Re_τ ZPG and APG TBL. On comparing ZPG and APG TBLs at nominally same Re_τ, it is found that the TNTI interface exists across a greater physical wall-normal distance in case of APG TBL as compared to ZPG TBL. Finally, the detection of the TNTI interface is used to estimate and compare conditional statistics for both TBL cases. In general, the conditionally-averaged turbulence statistics are found to be lower than the conventionally obtained mean statistics, based on the Reynolds decomposition, for both the TBL cases. However, owing to the significantly energetic outer region in an APG TBL, this drop in magnitude of the conditional statistics is much more significant than that noted for ZPG TBL.

Future work will focus on testing various TNTI detection methods and detailed comparisons between the TNTI of a ZPG and APG TBL. Further investigations of the conditionally-averaged statistics for higher order moments can also provide further insight into the TNTI flow physics.

Acknowledgements. I.M. and R.D. gratefully acknowledge funding from the US Office of Naval Research (ONR) and ONR Global program# N62909-23-1-2068. I.M. also acknowledges funding from the Australian Research Council. R. D. acknowledges support from University of Melbourne's Postdoctoral Fellowship.

References

1. da Silva, C.B., Hunt, J.C.R., Eames, I., Westerweel, J.: Interfacial layers between regions of different turbulence intensity. Annu. Rev. Fluid Mech. **46**, 567–590 (2014)
2. Clauser, F.H.: Turbulent boundary layers in adverse pressure gradients. J. Aeronaut. Sci. **21**(2), 91–108 (1954)
3. Harun, Z., Monty, J.P., Mathis, R., Marusic, I.: Pressure gradient effects on the large-scale structure of turbulent boundary layers. J. Fluid Mech. **715**, 477–498 (2013). https://doi.org/10.1017/jfm.2012.579
4. Knopp, T., et al.: Experimental analysis of the log law at adverse pressure gradient. J. Fluid Mech. **918** (2021). https://doi.org/10.1017/jfm.2021.296
5. Marusic, I., Chauhan, K.A., Kulandaivelu, V., Hutchins, N.: Evolution of zero-pressure-gradient boundary layers from different tripping conditions. J. Fluid Mech. **783**, 379–411 (2015). https://doi.org/10.1017/jfm.2015.501

6. Bross, M., Fuchs, T., Kähler, C.J.: Interaction of coherent flow structures in adverse pressure gradient turbulent boundary layers. J. Fluid Mech. **873**, 287–321 (2019). https://doi.org/10.1017/jfm.2019.130
7. Song, S., Eaton, J.: The effects of wall roughness on the separated flow over a smoothly contoured ramp. Exp. Fluids **33**(1), 38–46 (2002). https://doi.org/10.1007/s003480100307
8. Perry, A.E., Marušić, I.: A wall-wake model for the turbulence structure of boundary layers. Part 1. Extension of the attached eddy hypothesis. J. Fluid Mech. **298**, 361–388 (1995). https://doi.org/10.1017/S002211209500128X
9. Monty, J.P., Harun, Z., Marusic, I.: A parametric study of adverse pressure gradient turbulent boundary layers. Int. J. Heat Fluid Flow **32**(3), 575–585 (2011). https://doi.org/10.1016/j.ijheatfluidflow.2011.02.006
10. Ng, H.C., Marusic, I., Monty, J.P., Hutchins, N., Chong, M.S.: Oil film interferometry in high Reynolds number turbulent boundary layers. In: Proceedings of the 16^{th} Australasian Fluid Mechanics Conference (2007)
11. Fernholz, H.H., Janke, G., Schober, M., Wagner, P.M., Warnack, D.: New developments and applications of skin-friction measuring techniques. Meas. Sci. Technol. **7**(10), 1396 (1996)
12. Bobke, A., Vinuesa, R., Örlü, R., Schlatter, P.: History effects and near equilibrium in adverse-pressure-gradient turbulent boundary layers. J. Fluid Mech. **820**, 667–692 (2017). https://doi.org/10.1017/jfm.2017.249
13. Deshpande, R., van den Bogaard, A., Vinuesa, R., Lindić, L., Marusic, I.: Reynolds-number effects on the outer region of adverse-pressure-gradient turbulent boundary layers. Phys. Rev. Fluids **8**(12), 124604 (2023). https://doi.org/10.1063/5.0010167
14. Reuther, N., Kähler, C.J.: Effect of the intermittency dynamics on single and multipoint statistics of turbulent boundary layers. J. Fluid Mech. **897**, A11 (2020)
15. Yang, J., Yoon, M., Sung, H.J.: The turbulent/non-turbulent interface in an adverse pressure gradient turbulent boundary layer. Int. J. Heat Fluid Flow **86**, 108704 (2020). Elsevier
16. Chauhan, K., Philip, J., de Silva, C.M., Hutchins, N., Marusic, I.: The turbulent/non-turbulent interface and entrainment in a boundary layer. J. Fluid Mech. **742**, 119–151 (2014)
17. De, S., Anand, A., Diwan, S.S.: A wavelet-based detector function for characterizing intermittent velocity signals. Exp. Fluids **64**, 180 (2023)
18. Semin, N.V., Golub, V.V., Elsinga, G.E., Westerweel, J.: Laminar superlayer in a turbulent boundary layer. Techn. Phys. Lett. **37**(12), 1154–1157 (2011)
19. Fransson, J.H.M., Matsubara, M., Alfredsson, P.H.: Transition induced by free-stream turbulence. J. Fluid Mech. **527**, 1–25 (2005)
20. Hedley, T.B., Keffer, J.F.: Turbulent/non-turbulent decisions in an intermittent flow. J. Fluid Mech. **64**, 625–644 (1974)
21. Buxton, O.R.H., Chen, J.: The relative efficiencies of the entrainment of mass, momentum, and kinetic energy from a turbulent background. J. Fluid Mech. **977**, R2 (2023)
22. Krug, D., Philip, J., Marusic, I.: Revisiting the law of the wake in wall turbulence. J. Fluid Mech. **811**, 421–35 (2017)

Experimentally Detecting the Turbulent/ Non-turbulent Interface in Wall-Bounded Flows

Agastya Parikh and Christian J. Kähler(✉)

Universität der Bundeswehr München, Institut für Strömungsmechanik und Aerodynamik, 85577 Neubiberg, Germany
`{agastya.parikh,Christian.Kaehler}@unibw.de`
`https://www.unibw.de/lrt7`

Abstract. In experimental studies of the turbulent/ non-turbulent interface (TNTI) of wall-bounded flows, a significant challenge is accurate detection of the interface in 2D and 3D. Detection criteria based on turbulent kinetic energy (TKE) and homogeneity of the flowfield have been applied to PIV measurements of TBLs [2,15]. The use of local seeding (LS) as a passive tracer was also investigated to decouple TNTI detection from the reduced spatial resolution associated with velocimetric methods. This yielded the simple and robust particle image density detection method, which has good spatial resolution but lacks access to velocimetry in the potential flow [15]. With recent development of fluorescent DEHS and its application to tag the TBL, it is possible to obtain the entire flowfield in addition to segregating the flow into its turbulent and non-turbulent parts in air flows [8–10]. Finally, 3D reconstruction of the TNTI with imaging of the TBL at an oblique angle opens the door to more complex investigation and new insights of the interface [14].

Keywords: TNTI · PIV · Turbulent Boundary Layers · Mixing

1 Introduction

Experimental studies of wall-bounded turbulent flows are nearly as old as the field of fluid mechanics in its modern form. Early investigations were often grounded in a phenomenological approach, where flow visualisation highlighted the highly intermittent and convoluted structure of the turbulent boundary layer (TBL). Corrisin and Kistler motivated their seminal work on what would come to be termed turbulent/ non-turbulent interface (TNTI) by opening with a shadowgraph of the turbulent wake left by a bullet, where its interface with the quiescent flow is clearly visible [3]. Central to their characterisation of the TNTI as a thin "laminar superlayer" splitting the flow into turbulent and non-turbulent zones is the assertion that vorticity within the (rotational) turbulent part of the flow cannot be transmitted across the interface, beyond which the flow is considered to be inviscid [3]. The issue of the role of the TNTI in transferring mass and

J. Wang and I. Marusic (Eds.): IUTAM-TNTI 2024, IUTAM Bookseries 45, pp. 18–31, 2025.
https://doi.org/10.1007/978-3-031-78151-3_2

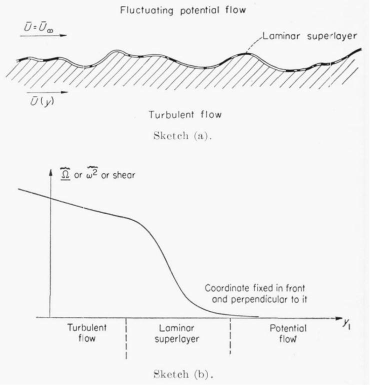

Fig. 1. Corrisin and Kistler's view of the TNTI, illustrating the nature of the flow above, within, and below the interface (a), and the corresponding behaviour of vorticity magnitude (b) as a function of distance from the interface [3].

momentum into the turbulent boundary layer, i.e. entrainment, was identified as being central to gaining a better understanding of the true nature of TBLs by Kovasznay [6]. This was understood to be intrinsically connected to the length of the interface as well as its multi-scale, fractal-like shape [6,12].

At the time, the limited diagnostic tools available meant that studies of the TNTI were limited to the datasets yielded by hot-wires and visualisations. However, the proliferation of particle image velocimetry (PIV) over the last 30 years has revived interest in investigations of the TNTI thanks to the availability of whole-field velocimetric data. Westerweel et al. combined the art of flow visualisation by using laser-induced-fluorescence (LIF) with PIV to identify and characterise the TNTI of a turbulent jet in an experimental setting [18]. Along with DNS of turbulent wakes performed by Bisset et al., this confirmed the theory that a jump in vorticity exists across the interface [1,18]. Kovasznay's ponderings about the mechanisms of mass and momentum transfer at the TNTI, too, were in part addressed by Westerweel et al. in their confirmation that small-scale ("nibbling") was the dominant source of entrainment (at least in turbulent jets), rather the long-held supposition that it was driven by large-scale engulfment events [2,17]. In experimental investigations of turbulent wall-bonded flows, progress has been slower in part due to the greater difficulty of achieving adequate spatial and temporal resolution in high-speed gas flows. Chauhan et al.'s study of the TNTI in TBLs was performed entirely using velocity-based methods, and showed that entrainment is closely linked to the length of the interface, highlighting the role of its fractal nature [2]. Notably, they concluded that while the conversion of entrained non-turbulent flow to a turbulent state is governed by nibbling, it is the large engulfment events that account for the overall rate of entrainment [2]. This, in turn, makes importance of accurate detection and good resolution of the multiple scales in the TNTI abundantly clear. The different methods developed over the years each have a distinct set of strengths and weaknesses with respect to this, which will be analysed with a particular focus on their suitability to experimental investigations in air flows.

2 Velocimetric Detection of the TNTI

As the TNTI definitionally decomposes a flow into its turbulent and non-turbulent parts, there are a few methods of detection which naturally present themselves when velocimetric data for the flowfield is available. Although advances in computing power have made DNS of turbulent wall-bounded flows available at ever-higher Reynolds numbers, investigations of these flows remain largely the domain of experiments. Consequently, the inherently high resolution of DNS which makes computing vorticity gradients trivial is not available - this limitation of using vorticity as a detection criterion is already noted by Westerweel et al., who identified that the thinness of the TNTI could pose a challenge for the resolution of gradients using PIV [18]. Other limitations imposed by the large variation in TNTI height and the presence of free-stream turbulence have also been identified [2, 15].

Chauhan et al. [2] proposed a criterion based on thresholding local turbulent kinetic energy (TKE) levels in order to provide a more practical detection method. However, uncertainty in estimating u' must be low, the freestream turbulence intensity must be known, and the mean flow must be sampled sufficiently to obtain converged statistics with low uncertainty [2, 15]. Reuther and Kähler further caution that in flows with pressure gradients, where large streamwise variations in U_∞ are present, the basic assumptions on which the TKE criterion is based no longer apply [15]. To address the inapplicability of the TKE criterion to flows which are unsteady, a TNTI detection method based on the homogeneity of the non-turbulent portion of the flow was proposed by Reuther and Kähler. For a well-conditioned wind tunnel and a reasonable choice of sampling window size, the local velocity at a coordinate, $U_{m,n} \approx \langle U \rangle$ in the non-turbulent region of the flow, thus allowing for straightforward discrimination between the turbulent and non-turbulent parts of the flow. Unlike the TKE criterion, however, the sampling window size must be relatively large to avoid the introduction of bias caused by the sharp gradients in the vicinity of the TNTI, reducing resolution [15].

3 Optical Detection of the TNTI

While the TNTI can be defined mathematically, perhaps the most striking and natural way to identify it in a flow is through visualisation. It can be expected that the spatial resolution of a purely visualisation-based approach is set by the pixel resolution of the camera used for imaging, representing a significant improvement over the vector-spacing based limits of the TKE and homogeneity criteria [15]. Unfortunately, while this is conceptually and practically straightforward, the lack of velocimetric information would significantly limit the scientific value of such a measurement. By using fluorescent dye as a tracer, Westerweel et al. simultaneously applied LIF and PIV to study the wake of a turbulent jet in water. Notably, using PIV to calculate profiles of vorticity with respect to the detected interface matched the predictions made by Corrisin and Kistler in Fig. 1, with the presence of a sharp gradient across the interface [18]. This PIV-LIF approach to TNTI detection is, however, limited in its applicability to investigations of wall-bounded shear flows at large Reynolds numbers. Primarily, this is because these experiments are conducted in gas-flow facilities, where implementation of LIF is not possible without the use of different gas species [4].

3.1 Particle Image Density Criterion

The gas-flow analogue to dye visualisation in liquid flows is smoke-flow visualisation, and in a manner reminiscent of early visualisations of boundary layers, Reuther and Kähler devised an approach whereby DEHS seeding particles were used as a passive tracer. Notably, this dictates that *only* the turbulent portion of the flow should be seeded, in this case by injecting local seeding into the boundary layer at the start of the tunnel test section [15]. Logically, regions with particles are considered to be turbulent, and regions without are considered to be non-turbulent. A significant advantage of this technique is that the absence of particles in the outer flow means that there is a near step change in image intensity across the TNTI. This makes it particularly robust, as unlike the TKE and homogeneity methods, its sensitivity to the choice of a threshold value for binarisation is low [15]. However, this precludes global seeding (GS) of the flow, as the particle image density criterion does not reliably detect the TNTI with use of a combined global and local seeding approach despite the presence of a visually-identifiable interface [15]. Consequently, PIV evaluation of the entire FOV is not possible, and only the boundary layer itself may be quantified.

4 Fluorescent PIV

While it is possible to use PIV to investigate the TNTI with thresholding of higher-order derived quantities such as vorticity or (more realistically) TKE, or simpler statistical measures such as homogeneity of the velocity field, there is a significant amount of complexity and uncertainty associated with the choice of threshold and penalty in spatial resolution. Furthermore, these methods are not easily generalisable, and are recognised as being difficult to use for investigations involving more realistic flows that feature higher levels of background turbulence in the freestream [5]. Based on the known limitations of existing methods, an improved TNTI detection technique would be:

- Robust and insensitive to thresholding
- Flow-agnostic, i.e. independent of the statistical state of the flow
- Capable of preserving velocimetric information over the FOV
- Capable of resolving the multiscale nature of the TNTI

4.1 Fluorescent Seeding

The LIF + PIV method used by Westerweel et al. does, in fact, meet these criteria, and is accordingly a good conceptual basis. The key challenge lies in developing an analogous method compatible with large-scale investigations in gas flow facilities. Fluorescence has been used in air for simultaneous (but independent) measurement of mixing sprays by Towers et al., effectively working as a form of flow tagging [16]. Here, the mixing of two crossed nebulisers was studied by doping the water fed to one of them with Rhodamine 640 and isolating its fluorescent emission by imaging through a long-pass filter. A similar system, applied to a larger wall-bounded flow could represent a way of combining the advantages of the particle image density approach tested by Reuther and Kähler and the general working principles of the LIF + PIV method [18].

This proposal, however, imposes several requirements on the experimental set-up. Most fundamentally, the use of recirculating (Göttingen-type) wind tunnels must be ruled out; the local injection of fluorescing particles into the flow is only valid if there is no possibility of tagged particles entering the global seeding system. In the absence of effective filtration of all the seeding particles from the wind tunnel loop (which is impractical, if not virtually impossible), only open-return (Eiffel-type) facilities may be used. A further requirement is the use of a non-toxic tagging substance. A serious problem with many fluorescent dyes is that they pose a serious health risk to researchers and the general environment [7,8]. Furthermore, the large seeding volumes associated with studies at high Reynolds numbers in large open-return wind tunnels present an additional complication, as fluorescent dyes and particles doped to fluoresce are well-documented as being very expensive, and they are effectively “single use” [8,11]. Therefore, a crucial requirement is that the fluorescent tagging used be economically feasible for large experiments.

4.2 Proof of Concept

Recent work conducted by Okada et al. has shown the viability of using Pyrromethene 567 (P567) as a fluorescent dye for seeding air flows. It is soluble in Di-Ethyl-Hexyl-Sebacate (DEHS), a common seeding liquid for wind tunnels, and does not affect the physical properties of the generator fluid or the particle size distribution [8]. This means that it can be introduced to an experimental set-up without the need for specialised seeding equipment or a change to the basic assumptions about the tracer particles as they pertain to PIV measurements. Based on the simultaneous PIV measurements using Mie scattering and fluorescence in Towers et al. and the fluorescing DEHS solution developed by Okada et al., a new technique for segregating the turbulent and non-turbulent parts of a gas flow is proposed [9,16]. Namely, the freestream is globally seeded with regular DEHS particles, while the boundary layer is seeded locally using fluorescent DEHS particles generated from a solution of P567 in DEHS following the approach of Reuther and Kähler [15]. Simultaneous imaging with one camera

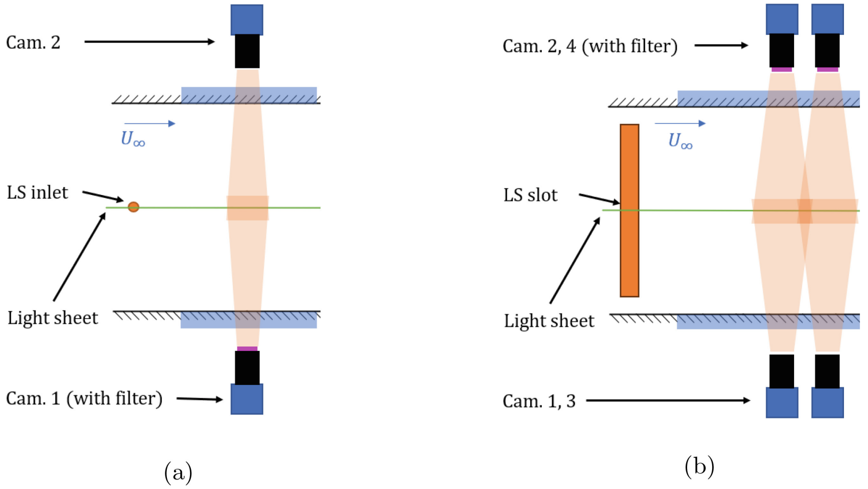

Fig. 2. (a) A top-down view of the test setup used to perform proof-of-concept experiments on the proposed fluorescent GS+LS approach described in Parikh et al., and (b) a top-down view of the updated TBL setup with local FPIV, from Okada et al. [8,10].

sensitised *only* to fluorescent emission with an optical filter and a second camera that is sensitive to all light allows for isolation of the locally-seeded region [10].

To explore the feasibility of the proposed technique, the boundary layer developing along the floor of the Atmospheric Wind Tunnel Munich (AWM) at the University of the Bundeswehr Munich was used as a test case by Parikh et al. [10]. The flow was globally seeded with (non-fluorescing) DEHS particles at the inlet tower of the AWM and local seeding was produced near the start of the test section with particles from a 1.60 g l^{-1} solution of P567. The streamwise-aligned wall-normal laser light sheet was generated using a low-speed dual-cavity Innolas Spitlight PIV 1000-15 Nd:YAG laser at an emission wavelength of 532 nm and pulse energy of 450 mJ. A pair of Imager sCMOS cameras were equipped with Zeiss Makro-Planar $f = 100$ mm lenses and placed on opposite sides of the wind tunnel. One camera was fitted with a 532 nm band-stop (notch) filter to be sensitive only to fluorescent emission. A schematic overview of the experimental set-up is shown in Fig. 2a.

This initial experiment was used to confirm that the use of FPIV was practical at large working distances. As seen in the exemplary images in Fig. 3 showing the raw Mie scattering and fluorescence-only particle images captured simultaneously, it is in principle possible to use fluorescence to isolate the local flow [10].

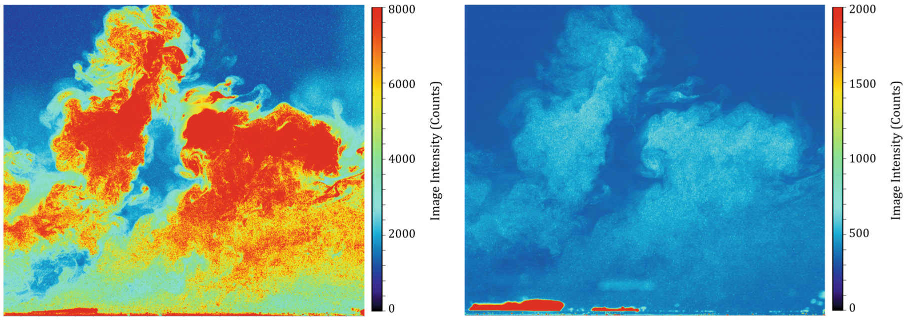

(a) (b)

Fig. 3. Raw particle images of the same FOV captured simultaneously with two cameras. The camera without a filter records all particles (a), and the camera with a notch filter is sensitive only to the fluorescent emission of particles in the LS zone (b). From Parikh et al. [10].

4.3 Post-processing

In order to extract useful information from the complementary datasets gathered, a number of approaches are possible. The first and perhaps most attractive approach is to follow the method in Towers et al. [16], where particles could be matched directly. In the experiment they describe, the imaged area seen by both cameras was made identical through the use of a complex system of mirrors. In order to apply this method to the experiment conducted in the AWM, the raw particle images first need to be dewarped by the application of a calibration, as the large working distances and size of the set-up make it functionally impossible to achieve an identical field of view with both cameras. The use of a polynomial calibration would enable correction for optical aberrations introduced by the lenses and theoretically reduce the error created when remapping the raw images. When attempted, this method had a very limited degree of success; although mapping and subsequent image matching was good, the distortions to the raw images introduced by applying the calibration made 1:1 pixel matching very difficult.

This is a practical issue in part due to the small imaged size of the particles as well as the difference in imaged intensity of the particles observed through Mie scattering and the particles observed purely through fluorescent emission. Although the apparent intensities of the particles can be corrected for, the difference in their imaged size is not so easily remedied. Although the application of a Gaussian filter to the images of the fluorescent particles helps somewhat, it is difficult to get a match that is of sufficiently high quality. However, the application of an erosion filter in combination with a Gaussian filter could be used as the basis for an alternative approach to post-processing the data.

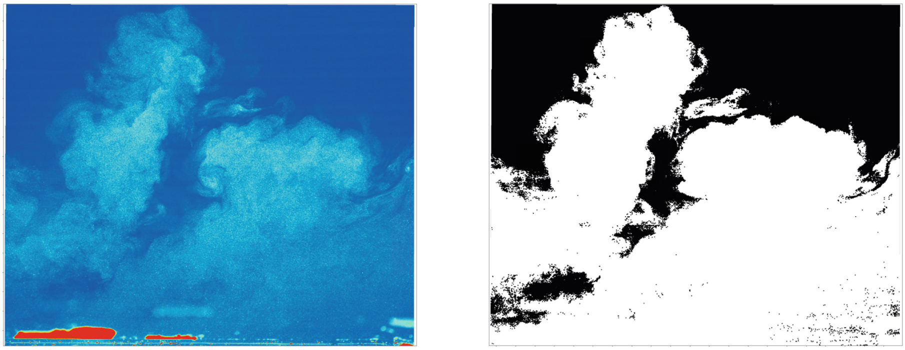

(a) Base image (b) 5 × 5 Erosion filter

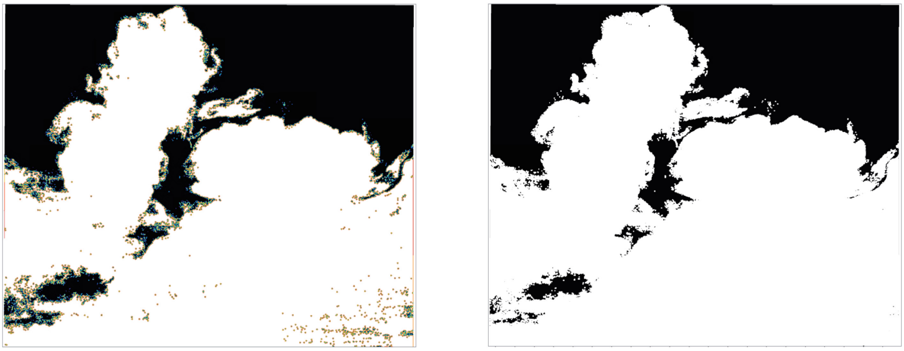

(c) 7 × 7 Gaussian filter (d) Binarised image

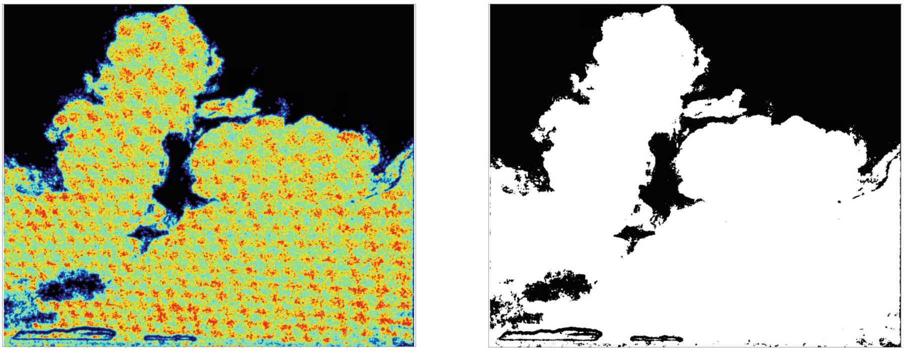

(e) PSD analysis (f) Binarised image

Fig. 4. The post-processing workflow when using a series of filters (a–d), and particle seeding density (a, e–f) illustrated for a single frame. Note that the coloured regions in (c) show where the Gaussian filter has smoothed out the blocky effects of the erosion filter.

As seen in Fig. 4a-d, the application of an erosion filter followed by the application of a Gaussian filter, over window sizes of 5×5 and 7×7 pixels, respectively, the area of the flow seeded with fluorescent particles can be delimited without generating a large amount of background noise. Followed by binarisation based on thresholding to the approximate intensity of the particles, a mask can be created, whereby the regions of the flow with fluorescent particles and those without are delimited. A variation of this approach is to directly use particle seeding density (PSD) rather than the erosion and Gaussian filters; in theory this introduces less error into estimation of the size and shape of the TNTI and entrained/extrained regions. The workflow is illustrated in Fig. 4e and f. Notably, however, it is more sensitive to reflections and leads to spurious binarisation of the particles - an effect that is best observed at the bottom left of the image.

4.4 TNTI Detection on a Large FOV

With confirmation of the technical feasibility of the dual GS+LS system with fluorescent particles discussed previously, the experimental set-up in Fig. 2a was modified to cover a larger FOV to ensure capture of the entire TNTI and the seeding system was updated to act as a trip to set the origin of the boundary layer being measured, see Fig. 2b. The FOV was expanded to a size of approximately $1.9\delta \times 3.9\delta$ in order to capture most extreme variations in instantaneous TBL height. 4000 images were collected to provide good statistical convergence of the dataset. As Mie scattering particle images (Fig. 5a) are available for the entire FOV, it was possible to compute velocity field using conventional 2D2C PIV and then overlay the detected TNTI, as shown in Fig. 5d. Based on a visual comparison of the binarised representation of the field and the TNTI, it is evident that this method is capable of resolving large and small scale features of the flow interface. However, certain regions of the TNTI are visibly filtered out, as is most clear in the centre of the FOV. This is believed to be a consequence threshold choice, and implementation of an analytical method, after the work of Prasad and Sreenivasan, is in progress [12].

5 Quasi-3D Reconstruction of the TNTI

While studies of turbulent flows have steadily been moving towards 3D measurements with tomographic PIV or 3D PTV methods, the TNTI has primarily been investigated in two dimensions. In part, this is due to the well-established difficulty associated with detection, but can also be partly attributed to the spatial and temporal limitations of current volumetric methods [13]. However, with modern calibration techniques, it is possible to dewarp and reconstruct images taken at stereoscopic viewing angles with good accuracy [13, 14]. With this and the particle image density detection method, Reuther demonstrated temporal tracking of the TNTI by imaging using a high-speed camera and a kHz laser system. At the measurement frequency and flow velocity used, the inter-frame convection distance of 1.4 mm was used to set the spacing of interface slices used for reconstruction, shown in Fig. 6 [14]. To reconstruct the interface, the slices were turned into a point cloud and interpolated using a spherical structuring element. A minimum radius of half the inter-slice spacing is required, however

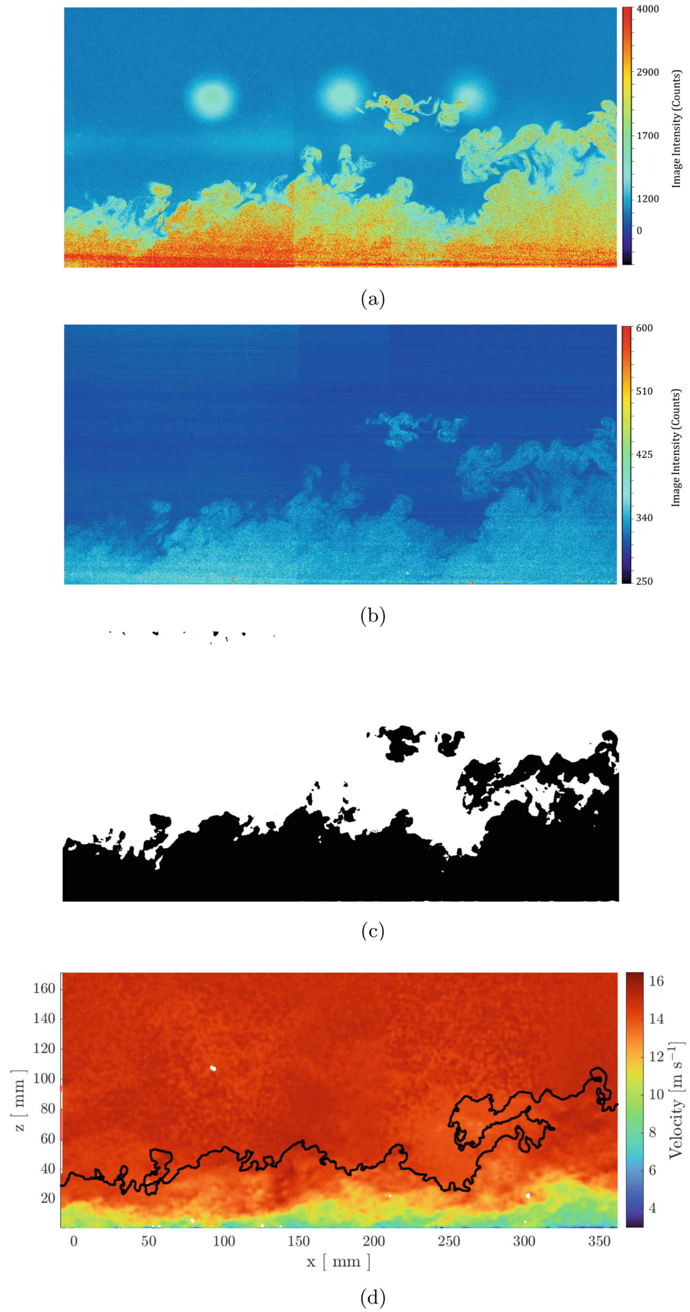

(a)

(b)

(c)

(d)

Fig. 5. Raw particle images of the same FOV captured simultaneously, Mie-scattering (a) and fluorescence-only (b). A binarised representation of the flow obtained using the PSD workflow (c), and the TNTI obtained from it overlaid on the global velocity field (d).

the practical size is somewhat larger as there are sharp gradients in the location of the TNTI between slices. Consequently, concave features of the 3D TNTI may be filtered away, but this is a necessary tradeoff to prevent the generation of a surface with many voids. Nevertheless, complex features of the interface are identifiable, including a large turbulent bulge in the centre of the domain. Reuther demonstrated this for a domain length of up to 8δ, and also performed the analysis at different freestream velocities.

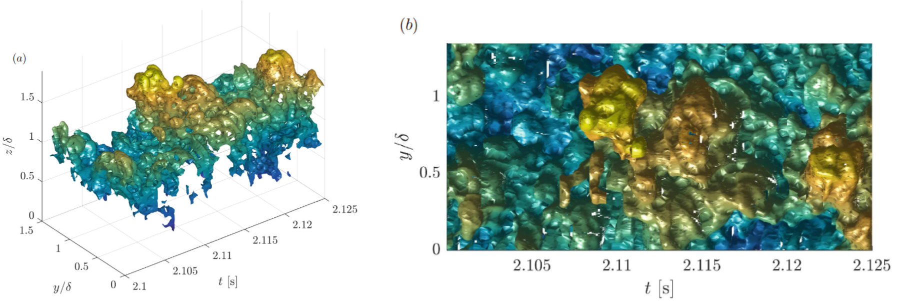

(a) (b)

Fig. 6. From Reuther [14]; isometric (a) and top-down (b) views of a 3D representation of the TNTI generated with high-speed imaging of a TBL. Warmer colours indicate greater distance from the wall.

The ability to reconstruct the TNTI in 3D represents an important step forward. Due to its connection to entrainment, characterisation of the fractal nature of the TBL through calculation of its fractal dimension, D_f, is a common diagnostic tool [2]. Reuther and Kähler applied the reconstruction method described to calculate D_f for a 3D TNTI with the aim of determining whether fractal properties are equal in all directions. The results shown in Table 1 indicate otherwise. With an increase in Reynolds number, the fractal dimension of an interface can be expected to grow as the flow hosts a broader spectrum of scales. Calculated two-dimensionally in the cross-stream wall-normal plane used for reconstruction, there is indeed a slight increase in D_f. The calculation of D_f for the reconstructed 3D TNTI, however, exhibits a greater relative change with increasing Reynolds number. This indicates that the increase in D_f, or the separation of scales, is not distributed isotropically, but rather exhibits a bias in the streamwise direction. Such behaviour can be rationalised by considering the "classical" slice of a TBL in the streamwise plane; the stretching and tilting of spanwise vortices into hairpin-like structures leads to the creation of large turbulent bulges associated with the intermittency in the height of the TBL. An additional observation is that despite the reduction in boundary layer height with increasing Re at a set location, the fractal dimension increases. This shows the shrinking of the smallest scales more than compensates for the slight shrinkage of the large scales ($\mathcal{O}\delta$). As entrainment is understood to be connected to "nibbling" at small scales, this further implies that the entrainment rate will, in general, increase with Reynolds number. Another more phenomenological insight the 3D reconstruction technique promises to provide relates to the detection of detached regions of the turbulent flow. In Westerweel et al.'s study of turbulent jets as well as Reuther and Kähler's study of the TBL, the question of "detrainment", i.e. the ejection of parts of the turbulent region into the potential flow, is raised [15,18]. In the case of TBLs, it is yet to be determined whether detached regions of flow, as seen in the centre of Fig. 5c, are indeed detached, or simply appear to be due to the location of the slice [15]. Combining the 3D reconstruction and fluorescent local seeding methods described and applying Taylor's frozen field hypothesis would make it possible to unambiguously classify these regions and answer a fundamental question about the behaviour of TBLs.

Table 1. Calculation of the mean fractal dimension D_f for the TNTI on a ZPG TBL in 2D and 3D at various freestream velocities. D_f for 2D is calculated in a cross-stream wall-normal plane. Unpublished data from Reuther.

U_∞ [m s^{-1}]	D_f, 2D [ ]	D_f, 3D [ ]
10	1.186 ± 0.022	2.203 ± 0.009
20	1.206 ± 0.028	2.286 ± 0.014
30	1.218 ± 0.032	2.339 ± 0.020

6 Conclusion

Investigations of the turbulent/ non-turbulent interface are increasingly common as optical detection techniques have become a standard diagnostic in experimental studies of turbulent wall-bounded flows. To better understand the nature of the transfer of momentum and mass between the turbulent and non-turbulent parts of the flow, accurate detection of the TNTI is crucial. Spatial filtering in PIV measurements of large-scale gas flows mean that detection of the vorticity jump across the interface is not practically possible, and other criteria must be used.

The TKE criterion introduced by Chauhan et al. shows good resolution of the small scales of the flow, but may filter out regions where the interfacial velocity approaches that of the freestream [2]. The flow must also be stationary on average and statistically converged, meaning that application to unsteady or pressure gradient flows is not possible [2,15]. Reuther and Kähler devised the flow homogeneity criterion to avoid these restrictions, but this comes at the cost of a reduction in spatial resolution and a failure to capture the small scales of the interface [15]. Detection by the use of a passive tracer, as performed on turbulent jets in water by Westerweel et al. is highly attractive. Imaging a boundary layer with only local seeding, Reuther and Kähler demonstrated the viability of using particle image density as a method by which to segregate the flow while unambiguously resolving the small and large scales of the interface [15]. However, the lack of velocimetric information about the external flow is a significant disadvantage. This limitation can now be overcome with the use of fluorescence to tag the locally-seeded portions of the flow. Experiments conducted by Parikh et al. and Okada et al. have shown the viability of simultaneously using fluorescing DEHS and normal DEHS to segregate the turbulent and non-turbulent portions of a boundary layer flow in air. This functions analogously to the passive tracer approaches of Westerweel et al. and Reuther and Kähler while obtaining the entire velocity field. The approach has been shown to work well with large FOVs, enabling good capture of the highly variable shape of the TNTI while yielding statistical information on the flow. This new development allows for the calculation of zonal statistics and could potentially be applied to better characterisation of the entrainment and detrainment behaviours of the TNTI.

Despite the large experimental effort focussed on detection of the TNTI and the increasing prevalence of 3D investigations of turbulent wall-bounded flows, analysis of the TNTI in 3D has not been performed. With the increased spatial resolution of passive scalar approaches, this may now be a possibility. The proof-of-concept 3D reconstruction of the TNTI on a turbulent performed by Reuther indicates that with the inclusion of velocimetric data, as promised by the fluorescent GS+LS approach, it may soon be possible to gain new insights about the nature of boundary layers.

References

1. Bisset, D.K., Hunt, J.C.R., Rogers, M.M.: The turbulent/non-turbulent interface bounding a far wake. J. Fluid Mech. **451**, 383–410 (2002). https://doi.org/10.1017/S0022112001006759
2. Chauhan, K., Philip, J., de Silva, C.M., Hutchins, N., Marusic, I.: The turbulent/non-turbulent interface and entrainment in a boundary layer. J. Fluid Mech. **742**, 119–151 (2014). https://doi.org/10.1017/jfm.2013.641
3. Corrisin, S., Kistler, A.L.: Free-stream boundaries of turbulent flows. NACA technical report 1244, NACA, Washington, D.C. (1955)
4. Danehy, P.M., et al.: Non-intrusive measurement techniques for flow characterization of hypersonic wind tunnels. NASA technical report NF1676L-31725, NASA Langley Research Center, Washington, D.C. (2018)
5. Hearst, J.R., de Silva, C.R., Dogan, E., Ganapathisubramani, B.: Uniform-momentum zones in a turbulent boundary layer subjected to freestream turbulence. J. Fluid Mech. **915**, A109 (2021). https://doi.org/10.1017/jfm.2021.102
6. Kovasznay, L.S.G.: Structure of the turbulent boundary layer. Phys. Fluids **10**(9), S25–S30 (1967). https://doi.org/10.1063/1.1762462
7. McKeon, B.J., et al.: Velocity, Vorticity, and Mach Number, chap. 5, pp. 215–472. Springer (2007). https://doi.org/10.1007/978-3-540-30299-5_5
8. Okada, M., Parikh, A., , Pinho, J., Kähler, C.J., Lavagnoli, S.: A fluorescent particle for PIV in gas phase flows. Exp. Fluids **65**(155), (2024). https://doi.org/10.1007/s00348-024-03889-8

9. Okada, M., Pinho, J., Lavagnoli, S.: Fluorescent tracer particles for PIV measurement in gas flows. In: Proceedings of the 20th International Symposium on Application of Laser and Imaging Techniques to Fluid Mechanics, vol. 20 (2022)
10. Parikh, A., Okada, M., Lavagnoli, S., Kähler, C.J.: Simultaneous fluorescent and mie-scattering PIV in gas flow. In: ISFV20 Book of Abstracts, vol. 20 (2023)
11. Pedocchi, F., Martin, J.E., García, M.H.: Inexpensive fluorescent particles for large-scale experiments using particle image velocimetry. Exp. Fluids **45**(1) (2008). https://doi.org/10.1007/s00348-008-0516-2
12. Prasad, R.R., Sreenivasan, K.R.: Scalar interfaces in digital images of turbulent flows. Exp. Fluids **7**, 259–264 (1989)
13. Raffel, M., Willert, C.E., Scarano, F., Kähler, C.J., Werely, S.T., Kompenhans, J.: Particle Image Velocimetry, 3 edn. Springer (2018). https://doi.org/10.1007/978-3-319-68852-7
14. Reuther, N.: Impact of the intermittent behavior on statistics in pressure gradient turbulent boundary layers. Ph.D. thesis, Universität der Bundeswehr München (2019)
15. Reuther, N., Kähler, C.J.: Evaluation of large-scale turbulent/non-turbulent interface detection methods for wall-bounded flows. Exp. Fluids **59** (2018). https://doi.org/10.1007/s00348-018-2576-2
16. Towers, D.P., Towers, C.E., Buckberry, C.H., Reeves, M.: A colour PIV system employing fluorescent particles for two-phase flow measurements. Meas. Sci. Technol. **10**(9) (1999). https://doi.org/10.1088/0957-0233/10/9/309. https://iopscience.iop.org/article/10.1088/0957-0233/10/9/309/pdf
17. Westerweel, J., Fukishima, C., Pedersen, J.M., Hunt, J.: Mechanics of the turbulent-nonturbulent interface of a jet. Phys. Rev. Lett. **95** (2005). https://doi.org/10.1103/PhysRevLett.95.174501. https://journals.aps.org/prl/pdf/10.1103/PhysRevLett.95.174501
18. Westerweel, J., Hofmann, T., Fukishima, C., Hunt, J.: The turbulent/non-turbulent interface at the outer boundary of a self-similar turbulent jet. Exp. Fluids **33**, 873–878 (2002). https://doi.org/10.1007/s00348-002-0489-5

The Effect of Background Turbulence on the Dynamics of Turbulent Jets and Entrainment Processes Across the Turbulent/Turbulent Interface

Susan J. Gaskin(✉) and Khashayar F. Kohan

Department of Civil Engineering, McGill University, Montreal, Québec H3A 0C3, Canada
susan.gaskin@mcgill.ca, khashayar.feizbakhshiankohan@mail.mcgill.ca

Abstract. Background turbulence disrupts the jet structure resulting in its rapid decay (mean velocity and passive scalar concentration) and a reduced entrainment, before jet breakdown when only turbulent diffusion acts. The effect of the background turbulence is characterized by its relative length scale, $\mathcal{L}$, and turbulence intensity, ξ, with ξ dominating the jet dynamics in the self-similar region. Large scales of the ambient turbulence advect the jet. Jet breakdown occurs at $\xi = 0.5$, while for $\xi < 0.5$, entrained small scales cause faster decay of the jet's large vortical structures and transfer of their energy to smaller scales. They also increase the jet rms increasing the radial scalar transport and differential diffusion, thereby increasing the mixing. Entrainment occurs across the turbulent/turbulent interface, the TTI, identified by a larger sharp jump in mean and rms passive scalar concentration, which is longer, more tortuous and has a higher fractal dimension than its quiescent counterpart, the TNTI.

Keywords: jets · background turbulence · turbulent entrainment · turbulent/turbulent interface

1 Introduction

In Civil Engineering, the ubiquitous discharge of effluents into rivers, lakes and coastal regions motivates the study of entrainment and turbulent mixing in jet flows as dilution is relied on to reduce the local impact of the pollutants. Understanding of jet mixing and dilution is also required in other contexts, e.g. chimney plumes, volcanic plumes, exhaled breaths (infection risk) and in other turbulent shear flows, e.g. wakes (windfarm layout), boundary layers (friction), and coaxial jets (noise). Although in engineering contexts the jet is released into turbulent background flows, predictions are based on laboratory studies in quiescent conditions. Twenty-five years ago, this was assumed to be conservative due to the assumed superposition of jet driven entrainment and of turbulent diffusion due

J. Wang and I. Marusic (Eds.): IUTAM-TNTI 2024, IUTAM Bookseries 45, pp. 32–47, 2025.
https://doi.org/10.1007/978-3-031-78151-3_3

to the ambient turbulence, an assumption not challenged due to the difficulty in creating an approximately homogeneous and isotropic turbulence (HIT) in the laboratory. The historical understanding of the effect of turbulent ambient flows on the dynamics of turbulent jets is reviewed. The changes to the decay of the velocity and passive scalar fields, and to the geometry of the jet/ambient interface are interpreted, demonstrating the reduced entrainment and increased mixing in a jet released into a turbulent ambient.

2 Integral Properties of Jets and the Conceptual Models of Entrainment Processes (pre-1990)

Entrainment, the net transport of fluid from a less turbulent to a more turbulent flow, can be described as due to an entrainment velocity, E_v, towards the interface between the turbulent shear flow and the ambient fluid resulting in a net outward motion of said interface at a boundary velocity E_b; see Fig. 1 [1]. For a turbulent axisymmetric jet in a quiescent ambient, in the self-similar region, entrainment occurs as a radially inward velocity that is proportional to a characteristic jet velocity [2], known as the entrainment hypothesis. The constant of proportionality α is of $\mathcal{O}(0.1)$, in both momentum and buoyancy driven flows, although is not universal [3]. The jet's mean centerline axial velocity and passive scalar are inversely proportional to downstream distance ($\overline{u_c} \propto x^{-1}, \overline{\phi_c} \propto x^{-1}$) and the jet velocity and passive scalar half-width are proportional to downstream distance ($\overline{b_{u,1/2}} \propto x, \overline{b_{\phi,1/2}} \propto x$) (e.g. [4]). This results in conservation of the mean momentum flux and the mean passive scalar flux with downstream distance ($M/M_0 \approx 1, F/F_0 \approx 1$). The normalized root mean square (rms) of the axial centerline velocity and scalar fluctuations asymptote to a constant value ($u_{rms,c}/\overline{u_c} \approx 0.25, \phi_{rms,c}/\overline{\phi_c} \approx 0.22$) [5]. Scalar profiles are slightly wider than the velocity profiles and increase at a slightly greater rate. Jet behavior is nominally independent of initial Reynolds number resulting in constant local Reynolds number [4].

The entrainment hypothesis of Morton, Taylor and Turner [2] provides robust predictions of entrainment rates, but does not describe the mechanisms of entrainment. Townsend's [6] equilibrium hypothesis describes engulfment, a large-scale inviscid process, in which large scale vortical structures of the turbulent flow fold-in and engulf ambient fluid subsequently mixed by small scale turbulence and molecular diffusion. Nibbling, as first described by Corrsin and Kistler [7] is a small-scale process of viscous and molecular diffusion transporting vorticity and scalars into the ambient along the outer edge of the primary turbulent flow, the turbulent/non-turbulent interface (TNTI) or the turbulent/turbulent interface (TTI). This thin layer propagates outward at the local entrainment velocity, v_n, whose thickness and velocity are of the order of the Kolmogorov microscale and velocity, respectively. The local entrainment occurs due to the small-scale vorticity structures, which increase the interfacial area, while the global entrainment rate is determined by the large-scale vortical structures, which induce the entrainment velocity [2]. Engulfment was first considered to be the dominant entrainment mechanism [8], until a numerical study indicated the possible dominance of nibbling [9].

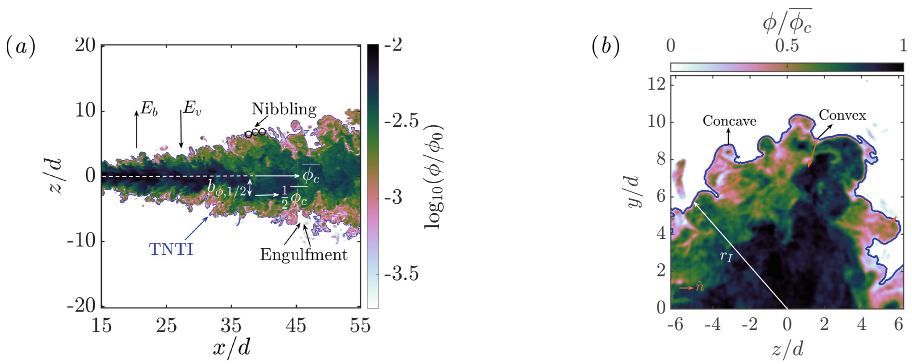

Fig. 1. (a) Sketch of a jet in a quiescent ambient showing the entrainment velocity, E_v, driven by the mean flow resulting in an expansion of the jet at an interface velocity, E_b, via the entrainment mechanisms of engulfment and nibbling (after [1]). The TNTI and scalar 'holes' are shown with the blue and magenta lines, respectively. (b) Selected geometric features of the TNTI, cross-section at $x/d = 50$ [10]. Here, ϕ_0 and $\overline{\phi_c}$ denote the jet-exit and ensemble-averaged centerline concentrations.

3 Changing Perspectives on the Effect of Background Turbulence on Buoyant Jet Flows in the '90 s from Increased to Reduced Entrainment

Two reviews on jet and plume behaviour from 1982 summarized the power law behavior of the main integral properties of mean trajectory, velocity, scalar concentration, and width of jets and plumes [3,11]. The effect of ambient turbulence on jet dilution was identified as a gap in knowledge [11]. Engineering models of buoyant jets (e.g. EPA model CORMIX [12]) neglected the influence of background turbulence until far downstream when the jet motions are negligible and only turbulent diffusion acts, while an additional term to account for the additional jet spread due to turbulence was hypothesized [13].

An early study on an advected line thermal, as a model of the limiting behaviour of a buoyant jet in a co- or crossflow, demonstrated that turbulence in the ambient flow resulted in more rapid decay and breakup of the jet structure [14]. The vortex pair structure, which drives entrainment due to its circulation, persists for long distances in a quiescent ambient, but was rapidly broken down in the approximately HIT ambient due to the smaller eddies in the turbulence, while the larger eddies resulted in its oscillation about it mean trajectory and a greater ensemble mean width growth [14]. The study concluded that the ambient turbulence disrupts the vortex pair structure, after which dilution is due mainly to turbulent diffusion [14]. The limitation of this study was the high intensity of the turbulence resulting in a very rapid disruption of the vortex pair structure.

In 1994, a revised entrainment hypothesis in support of the assumption of the superposition jet dilution and turbulent diffusion was proposed, in which a term is added to account for the jet entrainment due to ambient turbulence (based on a review of existing experimental data) [15], while Hunt [16] hypothesized that any tendency to break up a jet would tend to decrease the entrainment velocity. He suggested that when the entrainment velocity into the jet, E_v, was larger than the rms velocity of the external turbulence, $u_{rms,\infty}$, the external turbulence is entrained and does not affect the rate of spread, while, when E_v is of the order of $u_{rms,\infty}$, the self-preserving structure of the jet changes and the entrainment velocity decreases allowing the diffusing action of the turbulence to more effectively disperse the jet. In the following years, studies on the effect of background turbulence, produced with an oscillating grid, on jets and line plumes concluded that once the ratio of the turbulence intensity of the background flow to that of the jet or plume, ξ, reached a threshold $(2.5 - 25)$ the ambient eddies were no longer entrained as a passive substance, but broke down the plume [17] or jet [18,19] resulting in the observed greatly increased rate of spread, interpreted as increased dilution. However, the observations were limited by the experimental configuration, in which a decreasing jet turbulence evolved in an increasing ambient turbulence level and rapidly changing ratio of ambient to jet turbulence intensity [20].

The question on the effect of ambient turbulence on entrainment was framed next by considering the integrated momentum equation to the second order for a pure axisymmetric jet [20]

$$M_0 = 2\pi \int_0^\infty \left[\overline{u}^2 + u_{rms}^2 - \frac{1}{2}\left(v_{rms}^2 + w_{rms}^2 \right) \right] r\mathrm{d}r \tag{1}$$

where u', v', w' are the turbulent jet velocities in the axial and transverse directions [4]. The first term and second terms are due to the mean and rms jet velocity, respectively, while the third is due to the streamwise mean pressure variation. In a stagnant quiescent ambient, the contribution of the jet turbulence (rms) to the momentum integral is approximately 10% of that of the mean velocity [4]. The open question was whether and how ambient turbulence affected entrainment before jet break-up and whether the relative importance of the entrainment mechanisms changed [20].

In experiments on a plane jet in a shallow co-flow with five increasing levels of background turbulence [0%, 5–8%, 8–10%, 10–12%, 12–15%], jet velocities were measured by hot film anemometry and concentrations from greyscale levels of digital images [20,21]. Mean velocity decay increased with increasing turbulence intensity, while flow visualization illustrated the disruption of the jet structure and the resulting reduced entrainment rate (inferred from suppressed width growth) before jet break-up, followed by turbulent diffusion, which increased with turbulence intensity [20,21]. Jet driven entrainment was suppressed as per the Morton, Taylor and Turner [2] entrainment hypothesis and large scale engulfment reduced [21]. These results refuted the assumption of superposition of jet driven entrainment and turbulent diffusion, and were the first confirmation of Hunt's hypothesis that background turbulence will result in reduced entrainment due to break-up of the jet [20,21].

4 An Axisymmetric Turbulent Jet in a Turbulent Background: Jet Dynamics and Entrainment Processes Across the TTI

The axisymmetric jet flow permits a direct study of the effect of background turbulence on the jet structure, jet turbulence, entrainment rate and self-similarity based on the velocity and scalar field statistics [22–24], while mixing is inferred from differential diffusion [25]. As entrainment occurs through the TTI, entrainment mechanisms are inferred from its topology [10,26].

A better approximation to a HIT ambient was produced with a random jet array (RJA), in which jets, within a planar array, are randomly and independently activated [27,28]. In 2005, an RJA was built in a 1.5 × 2.4 × 0.9 m^3 open glass tank consisting of a planar array of 6 rows and 10 columns of jets (using bilge pumps for a zero net mass flow rate) at a spacing of M = 150 mm with a reflective boundary condition [25]; see Fig. 2. The jets were independently turned on and off for time intervals randomly selected from a normal distribution with (μ_{on}, σ_{on}) of (12, 4) s and $(\mu_{off}, \sigma_{off})$ of (108, 36) s resulting in 10% of jets on, on average [29]. The characteristics of the zero-mean flow RJA-generated turbulence in terms of the isotropy, $w_{rms}^{RJA}/v_{rms}^{RJA}$, turbulent kinetic energy (TKE), $k_\tau = 1/2\left[2\left(w_{rms}^{RJA}\right)^2 + \left(v_{rms}^{RJA}\right)^2\right]$, the turbulent Reynolds number, $Re_\tau = u_\tau l_\tau/\nu$, where the characteristic velocity $u_\tau = (2k_\tau/3)^{1/2}$ and l_τ the integral length scale is calculated from the spatial autocorrelation function of the streamwise velocity fluctuation, and the Taylor Reynolds number, $Re_{\lambda,\tau} = \left(\sqrt{150 k_\tau} l_\tau/\nu\right)^{1/2}$ are given in Table 1 [22,26,29]. The isotropy in the RJA plane was approximately 1.0. The skewness in the RJA plane (u, w) is close to zero, while normal to the plane (v) it is ≈ 1. The kurtoses were all super Gaussian (4.8 ± 0.8) [22,29].

The jet experiments were conducted in the approximately HIT (i: T2 and ii: T1, T2, T3, where i refers to experiments in §4.1 and ii to those in §4.2) in an open glass tank (1.5 × 2.4 × 0.9 m^3) equipped with the RJA. A constant turbulence level was maintained along the jet axis by issuing the axisymmetric jets, with $Re = 5800$ and 10600, from a pipe ($d = 8$ mm) oriented parallel to the plane of the RJA, see Fig. 2. The velocity field of the jet was measured using an ADV (25 Hz) or by flying hot-film anemometry [22]. The scalar concentrations of jet cross-sections at distances from $x/d = 20$ to 60 were obtained using planar laser induced fluorescence (PLIF) [23,24,26]. The dyed jet fluid was excited by a laser sheet (1.5–2 mm thick) formed with a continuous mode laser (1W, i: 514.5 nm or ii: 532 nm) reflecting off an octagonal mirror rotating at 12000 rpm. The fluorescence emitted by the dyed jet fluid (i: disodium fluorescein, $Sc = 2000$ or ii: Rhodamine 6G, $Sc = 2500$) was low pass filtered, captured by a 12

Table 1. Characteristics of the background turbulence. Note that w_{rms}^{RJA} and v_{rms}^{RJA} signify the rms velocity fluctuations of the RJA-generated turbulence along the $z-$ and $y-$coordinates, respectively.

Case	y/M	Isotropy ($w_{rms}^{RJA}/v_{rms}^{RJA}$)	TKE ($\mathrm{cm}^2\,\mathrm{s}^{-2}$)	$u_\mathcal{T}$ ($\mathrm{cm\,s}^{-1}$)	$l_\mathcal{T}$ (cm)	$Re_\mathcal{T}$	$Re_{\lambda,\mathcal{T}}$
T1	9.3	0.77	2.64	1.33	11.6	1540	152
T2	7.3	0.72	4.44	1.72	11.0	2000	173
T3	5.5	0.62	8.28	2.35	7.5	1760	163

bit CMOS digital camera (pco.dimax, 2016 × 2016 pixels) at i: 30 or ii: 50 Hz and, following a calibration, converted to scalar concentrations [23,26,38]. The resolution of the images was in the range of 1.4 to 7.3 Kolmogorov microscales (i: 0.4 mm/pixel and ii: 0.13, 0.25 mm/pixel) [23,24,26]. The measurements were validated against studies in the literature [22–24].

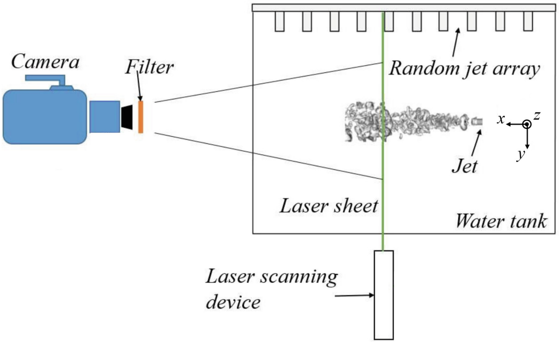

Fig. 2. Layout of experimental apparatus for axisymmetric jet experiments [23].

4.1 Jet Dynamics

The turbulent jet released into a HIT (Case T2) is subject to increasing relative turbulence intensity, $\xi = u_\mathcal{T}/u_{rms,jet}$ and decreasing relative length scale, $\mathcal{L} = l_\mathcal{T}/b_{\phi,1/2}$ as shown in Fig. 3(a) for jets of $Re = \{5800, 10600\}$ for downstream distances of $x/d = \{20, 30, 40, 50, 60\}$ [23]. Turbulent eddies greater than the jet half-width, $\mathcal{L} > 1$, cause the jet path to meander, which can be quantified by the standard deviation of the distance of the jet center of mass to the nominal jet axis; see Fig. 3(b,c) [23]. When $\mathcal{L}$ and ξ are of $\mathcal{O}(1)$, ξ has the dominant effect in the self-similar region [26,30]. The effect of ξ on the jet is obtained by conditioning the averages on the jet center of mass to effectively remove the effect of $\mathcal{L}$ (hereafter referred to as conditional averages) [23].

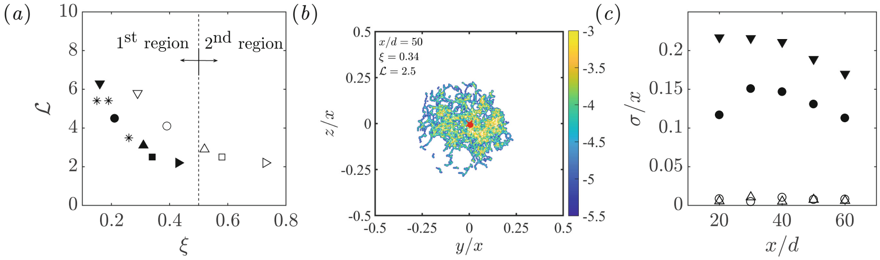

Fig. 3. (*a*) Relative turbulence intensity, ξ and relative length scale, $\mathcal{L}$, at axial distances of, i: $x/d = \{20, 30, 40, 50, 60\}$ in T2 [23] and, ii: $x/d = 25$ (*) in T1, T2 and T3 [26], from left to right, for jet $Re = 10600$ (solid), $Re = 5800$ (open). (*b*) Example of isocontours of the JPDF of the position of the jet center of mass in the HIT (T2) with $\xi = 0.34$ and $\mathcal{L} = 2.5$. (*c*) Normalized standard deviation (σ/x) of the distance of the jet center of mass to the nominal jet axis for $Re = 10600$ (○), $Re = 5600$ (▽), in quiescent (open) and HIT (T2) (solid) [23].

Reduced Entrainment and Rapid Jet Decay. In background turbulence, the jet structure is progressively disrupted such that two regions are observed [23]. In the first region, the larger scales of the turbulence cause the trajectory to meander, while the smaller scales are entrained disrupting the jet structure, resulting in a faster decay and reduced entrainment. The second region starts once the jet structure has been destroyed by the background turbulence, thus it has no entrainment and is subject only to turbulent diffusion [23]. The relative length of the perturbed jet region depends on the relative turbulence intensity as the jet is observed to be destroyed at $\xi = 0.5$ [23].

The increased rate of decay of the velocity by the background turbulence, shown ensemble averaged [22], Fig. 4(*a*,*b*), will result in a decrease in the jet entrainment according to the entrainment hypothesis [2]. The jet passive scalar concentration also has an increased rate of decay, for both the ensemble and conditional average; see Fig. 4(*a*, *b*) [23]. The velocity and scalar half-widths show an increased rate of spread in the turbulent background compared to the quiescent case until jet break-up [22,23]; Fig. 4(*c*, *d*). The destruction of the jet structure at $x/d = 40$ for $Re = 5800$ and beyond $x/d = 60$ for $Re = 10600$, Fig. 4(*d*), is shown by the lack of increase in the conditionally averaged width, noting that the conditional average reflects only the effect of the small scales of the HIT on jet evolution [23]. Intermittency profiles corroborate the location of the jet break-up and the comparison of the ensemble to conditionally averaged profiles indicate the degree of jet meandering [23]. Self-preservation of the jet is maintained when the product of the normalized mean centerline velocity, $\overline{u_c}/u_0$, and the normalized half-width, $b_{u,1/2}/d$ scales to a constant [4], which is observed for the jet velocity and scalar in a quiescent background ($\overline{\phi_c}/\phi_0 \times b_{\phi,1/2}/d \propto x^0$) [4,23]. The jet in a turbulent background demonstrates self-preservation before break-up, i.e. $\overline{\phi_c}/\phi_0 \times b_{\phi,1/2}/d = x^{-1.1} \times x^{1.1} \propto x^0$) [23]. This self-preservation is not evident from the ensemble averaged data, as it includes the meandering of the jet path by the large scales of the turbulence. Self-similarity can be shown by the collapse of the normalized concentration profiles [23]. The entrained ambient turbulence increases the turbulent velocity fluctuations in the jet (ensemble averages), which decay rapidly, reaching the level of the background turbulence shortly after jet break-up [22], while the scalar fluctuations are also increased, decreasing more rapidly with downstream distance; see Fig. 4(*e,f*) [23]. The difference in the ensemble and conditional average indicates the contribution due to jet meandering (20 - 30%), which ceases after jet breakup.

The reduction in the entrainment into a jet in a turbulent background flow can also be inferred from the mean momentum flux ($M = 2\pi \int_0^\infty \overline{u}^2\, r\mathrm{d}r$) and mean scalar flux ($F = 2\pi \int_0^\infty \overline{u}\overline{\phi}\, r\mathrm{d}r$) along the jet. In a quiescent background flow, both the momentum and scalar flux are approximately conserved as they contribute 90% and 92% to the total momentum and scalar flux [4,31]. In a turbulent background, the contribution of the mean fluxes to the total fluxes decreases approaching zero by $\xi = 0.58$ [23,24,32]; see Fig. 5, as the the jet structure is disrupted, reducing the mean velocity and resulting in an increase in the transfer of energy from the large scales to the small scales [33].

Increased Jet Mixing Inferred from Differential Diffusion. Increased differential diffusion of passive scalars occurs in a turbulent jet when molecular diffusion effects are more pronounced, occurring at jet/ambient interfaces [34,35] or regions of increased density of high concentration gradients. Experiments quantified differential diffusion in a turbulent jet in a turbulent background flow and compared it to that in the quiescent background case [25].

The axisymmetric jet of $Re = 10600$ containing two passive scalars was released into a quiescent ambient and into a HIT (Case T2, see Table 1). The jet was dyed with two fluorescent dyes, disodium fluorescein and sulforhodamine 101 with Schmidt numbers of 2000 and 5000 respectively [25]. At $x/d = 50$, a 514.5 nm laser beam (1.5 W) excited the dyes, whose emitted light was captured by two photomultiplier tubes as a pulsed signal of 150 μs at 650 to 1600 Hz (i.e. greater than the Kolmogorov frequency) at a resolution of $100 \times 100 \times 100\ \mu\mathrm{m}^3$, and converted to concentrations [36].

The differential diffusion is quantified by the rms of the normalized concentration difference, Z_{rms}. It is approximated up to the Kolmogorov scale by integrating its spectrum, $E_z(\kappa_1)$ from $\kappa_1\eta = 0$ to 1, where κ_1 is the longitudinal wavenumber, and $Z \equiv \phi_1/\overline{\phi_1} - \phi_2/\overline{\phi_2}$ is the concentration difference [37].

For a jet in a quiescent ambient, Z_{rms} decreases with increasing Reynolds number, but remains significant above the mixing transition ($Z_{rms} = 0.064$ at $Re = 10600$); see Fig. 6(a) [36]. The presence of differential diffusion at scales larger than the Kolmogorov time scale is indicated by non-zero Z_{rms} in time series plots for periods greater than this scale [36]. In HIT, the differential diffusion in a turbulent jet is greater at all radial locations than that in a quiescent background, and double at the centerline (Fig. 6a) [25]. In the quiescent background, there is a central region of the jet ($r/x < 0.08$) in which Z_{rms} is fairly constant after which it increases rapidly, while in the turbulent background

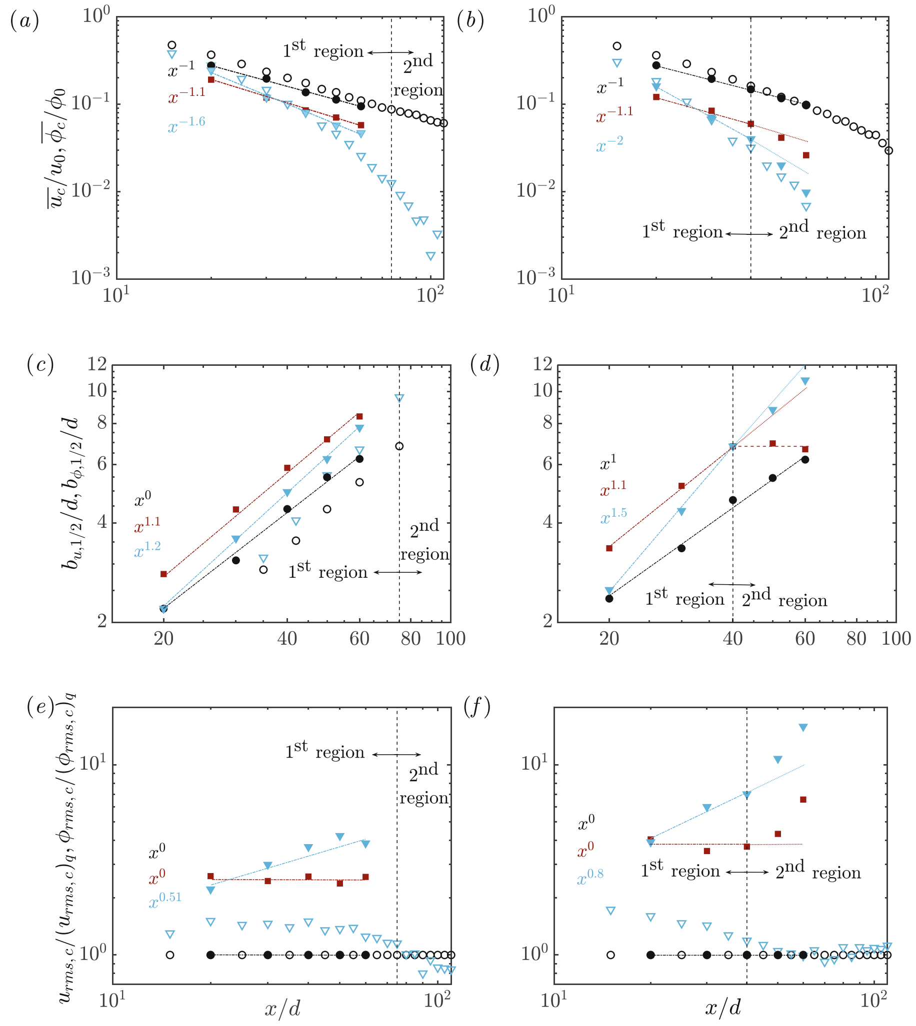

Fig. 4. Downstream decay of mean velocity and scalar concentration for (*a*) $Re = 10600$ and (*b*) $Re = 5800$. Downstream evolution of the velocity and scalar concentration half-width for (*c*) $Re = 10600$ and (*d*) $Re = 5800$. Downstream evolution of the relative velocity and scalar fluctuations for (*e*) $Re = 10600$ and (*f*) $Re = 5800$. Symbols: ○, ▽, □ are quiescent, ensemble averaged and averages conditioned on the center of mass of the jet in HIT (T2). Solid and open symbols are scalar and velocity statistics, respectively [22,23].

Z_{rms} increases linearly with radial position [25]. In the quiescent background, the PDFs of Z_{rms} are almost Gaussian at the centerline but become positively skewed ($S_z = 0.20$) and super Gaussian ($K_z = 7.65$) at $r/x = 0.125$, while in the turbulent background, the PDFs are positively skewed and super Gaussian at

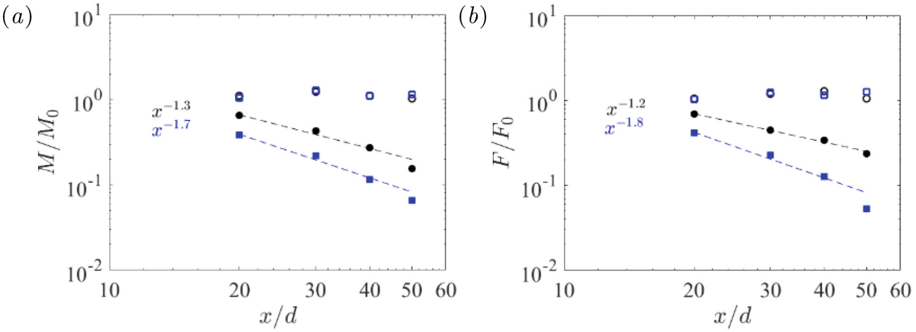

Fig. 5. The effect of background turbulence on the decay of (*a*) the mean momentum flux and (*b*) the mean scalar flux. Symbols: □ *Re* = 5800, ○ *Re* = 10600, open and closed symbols: quiescent and HIT background [23, 24].

the centerline and become more so with radial distance ($S_z = 0.16$ and 1.24 and $K_z = 6.3$ and 24 at the centerline and $r/x = 0.125$, respectively [25]) indicating greater instances of large fluctuations of Z_{rms}.

In summary, greater differential diffusion occurs in the jet in a turbulent background as the entrainment of the small scales of the background turbulence increases the rms velocity, thereby increasing the density of steep concentration gradients and the mixing. The linear increase in differential diffusion with radial position (in comparison to the quiescent background) indicates a greater outward radial transport of scalars. Note that the differential diffusion is underestimated as the averages are ensemble averages and so include the effect of the meandering of the jet path by the larger scales of the background turbulence.

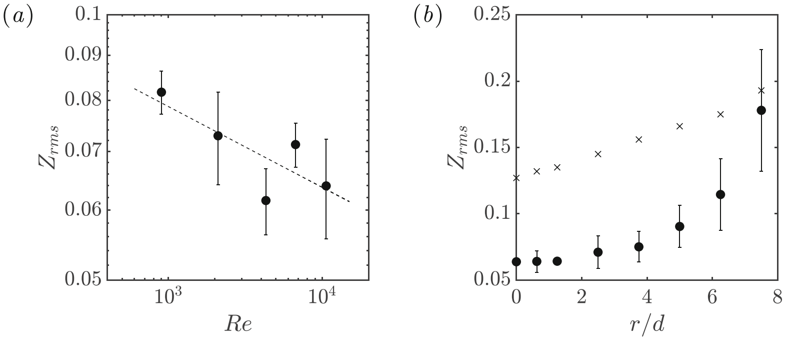

Fig. 6. (*a*) Reynolds number dependence of the differential diffusion, Z_{rms}, on the jet centerline in a quiescent ambient. The dashed line represents the best power-law fit to the data. (*b*) Radial profiles of Z_{rms} in a quiescent (○) and HIT (×) background. Data for *Re* = 10600 at $x/d = 50$ [25].

4.2 The Interfacial Layer Between the Jet and the Ambient

Entrainment into the jet occurs across the finite thickness of the TNTI or TTI at a global entrainment rate driven by the jet's large vortical structures [2], which induce an entrainment wind, E_v and contort and expand the interface area through which the ambient fluid is entrained. Entrainment occurs primarily by nibbling, a small-scale viscous process, by which the interface expands into the ambient flow at a local entrainment velocity, v_n, and with a small contribution to entrainment from large-scale inviscid engulfment [1]. In an irrotational ambient, the interface (TNTI), characterized by a sharp vorticity jump, is composed of a very thin outer layer, called the viscous superlayer (VSL), δ_v, which transports vorticity into the ambient by viscous diffusion with negligible inviscid vortex stretching at the local entrainment velocity, v_n, ($\mathcal{O}(u_\eta)$, u_η is the Kolmogorov velocity scale) [7]. The outer edge of the VSL is defined by an iso-surface with a zero rate of change of entrophy (note the zero enstrophy in the ambient) [1] and it has a thickness of $\overline{\delta_v} \approx 4 - 5\eta$ [39]. A turbulent sublayer (TSL), δ_σ, in which inertial effects become important (e.g. [1]) of thickness $\overline{\delta_\sigma} \approx 10\eta$ extends from the VSL to where enstrophy is comparable to that of the turbulent core, resulting is a total thickness of the TNTI of $\approx 15\eta$ [39]. In a turbulent ambient, the presence of turbulence on both sides of the interface (TTI), still defined by an enstrophy jump [30], results in a reduction of the viscous diffusion of vorticity [40], experimentally observed in a wake to be more than an order of magnitude smaller than that of inertial vorticity stretching [40]. Thus, the thickness of the VSL is reduced and the jump in vorticity at the TTI is mainted by vorticity stretching [40].

The entrainment flux into the jet is the product of the local entrainment velocity, v_n, and the area of the interface. The interface topology is a result of the multi-scale nature of the entrainment [41], which can be characterized by a fractal analysis. The TTI is has a greater tortuosity than the TNTI, which, in a wake, increases with ambient turbulence intensity [30]. The topology of the TNTI has been linked to the local entrainment process, with enhanced entrainment at convex segments (valley) compared to concave segments (bulge) [42,43] and at locations closer to versus further from the jet centerline [44]. Along the TNTI, higher values of passive scalar are associated with large vorticity structures, as indicated by low curvature, small interface angle and large radial distance, while small vorticity structures, having high interface curvature, higher interface angle and small radial distance, are found where concentrations are lower [10].

Topology and Entrainment Mechanisms of the TTI. The topology of the jet interface is modulated by the presence of turbulence in the ambient, whose effect on the jet dynamics and entrainment is informed by an investigation and characterization of the TTI compared to the TNTI [26]. The outline of the TNTI and TTI are found by applying a threshold, ϕ_t, to the instantaneous scalar concentration fields of the jet cross-sections [10,26]. The characteristics of the scalar jump and of the interface topology are observed in the far-field ($x/d = 25$) in a quiescent ambient and, in the first jet region [23],in increasing levels of HIT

(T1, T2 and T3, see Fig. 3*a* and Table 1). The scalar jump is identified along conditionally averaged profiles directed along the local interface normal direction ($x_n \geqslant 0$ and $x_n < 0$ representing jet and ambient regions, respectively). A sharp scalar mean and rms scalar jump occurs at the TTI as at the TNTI, which is steeper than that of the TNTI and increases in magnitude see Fig. 7(*a*,*b*) [26] and increases slightly in width [38] with increasing turbulence intensity. The greater jump at the TTI is hypothesized to reflect enhanced radial transport due to the greater jet scalar rms, as shown in Fig. 4(*e*,*f*) [23] and as inferred from the increased differential diffusion, see Fig. 6(*b*) [25], in a turbulent ambient.

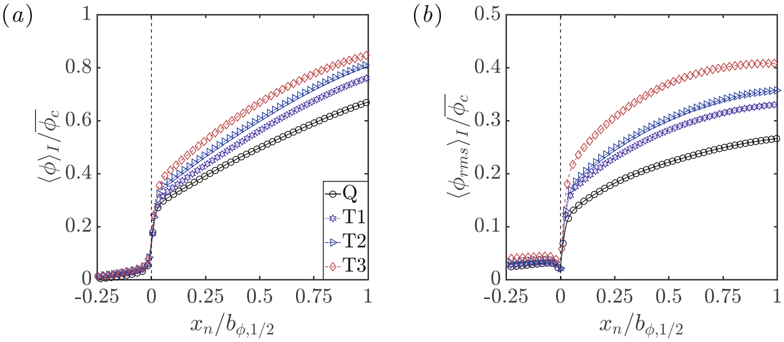

Fig. 7. Conditional profiles of (*a*) mean and (*b*) rms concentration. The boundary of the TNTI and TTI ($x_n = 0$) are shown with dashed black line [26].

The ambient turbulence increases the radial position, $\overline{r_I}$, of the TTIs compared to the TNTI, which increases with increasing ambient turbulence, as seen by the PDF of their radial distance, see Fig. 8*a* [26]. Large vortical structures transport high levels of passive scalar further from the jet axis, identified as low curvature surface elements, while the largest concentrations close to the jet axis occur at highly convex surface elements [10]. The turbulence in the ambient tends to increase the length, L_I, of the TTI relative to the TNTI, and increase its tortuosity, $T_I = L_I/2\pi\overline{r_I}$, both increasing with increasing ambient turbulence intensity [26]. The tortuosity increases due to the effect of large and small scale eddies, whose relative effect can be described by the increasing fractal dimension of the outline and the increased misalignment between the radial and normal unit vector of the interface with increased ambient turbulence intensity, see Fig. 8*b* [26]. The mean effect of the ambient turbulence is to stretch and corrugate the interface area increasing the area over which nibbling can occur, while, as net entrainment is reduced, the local entrainment velocity must decrease.

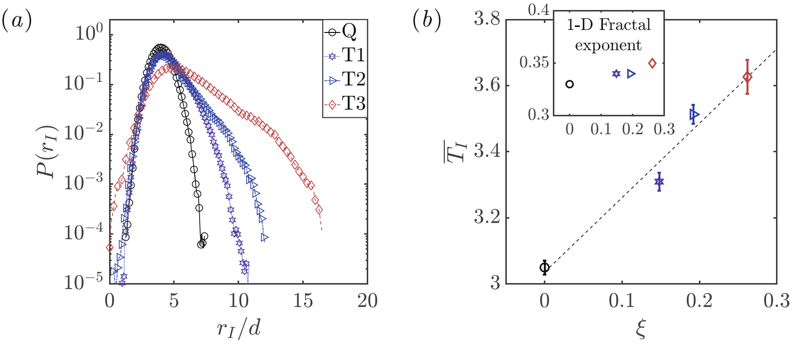

Fig. 8. (a) The PDFs of the interface position, conditioned on jet center of mass. (b) The mean tortuosity and one-dimensional fractal exponent (inset) of the TNTI and TTI [26]. The dashed line in (b) represents the best linear regression fit to mean tortuosity values.

5 Conclusions

Turbulence in the background flow acts to increase the rate of decay of a jet (both its mean velocity and passive scalar concentration) and reduce entrainment into the jet (region 1), before it breaks the jet up, whereupon all jet driven entrainment ceases and only turbulent diffusion occurs (region 2). Jet break-up is identified at a relative turbulence intensity, ξ, of 0.5, while for $\xi < 0.5$ the jet remains self-similar. The larger scales of the background turbulence (those greater than the jet integral scale) advect the jet causing the jet path to meander, while the smaller scales that are entrained modify the jet dynamics. Jet dynamics are affected due faster decay of larger vortical structures in the jet and the more rapid transfer of their energy to the smaller scales, while the entrained turbulence also increases the jet rms increasing the radial scalar transport and differential diffusion, thereby increasing the mixing. A sharp scalar jump exists at the TTI as for the TNTI, which is steeper, longer, more tortuous and has a greater fractal dimension than the TNTI, all increasing with ambient turbulence intensity. The jet in a turbulent ambient has a reduced net entrainment across a more tortuous (larger) interface, and, therefore, with a lower mean entrainment velocity, as expected due to the reduced mean jet velocity caused by the break-up of the larger vortical jet structures and the faster transfer of their energy to the smaller scales. This is summarized in Fig. 9(a,b) [23, 26]. In the future, an investigation of the effect of ambient turbulence on mixing in the jet, observed by simultaneous observation of the velocity and scalar fields, and on the jet dynamics as a function of the relative magnitude of shear at the interface would be of interest.

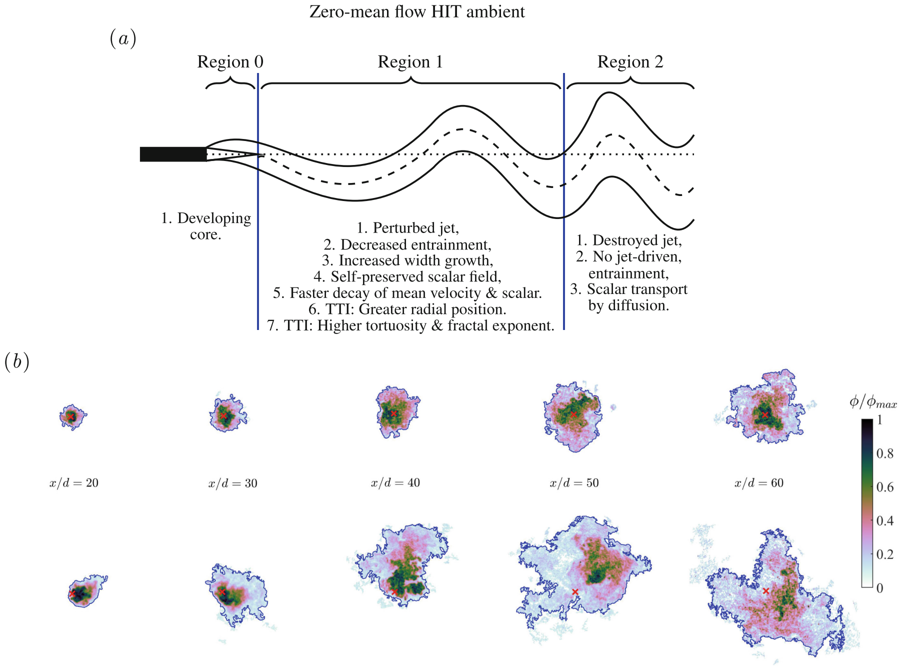

Fig. 9. (*a*) Summary of the effects of background turbulence on the jet dynamics and the TTI. (*b*) Jet cross-sections and TNTI/TTI for jet $Re = 5800$ in a quiescent (top) and HIT (T2) (bottom) ambient for $x/d = [20, 60]$, jet break-up at $x/d = 40$ [22,23,26].

References

1. da Silva, C.B., Hunt, J.C.R., Eames, I., Westerweel, J.: Interfacial layers between regions of different turbulence intensity. Ann. Rev. Fluid Mech. **46**, 567–590 (2014)
2. Morton, B.R., Taylor, G.I., Turner, J.S. : Turbulent gravitational convection from maintained and instantaneous sources. Proc. Roy. Soc. London Ser. A **234**(1196), 1–23 (1956)
3. Rodi, W. (ed.): Turbulent Buoyant Jets and Plumes. Pergammon Press (1982)
4. Hussein, H.J., Capp, S.P., George, W.K.: Velocity measurements in a high-Reynolds-number, momentum-conserving, axisymmetric, turbulent jet. J. Fluid Mech. **258**, 31–75 (1994)
5. Tennekes, H., Lumley, J.L. : A First Course in Turbulence. MIT Press (1972)
6. Townsend, A.A.: The mechanism of entrainment in free turbulent flows. J. Fluid Mech. **26**, 689–715 (1966)
7. Corrsin, S., Kistler, A.L.: Free-stream boundaries of turbulent flows. NACA Tech. Rep. **1244**, 1033 (1955)
8. Dahm, W.J.A., Dimotakis, P.E.: Measurements of entrainment and mixing in turbulent jets. AIAA J. **25**, 1216–1223 (1987)
9. Mathew, J., Basu, A.: Some characteristics of entrainment at a cylindrical turbulence boundary. Phys. Fluids **14**(7), 2065–2072 (2002)

10. Kohan, K.F., Gaskin, S.: The effect of the geometric features of the turbulent/non-turbulent interface on the entrainment of a passive scalar into a jet. Phys. Fluids **32**, 095114 (2020)
11. List, E.J.: Turbulent jets and plumes. Ann. Rev. Fluid Mech. **14**(1), 189–212 (2014)
12. Doneker, R.L., Jirka, G.H. : CORMIX1: an expert system for mixing zone analysis of conventional and toxic single port aquatic discharges. USEPA RPT. EPA/600/3-90/12. Environmental Research Laboratory, Athens, GA, USA (1990)
13. Slawson, P.R., Csanady, G.T.: The effect of atmospheric conditions on plume rise. J. Fluid Mech. **47**, 33–49 (1971)
14. Gaskin, S., Wood, I. R. : Advected line thermals in non-turbulent and turbulent ambient. In: 11th Australian Conference on Coastal and Ocean Engineering Preprints, pp. 748–751 (1993)
15. Wright, S. J. : The effect of ambient turbulence on jet mixing. In: Davies, P.A. and Valente Neves, M. J. (eds.) Recent research advances in the fluid mechanics of turbulent jets and plumes. NATO Science Series E, vol. 25, pp. 13–27 (1994). https://doi.org/10.1007/978-94-011-0918-5_2
16. Hunt, S.J. : Atmospheric jets and plumes. In: Davies, P.A. and Valente Neves, M. J. (eds.) Recent Research Advances in the Fluid Mechanics of Turbulent Jets and Plumes. NATO Sci. Ser. E, vol. 25, pp. 309–334 (1994)
17. Ching, C.Y., Fernando, H.J.S., Robles, A.: Breakdown of line plumes in turbulent environments. J. Geophys. Res. **100**(C3), 4707–4713 (1995)
18. Guo, Y., Davies, P.A., Fernando, H.J.S., Ching, C.Y. : Influence of background turbulence on the evolution of turbulent jets. In: Proceedings of the 28th IAHR World Congress, vol. D, no. 4, pp. 246 (1999)
19. Law, A.W.K., Cheng, N.-S., Davidson, M.J. : Jet Spreading in Oscillating-Grid Turbulence. In: Proceedings of the 3rd ISEH (IAHR), pp. 1–6 (2001)
20. Gaskin, S.J., McKernan, M., Xue, F.: The effect of background turbulence on jet entrainment: and experimental study of a plane jet in a shallow coflow. J. Hyd. Res. **42**(5), 531–540 (2004)
21. Gaskin, S.J., McKernan, M., Xue, F. : The influence of increased ambient turbulence on the evolution of a plane turbulent jet in a shallow co-flow. In: Proceedings of the 3rd ISEH (IAHR), vol. 123, pp. 1–6 (2001)
22. Khorsandi, B., Gaskin, S., Mydlarski, L.: Effect of background turbulence on an axisymmetric turbulent jet. J. Fluid Mech. **736**, 250–286 (2013)
23. Sahebjam, R., Kohan, K.F., Gaskin, S.: The dynamics of an axisymmetric turbulent jet in ambient turbulence interpreted from the passive scalar field statistics. Phys. Fluids **34**, 015129 (2022)
24. Pérez-Alvarado, A. : Effect of background turbulence on the scalar field of a turbulent jet. Ph.D. Thesis. McGill University (2016)
25. Lavertu, T. M. : Differential diffusion in a turbulent jet. Ph.D. Thesis, McGill University. (2006)
26. Kohan, K.F., Gaskin, S.J.: On the scalar turbulent/turbulent interface of axisymmetric jets. J. Fluid Mech. **950**, A32 (2022)
27. Variano, E.A., Bodenschatz, E., Cowen, E.A.: A random synthetic jet array driven turbulence tank. Exp. Fluids **37**, 613–615 (2004)
28. Variano, E.A., Cowen, E.A.: A random-jet-stirred turbulence tank. J. Fluid Mech. **604**, 1–32 (2008)
29. Pérez-Alvarado, A., Mydlarski, L., Gaskin, S.: Effect of the driving algorithm on the turbulence generated by a random jet array. Exp. Fluids **57**, 20 (2016)
30. Kankanwadi, K., Buxton, O.R.H.: Turbulent entrainment into a cylinder wake from a turbulent background. J. Fluid Mech. **905**, A35 (2020)

31. Wang, H., Law, A.W.K.: Second-order integral model for a round turbulent buoyant jet. J. Fluid Mech. **459**, 397–428 (2002)
32. Lai, A.C., Law, A.W.K., Adams, E.E.: A second-order integral model for buoyant jets with background homogeneous and isotropic turbulence. J. Fluid Mech. **871**, 271–304 (2019)
33. Homayounfar, F., Khorsandi, B., Gaskin, S.: Effect of turbulent coflows on the dynamics of turbulent twin jets. Phys. Fluids **36**, 035146 (2024)
34. Bilger, R.W., Dibble, R.W.: Differential molecular diffusion effects in turbulent mixing. Combust. Sci. Technol. **28**, 161–172 (1982)
35. Kerstein, A.R. : Linear-eddy modelling of turbulent transport. Part 3. Mixing and differential molecular diffusion in round jet. J. Fluid Mech. **258**, 31–75 (1990)
36. Lavertu, T.M., Mydlarski, L., Gaskin, S.J.: Differential diffusion of high-schmidt-number passive scalars in a turbulent jet. J. Fluid Mech. **612**, 439–475 (2008)
37. Saylor, J.R., Sreenivasan, K.R.: Differential diffusion in low Reynolds number water jets. Phys. Fluids **10**, 1135–1146 (1988)
38. Kohan, K.F., Gaskin, S.J.: Scalar mixing and entrainment in an axisymmetric jet subjected to external turbulence. Phys. Fluids **36**(10), 105142 (2024)
39. Silva, T.S., Zecchetto, M., da Silva, C.B.: The scaling of the turbulent/non-turbulent interface at high Reynolds numbers. J. Fluid Mech. **843**, 156–179 (2018)
40. Kankanwadi, K.S., Buxton, O.R.H.: On the physical nature of the turbulent/turbulent interface. J. Fluid Mech. **942**, A31 (2022)
41. Mistry, D., Philip, J., Dawson, J.R., Marusic, I.: Entrainment at multi-scales across the turbulent/non-turbulent interface nan axisymmetric jet. J. Fluid Mech. **802**, 690–725 (2016)
42. Wolf, M., Lüthi, B., Holzner, M., Krug, D., Kinzelbach, W., Tsinober, A.: Investigations on the local entrainment velocity in a turbulent jet. Phys. Fluids **24**, 105110 (2012)
43. Wolf, M., Holzner, M., Lüthi, B., Krug, D., Kinzelbach, W., Tsinober, A.: Erratum: "Investigations on the local entrainment velocity in a turbulent jet". Phys. Fluids **24**, 105110 (2012). Phys. Fluids 25, 019901 (2013)
44. Mistry, D., Philip, J.: Dawson: EKinematics of local entrainment and detrainment in a turbulent jet. J. Fluid Mech. **871**, 896–924 (2019)

Local Properties of the Turbulent/Non-turbulent Interface

Sarp Er, Jean-Philippe Laval, and Christos Vassilicos(✉)

Univ. Lille, CNRS, ONERA, Arts et Métiers Institute of Technology, Centrale Lille,
UMR 9014 - LMFL - Laboratoire de Mécanique des Fluides de Lille - Kampé de
Fériet, 59000 Lille, France
`john-christos.vassilicos@cnrs.fr`
`https://lmfl.cnrs.fr/perso/christos-vassilicos-home/`

Abstract. The effect of spatial resolution on local propagation velocity of the Turbulent/Non-Turbulent Interface (TNTI) is documented. A TNTI-local coordinate system and a Reynolds decomposition based on a TNTI-conditional averaging operation are introduced and used to assess the local velocity field and the mass and momentum balances at the TNTI layer. A clear jump of the TNTI-averaged Reynolds shear stress exists through the TNTI layer and the TNTI-averaged fluid velocity normal to the TNTI is determined by the correlation between the TNTI normal vector and the fluid velocity fluctuations around the TNTI-average fluid velocity. The TNTI-local fluid velocity field is compressive normal to the TNTI and stretching in the direction tangent to the TNTI, a structure that has important consequences.

Keywords: TNTI layer · interface · propagation velocity · fractal dimension · turbulent jets · entrainment/detrainment

1 Introduction

Recently, Er *et al.* [1] derived a relation between a globally defined average propagation velocity v_n of the TNTI and a TNTI fractal dimension. Their global definition views v_n as the ratio between the growth rate of the turbulent region's average volume to the average surface area of the TNTI and they estimated this surface area by assuming that it is fractal or fractal-like. They applied their approach to a temporally developing self-similar jet even though they noted that such a jet is fundamentally different from a spatially developing self-similar jet because it conserves volume rather than momentum flux and has zero rather than non-zero cross-stream mean flow velocity. The fractal dimensions that they extracted proved to be very sensitive functions of enstrophy threshold in the range of enstrophy thresholds within the TNTI layer, i.e. those enstrophy thresholds over which the turbulence volume does not vary much. This observation echoed previous observations ([2,3]) concerning strong threshold dependence of the fractal dimension of scalar iso-surfaces.

J. Wang and I. Marusic (Eds.): IUTAM-TNTI 2024, IUTAM Bookseries 45, pp. 48–65, 2025.
https://doi.org/10.1007/978-3-031-78151-3_4

The relation between the global v_n and the fractal dimension D_f turned out to capture the enstrophy threshold dependence of v_n via the entrophy threshold dependence of D_f in the Direct Numerical Simulations (DNS) of temporally developing planar jets of [1], but only for relatively low enstrophy thresholds for which D_f takes well-defined values up to about $D_f \approx 2.2$. (D_f is an increasing function of enstrophy threshold within the TNTI layer as iso-enstrophy surfaces (IES) are progressively smoother towards the outer non-turbulent edge of the layer.) At higher enstrophy thresholds corresponding to the fully turbulent side of the TNTI layer the fractal dimension turned out not to be well-defined in the DNS of [1] in the sense that the box-counting algorithm does not return a power law dependence between number of boxes covering the IES and size of these boxes (as previously found by Miller & Dimotakis [4], for example, for scalar interfaces in turbulent jets). However, a power-law fit through this non-power law dependence returns a fractal dimension fit with $D_f \approx 2.36$ for the iso-enstrophy surfaces at the turbulence edge of the TNTI layer. This is close to the fractal dimension 7/3 reported in many studies over the past 40 years (e.g. [5]).

A local rather than global definition of the TNTI propagation velocity v_n^l has been considered in [6,7] who showed that it leads to

$$v_n^l = -\frac{2\omega_i\omega_j s_{ij}}{|\boldsymbol{\nabla}\omega^2|} + \frac{2\nu\nabla\omega_i \cdot \nabla\omega_i}{|\boldsymbol{\nabla}\omega^2|} - \frac{\nu\nabla^2\omega^2}{|\boldsymbol{\nabla}\omega^2|}. \tag{1}$$

where ω_i is the local vorticity's component i ($i = 1, 2, 3$), s_{ij} is the local strain rate tensor, $\omega^2/2$ is the local enstrophy and ν is the fluid's kinematic viscosity. When v_n^l is negative/positive, the IES for which it is defined moves towards the non-turbulent/turbulent side of the TNTI layer signifying local entrainment/detrainment respectively.

In this paper we document the effect of spatial resolution on the local propagation velocity v_n^l and then proceed with a study of the local flow field at the TNTI.

2 Effect of Resolution on the Local Propagation Velocity

Obtaining the local propagation velocity v_n^l from DNS places strict resolution constraints. This is because first and second derivatives of enstrophy/vorticity need to be computed, and the terms in Eq. 1 are normalized by the magnitude of the gradient of enstrophy, which can become quite small as one moves towards the non-turbulent side of the TNTI through the viscous sublayer.

The present work is based on the direct numerical simulations PJ1, PJ2, PJ3, PJ4 and PJ5 of [1] (a detailed description of these DNS can be found in their paper). The flow fields from these simulations are interpolated in Fourier space into finer grids which consist of $N_x \times N_y \times N_z = (1536 \times 2304 \times 1536)$ elements in each direction. High resolution simulations are run for $t = 2T_{ref} \equiv 2H_J/U_J$, where H_J is the initial jet width and U_J is the initial streamwise velocity at the centre-plane ($x - z$ plane at $y = 0$, y being the coordinate along the direction of mean flow variation of the planar jet) with global Reynolds number $Re_J \equiv U_J H_J/\nu = 3200$ and time-local Taylor length-based Reynolds number $Re_\lambda \approx 45-65$ during the time evolution of the fully turbulent jet. The PJn-HR (High Resolution) data set is produced from PJn ($n = 1, 2, 3, 4, 5$). For example, to obtain the PJ1-HR data, the velocity field of PJ1 at $t/T_{ref} = 48$ is interpolated to a fine grid and then run with exact same parameters for a time $2T_{ref}$ which becomes the highly resolved case of PJ1 at instant of $t/T_{ref} = 50$. The spatial resolution $dx = dy = dz$ increases from $dy/\eta = 0.7$ for PJn to $dy/\eta = 0.46$ for PJn-HR at instant $t/T_{ref} = 50$ (η is the Kolmogorov scale on the centre-plane).

The PDF of the local propagation velocity can be seen in Fig. 1 for two iso-enstrophy surfaces within the TNTI layer, $\omega_{th}^2/\omega_{ref}^2 = 10^{-3}$ and $\omega_{th}^2/\omega_{ref}^2 = 10^{-6}$, where ω_{th}^2 is the threshold value of ω^2 defining the IES and ω_{ref}^2 (function of time) is ω^2 integrated over the centre-plane of the jet. It can be observed from Fig. 1(a) (iso-surface $\omega_{th}^2/\omega_{ref}^2 = 10^{-3}$) that the tails of the PDF vary with spatial resolution. For the positive values of v_n^l/u_η (detrainment) the tail of the PDF varies significantly between resolutions $dy/\eta = 1.4$ and $dy/\eta = 0.7$ but this part of the PDF converges for resolution $dy/\eta \leq 0.7$. However, for the negative values of v_n^l/u_η (entrainment), the tail of the PDF changes even from the medium resolution $dy/\eta = 0.7$ to the high-resolution $dy/\eta = 0.46$. The average value of the local propagation velocity v_n^l for $\omega_{th}^2/\omega_{ref}^2 = 10^{-3}$ is $\langle v_n^l\rangle_I/u_\eta = -0.268$, $\langle v_n^l\rangle_I/u_\eta = -0.544$ and $\langle v_n^l\rangle_I/u_\eta = -0.517$ for the cases with grid resolutions $dy/\eta = 1.4$, $dy/\eta = 0.7$ and $dy/\eta = 0.46$ respectively and the corresponding standard deviations are $\sigma_{v_n^l} = 1.267u_\eta$, $\sigma_{v_n^l} = 0.697u_\eta$ and $\sigma_{v_n^l} = 0.631u_\eta$ (u_η is the Kolmogorov velocity averaged over the centre-plane).

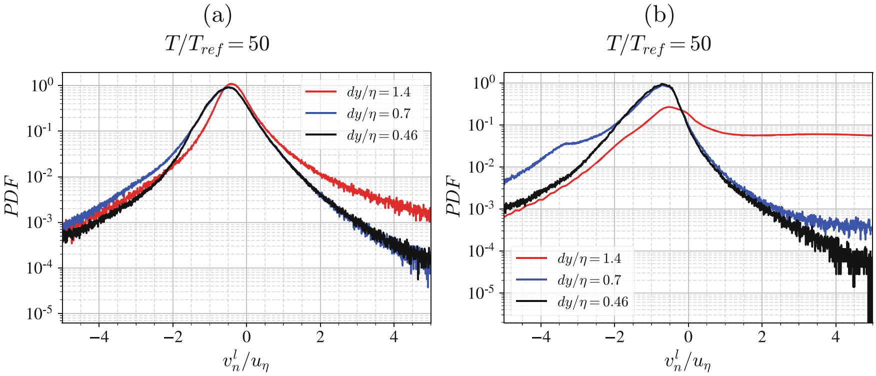

Fig. 1. PDF of v_n^l at time $t/T_{ref} = 50$ for simulations with varying resolutions of $dy/\eta = 1.4$, $dy/\eta = 0.7$ (PJ4), and $dy/\eta = 0.46$ (PJ4-HR). Iso-enstrophy surface (a) $\omega_{th}^2/\omega_{ref}^2 = 10^{-3}$, (b) $\omega_{th}^2/\omega_{ref}^2 = 10^{-6}$.

The effect of resolution is more dramatic for the IES $\omega_{th}^2/\omega_{ref}^2 = 10^{-6}$ as shown in Fig. 1(b). Now, the mean value of v_n^l over the iso-surface is $\langle v_n^l \rangle_I/u_\eta = 4.484$, $\langle v_n^l \rangle_I/u_\eta = -1.014$ and $\langle v_n^l \rangle_I/u_\eta = -0.906$ and the standard deviations are $\sigma_{v_n^l} = 8.466u_\eta$, $\sigma_{v_n^l} = 1.230u_\eta$ and $\sigma_{v_n^l} = 0.665u_\eta$ for the cases with grid resolutions $dy/\eta = 1.4$, $dy/\eta = 0.7$ and $dy/\eta = 0.46$ respectively.

In conclusion, the mean and standard deviations of v_n^l over the iso-surface $\omega_{th}^2/\omega_{ref}^2 = 10^{-3}$ may be starting to be captured with grid resolutions higher than η. However, this may not be quite the case for $\omega_{th}^2/\omega_{ref}^2 = 10^{-6}$ at the outer edge of the TNTI layer. The PDFs of v_n^l do not seem to be fully captured in either case. [1] found that iso-surfaces $\omega_{th}^2/\omega_{ref}^2 = 10^{-6}$ have a well-defined fractal dimension $D_f \approx 2.1$ thereby suggesting that this enstrophy threshold, even if in the outer non-turbulent side of the TNTI layer, is a relevant part of the TNTI layer's structure. If resolution problems make it difficult to obtain fully reliable information on local entrainment/detrainment in terms of the local propagation velocity v_n^l, it is nevertheless possible to extract information concerning the local velocity field at the TNTI. Following [8], and various authors since then, who obtained statistics of flow field variables conditional on interface location and, up to some extent, local orientation, we now present an analysis of the local flow field at the TNTI using a local reference frame at the TNTI which takes full account of its orientation.

We begin with the definition of the local coordinate system and its positioning. Then the definition of the TNTI-averaging operation is given. Two distinct but complementary averaging operations are explained, namely the $x-z$ averaging and the TNTI-averaging. We then proceed with the presentation of profiles of flow quantities that are averaged over the TNTI. A discussion on TNTI normal profiles follows which includes the investigation of the contributions of the mean flow $\mathbf{U}$ and fluctuating velocity $\mathbf{u}'$ on the TNTI-averaged velocity components.

3 Definition of the Local Coordinate System at the TNTI

Similarly to many previous studies, we introduce a local coordinate system to analyze the flow field near the TNTI and perform ensemble average operation conditioned on the interface location. The detection of the iso-enstrophy surfaces constituting the TNTI has been explained in [1]. The local coordinate system is defined for each point $\mathbf{X}_0$ on the IES detected by a specific ω_{th}^2, taking into account the position $\mathbf{X}_0$ and the orientation of the IES at that location (the IES is computed with subgrid accuracy by linear interpolation, see Sect. 2.6 in [9]). The enstrophy normal vector at each point is calculated as follows:

$$\mathbf{n} = \nabla\omega^2/|\nabla\omega^2|. \tag{2}$$

A local coordinate system is placed at each point on the IES, where the unit vectors of the local coordinate system are denoted by $\mathbf{e}_x$, $\mathbf{e}_y$ and $\mathbf{e}_z$. This local coordinate system is defined by a procedure starting with the positioning of the origin of the local coordinate system on a given point $\mathbf{X}_0$ on the IES. The condition for the local y-axis is chosen to be $\mathbf{e}_y = -\mathbf{n}$ so that the positive y-direction in the local coordinate system points towards the non-turbulent region. The unit vector $\mathbf{e}_y$ is referred to as the face normal vector since it indicates the local facing direction of the IES. The normal vector $\mathbf{n}$ is referred to as the enstrophy normal vector.

Apart from the local face normal direction, there is no evident constraint for the remaining two unit vectors which are tangential to the IES. Considering that the temporal planar jet flow has a non-zero mean velocity only in the global x-direction, we have chosen to maximize the projection of the $\mathbf{e}_x$ on the global x-axis. With the determination of the unit vectors $\mathbf{e}_y$ and $\mathbf{e}_x$, the local z-coordinate is defined by the cross-product of these two vectors. So the conditions defining the unit vectors of the local coordinate system $(\mathbf{X}_0, \mathbf{e}_x, \mathbf{e}_y, \mathbf{e}_z)$ at each point on the IES are:

$$\begin{aligned} \mathbf{e}_x \cdot \mathbf{k} &= 0, \\ \mathbf{e}_x \cdot \mathbf{n} &= 0, \\ |\mathbf{e}_x| &= 1, \end{aligned} \tag{3}$$

$$\mathbf{e}_y = -\mathbf{n}, \tag{4}$$

$$\mathbf{e}_z = \mathbf{e}_x \times \mathbf{e}_y. \tag{5}$$

The vectors $\mathbf{i}$, $\mathbf{j}$, $\mathbf{k}$ represent the unit vectors of the global coordinate system and correspond to the streamwise, cross-stream, and spanwise directions.

4 TNTI-Averaging Operation

The positioning of the local coordinate system is a precursor step for the generation of a local grid centred on the detected IES. Once the local coordinate system is positioned and the local 3D grid is placed, the global flow field variables are interpolated at the local grid points by using the trilinear interpolation method. Given the very high spatial resolution of the simulations, a trilinear interpolation is found to be sufficient for the post-processing of the interpolated fields including the computation of the second-order derivatives. The interpolated variables include, $\mathbf{u}$, ω vectors and scalars such as pressure p and ω^2. After the interpolation of the variables, a transformation is applied to the vector quantities by the application of a rotation operation $\mathbf{R}$ in order to decompose the vector fields with components in the local coordinate system $(\mathbf{e}_x, \mathbf{e}_y, \mathbf{e}_z)$. The rotation operation $\mathbf{R}$ which relates the expression of an arbitrary vector $\mathbf{a}$ in the global coordinate system with its expression in the local coordinate system $\mathbf{a}^l$ can be written as

$$\begin{bmatrix} a^l{}_1 \\ a^l{}_2 \\ a^l{}_3 \end{bmatrix} = \begin{bmatrix} \boldsymbol{e}_x \cdot \boldsymbol{i} & \boldsymbol{e}_x \cdot \boldsymbol{j} & \boldsymbol{e}_x \cdot \boldsymbol{k} \\ \boldsymbol{e}_y \cdot \boldsymbol{i} & \boldsymbol{e}_y \cdot \boldsymbol{j} & \boldsymbol{e}_y \cdot \boldsymbol{k} \\ \boldsymbol{e}_z \cdot \boldsymbol{i} & \boldsymbol{e}_z \cdot \boldsymbol{j} & \boldsymbol{e}_z \cdot \boldsymbol{k} \end{bmatrix} \begin{bmatrix} a_1 \\ a_2 \\ a_3 \end{bmatrix} \tag{6}$$

To ensure that the TNTI does not fold on itself and that there are no engulfed turbulent or non-turbulent regions near the interface, an additional condition called the *no multi-cross* condition is applied. This condition checks whether the TNTI normal axis, i.e., the local y-axis, crosses the TNTI multiple times within a certain distance on each side of the IES. We apply this condition because we are interested in capturing the variation of variables across the turbulent to non-turbulent sides of the interface. Normal axis crossing the interface multiple times will make the TNTI-average profiles hard to interpret and possibly affect the parts associated with the non-turbulent part of the TNTI-averaged data and is therefore omitted also in previous studies ([10,11]). Different methods have been used in the literature to overcome this issue, either by completely neglecting the points on the IES where the local normal axis has multiple crossings of the interface ([12]), or by defining a margin of length in order to exclude certain parts of the local profile from the conditional averaging operation ([13,14]) or by using an envelope surface rather than the full interface with all its contortions ([15]).

In the present work, we follow the methodology applied in [12]. On the non-turbulent side of the interface, a check is made to see if there is a point where $\omega^2(y_I) > c_{mc}\omega_{th}^2$ along the interface normal axis from the IES location (which is at $y_I/\eta = 0$) towards the non-turbulent region until the maximum extent of the interpolated region. On the turbulent side of the interface, a check is made to see if there is a point having $\omega^2(y_I) < (1/c_{mc})\omega_{th}^2$ from the IES location towards the direction of the turbulent core, again until the end of the local interpolated region. In the present study, a local interpolated region with size $-50 < y_I/dy < 50$ in the interface normal direction is used, meaning that the *no multi-crossing* check is carried out in this range (which corresponds to $-23 < y_I/\eta < 23$ where dy is the uniform grid size in all the directions and η is the Kolmogorov length scale computed at the centre-plane of the jet). Here, the free parameter c_{mc} is $c_{mc} = 5$ taking into account that the different thresholds analyzed are chosen with decade intervals in ω_{ref}^2 values. (Thus, choosing $c_{mc} = 10$ corresponds to the next threshold considered). This parameter serves as a modifier for the sensitivity of the *no multi-cross* condition, which is useful when the local grid used for the conditional analysis is of the same order or finer than the grid used for the TNTI detection. We checked that a reasonable change in the value of $c_{mc} = 5$ does not significantly change the results presented below.

Before moving to the local analysis of the interface and the application of the TNTI-averaging operation, it is beneficial to clarify the two distinct averaging operations used in this study. Firstly, we have the averaging over the homogeneous directions where $\langle\cdot\rangle$ denotes the averaged quantity in the two homogeneous directions of the global coordinate system i.e. x and z:

$$\mathbf{a} = \mathbf{A} + \mathbf{a}'. \tag{7}$$

A capital letter is used for the average in the homogeneous directions, i.e. $\mathbf{A} = \langle\mathbf{a}\rangle$.

For the second averaging operation, the local fields are averaged along the interface while keeping the local coordinates x_I, y_I, and z_I constant. This operation is denoted by $\langle\cdot\rangle_I$. When applied to a vector quantity, it leads to a result in the form

$$\mathbf{a} = \langle \mathbf{a} \rangle_I + \mathbf{a}''. \tag{8}$$

We stress that these are two different averaging operations and that the TNTI-average values of the fluctuating component $\mathbf{a}'$ in Eq. 7 are not identically zero i.e. $\langle \mathbf{a}' \rangle_I \not\equiv 0$. On the other hand, due to the definition of the TNTI averaging process, $\langle \mathbf{a}'' \rangle_I \equiv 0$.

For the temporally developing jet, the mean velocity profile is solely a function of y-direction at any given time, i.e. $U(y)$ (see [1]). Using Eq. 6, U can be expressed in terms of the TNTI local coordinates as $U(Y_0 + \mathbf{R}^{-1}(\mathbf{X}_0) \cdot \mathbf{x}_I)$. Both averaging operations, defined by Eqs. 7 and 8, are averages over spatial surfaces (the $x-z$ surface or an IES surface in the TNTI layer). We apply these operations at an instant in time and omit the time variable from the notation. Applying the decomposition Eq. 7 to the velocity vector at a given time and any location,

$$\mathbf{u}(x_I, y_I, z_I, \mathbf{X}_0) = U(Y_0 + \mathbf{R}^{-1}(\mathbf{X}_0) \cdot \mathbf{x}_I) + u'(x_I, y_I, z_I, \mathbf{X}_0). \tag{9}$$

Averaging the velocity vector conditionally on the TNTI location leads to

$$\mathbf{u}(x_I, y_I, z_I, \mathbf{X}_0) = \langle \mathbf{u}(x_I, y_I, z_I, \mathbf{X}_0) \rangle_I + u''(x_I, y_I, z_I, \mathbf{X}_0). \tag{10}$$

The velocity vector components in the local coordinate system are

$$\begin{aligned} u_l &= \mathbf{u} \cdot \mathbf{e}_x \\ v_l &= \mathbf{u} \cdot \mathbf{e}_y \\ w_l &= \mathbf{u} \cdot \mathbf{e}_z. \end{aligned} \tag{11}$$

Here, v_l is the TNTI normal component, and u_l and w_l are components of the velocity vector, tangential to the interface. Applying now the TNTI-average to these local vector components yields

$$\begin{aligned} u_l &= \langle \mathbf{U} \cdot \mathbf{e}_x \rangle_I + \langle \mathbf{u}' \cdot \mathbf{e}_x \rangle_I, \\ v_l &= \langle \mathbf{U} \cdot \mathbf{e}_y \rangle_I + \langle \mathbf{u}' \cdot \mathbf{e}_y \rangle_I, \\ w_l &= \langle \mathbf{U} \cdot \mathbf{e}_z \rangle_I + \langle \mathbf{u}' \cdot \mathbf{e}_z \rangle_I. \end{aligned} \tag{12}$$

The profiles of TNTI-averaged velocities and the mean local 3D fields are mostly obtained by this operation in the present paper. As the TNTI averaging operation is applied for fixed x_I, y_I, and z_I, it averages the $x-z$ averaged $\boldsymbol{U}$ over various global y-coordinate values.

Equation 10 and Eqs. 11 imply

$$\begin{aligned} u_l &= \langle \boldsymbol{u} \rangle_I \cdot \boldsymbol{e}_x(\boldsymbol{X}_0) + \boldsymbol{u}'' \cdot \boldsymbol{e}_x(\boldsymbol{X}_0) \\ v_l &= \langle \boldsymbol{u} \rangle_I \cdot \boldsymbol{e}_y(\boldsymbol{X}_0) + \boldsymbol{u}'' \cdot \boldsymbol{e}_y(\boldsymbol{X}_0) \\ w_l &= \langle \boldsymbol{u} \rangle_I \cdot \boldsymbol{e}_z(\boldsymbol{X}_0) + \boldsymbol{u}'' \cdot \boldsymbol{e}_z(\boldsymbol{X}_0) \end{aligned} \tag{13}$$

and applying the TNTI averaging operation we obtain

$$\begin{aligned} u_l &= \langle \boldsymbol{u} \rangle_I \cdot \langle \boldsymbol{e}_x \rangle_I + \langle \boldsymbol{u}'' \cdot \langle \boldsymbol{e}_x \rangle_I \rangle_I + \langle \boldsymbol{u}'' \cdot \boldsymbol{e}_x'' \rangle_I, \\ v_l &= \langle \boldsymbol{u} \rangle_I \cdot \langle \boldsymbol{e}_y \rangle_I + \langle \boldsymbol{u}'' \cdot \langle \boldsymbol{e}_y \rangle_I \rangle_I + \langle \boldsymbol{u}'' \cdot \boldsymbol{e}_y'' \rangle_I, \\ w_l &= \langle \boldsymbol{u} \rangle_I \cdot \langle \boldsymbol{e}_z \rangle_I + \langle \boldsymbol{u}'' \cdot \langle \boldsymbol{e}_z \rangle_I \rangle_I + \langle \boldsymbol{u}'' \cdot \boldsymbol{e}_z'' \rangle_I, \end{aligned} \tag{14}$$

where $\boldsymbol{e}(\boldsymbol{X_0}) = \boldsymbol{e} + \boldsymbol{e}''(\boldsymbol{X}_0)$ with $\langle \boldsymbol{e}'' \rangle_I = 0$. The second term on the right-hand side of these equations is zero due to the definition of TNTI-averaging in Eq. 8. Hence,

$$\begin{aligned}
u_l &= \langle \boldsymbol{u} \rangle_I \cdot \langle \boldsymbol{e}_x \rangle_I + \langle \boldsymbol{u}'' \cdot \boldsymbol{e}_x'' \rangle_I, \\
v_l &= \langle \boldsymbol{u} \rangle_I \cdot \langle \boldsymbol{e}_y \rangle_I + \langle \boldsymbol{u}'' \cdot \boldsymbol{e}_y'' \rangle_I, \\
w_l &= \langle \boldsymbol{u} \rangle_I \cdot \langle \boldsymbol{e}_z \rangle_I + \langle \boldsymbol{u}'' \cdot \boldsymbol{e}_z'' \rangle_I,
\end{aligned} \tag{15}$$

By applying the decomposition in Eq. 9 to the first terms on the right-hand side of Eqs. 15 we obtain,

$$\begin{aligned}
u_l &= \langle \boldsymbol{U} \rangle_I \cdot \langle \boldsymbol{e}_x \rangle_I + \boldsymbol{u}' \cdot \langle \boldsymbol{e}_x \rangle_I + \langle \boldsymbol{u}'' \cdot \boldsymbol{e}_x'' \rangle_I, \\
v_l &= \langle \boldsymbol{U} \rangle_I \cdot \langle \boldsymbol{e}_y \rangle_I + \boldsymbol{u}' \cdot \langle \boldsymbol{e}_y \rangle_I + \langle \boldsymbol{u}'' \cdot \boldsymbol{e}_y'' \rangle_I, \\
w_l &= \langle \boldsymbol{U} \rangle_I \cdot \langle \boldsymbol{e}_z \rangle_I + \boldsymbol{u}' \cdot \langle \boldsymbol{e}_z \rangle_I + \langle \boldsymbol{u}'' \cdot \boldsymbol{e}_z'' \rangle_I,
\end{aligned} \tag{16}$$

With respect to TNTI averaging, the fluctuations of the local velocity components are defined as follows:

$$\begin{aligned}
u_l'' &= u_l - u_l \\
v_l'' &= v_l - v_l \\
w_l'' &= w_l - w_l
\end{aligned} \tag{17}$$

By using this definition (Eq. 17) of fluctuating velocities, normal and cross stresses can be defined in the TNTI local coordinate system e.g. $\langle v_l''^2 \rangle_I$, $\langle u_l'' v_l'' \rangle_I$ similarly to the classical turbulent stress terms. We use turbulent stresses defined in this way in our discussion of the theoretical jump conditions proposed by [16] (see Sect. 6).

5 TNTI-Averaged Profiles of the Flow Field Variables

It has been demonstrated in [1] that the instant $t/T_{ref} = 50$ falls within the time range where the turbulent jet exhibits self-similarity and is unaffected by boundary conditions. For the present paper, TNTI-averaged profiles have been examined at different times with the PJ1 simulation, and it has been observed that $t/T_{ref} = 50$ is representative of a wide range of times in the aforementioned time range. All results presented here are obtained from the PJn-HR simulations at $t/T_{ref} = 50$ unless stated otherwise. In order to increase statistical convergence, the results are obtained as the ensemble average over the five simulations whenever possible. In case a specific result is based on data from a single simulation rather than the ensemble average, this is explicitly mentioned in the caption.

In this section, the analysis is conducted using a local grid that spans from $-50dy$ to $50dy$ in each direction of the local coordinate system, which corresponds to a range -23η to 23η in the local coordinates y_I, x_I, and z_I. The points $\boldsymbol{X}_0$ considered on the interface are the numerical mesh points where the enstrophy is closest to the enstrophy threshold. It is worth mentioning that the *no multi-crossing* condition results in the exclusion of 40% of the total number of points for the IES of $\omega_{th}^2/\omega_{ref}^2 = 10^{-3}$.

Now that the TNTI-averaging operation is defined, let's attempt to quantify differences between different ω_{th}^2 values. Figure 2 presents a comparison of TNTI-average profiles of ω^2 for the IES of $\omega_{th}^2/\omega_{ref}^2 = 10^{-3}$ and the IES of $\omega_{th}^2/\omega_{ref}^2 = 10^{-6}$. The $< \omega^2 >_I / \omega_{ref}^2$ profile is shown with the solid line for the IES of $\omega_{th}^2/\omega_{ref}^2 = 10^{-6}$. The y_I location where $< \omega^2 >_I / \omega_{ref}^2 = 10^{-3}$ on this profile is marked with a red vertical dashed line. The TNTI-average profile of $\langle \omega^2 \rangle_I / \omega_{th}^2$ for the IES of $\omega_{th}^2/\omega_{ref}^2 = 10^{-3}$ is plotted on top, by offsetting its origin ($y_I/\eta = 0$ location) to coincide with the origin corresponding to the $\omega_{th}^2/\omega_{ref}^2 = 10^{-6}$ IES. The offset between these two profiles is found to be 2.85η.

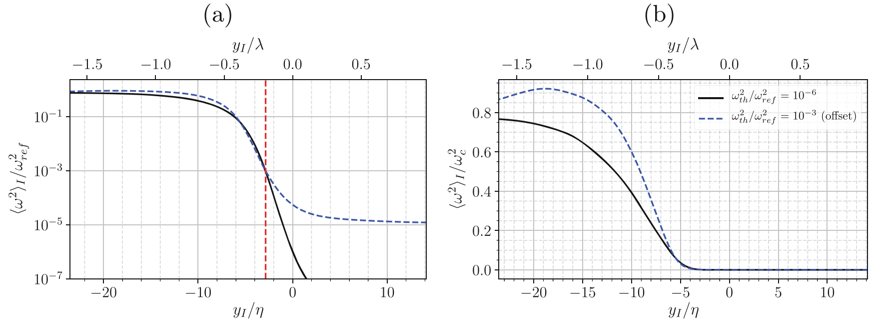

Fig. 2. Profiles of $\langle \omega^2 \rangle_I$ for IES of $\omega_{th}^2/\omega_{ref}^2 = 10^{-6}$ and $\omega_{th}^2/\omega_{ref}^2 = 10^{-3}$ at $t/T_{ref} = 50$. The red line shows the y_I location where $\langle \omega^2 \rangle_I / \omega_{ref}^2 = 10^{-3}$ in the TNTI-average profile obtained for the IES of $\omega_{th}^2/\omega_{ref}^2 = 10^{-6}$. (a) $\langle \omega^2 \rangle_I$ in log-lin plot, (b) $\langle \omega^2 \rangle_I$ in lin-lin plot

Even though three orders of magnitude difference in $\omega_{th}^2/\omega_{ref}^2$ leads to a slight change of the spatial location of the IES i.e. $\approx 2.85\eta$, the effect of the variation of the contortions of the IES is more dramatic on the TNTI-averaged profiles. Figure 2 shows the TNTI-average profiles in a linear plot, in order to see their differences more clearly. A much steeper gradient is observed for the $\langle \omega^2 \rangle_I$ profile obtained by averaging over the $\omega_{th}^2/\omega_{ref}^2 = 10^{-3}$ IES. This is due to the different geometrical structure of the IES reflected by the increasing D_f with increasing $\omega_{th}^2/\omega_{ref}^2$ within the TNTI layer as shown in [1]. Due to the IES orientation being more turbulent for $\omega_{th}^2/\omega_{ref}^2 = 10^{-3}$, the gradient obtained for this IES is higher.

We now turn to the profiles along the interface normal direction of the TNTI-averaged local velocity components, see Fig. 3(a), namely $< u_l >_I$, $< v_l >_I$, and $< w_l >_I$. These profiles are normalized by the centre-plane Kolmogorov velocity u_η. A rapid change is observed in both $< u_l >_I$ and $< v_l >_I$ across the TNTI. On the other hand, $< w_l >_I$ remains zero throughout the interfacial layer which is due to our definition of the local coordinate system which forces

$< \mathbf{e}_z >_I$ to be aligned with the global z direction (except at locations where the interface folds on itself) given that $\boldsymbol{e}_x$ is chosen to align maximally with the global streamwise direction. Looking at Eq. 12 for $< w_l >_I$, both terms on its right hand side vanish. The global mean flow velocity $\mathbf{U}$ does not have a component in the global z-direction, the TNTI orientation $\mathbf{e}_z$ does not have a preferential orientation around the spanwise axis and is also uncorrelated from the velocity fluctuations $\mathbf{u}'$. Consequently, both terms on the right hand side of Eq. 12 vanish and so $< w_l >_I$ remains zero along the interface normal y_I axis.

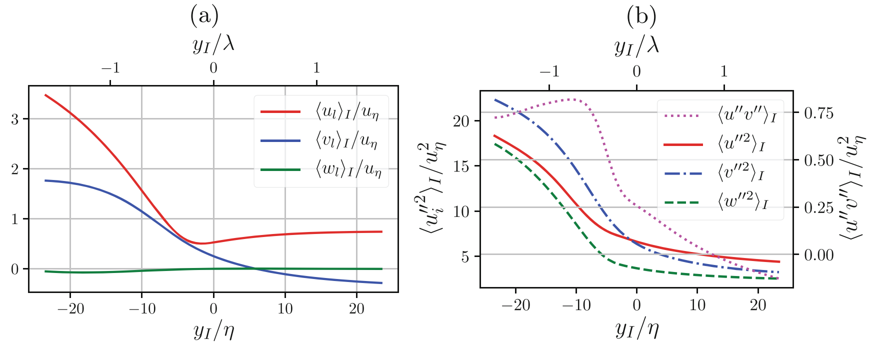

Fig. 3. TNTI-averaged profiles of local velocity components and the local normal and shear turbulent stresses for the IES of $\omega_{th}^2/\omega_{ref}^2 = 10^{-3}$ at $t/T_{ref} = 50$. (λ is the Taylor length on the centre-plane.)

In relation to the way that the orientation of $\mathbf{e}_x$ is chosen, $< u_l >_I$ remains positive along the TNTI-average profile due to the jet having mean velocity in the global streamwise direction (see Eq. 12 for $< u_l >_I$). In contrast, the TNTI-averaged local normal velocity $< v_l >_I$ crosses zero at a certain point.

In the region $y_I/\eta < 0$, $< v_l >_I$ remains positive. This indicates that the interface perceives a local normal velocity pointing from the turbulent core towards the non-turbulent region. Furthermore, the negative gradient $d < v_l >_I / dy_I < 0$ along the normal TNTI axis suggests that the velocity field tends to be compressive in the normal direction at the interface. In fact, the local $< v_l >_I$ profile shows that the interface perceives a velocity field that moves towards it from both the turbulent and non-turbulent directions. Also, the fact that the TNTI-average velocity component $< v_l >_I$ is non-zero along the y_I axis is interesting in itself as the mean velocity obtained by global $x - z$ averaging does not have a component in the cross-stream direction i.e. $V(y) = 0$ given that our jet is temporally rather than spatially developing.

Figure 3(b) presents the profiles of local stresses, defined by the fluctuating velocities with respect to the TNTI-average velocity values, obtained from Eqs. 17. The normal stresses i.e., $< u''^2 >_I$, $< v''^2 >_I$, and $< w''^2 >_I$, exhibit significantly higher magnitudes than the cross/stress term $< u''v'' >_I$. These normal stresses maintain non-zero values even on the non-turbulent side of the interface, extending as far as $y_I/\eta = 24$. However, their magnitudes decrease rapidly from the turbulent side of the IES to the non-turbulent region, particularly in the region between $y_I/\eta \approx -13.7$ and $y_I/\eta \approx -1.5$.

The profile of $< u''v'' >_I$ displays an even steeper gradient, primarily occurring between $y_I/\eta \approx -7.2$ and $y_I/\eta \approx -2.1$. This suggests that the TNTI is characterized by a pronounced jump in $< u''v'' >_I$ along the normal direction. It can be noted that the very high gradient of the profile of $< u''v'' >_I$ is observed on the turbulent side of the $\omega_{th}^2/\omega_{ref}^2 = 10^{-3}$ IES between $y_I/\eta \approx -2$ and $y_I/\eta \approx -10.5$.

We now analyse the decomposition presented in Eq. 16 in order to investigate the contributions of $\mathbf{U}$, $\mathbf{u}'$ and the orientation of the local coordinate system $\mathbf{e}$ (associated with the local TNTI orientation) to the components of the TNTI-averaged velocity $\boldsymbol{u}$. In Fig. 4, we present the profiles of $< u_l >_I$ and $< v_l >_I$ and of the three terms on the right-hand side of Eq. 16. The first term is the contribution from the scale product of the mean flow obtained by $x-z$ averaging and the mean orientation of the TNTI. The second term accounts for the effects of the velocity fluctuation field with respect to $x-z$ mean. And finally, the third term accounts for the velocity and orientation fluctuations with respect to the TNTI average: it is the correlation between the fluctuations of the velocity and of the interface orientation around their TNTI average.

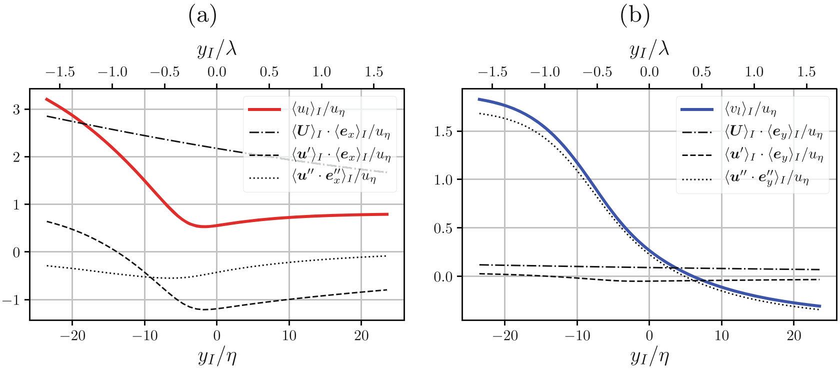

Fig. 4. TNTI-local profiles of $< u_l >_I$ and $< v_l >_I$ and of the terms on the right hand side of Eq. 16, for the $\omega_{th}^2/\omega_{ref}^2 = 10^{-3}$ IES at $t/T_{ref} = 50$ for the PJ4-HR simulation. (λ and η are, respectively, the Taylor length and Kolmogorov microscale on the centre-plane.)

Starting with the first term, the contribution of the mean velocity profile $\boldsymbol{U}$ varies linearly on the local y_I/η axis for both component of the local TNTI-averaged velocity. Naturally, the highest contribution is in the component of $< u_l >_I$, due to the positioning of the local coordinate system ensuring that the alignment of $\mathbf{e}_x$ is maximal with the global streamwise vector $\mathbf{i}$. Due to the fact that the axis goes towards the centre-plane of the jet for decreasing values of

y_I/η, the contribution of $\mathbf{U}$ increases in that direction. But there is no specific location in the local profile of $\langle \mathbf{U} \rangle_I \cdot \langle \mathbf{e}_x \rangle_I$ (and also the local profile of $\langle \mathbf{U} \rangle_I \cdot \langle \mathbf{e}_y \rangle_I$ for that matter) where it undergoes a dramatic change at the TNTI location.

On the other hand, Fig. 4(a) reveals a significant variation of $< u_l >_I$ in the y_I direction when crossing the interface. It is evident that this jump is caused by TNTI averaging of the fluctuating velocity $\mathbf{u}'$ (fluctuation around the $x - z$ mean). The term $< \mathbf{u}' >_I \cdot < \mathbf{e}_x >_I$ crosses zero at $y_I/\eta = -13.8$ and for higher values of y_I beyond this point, it contributes negatively to the profile of $< u_l >_I$. Although the third term also contributes to the profile of $< u_l >_I$, the primary factor driving the jump in $< u_l >_I$ across the TNTI is the second term, which includes the effects of the $\mathbf{u}'$ field.

The impact of $\mathbf{U}$ is not particularly significant on the interface normal velocity component $< v_l >_I$. The local v_l profile is primarily, if not mainly, influenced by the correlation $< \mathbf{u}'' \cdot \mathbf{e}''_y >_I$ between fluctuations $\mathbf{u}''$ around the TNTI-average of the fluid velocity and orientation of the interface. In other words, the average interface normal velocity, perceived by the TNTI in the local reference frame is determined by the correlation between $\boldsymbol{u}''$ and $\boldsymbol{e}''_y$.

6 Jump Condition for the Tangential Velocity and the Vorticity at the Interface

The TNTI-averaged profiles presented in Sect. 5 allow us to investigate the analysis conducted by [16] on the interface. In the study of [16], the interface between the turbulent and non-turbulent regions was analyzed by placing a small control volume (CV) over a segment of the interface (interface referred to as *superlayer* in the original paper). Figure 5 shows a schematic of the CV described in [16].

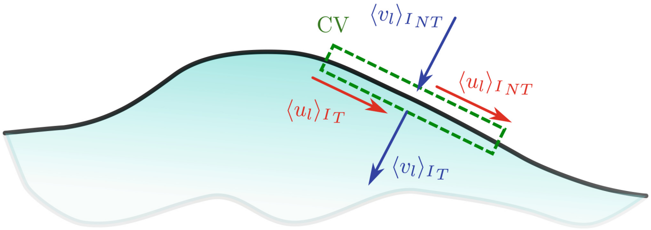

Fig. 5. Schematic of the local control volume defined similar to [16] (*shown in dashed green line*). The subscripts T and NT are used for the quantities in the turbulent and non-turbulent sides of the control volume.

In the analysis presented in [16], the mean velocity at the interface is expressed by two components: one aligned with the normal direction and the other in the interface's tangential direction. The positioning of the local coordinate system chosen in the present study is important in this context (Eqs. 3, 4, and 5). As shown in Fig. 3(a), the TNTI-average velocity vector $< \mathbf{u} >_I$

has components in the interface normal direction $< v_l >_I$ and in the tangential direction $< u_l >_I$, whereas the second tangential average velocity component $< w_l >_I$ is zero, compatible with the mean velocity components defined in [16] (see Fig. 3a).

The interface is considered to be a sheet-like surface with an infinitesimal thickness in [16], thus the CV covering a section of the interface is also considered to have a negligible thickness, thus neglecting the fluxes at the side surfaces of the CV and only considering the fluxes in the interface normal direction. Furthermore, the viscous stresses on either side of the interface are neglected in the analysis by W.C. Reynolds [16]. Given these assumptions, the conservation equations for mass and momentum in the TNTI normal and tangential directions are written for the CV with certain terms omitted. Starting with the mass balance for the control volume, the relation is written as;

$$[< v_l >_I]_{NT} = [< v_l >_I]_T. \tag{18}$$

Here, v_l is the mean TNTI normal velocity and the subscripts NT and T distinguish, in principle, between its value at the non-turbulent and turbulent sides of the interface (see Fig. 5). The balance is written in the TNTI local coordinate system where the mean/fluctuating velocities with respect to the TNTI-averaging operation are also expressed with components that are normal and tangential to the interface. As the CV is taken to be infinitesimally thin in the TNTI's normal direction, the faces of the CV normal to the TNTI tangential directions are neglected and we end up with a mass balance involving only fluxes in the normal direction of the interface [16]. This directly implies that the interface normal velocity should remain constant across the interface.

To assess the validity of this conclusion, Fig. 3(a) can be re-visited. It becomes apparent from this figure that the TNTI normal component $< v_l >_I$ varies across the interface, and its derivative along the y_I direction exhibits high values, particularly in the proximity of the IES. Considering the CV positioned as in the work of W.C. Reynolds [16], which fully contains the jump of vorticity at the interface, there is a significant difference between the values of $< v_l >_I$ at the turbulent and non-turbulent sides of the interface. This result contradicts Eq. 18 and leads to a questioning of the assumptions made in [16] for obtaining the balance of quantities inside the CV.

The primary problem arises because the variation in the TNTI-averaged normal velocity $< v_l >_I$ directly implies the presence of a significant gradient of $< u_l >_I$ in the tangential direction of the IES. Furthermore, considering that the jump in vorticity occurs over a certain distance and is not as sharp as depicted in [16], this gradient of $< u_l >_I$ suggests significant flow of mass through the neglected side surfaces of the CV.

Secondly, the momentum balance in the normal and tangential directions are written as follows in [16],

$$[< p >_I]_{NT} = [< p >_I + \langle \rho v_l''^2 \rangle_I]_T, \tag{19}$$

$$\rho < v_l >_I ([< u_l >_I]_{NT} - [< u_l >_I]_T) - [\rho \langle v_l'' u_l'' \rangle_I]_T = 0. \tag{20}$$

Here, $< p >_I$ denotes the TNTI-averaged pressure and $< v_l''^2 >_I$ is the turbulent normal stress, which is considered only for the turbulent side in the model proposed by W.C. Reynolds [16]. In Eq. 20, $-(\rho\langle v_l'' u_l''\rangle_I)$ is the turbulent shear stress at the boundary and similarly to Eq. 19, it has been considered only for the turbulent side of the CV.

Another important point related to this equation is that the mean velocity $< v_l >_I$ has to be defined for the first term of Eq. 20. In the analysis made by [16], the conservation of mass yields the equality given in Eq. 18 and there is no ambiguity in the choice of $< v_l >_I$ appearing in Eq. 20 because Eq. 18 states that it does not vary across the TNTI. On the other hand, a significant jump in the value of $< v_l >_I$ across the TNTI is observed in the present study (see Fig. 3a). To avoid introducing any modification to Eq. 20, $< v_l >_I$ in Eq. 20 can be defined by taking the average value $[< v_l >]_m$ of $< v_l >_I$ along the extent of the CV along the y_I axis. Looking at Eq. 20, a jump in the TNTI mean tangential velocity is expected in case the turbulent shear stress is non-zero on the turbulent side of the interface. There is indeed a jump in $< u''v'' >_I$ across the interface as shown in Fig. 3(b) and the values of the TNTI-averaged tangential velocity $< u_l >_I$ rise sharply on the turbulent side of the IES across the TNTI layer (see Fig. 3a). The local profiles obtained in the present study support the presence of a jump in the values of TNTI-averaged tangential velocity between the turbulent and non-turbulent sides of the interface.

Having computed the TNTI-averaged profiles of velocity, pressure, turbulent stresses and vorticity, the mass/momentum balances proposed in [16] can be checked to see if they hold near the detected IES. In order to make this check, we make use of the 1D TNTI-averaged profiles presented in Sect. 5 in the interface normal direction.

Twentieth century approaches to the TNTI regarded it as a surface with infinitesimal thickness, featuring nearly singular jumps in flow variables such as tangential velocity and span-wise vorticity. Twenty first century studies have used DNS to resolve the TNTI and perceive it as a TNTI layer with continuous variation of quantities across its thickness, even though TNTI-local gradients can indeed be very high. Due to this continuous variation, the choice of the location and the thickness of the CV to check the relations proposed in [16] becomes important.

Before presenting our results relating to the balance Eqs. 18, 19 and 20 we start by defining how the CV is placed. To do so, we plot in Fig. 6 the profiles of ω^2 and of the magnitudes of the local vorticity components ω_x^l, ω_y^l and ω_z^l all normalized by the mean centre-plane value of $|\omega_z|$. We also plot the gradient $-du_l/dy_I$ in the interface normal direction normalised in the same way. The centre-plane mean value of $|\omega_z|$, is used for the normalization of all the profiles as $\langle|\omega_x|\rangle_c \approx \langle|\omega_y|\rangle_c \approx \langle|\omega_z|\rangle_c$ at the centre-plane of the jet, due to local isotropy. (In relation to the term $-du_l/dy_I$, it should be noted that the derivative operation d/dy_I commutes with the TNTI-averaging operation $\langle\cdot\rangle_I$.) The position of the CV's side denoted by T (turbulent side) is chosen at the maximum of the local profile $< |\omega_z^l| >_I$, i.e. at $y_I/\eta = -10.3$. The position of the CV's side denoted by N (non-turbulent side) is chosen at $y_I/\eta = 1$ (see Fig. 6). Reasonably small changes to this choice do not change our conclusions.

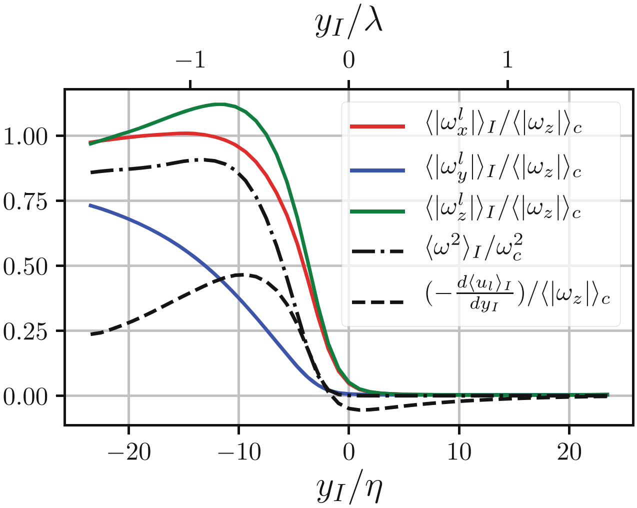

Fig. 6. TNTI-averaged profiles of $\langle|\omega_x^l|\rangle_I$, $\langle|\omega_y^l|\rangle_I$, $\langle|\omega_z^l|\rangle_I$, $\langle\omega^2\rangle_I$ and the gradient of local u_l velocity in the TNTI normal direction $-du_l/dy_I$, normalized by the mean $|\omega_z|$ at the centre-plane of the jet. The interface location ($y_I = 0$) used for the conditioning of the profile is defined with the $\omega_{th}^2/\omega_{ref}^2 = 10^{-3}$ IES. Distance y_I from the IES is normalized by the Kolmogorov length scale η (bottom axis) and the Taylor length λ (top axis) computed at the centre-plane of the jet.

Using the local mean/fluctuating variables obtained on the basis of TNTI averaging, the balances of mass and normal/tangential momentum proposed in [16] are evaluated as follows from our DNS:

$$B_c^R \equiv \frac{[< v_l >_I]_{NT}}{[< v_l >_I]_T} = 0.17, \tag{21}$$

$$B_{nm}^R \equiv \frac{[< p >_I]_{NT}}{[< p >_I + \langle\rho v_l''^2\rangle_I]_T} = 1.40, \tag{22}$$

$$B_{tm}^R \equiv \frac{[< v_l >_I]_m([< u_l >_I]_{NT} - [< u_l >_I]_T)}{[\langle u_l'' v_l''\rangle_I]_T} = -0.83. \tag{23}$$

The superscript R is a reminder of the relations $B_c^R = B_{nm}^R = B_{tm}^R = 1$ given by W.C. Reynolds [16] . A very large deviation from $B_c^R = 1$ is present, i.e. a large deviation from the form given in Eq. 18 of the continuity equation which states that the interface normal velocity is equal on both sides of the CV. However, as has been shown in Fig. 3(a), the value of $< v_l >_I$ is not the same at the upper and lower sides of the CV. It varies across the thickness of the TNTI and a change in the sign of v_l even occurs along the y_I/η axis. This indicates that there is considerable mass flux through the CV faces perpendicular to the interface which is not accounted for in the analysis of W.C. Reynolds [16].

Considering the normal momentum balance, the deviation from $B^R_{nm} = 1$ is smaller than the deviation from $B^R_c = 1$ (see Eq. 22). The deviation from the normal momentum balance given in [16] is mainly due to the neglected $< {v_l''}^2 >_i$ term on the non-turbulent side of the interface. It can be seen in Fig. 3(b) that even though the normal stress reduces significantly across the interface, it does not go to zero in the non-turbulent region. Thus neglecting this term contributes to the 40% deviation from Eq. 19.

The tangential momentum devation from $B^R_{tm} = 1$ is quite dramatic as the value of B^R_{tm} returned by our DNS is in fact negative, let alone different from 1. This is because $< u''v'' >_I$ takes positive rather than negative values.

An attempt can be made to improve the momentum balances obtained in [16]. With the introduction of the neglected terms, the equations for the normal and tangential momentum balance are:

$$[< p >_I + \rho \langle {v''}^2_l \rangle_I + \rho < v_l >^2_I]_{NT} = [< p >_I + \rho \langle {v''}^2_l \rangle_I + \rho < v_l >^2_I]_T, \quad (24)$$

$$[\rho < v_l >_I < u_l >_I + \rho < u''v'' >_I]_{NT} = \rho[< v_l >_I < u_l >_I + < u''v'' >_I]_T. \quad (25)$$

The deviations from these balances (the superscript F is for "full terms") are found to be;

$$B^F_{nm} \equiv \frac{[< p >_I + \rho \langle {v''}^2_l \rangle_I + \rho < v_l >^2_I]_{NT}}{[< p >_I + \rho \langle {v''}^2_l \rangle_I + \rho < v_l >^2_I]_T} = 1.11, \quad (26)$$

$$B^F_{tm} \equiv \frac{\rho[< v_l >_I < u_l >_I]_{NT} - \rho[< v_l >_I < u_l >_I]_T}{\rho[< u''v'' >_I]_T - \rho[< u''v'' >_I]_{NT}} = -3.08. \quad (27)$$

Equations 26 and 27 include the neglected terms in [16]. The value of $B^F_{nm} = 1.11$ (Eq. 26) is an improvement over the value $B^R_{nm} = 1.40$ in Eq. 22. However, the deviation from $B^R_{tm} = 1$ for the tangential momentum is increased when the omitted terms are included. Another way to assess the tangential momentum balance Eq. 25 is to calculate the ratio of fluxes on the top and bottom boundaries, i.e.

$$B^F_{tm,2} \equiv \frac{[\rho < v_l >_I < u_l >_I + \rho < u''v'' >_I]_{NT}}{[\rho < v_l >_I < u_l >_I + \rho < u''v'' >_I]_T} = 0.127. \quad (28)$$

The sizeable deviation from the tangential momentum balance Eq. 25 is apparent in both Eq. 27 and Eq. 28 for the CV considered here.

7 Conclusion

The approach in [16], placing a very thin CV on the interface, appears to have some shortcomings.

- The most important shortcoming stems from the fact that the TNTI is a TNTI layer and the jump of ω^2 defining it occurs with a certain thickness. There is significant tangential velocity at the interface location and considerable average outflow of mass/momentum from the side boundaries of the CV which are neglected in the analysis of [16] where the interface is considered to be much sharper and the CV is taken with negligible thickness in the interface normal direction.
- Secondly, the $< v_l >_I$ varies significantly across the interface as shown by Fig. 3(a). This significant variation of $< v_l >_I$ across the TNTI relates to the previous point made and highlights the importance of the outflux from the side boundaries of the CV.

As the departures from the mass and momentum balances of [16] are mainly due to this normal-compression/tangent stretching feature of the TNTI local velocity field, the inclusion of the omitted terms at the CV's TNTI-tangent boundaries on both sides of the TNTI is not enough to correct the observed imbalances even though it does reduce the departure from the normal momentum balance in [16].

Finally, a jump of the TNTI-averaged Reynolds shear stress is clearly detectable through the TNTI layer and the TNTI-averaged fluid velocity normal to the TNTI is determined by the correlation between the TNTI normal vector and the fluid velocity fluctuations around the TNTI-average fluid velocity. Furthermore, spatial resolution proves to be a serious limiting factor for the accurate computational estimation of the TNTI's local propagation velocity.

References

1. Er, S., Laval, J.-P., Vassilicos, J.C.: Length scales and the turbulent/non-turbulent interface of a temporally developing turbulent jet. J. Fluid Mech. **970**, A33 (2023). https://doi.org/10.1017/jfm.2023.654
2. Flohr, P., Olivari, D.: Fractal and multifractal characteristics of a scalar dispersed in a turbulent jet. Physica D **76**(1–3), 278–290 (1994)
3. Lane-Serff, G.F.: Investigation of the fractal structure of jets and plumes. J. Fluid Mech. **249**, 521–534 (1993)
4. Miller, P.L., Dimotakis, P.E.: Stochastic geometric properties of scalar interfaces in turbulent jets. Phys. Fluids A **3**(1), 168–177 (1991)
5. Sreenivasan, K.R.: Fractals and multifractals in fluid turbulence. Ann. Rev. Fluids Mech. **23**(1), 539–604 (1991)
6. Holzner, M., Luthi, B.: Laminar superlayer at the turbulent boundary. Phys. Rev. Lett. **106**, 134503 (2011)
7. van Reeuwijk, M., Holzner, M.: The turbulence boundary of a temporal jet. J. Fluid Mech. **739**, 254–275 (2014)
8. Bisset, D.K., Hunt, J.C.R., Rogers, M.M.: The turbulent/non-turbulent interface bounding a far wake. J. Fluid Mech. **451**, 383–410 (2002)
9. Er, S.: Inner structure, turbulent transfer and cascade properties of the turbulent/non-turbulent interface of a turbulent jet. Ph.D. thesis, 15 December 2023 (2023)

10. da Silva, C.B., Pereira, J.C.F.: Invariants of the velocity-gradient, rate-of-strain and rate-of-rotation tensors across the turbulent/non-turbulent interface in jets. Phys. Fluids **22**, 1–18 (2008)
11. Watanabe, T., Sakai, Y., Nagata, K., Ito, Y., Hayase, T.: Vortex stretching and compression near the turbulent/non-turbulent interface in a planar jet. J. Fluid Mech. **758**, 754–785 (2014)
12. Zhou, Y., Vassilicos, J.C.: Energy cascade at the turbulent/non-turbulent interface. Phys. Rev. Fluids **5**, 064604 (2020)
13. Watanabe, T., da Silva, C.B., Nagata, K.: Non-dimensional energy dissipation rate near the turbulent/non-turbulent interfacial layer in free shear flows and shear free turbulence. J. Fluid Mech. **875**, 321–344 (2019)
14. Watanabe, T., da Silva, C.B., Nagata, K.: Scale-by-scale kinetic energy budget near the turbulent/non-turbulent interface. Phys. Rev. Fluids **5**, 124610 (2020)
15. Westerweel, J., Fukushima, C., Pedersen, J.M., Hunt, J.C.R.: Mechanics of the turbulent/non-turbulent interface of a jet. Phys. Rev. Lett. **95**, 174501 (2009)
16. Reynolds, W.C.: Large-scale instabilities of turbulent wakes. J. Fluid Mech. **54**(3), 481–488 (1972)

Effect of Fractal Orifice on Characteristics of Turbulent/Non-turbulent Interface in Synthetic Jet Flow

Congyi Xu and Jinjun Wang(✉)

Fluid Mechanics Key Laboratory of Education Ministry, Beihang University,
Beijing 100191, China
{xucongyi,jjwang}@buaa.edu.cn

Abstract. Synthetic jets with circular and fractal orifices are experimentally investigated using time-resolved stereoscopic particle image velocimetry. The synthetic jet with circular orifice exhibit more rapid centreline velocity decay and half-width growth, indicating superior entrainment over the continuous jet. The synthetic jets with fractal orifices show intermediate entrainment performance between the round synthetic jet and continuous jet. The analysis on turbulent/non-turbulent interface (TNTI) properties reveals that the fractal orifice reduces the mean value and fluctuation of the radial position of the TNTI, as well as the tortuosity of the TNTI. This reduction in TNTI properties leads to a decrease in the area where nibbling occur. Consequently, synthetic jets with fractal orifices exhibit inferior entrainment performance compared to those with circular orifices.

Keywords: jets · turbulent mixing · mixing enhancement

1 Introduction

Synthetic jets [9,21] are active flow control techniques developed over the past three decades. Due to their advantages, including no external air source, simple actuator structure, and superior entrainment characteristics, synthetic jets have found applications in various flow control fields [14,28].

Synthetic jets have been extensively studied through experimental and numerical methods, leading to proposed insights into their entrainment mechanism. Earlier studies [5,15,26] typically attributed the enhanced entrainment of synthetic jets to the effect of vortex rings or strong velocity fluctuations in the near field. However, recent observations [33,34] indicate that the enhanced entrainment occurs in the transition region between the near field, dominated by vortex rings, and the far field, where the flow is fully developed.

To further reveal the mechanism of turbulent entrainment, the turbulent/non-turbulent interface (TNTI) is studied. The TNTI is a very thin fluid layer that separates turbulent and non-turbulent regions, and turbulent

J. Wang and I. Marusic (Eds.): IUTAM-TNTI 2024, IUTAM Bookseries 45, pp. 66–78, 2025.
https://doi.org/10.1007/978-3-031-78151-3_5

entrainment is actually the process by which irrotational fluid crosses the TNTI into the turbulent region. The results of TNTI studies on various flows, such as jets [4,22,23,32], wakes [8,11,16], turbulent boundary layers [2,7,20,31,37,38], mixing layers [1,10] and other flows [17–19,36], show that the geometric and dynamic characteristics of the TNTI play a crucial role in the entrainment process.

The studies of the TNTI in synthetic jet flows show that the high-efficiency entrainment of synthetic jet is also related to the aforementioned characteristics [34,35]. In terms of the geometric characteristics of the TNTI, the TNTI in synthetic jet flows exhibits more violent fluctuation and higher fractal dimension in the near field compared to the continuous jet. This results in a larger surface area for the nibbling process, which enhances local entrainment [34]. In terms of the dynamic characteristics of the TNTI, the small-scale vortices near the TNTI enhance the production of enstrophy by amplifying the compressive strain field perpendicular to the TNTI, and the alignment of the extensive strain parallel to the TNTI with the vorticity vector results in larger enstrophy production [22,30]. The results obtained from different synthetic jets demonstrate a strong correlation between vortex ring breakdown and entrainment enhancement. It has been explored that the "breakdown of the vortex ring", rather than the vortex ring itself, enhances the entrainment in the synthetic jet. This breakdown leads to the transfer of turbulent kinetic energy in synthetic jet flows from large-scale to small-scale. As a result, the small-scale vortices near the TNTI are enhanced, resulting in increased enstrophy production and thereby enhancing local entrainment [35].

The effect of non-circular orifice shapes on synthetic jets has been studied. It has been found that rectangular [29] and elliptical [25] orifices enhance the entrainment of synthetic jets due to the axis-switching mechanism. Conversely, previous studies [3,4] on continuous jets with fractal orifices have shown that they suppress large-scale coherent structures in the near field, resulting in a reduced entrainment performance. Although there have been studies on continuous jets with fractal orifices, the studies on synthetic jets with fractal orifices are still lacking. Will the fractal orifice suppress the vortex ring of the synthetic jet, resulting in reduced entrainment, or will it accelerate the vortex ring breakdown due to its rough edge, resulting in enhanced entrainment? How does the fractal orifice modify the TNTI in the near field of the synthetic jet, thereby influencing its entrainment characteristics? These questions remain to be studied. This paper aims to answer the above questions by studying synthetic jets with circular and fractal orifices.

2 Experimental Methods

2.1 Apparatus

A brief description of the continuous jet nozzle and synthetic jet actuator is provided here, and detailed information about the device can be found in previous

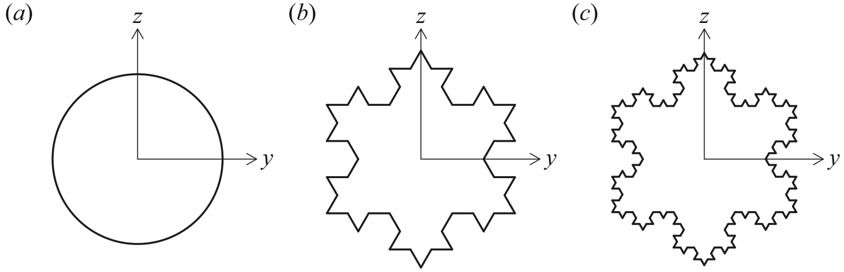

Fig. 1. Jet orifices. (a) Circular, (b) Koch snowflake fractal with 2 iterations, and (c) Koch snowflake fractal with 3 iterations.

work [34]. The seeded airflow, controlled by the flow controller, forms a continuous jet after passing through the honeycomb, screen, and contraction section of the continuous jet nozzle. The synthetic jet is generated by an actuator utilizing a piezoelectric ceramic diaphragm. A sinusoidal signal, generated by the Tektronix AFG1062 signal generator, is amplified by the Aigtek ATA-214 voltage amplifier and applied to the piezoelectric ceramic diaphragm to produce the synthetic jet at the orifice. As shown in Fig. 1, the orifice shapes are circular and Koch snowflake fractal with 2 and 3 iterations, respectively. The circular orifice diameter D and the equivalent diameter $D_e = \sqrt{4S/\pi}$ of the fractal orifice are both 5 mm, where S is the orifice area. Hereafter, both the circular orifice diameter and the equivalent diameter will be denoted by D. The time-averaged blowing velocity U_0 at the synthetic jet actuator orifice can be calculated from

$$U_0 = \frac{1}{T}\int_0^{T/2} u_0(t)\, dt, \tag{1}$$

where the velocity $u_0(t)$ at the synthetic jet actuator orifice can be described by the sinusoidal function $u_0(t) = U_{max}\sin(2\pi f t)$. $T = 1/f$ is the excitation period. U_{max} is the maximum velocity at the orifice over an excitation cycle. The jet Reynolds number Re_j based on the time-averaged blowing velocity U_0 and the orifice diameter D is defined as

$$Re_j = \frac{U_0 D}{\nu}, \tag{2}$$

where ν is the kinematic viscosity. The details on characteristics of the synthetic actuators can be found in previous work [34,35]. In the present experiment, the driving frequency of the piezoelectric ceramic diaphragm is set at the resonance frequency of 500 Hz, and the time-averaged blowing velocity U_0 at the orifice is adjusted by changing the driving voltage. The synthetic jets with circular orifice and fractal orifices are studied at jet Reynolds number $Re_j = 3150$, and the continuous jet at the same jet Reynolds number with circular orifice is taken as a contrast. For simplicity, we refer to the continuous jet with a circular orifice as CJ-round, the synthetic jet with a circular orifice as SJ-round, and synthetic jets with 2 and 3 iterations of the Koch snowflake fractal orifice as SJ-koch2 and SJ-koch3, respectively.

2.2 Particle Image Velocimetry Measurement

Time-resolved stereoscopic particle image velocimetry (TR-SPIV) experiments are conducted in a container with a size of $0.5\,\mathrm{m} \times 0.5\,\mathrm{m} \times 1\,\mathrm{m}$. The coordinate system is defined in Fig. 2, and the centre of the orifice is taken as the origin. A 3 mm thick laser sheet, produced by the Beamtech Vlite-Hi-527 Nd:YAG dual-cavity laser, illuminates the y-z cross-stream plane. The particle images are captured by two Photron Nova R2 high-speed cameras with Nikon 85 mm tilt-shift lenses. The field of view is approximately $24D \times 24D$ $(y \times z)$. The entire field of view is focused by satisfying the Scheimpflug condition. The image size is 1472×2048 pixels $(y \times z)$, and the sampling frequency is 500 Hz. For each jet, the sampling plane starts from $x = 4D$ until $x = 20D$, and the interval is $2D$. The particle images are processed by the multi-pass iterative Lucas-Kanade algorithm [6,24] to obtain the pixel displacements. A interrogation window size of 32×32 pixels with 75% overlap is employed. The uncertainty of particle displacement is approximately 0.1 pixels. Since the mean particle displacement between two frames is approximately 10 pixels, the relative uncertainty of velocity is approximately 1%. The three velocity components in TR-SPIV are reconstructed from two cameras by the polynomial method [27]. The velocity uncertainty in TR-SPIV is approximately 1.5% considering the reconstruction. The streamwise velocity mean profiles and root mean square profiles obtained from TR-SPIV and TR-2DPIV at the same streamwise positions are presented in Fig. 3(a-d). The consistency of the profiles confirms the reliability of the present experiment.

3 Results

3.1 Jet Characteristics

As shown in Fig. 4, the inverse centreline velocity $1/\bar{u}_{cl}$ and the half-width $r_{1/2}$ increase with the downstream distance. These two quantities of synthetic jets grow faster than that of the continuous jet for $x/D > 8$, indicating enhanced entrainment for all three synthetic jets. However, the entrainment of the two fractal synthetic jets is weaker than that of the SJ-round. This difference may be attributed to the modification of the TNTI, which will be examined in the following sections. Additionally, it is observed that the results obtained for the two fractal synthetic jets, both in the current section and subsequent sections, are almost identical. This similarity is mainly due to the fact that the side length of the fractal orifice for SJ-koch3 (about 0.2 mm) is already equivalent to the Kolmogorov scale (about 0.1-0.3 mm at $x/D = 4$), so that it cannot significantly affect the flow field.

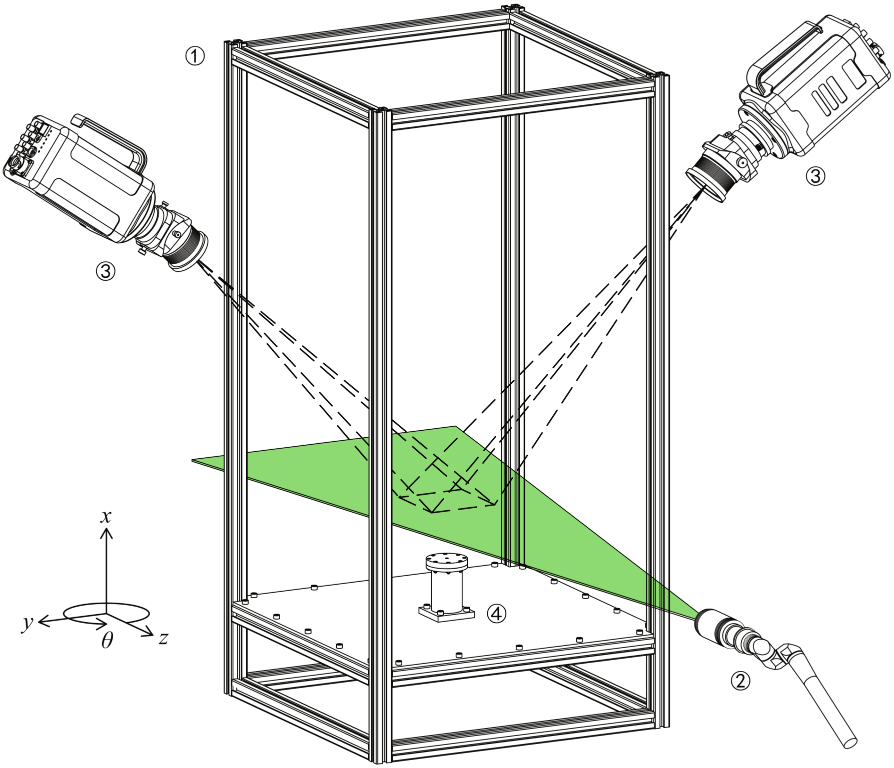

Fig. 2. Schematic of the (1) container, (2) laser head connected to a light arm, (3) high-speed camera, and (4) jet generator (continuous jet nozzle or synthetic jet actuator).

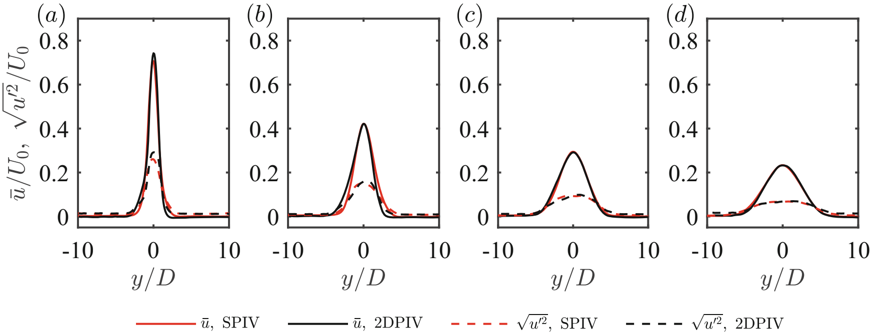

Fig. 3. Streamwise velocity mean profiles and root mean square profiles obtained from TR-SPIV and TR-2DPIV at (a) $x/D = 6$, (b) $x/D = 10$, (c) $x/D = 14$, and (d) $x/D = 18$. The TR-2DPIV data used in the present study is obtained from the experiments conducted by Xu et al. [35].

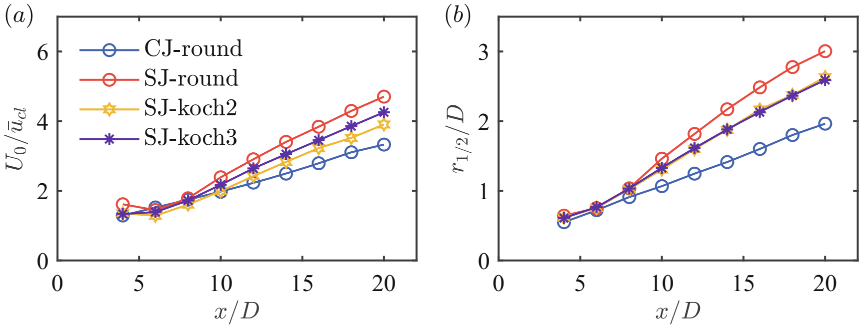

Fig. 4. Variations of the (a) inverse centreline velocity $1/\bar{u}_{cl}$ and (b) the half-width $r_{1/2}$, normalized by U_0 and D, respectively.

3.2 TNTI Detection Method

TNTIs are detected by applying a threshold to the instantaneous vorticity fields. The streamwise deviation used for calculating $\omega = (\omega_x^2 + \omega_y^2 + \omega_z^2)^{1/2}$ is obtained with Taylor's hypothesis. The thresholds for each streamwise position are determined using an empirical process based on evaluating the area-averaged values. For a given variable f, a conditional average function [23] is introduced as

$$\widetilde{f}\,(\omega_{th}) = \frac{\int (f\,da)\,|_{\omega>\omega_{th}}}{\int\, da|_{\omega>\omega_{th}}}. \tag{3}$$

The conditional averaged values of vorticity magnitude with threshold for SJ-round is shown in Fig. 5(a). Since $\widetilde{\omega}$ represents the area-averaged values of ω across all the points inside the region where the local vorticity magnitude is larger than the given threshold value, $\omega > \omega_{th}$, $\widetilde{\omega}$ increases monotonically as ω_{th} increases. The inflection point of passive scalar is used as a threshold to detect TNTI in previous studies [13,23]. The second derivative of the $\widetilde{\omega}$ is presented in Fig. 5(b), and the vorticity magnitude thresholds are determined by the ω_{th} values where $\partial^2\widetilde{\omega}/\partial\omega_{th}^2 = 0$. The same method is used to determine the TNTI in other jets. As an example, Fig. 6 illustrates the instantaneous vorticity magnitude field of SJ-round in logarithmic scaling at $x/D = 20$. Visually, the TNTI, represented by the solid black line, exhibits numerous wrinkles related with the evolution of flow structure, indicating a highly distorted shape.

3.3 Characteristics of TNTI

The TNTI radial position represents the distance between the TNTI and jet centreline. Figure 7 illustrates the variations of the mean value $\overline{r_i}$ and root mean square $r.m.s.(r_i)$ of TNTI radial position. These parameters represent the average expansion and fluctuation of the turbulent region in the cross-stream plane, respectively. The difference in $\overline{r_i}$ among the four cases becomes significant after $x/D = 8$, which coincides with the vortex ring breakdown position reported

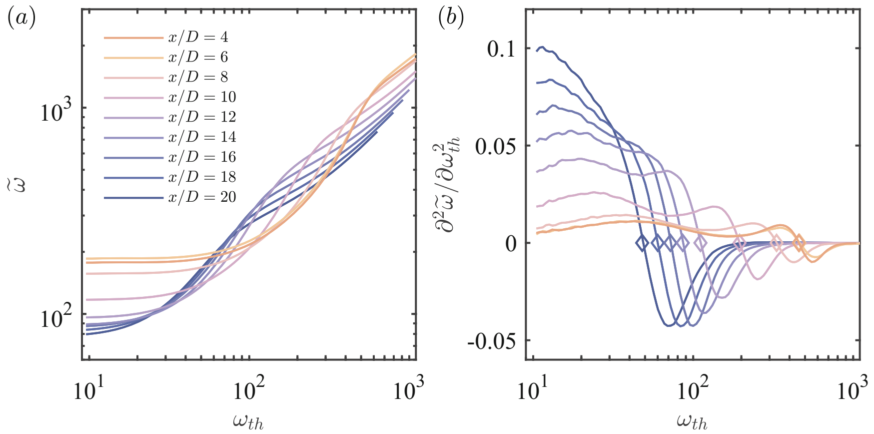

Fig. 5. (a)Conditional averaged vorticity magnitude $\widetilde{\omega}$ with threshold ω_{th} for SJ-round. (b)Second derivative $\partial^2\widetilde{\omega}/\partial\omega_{th}^2$ of the conditional profiles in plot (a). The diamond marks the position of $\partial^2\widetilde{\omega}/\partial\omega_{th}^2 = 0$, corresponding to the abscissa of the inflection point in plot (a).

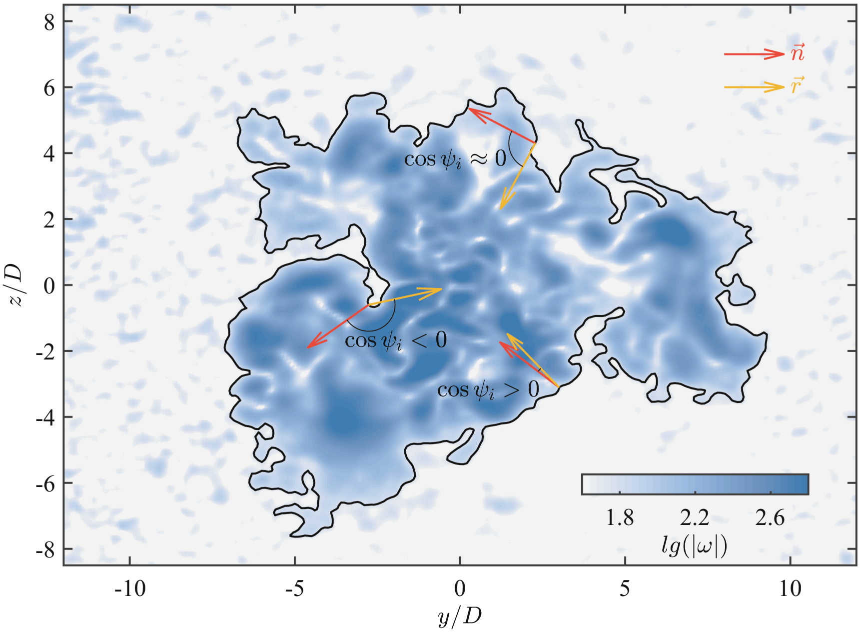

Fig. 6. Instantaneous vorticity magnitude field of SJ-round in logarithmic scaling at $x/D = 20$. the TNTI is denoted by the black solid line. The red and yellow arrows represent the normal vector $\boldsymbol{n}$ of the TNTI and the vector $\boldsymbol{r}$ pointing towards the centreline of the jet, respectively.

in a previous study [35]. For $x/D > 8$, both the $\overline{r_i}$ and the $r.m.s.(r_i)$ of the fractal synthetic jets are smaller than those of the SJ-round. This observation suggests that the suppression of the vortex ring by the fractal orifice also affect its subsequent breakdown process.

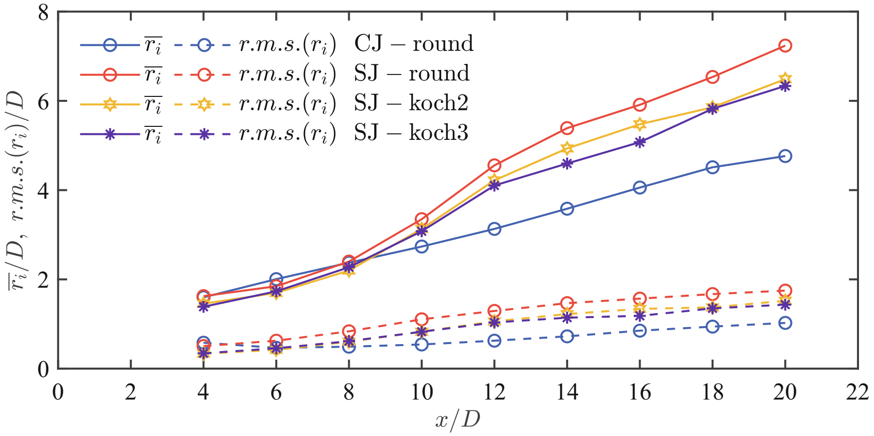

Fig. 7. Variations of the mean value and root mean square of TNTI radial position.

The variations of the probability density function of the TNTI radial position r_i normalized by the jet half-width $r_{1/2}$ are shown in Fig. 8. For $x/D < 10$, the r_i distributions of the fractal synthetic jets are narrower than that of SJ-round. This is attributed to the suppression of coherent structures by the fractal orifice, leading to the inhibition of large-scale excursions of the TNTI. Further downstream, the TNTI fluctuations of the synthetic jets become stronger. The probability density functions of r_i for the synthetic jets exhibit a non-Gaussian, non-zero-skewness distribution, similar to that previously reported in cylinder wake [8]. Given that vortices in the cylinder wake are alternately shed, the current observation suggests that the vortex ring of the synthetic jet undergoes breakdown, leading to the appearance of asymmetric flow structures. As the flow develops, the probability density functions of r_i for all jets show nearly identical distributions and can be normalized by the $r_{1/2}$ in the far field [34].

As shown in Fig. 6, the TNTI angle ψ_i is defined as the angle between the normal vector $\boldsymbol{n}$ of the TNTI and the vector $\boldsymbol{r}$ pointing towards the centreline of the jet [12]. The probability density functions of the cosine of TNTI angle $\cos\psi_i$ for all jets are presented in Fig. 9. These probability density distributions resemble those reported in the previous papers [12,13]: the probability density is concentrated at $\cos\psi_i = 1$ and $\cos\psi_i = -1$, corresponding to the alignment and reversal of $\boldsymbol{n}$ and $\boldsymbol{r}$, respectively. Moreover, the probability density is higher at $\cos\psi_i = 1$. This result is expected, because if the TNTI was unwrinkled, the value of $\cos\psi_i$ would be entirely concentrated at 1. Values of $\cos\psi_i$ less than 0 indicate the folding of the TNTI due to the rollup of the vortex, as illustrated in

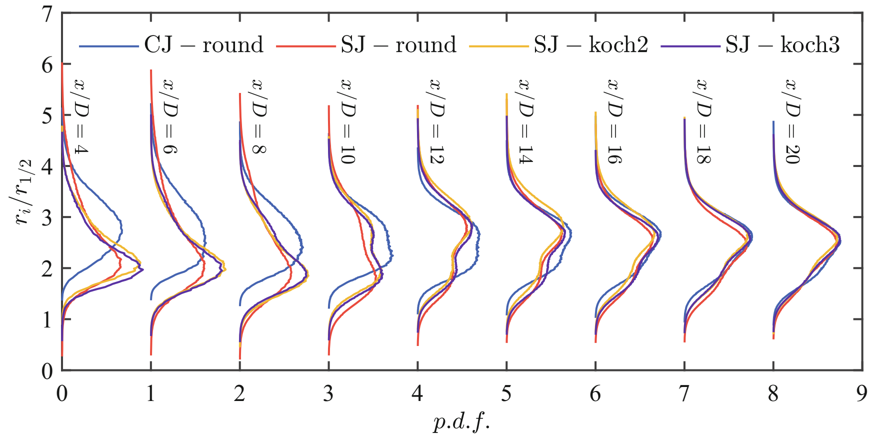

Fig. 8. Variations of the probability density function of the TNTI radial position r_i normalized by the jet half-width $r_{1/2}$. To separate different lines, the profiles are horizontally shifted by 1 from the upstream profiles.

Fig. 6. Now, focus on the part where the $\cos\psi_i$ is less than 0. For $x/D < 10$, the probability densities of the synthetic jet with fractal orifices are lower than that of SJ-round, and even approaches that of CJ-round. However, for $x/D > 10$, the probability densities begin to approach that of SJ-round. At $x/D = 20$, despite some remaining differences, the probability density functions of all jets are very similar as the flow develops. The geometry of the TNTI is highly distorted, and in order to quantify this property, the tortuosity of the TNTI [4] is defined as

$$tortuosity = \frac{L_{TNTI}}{2\pi\overline{r_i}}, \tag{4}$$

where L_{TNTI} represents the mean value of the TNTI length across all the snapshots. As shown in Fig. 10, the TNTI tortuosity increases as the jet develops. In the streamwise range studied, the TNTI tortuosity of SJ-round is greater than that of CJ-round. Especially, at the previously reported vortex ring breakdown position (approximately at $x/D = 10$), the TNTI tortuosity increases significantly faster than that of CJ-round. This indicates that the vortex ring breakdown in the synthetic jet leads to a more abundant hierarchical structure at the edge of the turbulent region. For $x/D < 8$, the TNTI tortuosities of SJ-koch2 and SJ-koch3 are less than that of SJ-round and decrease to the level of CJ-round. However, for $x/D > 8$, the TNTI tortuosities of these two cases still exhibit more rapid growth than that of CJ-round, and their growth is roughly the same as that of SJ-round. Therefore, the fractal orifice reduces the TNTI tortuosity by suppressing the vortex ring without modifying the breakdown position, thus reducing the nibbling area and resulting in reduced entrainment compared to SJ-round.

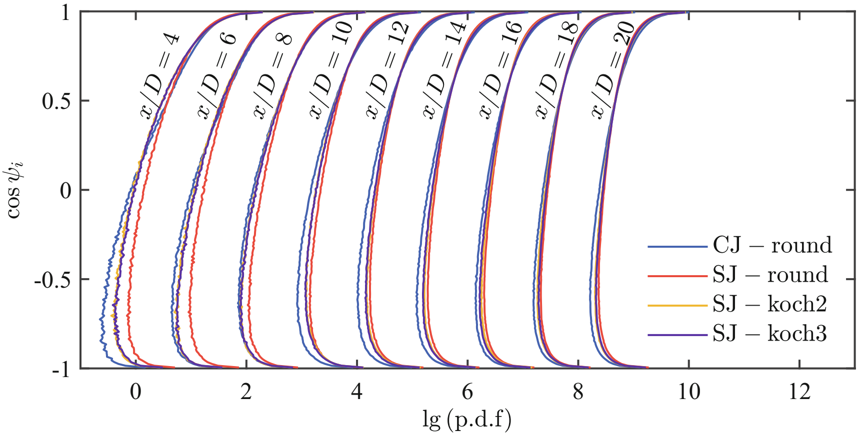

Fig. 9. Variations of the probability density function of the cosine of TNTI angle $\cos\psi_i$. To separate different lines, the profiles are horizontally shifted by 1 from the upstream profiles.

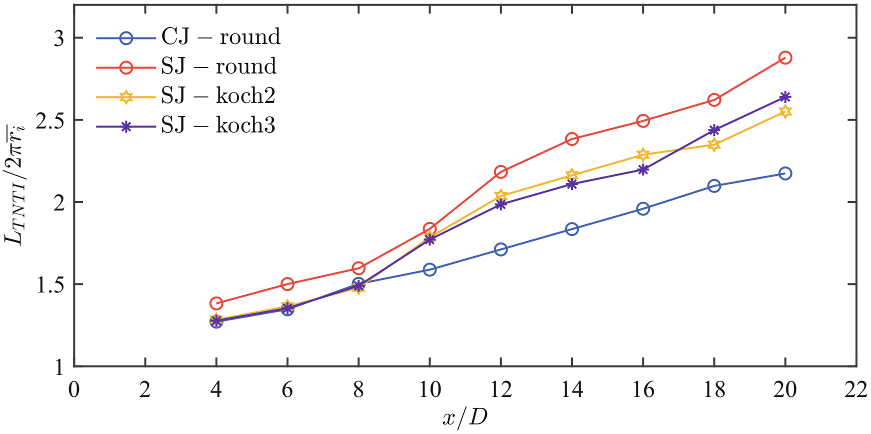

Fig. 10. Variations of the TNTI tortuosity.

4 Conclusion

The measurements are conducted using time-resolved stereoscopic particle image velocimetry on synthetic jets with circular and fractal orifices, as well as a continuous jet with a circular orifice. Compared to CJ-round, SJ-round exhibits more rapid centreline velocity decay and half-width growth, indicating greater entrainment of the synthetic jet. For the synthetic jets with fractal orifices, SJ-koch2 and SJ-koch3 demonstrate intermediate entrainment performance between CJ-round and SJ-round. There is little difference between the results of SJ-koch2 and SJ-koch3, which mainly due to the fact that the orifice length of the Kolmogorov scale of SJ-koch3 cannot significantly affect the flow field. The appropriate vorticity threshold is determined using a conditional average function to detect the TNTI. The analysis on TNTI properties reveals that the fractal orifice reduces the mean value and fluctuation of the radial position of the TNTI, as well as the tortuosity of the TNTI. This reduction in TNTI properties leads to a decrease in the area where nibbling occur. Consequently, synthetic jets with fractal orifices exhibit inferior entrainment performance compared to those with circular orifices.

References

1. Balamurugan, G., Rodda, A., Philip, J., Mandal, A.C.: Characteristics of the turbulent non-turbulent interface in a spatially evolving turbulent mixing layer. J. Fluid Mech. **894**, A4 (2020). ARTN A4 PII S0022112020002414 https://doi.org/10.1017/jfm.2020.241
2. Borrell, G., Jimenez, J.: Properties of the turbulent/non-turbulent interface in boundary layers. J. Fluid Mech. **801**, 554–596 (2016). https://doi.org/10.1017/jfm.2016.430
3. Breda, M., Buxton, O.R.H.: Influence of coherent structures on the evolution of an axisymmetric turbulent jet. Phys. Fluids **30**(3), 035109 (2018). https://doi.org/10.1063/1.5019668
4. Breda, M., Buxton, O.R.H.: Behaviour of small-scale turbulence in the turbulent/non-turbulent interface region of developing turbulent jets. J. Fluid Mech. **879**, 187–216 (2019). https://doi.org/10.1017/jfm.2019.676
5. Cater, J.E., Soria, J.: The evolution of round zero-net-mass-flux jets. J. Fluid Mech. **472**, 167–200 (2002). https://doi.org/10.1017/S0022112002002264
6. Champagnat, F., Plyer, A., Le Besnerais, G., Leclaire, B., Davoust, S., Le Sant, Y.: Fast and accurate PIV computation using highly parallel iterative correlation maximization. Exp. Fluids **50**(4), 1169–1182 (2011). https://doi.org/10.1007/s00348-011-1054-x
7. Chauhan, K., Philip, J., de Silva, C.M., Hutchins, N., Marusic, I.: The turbulent/non-turbulent interface and entrainment in a boundary layer. J. Fluid Mech. **742**, 119–151 (2014). https://doi.org/10.1017/jfm.2013.641
8. Chen, J.G., Buxton, O.R.H.: Spatial evolution of the turbulent/turbulent interface geometry in a cylinder wake. J. Fluid Mech. **969**, A4 (2023). https://doi.org/10.1017/jfm.2023.547
9. Glezer, A., Amitay, M.: Synthetic jets. Annu. Rev. Fluid Mech. **34**(1), 503–529 (2002). https://doi.org/10.1146/annurev.fluid.34.090501.094913
10. Jahanbakhshi, R., Madnia, C.K.: The effect of heat release on the entrainment in a turbulent mixing layer. J. Fluid Mech. **844**, 92–126 (2018). https://doi.org/10.1017/jfm.2018.122
11. Kankanwadi, K.S., Buxton, O.R.H.: On the physical nature of the turbulent/turbulent interface. J. Fluid Mech. **942**, A31 (2022). https://doi.org/10.1017/jfm.2022.388
12. Kohan, K.F., Gaskin, S.: The effect of the geometric features of the turbulent/non-turbulent interface on the entrainment of a passive scalar into a jet. Phy. Fluids **32**(9) (2020). Artn 095114 https://doi.org/10.1063/5.0019860

13. Kohan, K.F., Gaskin, S.J.: On the scalar turbulent/turbulent interface of axisymmetric jets. J. Fluid Mech. **950**, A32 (2022). https://doi.org/10.1017/jfm.2022.825
14. Krishan, G., Aw, K.C., Sharma, R.N.: Synthetic jet impingement heat transfer enhancement - a review. Appl. Therm. Eng. **149**, 1305–1323 (2019). https://doi.org/10.1016/j.applthermaleng.2018.12.134
15. Krishnan, G., Mohseni, K.: Axisymmetric synthetic jets: an experimental and theoretical examination. AIAA J. **47**(10), 2273–2283 (2009). https://doi.org/10.2514/1.42967
16. Li, B.L., Yang, Z.X., Zhang, X., He, G.W., Deng, B.Q., Shen, L.: Using machine learning to detect the turbulent region in flow past a circular cylinder. J. Fluid Mech. **905** (2020). https://doi.org/10.1017/jfm.2020.725
17. Li, S.C., Long, Y.G., Wang, J.J.: Turbulent/non-turbulent interface for laminar boundary flow over a wall-mounted fence. Phys. Fluids **34**(12), 125113 (2022). https://doi.org/10.1063/5.0128609
18. Li, S.C., Wang, J.J., Pan, C., Liu, P.Q.: Properties of the turbulent/non-turbulent interface under the influence of fence. Phys. Gases (2022). https://doi.org/10.19527/j.cnki.2096-1642.0966
19. Li, S.C., Wu, D., Cui, G.Y., Wang, J.J.: Experimental study on properties of turbulent/non-turbulent interface over riblets surfaces at low Reynolds numbers. Chin. J. Theor. Appl. Mech. **52**(6), 1632–1644 (2020). https://doi.org/10.6052/0459-1879-20-211
20. Long, Y.G., Wang, J.J., Pan, C.: Universal modulations of large-scale motions on entrainment of turbulent boundary layers. J. Fluid Mech. **941**, A68 (2022). https://doi.org/10.1017/jfm.2022.355
21. Lu, Y.R., Wang, J.J.: Review and prospect on the efficient synthetic jet. Adv. Mech. **54**(1), 1–25 (2024). https://doi.org/10.6052/1000-0992-23-038
22. Mistry, D., Philip, J., Dawson, J.R.: Kinematics of local entrainment and detrainment in a turbulent jet. J. Fluid Mech. **871**, 896–924 (2019). https://doi.org/10.1017/jfm.2019.327
23. Mistry, D., Philip, J., Dawson, J.R., Marusic, I.: Entrainment at multi-scales across the turbulent/non-turbulent interface in an axisymmetric jet. J. Fluid Mech. **802**, 690–725 (2016). https://doi.org/10.1017/jfm.2016.474
24. Pan, C., Xue, D., Xu, Y., Wang, J.J., Wei, R.J.: Evaluating the accuracy performance of Lucas-kanade algorithm in the circumstance of PIV application. Sci. China-Phys. Mech. Astron. **58**(10), 104704 (2015). https://doi.org/10.1007/s11433-015-5719-y
25. Shi, X.D., Feng, L.H., Wang, J.J.: Evolution of elliptic synthetic jets at low Reynolds number. J. Fluid Mech. **868**, 66–96 (2019). https://doi.org/10.1017/jfm.2019.162
26. Smith, B.L., Swift, G.W.: A comparison between synthetic jets and continuous jets. Exp. Fluids **34**(4), 467–472 (2003). https://doi.org/10.1007/S00348-002-0577-6
27. Soloff, S.M., Adrian, R.J., Liu, Z.C.: Distortion compensation for generalized stereoscopic particle image velocimetry. Meas. Sci. Technol. **8**(12), 1441–1454 (1997). https://doi.org/10.1088/0957-0233/8/12/008
28. Wang, J.J., Feng, L.H.: Flow Control Techniques and Applications. Cambridge University Press (2018). https://doi.org/10.1017/9781316676448
29. Wang, L., Feng, L.H., Wang, J.J., Li, T.: Evolution of low-aspect-ratio rectangular synthetic jets in a quiescent environment. Exp. Fluids **59**(6), 91 (2018). https://doi.org/10.1007/s00348-018-2544-x

30. Watanabe, T., Sakai, Y., Nagata, K., Ito, Y., Hayase, T.: Vortex stretching and compression near the turbulent/non-turbulent interface in a planar jet. J. Fluid Mech. **758**, 754–785 (2014). https://doi.org/10.1017/jfm.2014.559
31. Wei, Q.Q., Wang, P., Zheng, X.J.: Modulations of turbulent/non-turbulent interfaces by particles in turbulent boundary layers. J. Fluid Mech. **983** (2024). https://doi.org/10.1017/jfm.2024.82
32. Westerweel, J., Fukushima, C., Pedersen, J.M., Hunt, J.C.: Mechanics of the turbulent-nonturbulent interface of a jet. Phys. Rev. Lett. **95**(17), 174501 (2005). https://doi.org/10.1103/PhysRevLett.95.174501
33. Xia, X., Mohseni, K.: Transitional region of a round synthetic jet. Phys. Rev. Fluids **3**(1), 011901 (2018). https://doi.org/10.1103/PhysRevFluids.3.011901
34. Xu, C.Y., Long, Y.G., Wang, J.J.: Entrainment mechanism of turbulent synthetic jet flow. J. Fluid Mech. **958**, A31 (2023). https://doi.org/10.1017/jfm.2023.102
35. Xu, C.Y., Wang, J.J.: Vortex ring breakdown dominating the entrainment of a synthetic jet. J. Fluid Mech. **980**, A5 (2024). https://doi.org/10.1017/jfm.2023.1100
36. Zhang, H.Y., Rival, D.E., Wu, X.H.: Kinematics of the turbulent and nonturbulent interfaces in a subsonic airfoil flow. AIAA J. **59**(6), 2155–2168 (2021). https://doi.org/10.2514/1.J059651
37. Zhang, X.X., Watanabe, T., Nagata, K.: Reynolds number dependence of the turbulent/non-turbulent interface in temporally developing turbulent boundary layers. J. Fluid Mech. **964**, A8 (2023). https://doi.org/10.1017/jfm.2023.329
38. Zhuang, Y., Tan, H.J., Wang, W.X., Li, X., Guo, Y.J.: Fractal features of turbulent/non-turbulent interface in a shock wave/turbulent boundary-layer interaction flow. J. Fluid Mech. **869** (2019). ARTN R6 https://doi.org/10.1017/jfm.2019.299

Enhancement of Passive Scalar Mixing in a Shear-Free Turbulent Front

Tomoaki Watanabe(✉)

Department of Mechanical Engineering and Science, Kyoto University,
Kyoto 615-8540, Japan
`watanabe.tomoaki.8x@kyoto-u.ac.jp`

Abstract. A localized turbulent region expands spatially by entraining surrounding non-turbulent fluid, demarcated by the turbulent/non-turbulent interface (TNTI) layer. Small-scale vortex tubes and shear layers within this TNTI layer play a pivotal role in the process of entrainment. Shear layers in turbulence are known to be unstable against perturbations with wavelengths approximately 30 times the Kolmogorov scale. This study conducts numerical experiments aimed at investigating the potential for enhancing passive scalar mixing through the excitation of small-scale shear instability. Direct numerical simulations (DNS) are conducted for a turbulent front with a passive scalar transfer evolving in the absence of mean shear, where solenoidal velocity perturbations of constant wavelength are introduced outside the turbulent region. These perturbations are found to enhance the entrainment rate significantly when their wavelength coincides with the unstable mode of shear layers. Despite the increased entrainment rate facilitated by the excitation of small-scale shear instability, passive scalar statistics dominated by large-scale scalar distributions, such as mean scalar and root-mean-squared scalar fluctuations, remain largely unaffected. However, this enhanced entrainment rate results in the amplification of the scalar dissipation rate, which provides a measure of scalar mixing at small scales. These findings indicate that exciting small-scale shear instability can effectively enhance entrainment and small-scale scalar mixing in intermittent turbulent flows.

Keywords: Turbulent/non-turbulent interface · Entrainment · Turbulent mixing

1 Introduction

Turbulent entrainment refers to the process by which turbulent flow draws in surrounding non-turbulent fluid. This phenomenon is prevalent in canonical turbulent flows, such as jets, wakes, and boundary layers, which exhibit large-scale intermittency. At a fixed location within these flows, regions of turbulent and non-turbulent fluids are intermittently observed. A thin interface layer,

J. Wang and I. Marusic (Eds.): IUTAM-TNTI 2024, IUTAM Bookseries 45, pp. 79–93, 2025.
https://doi.org/10.1007/978-3-031-78151-3_6

known as the turbulent/non-turbulent interface (TNTI), demarcates the turbulent region from the non-turbulent fluid. The TNTI layer is characterized by its minimal thickness, which scales with the Kolmogorov scale, and exhibits a complex geometry shaped by turbulent motions across a broad range of length scales [1]. The structure of the TNTI layers has been analyzed through two- or three-dimensional velocity measurements utilizing particle image velocimetry and direct numerical simulations (DNS) [2,3]. The TNTI layer comprises an outer viscous superlayer and an inner turbulent sublayer. The turbulent and non-turbulent regions can be distinguished by the presence of vorticity, $\boldsymbol{\omega} = \nabla \times \boldsymbol{u}$. Turbulent entrainment is thus conceptualized as a mechanism through which non-turbulent fluid acquires enstrophy, $\omega^2/2 = (\boldsymbol{\omega} \cdot \boldsymbol{\omega})/2$, within the TNTI layer [4,5]. In the viscous superlayer, the growth of $\omega^2/2$ is attributed to viscous diffusion from the turbulent sublayer, while the contribution of inviscid vortex stretching to enstrophy amplification is considered negligible. Conversely, vortex stretching significantly enhances enstrophy within the turbulent sublayer. This transport of enstrophy within the TNTI layer is elucidated by the presence of small-scale vortical structures, such as vortex tubes and sheets, within the turbulent sublayer [6–10]. These structures, characterized by high enstrophy, facilitate an outward viscous diffusion of enstrophy. Moreover, the production of enstrophy via vortex stretching occurs within these structures [6,11,12]. Vortex tubes and sheets play a pivotal role in the process of entrainment.

The TNTI layer also plays a crucial role in scalar mixing [13]. In scenarios where two chemicals are introduced separately into turbulent and non-turbulent flows, the mixing and subsequent chemical reactions are primarily facilitated by the entrainment of the non-turbulent fluid [14–16]. A significant scalar concentration gradient is observed within the TNTI layer, particularly in the direction normal to the interface [17–20]. This pronounced gradient drives the transfer of scalar concentrations by molecular diffusion between the turbulent and entrained fluids. While molecular diffusion tends to smooth the scalar profile within the TNTI layer, the process of inertial scalar transport from the turbulent core region sustains a steep scalar gradient within the TNTI layer [21,22]. These early studies have led to recent investigations of turbulent mixing near the TNTI layer in more complex flows, such as turbulent combustion [23] and buoyant plumes [24]. The analysis of scalar transport near the TNTI layer in jet flames has elucidated the role of the local entrainment process in flame stabilization [25]. Additionally, the nucleation of oil droplets in a jet flow was detailed through concentration measurements in the vicinity of the TNTI layer [26].

Turbulence has been examined from a structural perspective, revealing that at small scales, high enstrophy regions are found within tubular or sheet-like structures, known as vortex tubes and sheets, respectively [11,27]. Various methods have been developed to identify vortex tubes, with one approach identifying them as regions exhibiting large positive values of the second invariant of a velocity gradient tensor [28]. The dimensions of vortex tubes are generally determined by the Kolmogorov scale [6,11]. For many vortex tubes, the relationship between the diameter and the local vortex stretching rate closely aligns with predictions by the Burgers' vortex model. Vortex sheets, characterized by intense shear and referred to as shear layers, have received comparatively less attention due to identification challenges [29]. Recent advancements in the study of shear layers employ a triple decomposition [30,31]. This decomposition is relevant to the Rortex-based decomposition [32] and Schur decomposition [33]. These methods separate three motions of shear, rigid-body rotation, and irrotational strain (elongation) from the velocity gradient tensor. Shear layers are identifiable through the intensity of shearing motion [12,34]. Recent studies using this decomposition have elucidated the statistical properties of shear layers. Similar to vortex tubes, the thickness of shear layers scales with the Kolmogorov scale [12,35,36]. Additionally, the relationship between the thickness and vortex stretching rate aligns with Burgers' vortex layers. Similar layer structures appear in turbulence as regions with a high scalar dissipation rate. However, it has been shown that shear layers are irrelevant to strongly dissipative regions of passive scalar fluctuations [36]. The velocity field induced by shear layers can be reconstructed using the Biot-Savart law applied to the shear component of vorticity vectors. Analyses of reconstructed velocity fields have demonstrated that shear layers significantly contribute to the energy cascade [37]. Shear layers appear near vortex tubes, and their interaction can be crucial in the formation of a biaxial strain acting on the shear layers [38,39]. Due to the strain and shear, vortex stretching actively occurs in the shear layers [12,40]. These investigations have confirmed the importance of shear layers in various turbulence properties.

Shear layers in turbulence are inherently unstable and shear instability produces vortex tubes [12,41]. Numerical simulations were performed for an isolated shear layer, modeled with the mean flow pattern observed around shear layers in turbulence [42]. Even in the absence of external perturbations, the shear layer exhibits inherent instability due to self-induced velocity from shear vorticity, particularly when the layer possesses a small aspect ratio. This stands in contrast to a uniform shear layer with an infinite aspect ratio, which remains stable in the absence of perturbations. The formation of a vortex from a shear layer with a finite aspect ratio is promoted under the influence of perturbations of a specific wavelength. Coupled with observations of shear layers in turbulence, these findings suggest that the instability of many shear layers in turbulence is excited by perturbations with a wavelength approximately 30 times the Kolmogorov scale. Furthermore, the response of shear layers to such perturbations was investigated through DNS of decaying isotropic turbulence [42]. Upon the influence of perturbations near this critical wavelength, numerous shear layers collapse rapidly, leading to an increased number density of vortex tubes. This rise in the number of vortex tubes, in turn, results in a greater number density of shear layers, which form around the vortex tubes [39].

These investigations into entrainment and the instability of shear layers suggest that stimulating shear instability near the TNTI layer could lead to enhanced passive scalar mixing, alongside the process of entrainment. This study aims to explore the potential for enhancing mixing by introducing perturbations with a wavelength corresponding to the unstable mode of shear layers. For this purpose, DNS is performed for a shear-free turbulent front with passive scalar transfer. Perturbations are introduced in the non-turbulent region, affecting the entrainment process from outside of turbulence. It will be shown that entrainment and small-scale scalar mixing are enhanced when the perturbations have a wavelength matching the small-scale shear instability.

The flow setup in this study will aid in understanding the modulation of the TNTI layer. In particle-laden flows, particles can disturb the flow field, and recent studies have explored the modulations of the TNTI layer by solid particles [43]. The small-scale shear instability within the TNTI layer may be relevant to particle effects on turbulent entrainment when the particle size matches the unstable wavelength of the shear layers. Additionally, the unstable mode of shear layers within the TNTI layer can be important for the interface between two different turbulent regions, known as a turbulent/turbulent interface (TTI) layer. The TTI layer forms along the shear layers, and entrainment by a primary turbulent region from background turbulence is expected to be influenced by these shear layers [44]. Vortex stretching actively occurs within the shear layers, thus enstrophy production is not negligible within the entire TTI layer, unlike the viscous superlayer for the TNTI layer [45]. Recent investigations of the TTI layer have revealed that background turbulence alters the interface geometry and the entrainment rate of primary turbulence [46–49]. These studies often consider large-scale background turbulence whose integral scale is comparable to that of primary turbulence. The present findings are applicable to understanding the impact of small-scale background turbulence on entrainment and scalar mixing. The characteristic velocity of shear layers is the Kolmogorov velocity scale, which decreases as the Reynolds number increases. Therefore, even weak perturbations can excite its instability at a high Reynolds number as long as the perturbation wavelength matches the instability mode [42]. This feature can be important in establishing control strategies for turbulent entrainment. Therefore, shear instability within the TNTI layer has many potential applications in engineering fields, such as flows around airfoils [50] and turbulent combustion [25]. Controlling entrainment with small-scale disturbance might also be important in meteorological fields, where small-scale instability might be leveraged to control atmospheric phenomena with small-scale and weak disturbances from human activity [51]. For example, cloud evolutions are often influenced by the entrainment process at the edge, which has recently been studied in terms of the TNTI layer [52,53].

2 DNS of a Shear-Free Turbulent Front Subject to External Perturbations

2.1 A Shear-Free Turbulent Front

DNS is conducted for a shear-free turbulent front with passive scalar transfer [54,55]. The flow is initiated by introducing homogeneous isotropic turbulence (HIT) into a quiescent fluid. This setup allows the turbulent region to expand by entraining the surrounding non-turbulent fluid, without being influenced by mean shear. The computational domain is configured as a cube with dimensions L^3, discretized into N^3 grid points. The incompressible Navier–Stokes equations, coupled with the advection-diffusion equation for a passive scalar ϕ, govern the flow evolution. These equations are expressed as follows:

$$\frac{\partial u_j}{\partial x_j} = 0, \tag{1}$$

$$\frac{\partial u_i}{\partial t} + \frac{\partial u_i u_j}{\partial x_j} = -\frac{1}{\rho}\frac{\partial p}{\partial x_i} + \nu \frac{\partial^2 u_i}{\partial x_j \partial x_j}, \tag{2}$$

$$\frac{\partial \phi}{\partial t} + \frac{\partial u_j \phi}{\partial x_j} = D \frac{\partial^2 \phi}{\partial x_j \partial x_j}, \tag{3}$$

where x_i denotes position, t time, u_i the velocity vector, p pressure, ρ density, and ν the kinematic viscosity. The diffusivity coefficient for ϕ is represented by D. The Schmidt number, $Sc = \nu/D$, is assumed to be unity. These equations are solved using an in-house finite-difference code based on the fractional step method [12]. Spatial and temporal discretizations employ the fourth-order fully conservative central difference and third-order Runge–Kutta schemes, respectively [56]. The Poisson equation for pressure is solved using the BiCGStab method.

The initial velocity field for the shear-free turbulent front is generated by applying a top-hat function $C(y)$ to the velocity field HIT, $\boldsymbol{u}_{HIT}$, resulting in $C\boldsymbol{u}_{HIT}$:

$$C(y) = 0.5 + 0.5\tanh\left[\frac{4}{\Delta_I}\left(1 - \frac{2|y - L/2|}{L_T}\right)\right], \tag{4}$$

where $C(y) = 1$ closely approximates the central region $|y| \lesssim L_T/2$ and $C(y) = 0$ elsewhere. This configuration ensures statistical homogeneity along the x and z directions, with a distinct interface perpendicular to the y direction. The coordinate system (x, y, z) is defined with $y = 0$ at the domain center and $(x, z) = (0, 0)$ at the corner of the x–z plane. The statistical properties of HIT are evaluated using a volume average denoted by $\overline{f}$ for any variable f, with $f' = f - \overline{f}$ representing its fluctuating component. The average kinetic energy dissipation rate is $\varepsilon = \overline{2\nu S_{ij} S_{ij}}$, where $S_{ij} = (\partial u_i/\partial x_j + \partial u_j/\partial x_i)/2$ is the rate-of-strain tensor. The Kolmogorov length, time, and velocity scales are defined as $\eta = (\nu^3/\varepsilon)^{1/4}$, $\tau_\eta = (\nu/\varepsilon)^{1/2}$, and $u_\eta = (\nu\varepsilon)^{1/4}$, respectively. Subscript 0 indicates initial HIT statistics, such as η_0 and $u_{\eta 0}$. The initial turbulent region has a width of $L_T = L/3$ and the interfacial layer thickness of $\Delta_I = 10\eta_0$. The initial scalar profile is given by $\phi = C(y)$, distinguishing the turbulent region ($\phi > 0$) from the exterior ($\phi = 0$).

The DNS database of statistically steady HIT subject to a linear forcing [57] is used to generate the initial field. The simulation parameters were determined to realize HIT with the time-averaged Reynolds number $Re_{L0} = u_{rms0} L_{I0}/\nu = 350$, where $u_{rms} = \sqrt{\overline{u'^2}}$ is the root-mean-squared (rms) velocity fluctuation and L_I

is the characteristic length scale of large-scale motion defined as $L_I = u_{rms}^3/\varepsilon$. The computational domain size L^3 is $(5.3L_{I0})^3$ based on the time average of L_{I0} of HIT. Five snapshots are used as the initial conditions of the turbulent front. Based on ensemble averages, the turbulent Reynolds number $Re_\lambda = u_{rms}\lambda/\nu$ defined with the Taylor microscale $\lambda = \sqrt{15\nu u_{rms}^2/\varepsilon}$ and the rms velocity fluctuations is $Re_{\lambda 0} = 72$. The number of grid points N^3 is 512^3, for which the grid spacing $\Delta = L/N$ is $0.8\eta_0$. The subsequent simulation of the turbulent front also uses the same computational parameters by modifying the velocity field of HIT with Eq. (4). As the turbulent front decays, η increases with time, ensuring that Δ is smaller than 0.8η. Figure 1 shows the two-dimensional distributions of ϕ, visualizing the temporal evolution of the shear-free turbulent front. The turbulent region with $\phi > 0$ spatially expands with time by entraining the external fluid with $\phi = 0$.

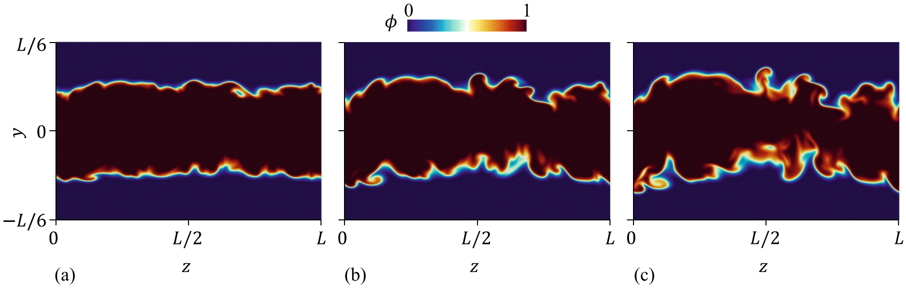

Fig. 1. Development of the shear-free turbulent front without perturbations. Two-dimensional distributions of the passive scalar ϕ are visualized at (a) $t = 2\tau_{\eta 0}$, (b) $t = 4\tau_{\eta 0}$, and (c) $t = 6\tau_{\eta 0}$.

This study delves into the effects of introducing perturbations external to the turbulent region. Building on insights from a prior investigation of the perturbation response of decaying HIT [42], solenoidal perturbations are superimposed on the initial velocity field. These perturbations are represented by sinusoidal functions as follows:

$$\boldsymbol{u}_P = (1 - C)\left[u_f \sin(2\pi y/\lambda_f), u_f \sin(2\pi z/\lambda_f), u_f \sin(2\pi x/\lambda_f)\right], \tag{5}$$

where the amplitude u_f and the wavelength λ_f define the perturbation characteristics. Given the nature of $C(y)$, the influence of $\boldsymbol{u}_P$ sharply declines from the outside towards the turbulent region. Perturbation parameters u_f and λ_f are determined based on $u_{\eta 0}$ and η_0, respectively. The study considers two values for λ_f: $\lambda_f = 30\eta_0$, corresponding to the unstable mode of shear instability, and $\lambda_f = 140\eta_0$, which is unrelated to the instability. Prior work has assessed the role of u_f in exciting shear instability within HIT [42]. The perturbation effects are determined by the ratio of u_f to $u_{\eta 0}$ for $\lambda_f \approx 30\eta_0$. Herein, u_f is set at $u_f/u_{\eta 0} = 1.4$. In addition to these perturbed cases, a shear-free turbulent front without of perturbations is also simulated as a reference case for comparative analysis. The influence of the perturbations is elucidated by comparing the perturbed cases with the unperturbed baseline. The simulation time spans over $10\tau_{\eta 0}$. Notably, the perturbation effects on shear instability in decaying HIT were shown to prevail within a few times the Kolmogorov time scale [42]. The shear-free turbulent front exhibits statistical homogeneity on the x–z planes, and spatial averages across the x–z planes are taken as functions of y and t. In addition, ensemble averages are taken for five simulations initialized with different snapshots of HIT.

Compared to other turbulent shear flows, shear-free turbulence offers the advantage of initial statistical homogeneity within the turbulent region. A critical parameter in the present DNS is the ratio of the perturbation wavelength λ_f to the Kolmogorov scale η. Given that η remains constant within the initial turbulent region, adopting a constant λ_f ensures that the ratio λ_f/η is also constant. In contrast, in turbulent shear flows, η and other length scales vary spatially within the turbulent region, complicating the interpretation of results based on the ratio between the perturbation wavelength and turbulence length scales. Previous studies have demonstrated that the characteristics of the TNTI and small-scale shear layers are largely unaffected by mean shear [10,58]. Although the present DNS excludes mean shear effects, the findings are anticipated to be relevant for more complex flows with mean shear, such as jets and mixing layers.

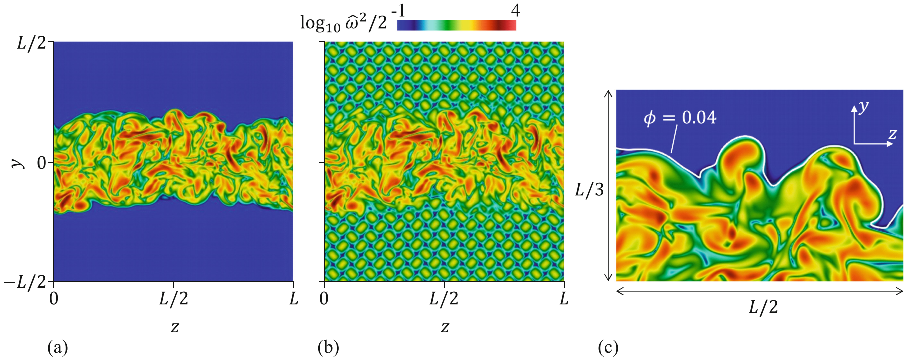

Fig. 2. Enstrophy distributions at $t = 4\tau_{\eta 0}$ in (a) the unperturbed case and (b) the perturbed case with $\lambda_f = 30\eta_0$. (c) The iso-scalar line of $\phi = 0.04$ and enstrophy distribution near the TNTI layer at $t = 7\tau_{\eta 0}$. Enstrophy is normalized as $\hat{\omega}^2/2 = (\omega^2/2)/(u_{rms0}^2/L_0^2)$.

2.2 The Evaluation of the Entrainment Rate with Isosurface Area Density

The entrainment rate is quantified by examining the boundary propagation of the turbulent front. Figure 2 depicts the two-dimensional distributions of enstrophy, $\omega^2/2$, in the turbulent front, both with and without the introduction of initial perturbations. As outlined in Eq. (5), vortical perturbations result in a spatially periodic variation in enstrophy, which is notably apparent outside the turbulent front in Fig. 2(b). Consequently, enstrophy is deemed unsuitable for the identification of the TNTI layer, which is more accurately identified using the passive scalar. Previous research has demonstrated that enstrophy and passive scalar isosurfaces, for $Sc = 1$, align closely in terms of their location and shape at the outer edge of the TNTI layer [17,59]. The outer boundary of the TNTI layer is determined by an isosurface of $\phi = \phi_{th}$, for which the turbulent front is defined by $\phi > \phi_{th}$. Here, $\phi_{th} = 0.04$ is selected based on the threshold dependence of the turbulent volume [60]. For the unperturbed case, Fig. 2 compares the iso-scalar line of $\phi = \phi_{th}$ and the enstrophy distribution. The iso-scalar line precisely delineates the boundary between rotational and irrotational fluids. The TNTI layer encompasses both the outer viscous superlayer and the inner turbulent sublayer, with the isosurface of ϕ residing at the outer boundary of the viscous superlayer, adjacent to the irrotational fluid. Thus, this isosurface is referred to as the irrotational boundary [21].

The entrainment rate is calculated as the surface integral of the propagation velocity of the irrotational boundary. This calculation is performed for a specific time step to derive the entrainment rate as a function of time. The surface integral is computed using an isosurface area density, Σ', as detailed by Blakeley et al. [61]. The function $X(x, y, z)$, serving as an indicator of the turbulent front, is defined by:

$$X = \begin{cases} 1 & \text{outside the turbulent front } (\phi(x,y,z) \leq \phi_{th}) \\ 0 & \text{inside the turbulent front } (\phi(x,y,z) > \phi_{th}) \end{cases}. \tag{6}$$

The isosurface area density for the scalar isosurface of $\phi(x, y, z) = \phi_{th}$ is specified as follows:

$$\Sigma'(x,y,z) = -\frac{1}{\sqrt{(\partial\phi/\partial x_i)^2}} \frac{\partial X}{\partial x_j} \frac{\partial \phi}{\partial x_j}. \tag{7}$$

The total area of the isosurface within the computational domain $\mathcal{V}$ is calculated by the volume integral of the isosurface area density, $A = \iiint_{\mathcal{V}} \Sigma' dxdydz$. For any function f, its surface integral, denoted as $\langle f \rangle_S$, is written with a volume integral, $\langle f \rangle_S = \iiint_{\mathcal{V}} f\Sigma' dxdydz$. The propagation velocity of a scalar isosurface at a point (x, y, z) is determined as $v_P(x, y, z) = |\nabla\phi|^{-1} D\nabla^2\phi$, with the propagation direction represented by $\boldsymbol{n} = -\nabla\phi/|\nabla\phi|$. The volume of the turbulent front, V_T, is obtained by integrating $(1 - X)$ over the domain, $V_T = \iiint_{\mathcal{V}}(1 - X)dxdydz$. The entrainment rate, $\dot{V}_T$, quantifies the temporal change in V_T and is defined through the surface integral of v_P on the irrotational boundary as $\dot{V}_T = \langle v_P \rangle_S$.

Positive $\dot{V}_T$ values signify the expansion of the turbulent front by entraining external fluid.

3 Results and Discussion

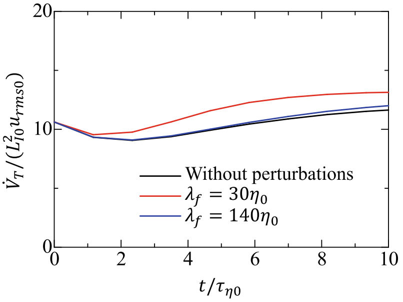

Fig. 3. Temporal variations of entrainment rate $\dot{V}_T$.

Figure 3 presents the temporal variation in the entrainment rate, $\dot{V}_T$, comparing the cases with and without perturbations over time. Initially, for $t/\tau_{\eta 0} \lesssim 1$, the entrainment rate appears consistent across all cases. The introduction of perturbations with $\lambda_f = 30\eta_0$ notably increases $\dot{V}_T$ in comparison to the unperturbed case. Conversely, the entrainment rate remains largely unchanged in the presence of perturbations with $\lambda_f = 140\eta_0$, despite an identical perturbation amplitude of $u_f = 1.4u_{\eta 0}$ to that in the $\lambda_f = 30\eta_0$ case. The differential impact of these perturbations was previously explored in isotropic turbulence through the visualization of shear layers and the assessment of the number of vortices [42]. Perturbations with $\lambda_f = 30\eta_0$ were shown to promote shear instability, leading to rapid vortex formation. It was also shown that shear layers exhibit minimal response to perturbations with a wavelength irrevent to the shaer instability. Perturbations effectively influence entrainment when their wavelength aligns with the unstable mode of shear instability. For the present case, the perturbations of $\lambda_f = 30\eta_0$ elevate the entrainment rate by 17% relative to the unperturbed case, underscoring the pivotal role of small-scale vortices and shear layers in the entrainment mechanism.

The above investigations reveal that entrainment is effectively promoted by perturbations when the wavelength aligns with the unstable mode of shear instability. The consequences of the entrainment enhancement on scalar mixing are assessed through passive scalar statistics. Figure 4(a) presents the lateral distribution of the mean scalar, $\overline{\phi}$, across three time instances, showcasing the evolution of a scalar mixing layer within the turbulent front. The scalar mixing layer, characterized by $0 < \overline{\phi} < 1$, broadens in the y direction over time. Notably, despite the increase in the entrainment rate, the profile of $\overline{\phi}$ remains largely consistent, irrespective of perturbations. Figure 4(b) shows the profile of rms scalar

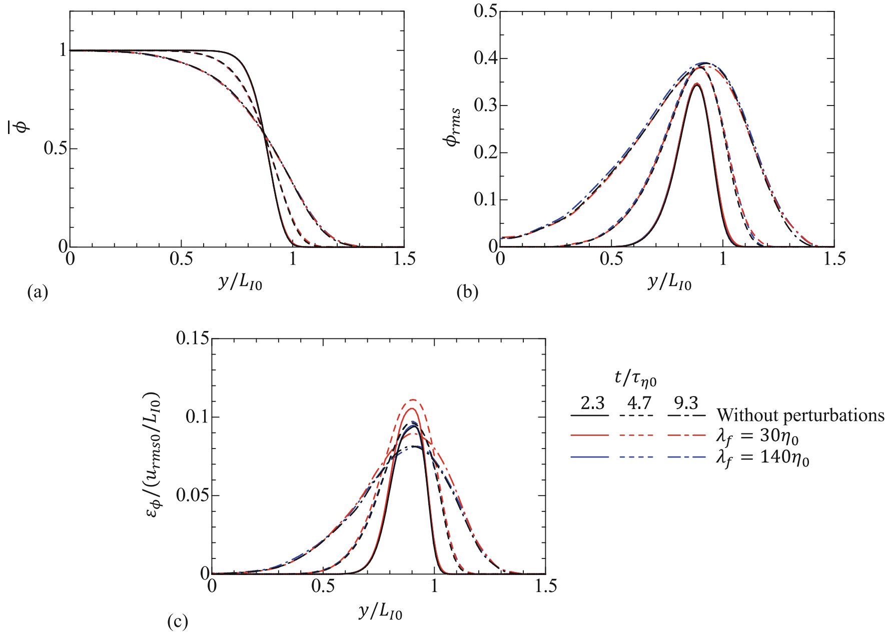

Fig. 4. Lateral distributions of (a) mean scalar $\overline{\phi}$, (b) rms scalar fluctuations ϕ_{rms}, and (c) averaged dissipation rate of scalar fluctuations ε_ϕ.

fluctuations, $\phi_{rms} = \sqrt{\overline{\phi'^2}}$. Initially, ϕ_{rms} is zero due to $\phi = C(y)$; however, as the turbulent front develops, scalar fluctuations are generated by the turbulent scalar flux in the y direction, $\overline{v'\phi'}$. This flux contributes to the production term of scalar variance, $-2\overline{v'\phi'}(\partial\overline{\phi}/\partial y)$. Thus, ϕ_{rms} peaks in areas with a significant mean scalar gradient. The expansion of the scalar mixing layer over time results in a spatially broader distribution of ϕ_{rms}. The presence of perturbations appears to have minimal effects on ϕ_{rms}, which exhibits nearly identical profiles for all cases. While perturbations with $\lambda_f = 30\eta_0$ increases the entrainment rate by exciting the shear instability at small scales, they do not alter mean scalar profiles or rms scalar fluctuations significantly, as these scalar statistics are dominated by large-scale scalar distributions. Figure 4(c) exhibits the lateral profile of the averaged dissipation rate of scalar fluctuations, $\varepsilon_\phi = \overline{D\nabla\phi \cdot \nabla\phi}$. Contrary to the behaviors of mean scalar and rms scalar fluctuations, perturbations with $\lambda_f = 30\eta_0$ lead to a pronounced increase in ε_ϕ. This enhancement in scalar dissipation rate is not observed for $\lambda_f = 140\eta_0$. Thus, the entrainment enhancement affects the scalar statistics related to small-scale scalar fluctuations.

The analysis of the scalar energy spectrum provides insights into the scale-dependent effects of perturbations on scalar mixing. The Fourier transform of the scalar field, ϕ, along the x direction and its complex conjugate are represented as $\hat{\phi}(k_x, y, z)$ and $\hat{\phi}^*(k_x, y, z)$, respectively, where k_x is the wavenumber in the x direction. The energy spectrum of ϕ, denoted as $E_\phi(k_x, y)$, is defined as

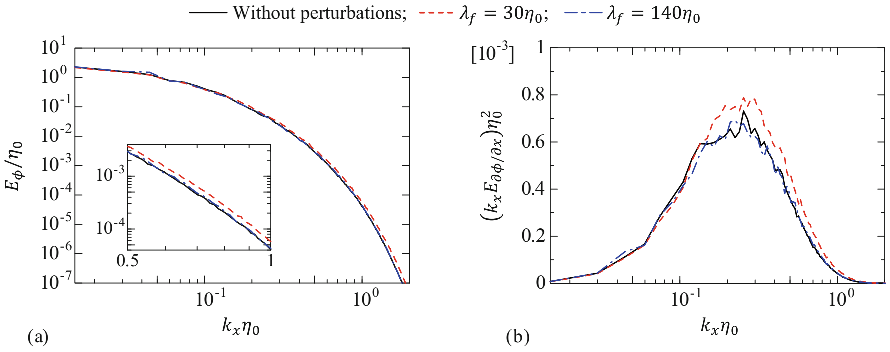

Fig. 5. Energy spectra of (a) scalar fluctuations ϕ', E_ϕ and (b) scalar gradient $\partial\phi/\partial x$, $E_{\partial\phi/\partial x}$ at $t = 8\tau_{\eta 0}$.

$E_\phi(k_x, y) = \mathrm{Re}[\overline{\hat{\phi}\hat{\phi}^*}]$, where Re represents a real part of complex variables and the average is taken spatially in the z direction. This spectrum is specifically evaluated at a position $y/L_{I0} = 0.89$, near the center of the scalar mixing layer.

Figure 5(a) reveals the energy spectrum E_ϕ at $t = 8\tau_{\eta 0}$, a point in time when perturbations have already enhanced both the entrainment and scalar dissipation rates. The introduction of perturbations, irrespective of their wavelength, shows minimal impact on the overall shape of the spectrum. Notably, the spectra at lower wavenumbers (representing large scales) closely align across cases, indicating that perturbations do not significantly alter large-scale scalar distributions. However, the introduction of perturbations with $\lambda_f = 30\eta_0$ leads to an elevated E_ϕ at high wavenumbers compared to the unperturbed case. This influence is not observed for $\lambda_f = 140\eta_0$.

Figure 5(b) presents the energy spectrum of the scalar gradient, $E_{\partial\phi/\partial x}$, premultiplied by the wavenumber, k_x. The premultiplied spectrum is displayed on a semi-logarithmic scale to assess the contribution of each scale to $\overline{(\partial\phi/\partial x)^2}$, which is associated with the scalar dissipation rate. This relationship is expressed as $\overline{(\partial\phi/\partial x)^2} = \int E_{\partial\phi/\partial x} dk_x$ and can be reformulated as $\overline{(\partial\phi/\partial x)^2} = \int k_x E_{\partial\phi/\partial x} d(\log_{10} k_x)$. Thus, the area under the curve of $k_x E_{\partial\phi/\partial x}$ represents the contribution to $\overline{(\partial\phi/\partial x)^2}$ at the scale of $\log_{10} k_x$. Introducing perturbations with $\lambda_f = 30\eta_0$ increases $k_x E_{\partial\phi/\partial x}$ for $k_x\eta_0 \gtrsim 0.15$ compared to the unperturbed case, while no such increase is observed for $\lambda_f = 140\eta_0$. Given that the scalar gradient is predominantly influenced by small-scale scalar fluctuations, this enhancement in $k_x E_{\partial\phi/\partial x}$ reflects a corresponding change in E_ϕ at high wavenumbers, indicating that small-scale scalar fluctuations are amplified with the introduction of perturbations at $\lambda_f = 30\eta_0$. Such perturbations efficiently promote small-scale shear instability, thereby enhancing the entrainment rate. These observations imply that enhanced entrainment promotes rapid scalar mixing at small scales without affecting the large-scale scalar distribution.

4 Conclusions

DNS has been performed to investigate the potential for enhancing passive scalar mixing through the excitation of small-scale shear instability. This study simulates a turbulent front without mean shear, subjected to external perturbations of constant wavelength. When the wavelength corresponds with the unstable mode of shear layers, as documented in previous research [42], the perturbations lead to an increase in the entrainment rate. This enhancement of entrainment does not occur for perturbations with wavelengths irrelevant to the shear instability. The impact of this entrainment enhancement on scalar mixing has been evaluated using passive scalar statistics. The mean scalar profile and rms scalar fluctuations, primarily influenced by large-scale scalar distributions, remain unaffected by the increased entrainment rate. However, the scalar dissipation rate experiences amplification as a result of increased entrainment. This amplification is attributed to enhanced scalar fluctuations at small scales. The characteristics of shear layers are defined by Kolmogorov scales, and the length and velocity scales of the shear layers, normalized by Kolmogorov scales, are consistent across different flows and Reynolds numbers. The findings suggest that small-scale shear instability can be exploited to enhance entrainment and small-scale scalar mixing in various intermittent turbulent flows.

Acknowledgements. Numerical simulations presented in this paper were performed using the high-performance computing systems at the Japan Agency for Marine-Earth Science and Technology and Nagoya University. This work was also supported by a Collaborative Research Project on Computer Science with High-Performance Computing in Nagoya University and by JSPS KAKENHI Grant Number JP22K03903.

References

1. da Silva, C.B., Hunt, J.C.R., Eames, I., Westerweel, J.: Interfacial layers between regions of different turbulence intensity. Annu. Rev. Fluid Mech. **46**, 567–590 (2014)
2. Bisset, D.K., Hunt, J.C.R., Rogers, M.M.: The turbulent/non-turbulent interface bounding a far wake. J. Fluid Mech. **451**, 383–410 (2002)
3. Westerweel, J., Fukushima, C., Pedersen, J.M., Hunt, J.C.R.: Mechanics of the turbulent-nonturbulent interface of a jet. Phys. Rev. Lett. **95**(17), 174501 (2005)
4. Holzner, M., Lüthi, B.: Laminar superlayer at the turbulence boundary. Phys. Rev. Lett. **106**(13), 134503 (2011)
5. Taveira, R.R., da Silva, C.B.: Characteristics of the viscous superlayer in shear free turbulence and in planar turbulent jets. Phys. Fluids **26**(2), 021702 (2014)
6. da Silva, C.B., Dos Reis, R.J.N., Pereira, J.C.F.: The intense vorticity structures near the turbulent/non-turbulent interface in a jet. J. Fluid Mech. **685**, 165–190 (2011)
7. Jahanbakhshi, R., Vaghefi, N.S., Madnia, C.K.: Baroclinic vorticity generation near the turbulent/non-turbulent interface in a compressible shear layer. Phys. Fluids **27**(10), 105105 (2015)

8. Watanabe, T., Jaulino, R., Taveira, R.R., da Silva, C.B., Nagata, K., Sakai, Y.: Role of an isolated eddy near the turbulent/non-turbulent interface layer. Phys. Rev. Fluids **2**(9), 094607 (2017)
9. Neamtu-Halic, M.M., Krug, D., Mollicone, J.P., van Reeuwijk, M., Haller, G., Holzner, M.: Connecting the time evolution of the turbulence interface to coherent structures. J. Fluid Mech. **898**, A3 (2020)
10. Hayashi, M., Watanabe, T., Nagata, K.: The relation between shearing motions and the turbulent/non-turbulent interface in a turbulent planar jet. Phys. Fluids **33**(5), 055126 (2021)
11. Jiménez, J., Wray, A.A.: On the characteristics of vortex filaments in isotropic turbulence. J. Fluid Mech. **373**, 255–285 (1998)
12. Watanabe, T., Tanaka, K., Nagata, K.: Characteristics of shearing motions in incompressible isotropic turbulence. Phys. Rev. Fluids **5**(7), 072601(R) (2020)
13. Westerweel, J., Fukushima, C., Pedersen, J.M., Hunt, J.C.R.: Momentum and scalar transport at the turbulent/non-turbulent interface of a jet. J. Fluid Mech. **631**, 199–230 (2009)
14. Watanabe, T., Sakai, Y., Nagata, K., Ito, Y., Hayase, T.: Reactive scalar field near the turbulent/non-turbulent interface in a planar jet with a second-order chemical reaction. Phys. Fluids **26**(10), 105111 (2014)
15. Cifuentes, L., Kempf, A., Dopazo, C.: Local entrainment velocity in a premixed turbulent annular jet flame. Proc. Combus. Inst. **37**(2), 2493–2501 (2019)
16. Gauding, M., Bode, M., Denker, D., Brahami, Y., Danaila, L., Varea, E.: On the combined effect of internal and external intermittency in turbulent non-premixed jet flames. Proc. Combust. Inst. **38**(2), 2767–2774 (2021)
17. Gampert, M., Boschung, J., Hennig, F., Gauding, M., Peters, N.: The vorticity versus the scalar criterion for the detection of the turbulent/non-turbulent interface. J. Fluid Mech. **750**, 578–596 (2014)
18. Watanabe, T., Riley, J.J., Nagata, K.: Effects of stable stratification on turbulent/nonturbulent interfaces in turbulent mixing layers. Phys. Rev. Fluids **1**(4), 044301 (2016)
19. Mistry, D., Philip, J., Dawson, J.R., Marusic, I.: Entrainment at multi-scales across the turbulent/non-turbulent interface in an axisymmetric jet. J. Fluid Mech. **802**, 690–725 (2016)
20. Kohan, K.F., Gaskin, S.: The effect of the geometric features of the turbulent/non-turbulent interface on the entrainment of a passive scalar into a jet. Phys. Fluids **32**(9), 095114 (2020)
21. Watanabe, T., Sakai, Y., Nagata, K., Ito, Y., Hayase, T.: Turbulent mixing of passive scalar near turbulent and non-turbulent interface in mixing layers. Phys. Fluids **27**(8), 085109 (2015)
22. Watanabe, T., Naito, T., Sakai, Y., Nagata, K., Ito, Y.: Mixing and chemical reaction at high Schmidt number near turbulent/nonturbulent interface in planar liquid jet. Phys. Fluids **27**(3), 035114 (2015)
23. Chakraborty, N., Klein, M., Im, H.G.: A comparison of entrainment velocity and displacement speed statistics in different regimes of turbulent premixed combustion. Proc. Combust. Inst. **38**(2), 2985–2992 (2021)
24. Khan, J.R., Rao, S.: Properties of the turbulent/non-turbulent layer of a turbulent Boussinesq plume: a study using direct numerical simulation. Phys. Fluids **35**(5), 055140 (2023)
25. Ren, J., Wang, H., Luo, K., Fan, J.: Investigation of entrainment and its effect on flame stabilization in a turbulent high Karlovitz number premixed jet flame using direct numerical simulation. Flow, Turbul. Combust. **112**(2), 537–556 (2024)

26. Lee, Y.A., Huisman, S.G., Lohse, D.: Mixing and solvent exchange near the turbulent/non-turbulent interface in a quasi-2D jet. Int. J. Multiphase Flow **169**, 104608 (2023)
27. Horiuti, K.: A classification method for vortex sheet and tube structures in turbulent flows. Phys. Fluids **13**(12), 3756–3774 (2001)
28. Davidson, P.A.: Turbulence: An Introduction for Scientists and Engineers. Oxford Univ, Pr (2004)
29. Horiuti, K., Takagi, Y.: Identification method for vortex sheet structures in turbulent flows. Phys. Fluids **17**(12), 121703 (2005)
30. Kolář, V.: Vortex identification: new requirements and limitations. Int. J. Heat Fluid Flow **28**(4), 638–652 (2007)
31. Nagata, R., Watanabe, T., Nagata, K., da Silva, C.B.: Triple decomposition of velocity gradient tensor in homogeneous isotropic turbulence. Comput. Fluids **198**, 104389 (2020)
32. Liu, C., Gao, Y., Tian, S., Dong, X.: Rortex-A new vortex vector definition and vorticity tensor and vector decompositions. Phys. Fluids **30**(3), 035103 (2018)
33. Kronborg, J., Hoffman, J.: The triple decomposition of the velocity gradient tensor as a standardized real Schur form. Phys. Fluids **35**(3), 031703 (2023)
34. Eisma, J., Westerweel, J., Ooms, G., Elsinga, G.E.: Interfaces and internal layers in a turbulent boundary layer. Phys. Fluids **27**(5), 055103 (2015)
35. Hayashi, M., Watanabe, T., Nagata, K.: Characteristics of small-scale shear layers in a temporally evolving turbulent planar jet. J. Fluid Mech. **920**, A38 (2021)
36. Fiscaletti, D., Buxton, O.R.H., Attili, A.: Internal layers in turbulent free-shear flows. Phys. Rev. Fluids **6**(3), 034612 (2021)
37. Enoki, R., Watanabe, T., Nagata, K.: Statistical properties of shear and nonshear velocity components in isotropic turbulence and turbulent jets. Phys. Rev. Fluids **8**(10), 104602 (2023)
38. Horiuti, K., Fujisawa, T.: The multi-mode stretched spiral vortex in homogeneous isotropic turbulence. J. Fluid Mech. **595**, 341–366 (2008)
39. Watanabe, T., Nagata, K.: Energetics and vortex structures near small-scale shear layers in turbulence. Phys. Fluids **34**(9), 095114 (2022)
40. Pirozzoli, S., Bernardini, M., Grasso, F.: On the dynamical relevance of coherent vortical structures in turbulent boundary layers. J. Fluid Mech. **648**, 325–349 (2010)
41. Vincent, A., Meneguzzi, M.: The dynamics of vorticity tubes in homogeneous turbulence. J. Fluid Mech. **258**, 245–254 (1994)
42. Watanabe, T., Nagata, K.: The response of small-scale shear layers to perturbations in turbulence. J. Fluid Mech. **963**, A31 (2023)
43. Wei, Q., Wang, P., Zheng, X.: Modulations of turbulent/non-turbulent interfaces by particles in turbulent boundary layers. J. Fluid Mech. **983**, A15 (2024)
44. Nakamura, K., Watanabe, T., Nagata, K.: Turbulent/turbulent interfacial layers of a shearless turbulence mixing layer in temporally evolving grid turbulence. Phys. Fluids **35**(4), 045117 (2023)
45. Kankanwadi, K.S., Buxton, O.R.H.: On the physical nature of the turbulent/turbulent interface. J. Fluid Mech. **942**, A31 (2022)
46. Kankanwadi, K.S., Buxton, O.R.H.: Turbulent entrainment into a cylinder wake from a turbulent background. J. Fluid Mech. **905**, A35 (2020)
47. Kohan, K.F., Gaskin, S.J.: On the scalar turbulent/turbulent interface of axisymmetric jets. J. Fluid Mech. **950**, A32 (2022)
48. Chen, J., Buxton, O.R.H.: Spatial evolution of the turbulent/turbulent interface geometry in a cylinder wake. J. Fluid Mech. **969**, A4 (2023)

49. Huang, J., Burridge, H.C., van Reeuwijk, M.: Local entrainment across a TNTI and a TTI in a turbulent forced fountain. J. Fluid Mech. **977**, A13 (2023)
50. Long, Y., Wang, J., Wang, J.: Turbulent/non-turbulent interface in a low-Reynolds-number transitional boundary layer over a multi-element airfoil. Phys. Fluids **34**(10), 102111 (2022)
51. Hiruma, D., Onishi, R., Takahashi, K., Fukagata, K.: Sensitivity study on storm modulation through a strategic use of consumer air conditioners. Atmos. Sci. Lett. **23**(7), e1091 (2022)
52. Mellado, J.P.: Cloud-top entrainment in stratocumulus clouds. Annu. Rev. Fluid Mech. **49**, 145–169 (2017)
53. Nair, V., Heus, T., van Reeuwijk, M.: A lagrangian study of interfaces at the edges of cumulus clouds. J. Atmos. Sci. **78**(8), 2397–2412 (2021)
54. Silva, T.S., Zecchetto, M., da Silva, C.B.: The scaling of the turbulent/non-turbulent interface at high Reynolds numbers. J. Fluid Mech. **843**, 156–179 (2018)
55. Cimarelli, A., Cocconi, G., Frohnapfel, B., De Angelis, E.: Spectral enstrophy budget in a shear-less flow with turbulent/non-turbulent interface. Phys. Fluids **27**(12), 125106 (2015)
56. Morinishi, Y., Lund, T.S., Vasilyev, O.V., Moin, P.: Fully conservative higher order finite difference schemes for incompressible flow. J. Comput. Phys. **143**(1), 90–124 (1998)
57. Rosales, C., Meneveau, C.: Linear forcing in numerical simulations of isotropic turbulence: physical space implementations and convergence properties. Phys. Fluids **17**(9), 095106 (2005)
58. Zecchetto, M., da Silva, C.B.: Universality of small-scale motions within the turbulent/non-turbulent interface layer. J. Fluid Mech. **916**, A9 (2021)
59. Watanabe, T., Zhang, X., Nagata, K.: Turbulent/non-turbulent interfaces detected in DNS of incompressible turbulent boundary layers. Phys. Fluids **30**(3), 035102 (2018)
60. Taveira, R.R., Diogo, J.S., Lopes, D.C., da Silva, C.B.: Lagrangian statistics across the turbulent-nonturbulent interface in a turbulent plane jet. Phys. Rev. E **88**(4), 043001 (2013)
61. Blakeley, B.C., Olson, B.J., Riley, J.J.: Self-similarity of scalar isosurface area density in a temporal mixing layer. J. Fluid Mech. **951**, A44 (2022)

Universal Features of Turbulent/Non-turbulent and Turbulent/Turbulent Interfaces

Pedro D. Alves[1], Marco Zecchetto[1], Ricardo P. Xavier[1], Oliver Buxton[2], and Carlos B. da Silva[1(✉)]

[1] Instituto Superior Técinco, Universidade de Lisboa, Lisboa, Portugal
`carlos.silva@tecnico.ulisboa.pt`
[2] Department of Aeronautics, Imperial College London, South Kensington, London SW7 2AZ, UK
`https://fenix.tecnico.ulisboa.pt/homepage/ist30274`

Abstract. The characteristics of turbulent/non-turbulent interfaces and turbulent/turbulent interfaces (TNTI and TTI) are analysed by new carefully designed direct numerical simulations (DNS). Whereas TNTIs separate the turbulent from the non-turbulent region in free shear flows and turbulent boundary layers, TTIs appear whenever two regions of distinct turbulent characteristics interact such as in turbulent jets and wakes surrounded by external turbulent flow, or strongly perturbed turbulent boundary layers, i.e., when the external flow is in turbulent condition. Direct numerical simulations (DNS) of temporally evolving and spatially evolving TTIs are carried out to analyse the conditional mean profiles of enstrophy. Preliminary results suggest that, if properly normalised using the mean local Kolmogorov velocity and length scale, these conditional mean profiles are universal.

Keywords: Turbulent/non-turbulent interface (TNTI) · Turbulent/turbulent interface (TTI) · Free shear flows · Turbulent entrainment

1 Introduction

Turbulent/turbulent interfaces (TTI) are omnipresent in engineering and natural flows and arise whenever a turbulent flow region is bounded by fluid in a turbulent state [1,2]. Examples include turbulent jets and wakes surrounded by external turbulent flow, or strongly perturbed turbulent boundary layers. The characteristics of TTIs impose the exchanges of mass, momentum and scalars e.g. heat in many turbulent flows, and are responsible for the entrainment and mixing rates governing many key aspects of their dynamics e.g. the spreading rates of perturbed free shear flows [3]. Despite their relevance to many applications these interfaces have started to be investigated only recently and many important aspects of their dynamics and characteristics are still unknown.

J. Wang and I. Marusic (Eds.): IUTAM-TNTI 2024, IUTAM Bookseries 45, pp. 94–109, 2025.
https://doi.org/10.1007/978-3-031-78151-3_7

The investigation of TTIs started as a natural follow up of the investigation of turbulent/non-turbulent interfaces (TNTI) that has mobilised the turbulence community for the last 20 years [4–8]. TNTIs appear at the edges of turbulent free shear flows such as jets [9,10], wakes [4], mixing layers [11], and turbulent boundary layers [12], and separate the turbulent core region of the flow from the non-turbulent (or irrotational) flow region. It has been shown that TNTI are extremely thin, but have a two layer structure, where viscous effects are important only in one of these two sublayers (the so called viscous superlayer - VLS), and a second sublayer where the enstrophy production mechanism prevails (the turbulent sublayer)[13–16]. Moreover, it has been shown that the thickness of TNTIs scales with the Kolmogorov micro-scale [17]. Nothing close to this knowledge is available today regarding TTIs, and many questions regarding TTIs remain largely unknown [15–18]. Such questions include: i) what is the structure of the TTI? ii) what are the scaling laws governing this interface? iii) How is the turbulent entrainment across the TTI imposed by the turbulence characteristics from the two sides? iv) what is the role played by the large and small scales of motion in this process? v) what prevails when two turbulent regions interact? vi) is the structure of TTIs Universal? vii) Are there simple physical cartoons to explain these mechanisms? Finally, viii) is it possible to control the entrainment rate across TTIs by manipulating the flow? A systematic research on the characteristics of TTIs has begun only recently [1,2,18,19], and has been carried out almost exclusively by using experimental methods, and only one set direct numerical simulations (DNS) of TTIs presently exists [20].

The long term goal of the present work is to clarify some of the above questions, focussing on the physical mechanisms governing the dynamical aspects of turbulent/turbulent interfaces (TTIs) and in particular their relation to the dynamics of TNTIs. The research work makes use of two highly accurate in house Navier-Stokes solvers used to carry out direct numerical simulations (DNS) of spatially evolving TTIs, and uses an innovative approach which consists in using instantaneous velocity fields generated from DNS of isotropic turbulence to ’feed’ the initial condition of spatially evolving TTIs. This creates an unprecedented level of control on the initial conditions and allows one to impose and assess the effects of the turbulent characteristics from each one of the two sides of the TTIs in the evolution of TTIs.

2 Direct Numerical Simulations of TNT and TT Interfaces

The TNTI discussed in the present work is the one arising in the DNS of temporally evolving turbulent planar wakes described in [16]. The solver uses classical pseudo-spectral methods (collocation method) for spatial discretization [21], and a three-step 3rd-order explicit Runge-Kutta scheme for the temporal advancement [22]. The simulations are fully de-aliased using the 2/3 rule and use an uniform and isotropic grid ($\Delta x = \Delta y = \Delta z$). This code is described in detail in

[17] and references therein. For this simulation the initial mean velocity is prescribed by an hyperbolic-tangent profile, as in [23,24], and a three-component velocity fluctuating [25] is superimposed by a convolution function that restricts the initial velocity noise to the initial shear layer region of the wake. The initial Reynolds number is $Re_H = (U_1 - U_2)H/\nu = 18000$, and the computational domain extends to $(L_x, L_y, L_z) = (7H, 7H, 1.75H)$, and uses a total of $(N_x \times N_y \times N_z) = (2048 \times 2048 \times 512)$ collocation points.

For the TTIs both temporal and spatial DNS are used and the procedure to generate these simulations is briefly described in this section. The temporal simulations employ an in-house Navier-Stokes solver using classical pseudo-spectral methods for spatial discretization and a 3-stage, 3^{rd}-order Runge-Kutta scheme for temporal advancement. The simulations are carried out in a triple periodic domain of sizes $2\pi \times 2\pi \times 2\pi$ using $N_1 \times N_2 \times N_3 = N^3$ collocation points, and are preceded by a total of four (4) DNS of statistically stationary (forced) homogeneous isotropic turbulence (HIT) carried out with the same code (full details are given in [26]). Statistical stationarity is obtained by imposing a power input through the imposed forcing f_i which balances the viscous dissipation rate, $P = \varepsilon$, where $P = \overline{f_i u_i}$ is the power of the input forcing and $\varepsilon = 2\nu \overline{s'_{ij} s'_{ij}}$, is the viscous dissipation rate, while $s_{ij} = (\partial u_i/\partial x_j + \partial u_j/\partial x_i)/2$ is the rate-of-strain tensor (u_i is the velocity vector). The simulations use a total number of $N^3 = 512^3$ collocation points, and use the same kinematic viscosity, $\nu = 0.0022$. The goal of these HIT simulations is to provide a range of different parameters for the Taylor based Reynolds number $Re_\lambda = u'\lambda/\nu$, root-mean-square velocity $u' = \sqrt{\overline{u'^2}}$, longitudinal integral scale L_{11}, and root-mean-square vorticity $\omega' = \sqrt{\overline{\omega'_i \omega'_i}}$, where $\lambda = \left(15\nu\overline{u'^2}/\varepsilon\right)^{1/2}$ is the Taylor micro-scale, and ω_i is the vorticity vector. The 'overline' represents an average and the prime $'$ the fluctuating part of the the variable, according to the Reynolds decomposition, $u_i = \overline{u_i} + u'_i$. Table 1 describes the main physical parameters of the four HIT simulations.

Table 1. Summary of the characteristics of the HIT simulations used to generate TTIs: Re_λ: Taylor based Reynolds number; k_p: Forcing peak location; P: Power of the input forcing; L_{11}: longitudinal integral scale; ω': root-mean-square vorticity fluctuations; $k_{max}\eta$: resolution.

Simulation	Re_λ	k_p	P	L_{11}	ω'	$k_{max}\eta$
HIT1	120	3	0.564	1.0	12.9	2.0
HIT2	190	3	9.033	1.0	50.0	1.0
HIT3	80	5	0.564	0.5	13.2	2.0
HIT4	120	5	10.0	0.5	55.5	1.0

Since the number of collocation points and the values of the kinematic viscosity need to be the same in all simulations, we have manipulated the magnitude of the input forcing power P and the peak location of this forcing k_p, and also the resolution $k_{max}\eta$, making sure it is at least $k_{max}\eta = 1$.

The selection of these parameters is based in a few simple equations. By using the fact that in statistically stationary conditions the power input of the forcing is equal to the viscous dissipation rate, $P = \varepsilon$, and using the definition of the non-dimensional dissipation, C_ε,

$$\varepsilon = C_\varepsilon \frac{u'^3}{L_{11}}, \tag{1}$$

together with the definition of the Taylor based Reynolds number $Re_\lambda = u'\lambda/\nu$, and the Kolmogorov micro-scale $\eta = \left(\nu^3/\varepsilon\right)^{1/4}$, one arrives at expressions for the maximum attainable Reynolds number (for given integral scale L_{11} and resolution $k_{max}\eta$)

$$Re_\lambda = \sqrt{15}\left(\frac{L_{11}}{C_\varepsilon}\right)^{2/3}\left(\frac{N}{2}\right)^{2/3}\left(\frac{A}{k_{max}\eta}\right)^{2/3}, \tag{2}$$

where $A = 3/2$ (fully de-aliased simulations). In the estimation we have used $C_\varepsilon = 0.44$ for forced HIT [27]. The kinematic viscosity ν and forcing power P that correspond to these condition are related by

$$P = \nu^3\left(\frac{A}{k_{max}}\frac{N}{2}\right)^4. \tag{3}$$

and the corresponding resolution is,

$$k_{max}\eta = A\left(\frac{N}{2}\right)\left(\frac{\nu^3}{P}\right)^{1/4}. \tag{4}$$

Equation (2) can also be written as function of ν and P,

$$Re_\lambda = \sqrt{15}\left(\frac{L_{11}}{C_\varepsilon}\right)^{2/3}\left(\frac{P^{1/3}}{\nu}\right)^{1/2}. \tag{5}$$

2.1 Temporal DNS of TTIs

Using the velocity fields from these simulations we carry out DNS of TTIs, where the outer and inner regions of the computational domain are ‘filled’ with different HIT flows/cases. The list of these (temporal) DNS of TTIs is shown in Table 2.

Figure 1 shows contours of vorticity magnitude for the temporal DNS of TTI in one (x, y) plane corresponding to the simulation TTI23 at six (6) different times. Contours of passive scalar with Schmidt number equal to $Sc = 1$ are shown for the same cases in Fig. 2 (the simulations are continued for longer times). For this particular simulation the Reynolds number in the two regions varies between $Re_\lambda = 190$ (inner region) to 80 (outer region), and the magnitude of the vorticity fluctuations varies between $\omega' = 50.0$ (inner region) to 13.2 (outer region). The

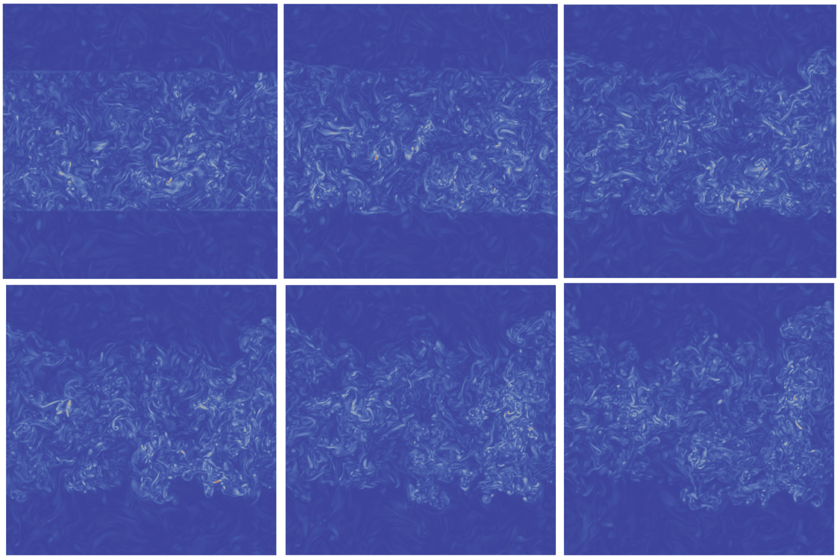

Fig. 1. Contours of vorticity magnitude in one (x, y) plane for the temporal DNS corresponding to the simulation TTI23 for six (6) different times.

Table 2. Summary of TTI simulations. The same notation is used to name both the temporal and the spatial simulations

Simulation	Outer layer	Inner layer
TTI12	HIT1	HIT2
TTI13	HIT1	HIT3
TTI14	HIT1	HIT4
TTI23	HIT2	HIT3
TTI24	HIT2	HIT4
TTI34	HIT3	HIT4

integral scale is also quite different, with one region exhibiting twice the integral scale of the other region.

It is clear that the two turbulent regions interact quite strongly as time progresses, and the inner region seems to spread into the outer region (this fact is even more clear in the latter stages of the simulation).

2.2 Spatial DNS of TTIs

The spatial simulations of TTIs use an highly accurate pseudo-spectral and 6th-order Compact finite differences schemes [21,28], and an explicit 3rd-order Runge-Kutta scheme for time-advancement [22], while the pressure-velocity coupling is treated with the fractional step method of Kim and Moin (1985) [29].

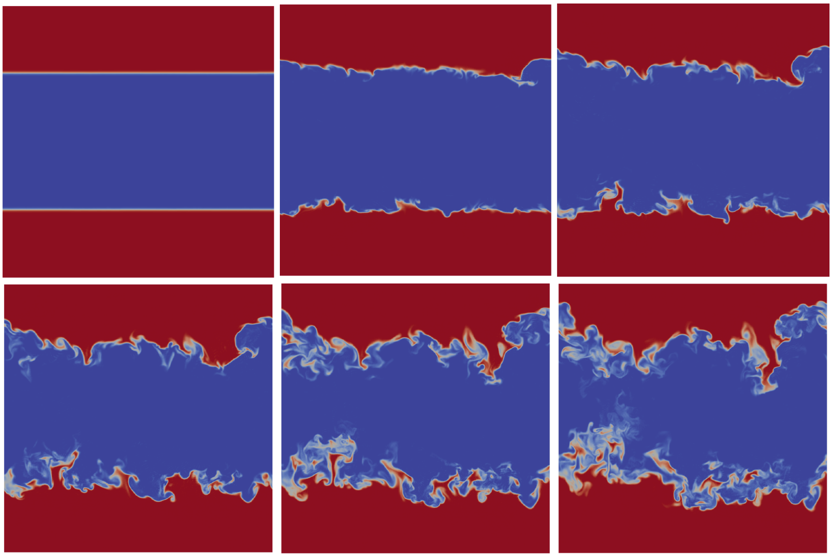

Fig. 2. Contours of passive scalar for the temporal DNS corresponding to the simulation TTI23 for six (6) different times.

Inflow and outflow boundary conditions are employed at the boundaries at the streamwise direction (x). Periodic boundary conditions are used in the other boundaries, i.e., at the sides (z), and top/bottom (y) boundaries of the domain. The computational code and numerical methods have been described in detail in [30,31]. This code was recently modified in order to allow the inflow boundary condition to read input data generated by the HIT code, i.e., instantaneous velocity fields generated from the HIT code are used as inlet condition of the SPJET code (the grids and spatial discretisation schemes are exactly the same in this plane), together with a constant mean (convection) velocity, which allows for the simulation of interfaces between two different flows, each one originated from an HIT simulation, and provides an unprecedented level of control on the characteristics of the turbulence from each one of the two turbulent regions. In short, the numerical DNS codes open up a totally new dimension regarding the possibilities of simulating TTIs. It is possible to define several cases of HIT flows, with particular values of the integral scale, or root-mean-square velocity, and to insert these different fields as inlet conditions to generate a large data bank of new DNS of TTIs for further study. Notice that in these innovative DNS the effects of mean shear are totally absent, and it is possible to assess the effects played on the TTI by a single isolated variable, which is very difficult or impossible to achieve in experiments. Finally, the research team has at is disposition a large number of post-processing codes that allow a detailed investigation of many aspects of turbulence physics, such as the possibility of assessing local/conditional statistics of the flow in relation to the position of the TTI layer.

Figures 3 (a) and (b) illustrate the spatial development of the TTI through the iso-surfaces of vorticity magnitude and passive scalar, corresponding to the case TTI13. In this case the inner and outer turbulent regions exhibit the same level of vorticity fluctuations, but the inner layer has twice the value of the integral scale of the outer layer, to where it seems to be spreading.

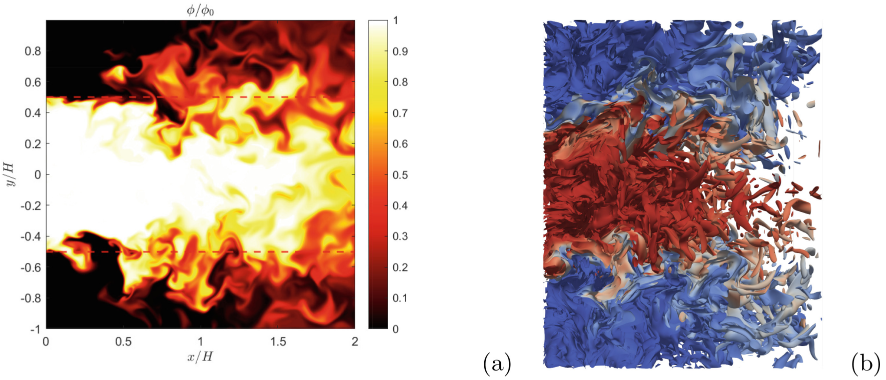

(a) (b)

Fig. 3. (a) Contours of instantaneous passive scalar for the spatial DNS of TTI13 in a (x, y) plane; (b) Iso-surfaces of instantaneous vorticity magnitude coloured by passive scalar for the spatial DNS of TTI13.

3 Results

3.1 Turbulent/Non-turbulent Interfaces

Since the work of [4], conditional statistics with respect to the distance from the TNTI have been used in several experiments and numerical simulations, e.g., [9,11,16,17,32–34] and are denoted here by $\langle\rangle_I$ as enable the unambiguous separation of turbulent and irrotational fluid and preserve flow features that would be otherwise masked. The procedure used to obtain such statistics follows 3 steps: *i)* the location of the outer edge of the TNTI, the so called irrotational boundary (IB), is obtained as an iso-surface of the vorticity magnitude; *ii)* a local normal axis is then placed with its origin at each of the IB points with direction aligned to the local gradient of vorticity magnitude; *iii)* the conditional statistics are then computed as function of the distance y_I to the TNTI layer interpolating the field under study into this (local) normal (Figs. 4 and 5).

In this subsection we discuss these statistics in detail using the conditional enstrophy obtained from a DNS of a turbulent planar wake described above [16]. Unlike one point statistics, where the reference origin is a static one, in conditional statistics the reference origin belongs to either the outermost surface of

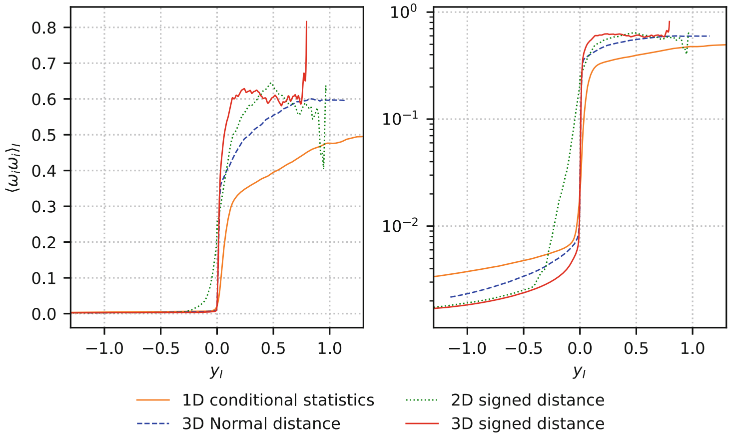

Fig. 4. Enstrophy profiles of the same plane wake using the different statistical condition methods

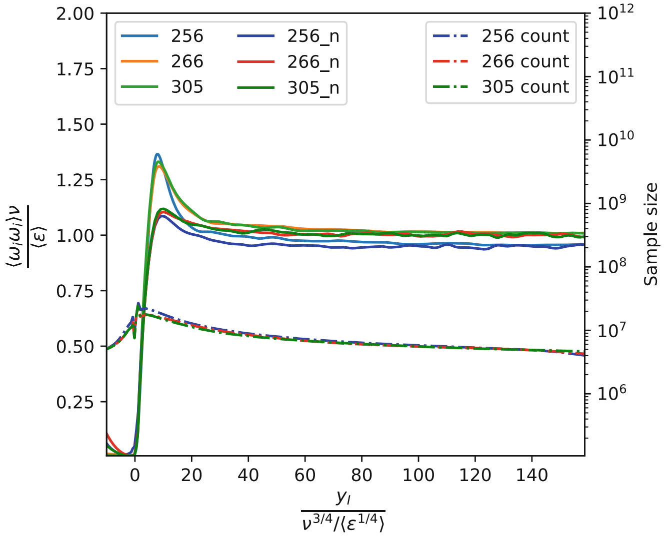

Fig. 5. Zecchetto and Silva [16] normalisation of the enstrophy profiles. The different lines are identified by the Re_λ of the respective simulation from [16]. The "n" identifies the lines where the 3D normals method was applied, the remaining one being the signed distance ones. On the right side axis can be seen the sample size for the signed distance method. Besides the higher maximum in the signed distance profiles, all the profiles overlap with the ones from the same methods. The turbulent core plateau is attained with this normalisation even in the case of the signed distance method, thus portraying the homogeneity of small scales in the turbulent core.

the turbulent/non-turbulent interface, the irrotational boundary, or the surface known as the interface envelope, a surface that contains the points of the farthest points of the irrotational boundary when measured in a fixed axis and in relation to the turbulent region. From this point on, the conditional statistics methods differ on the way of measuring the distance to the interface. These range from 1D statistics, where the distance to the interface is measured along parallel axis for all surface points, 2D statistics, where the distance is measured in axis formed by the projection of the interface normal to multiple planes that intersect the surface and are parallel among each other (common in experimental setups due to certain limitations), and 3D statistics, where the distance is measured along the axis formed by the surface normal. All methods provide distinct results, where the 3D case is considered to be the most accurate one. However, all these methods may skew the result, as the measured distances may in certain circumstances not be equal to the real interface distance, or in other cases may result in multiple usages of the same point for different distance statistic computation. As to avoid this, [12] considered a case where instead of using the normal distance one would use the signed distance field.

The signed distance field (SDF) consists of the distance to a given surface, Ω, where the value at each point corresponds to the minimum distance from set point to any point of the surface, where the field sign identifies if the point in question belongs to the inner or outer region of Ω. One may resort to the particular case of the Eikonal equation, $|\nabla u(\overrightarrow{x})| = f(\overrightarrow{x})^{-1}$ with $f(\overrightarrow{x}) = 1$ in all domain, where the field $u(\overrightarrow{x})$ that satisfies this equation, with boundary condition $u(\overrightarrow{x} = \Omega) = 0$, is equal to the SDF [35,36]. To solve this partial differential equation we resorted to the Fast Marching Method (FMM) [37]. Having found the SDF, in the same way that in the aforementioned methods we take the statistics at a given distance to the TNTI, the set of points that comprise the same distance can be obtained by the identification of the isosurfaces of set SDF, where statistics may be computed over points belonging to these isosurfaces, thus no skewness arises due to multiple usages of the same points as presented in the normal distance methods.

Although [12] expressed that no significant difference was there between the 3D statistics and the signed distance methods, only observed in close proximity to the irrotational boundary, and a significant computational cost, resulting in diminishing returns. Moreover, in the case where the interface envelope is used, the signed distance method may result in erroneous distance measurements as well, thus requiring the identification of the complete irrotational boundary. With the implementation of new algorithms and using the full 3D field, the signed distance method was compared to the classical methods. The application of these method has shown that in fact in the very close proximity to the IB, the results are coincident. However, as the distance from the IB increases, more are the distinctions that similarities. To illustrate these differences, the enstrophy from a simulation of a temporal plane wake from [16] was analysed with several methods (4). Whilst in the vicinity of the IB the profiles are the same, the peak in the vicinity of the TNTI of the 3D signed distance method is higher, and the values in the irrotational region are the lowest in the 3D signed distance method. Moreover, it can be seen that there is a significant discrepancy between the 2D and 3D signed distance methods, which could justify the conclusions presented in [12], something that must be taken into account when analysing experimental data. Also to note, is the irregularity of the 3D signed distance profile in the turbulent core. This is due to the collapse of iso-distance surfaces, thus reducing the statistic sample in this region, which contrasts with the classical turbulent core plateau, raising the hypothesis that the plateau in the turbulent core region may just be a result of random sampling of points in the turbulent region. In order to verify the physical validity of the statistics, the normalisation presented in [16], which has a physical basis, was applied to the three temporal wakes therein (5), using the 3D normals and signed distance. In this figure we can observe that the physical relations still hold when applying the signed distance method, further validating the method.

3.2 Turbulent/Turbulent Interfaces: Temporal Simulations

In the present work we used this procedure to compute conditional statistics in relation to the position of the boundary between the two different turbulent regions, the TTI layer [1,2]. The only difference here is that the passive scalar with value of $\theta = 0.5$ is used to define this boundary, instead of the vorticity magnitude, as in studies of the TNTI layer. Analysis of the effects of the Schmidt number in these statistics showed that virtually no differences are observed in the conditional profiles when one uses a Schmidt number of $Sc = 1$, 10, or 50, i.e., using each one of these values leads to virtually the same conditional profiles of several quantities.

Figure 6 shows conditional mean profiles of enstrophy $\langle \omega_i \omega_i \rangle_I$ normalised by the values of the Kolmogorov velocity and length scale in the inner turbulent region ($\langle u_\eta \rangle_T$ and $\langle \eta \rangle_T$), as function of the distance from the TTI, for all the temporal DNSs of TTIs. As expected all the profiles collapse in the inner region ($y_I > 0$), but not in the outer region ($y_I < 0$), but they show a very sharp enstrophy variation across the interface, except for the cases TTI13 and TTI24, where the vorticity fluctuations are similar in the two adjacent turbulent regions.

Figure 7 shows the same profiles but now normalised by the local mean values of the Kolmogorov velocity and length scale ($\langle u_\eta \rangle_I$ and $\langle \eta \rangle_I$). If one switches the two regions in the DNS of TTI23 (turning this into a TTI32 case) by placing the flow region with the weakest vorticity in the inner region, one observes an interesting phenomenon. The conditional profiles can be separated into two sets, where in each set the conditional enstrophy profiles collapse. In the first set (I) we have the simulations TTI12, TTI14, TTI23 and TTI34, and in the second set (II) have the DNS from cases TTI13 and TTI24. All the curves from set I display asymmetric conditional profiles, with two peaks representing a local minimum and local maximum. The maximum is at the side with stronger vorticity magnitude, and the minimum is located in the side with the smaller vorticity. The differences in Reynolds number and integral scale do not affect the shape of these curves in any meaningful way. In the second set we find TTIs that are roughly symmetric and display a minimum between two equal peaks. Thus, when properly normalised all the profiles roughly collapse into one of the two curves. Notice that the different values of the Reynolds number and of integral scale do not affect these profiles.

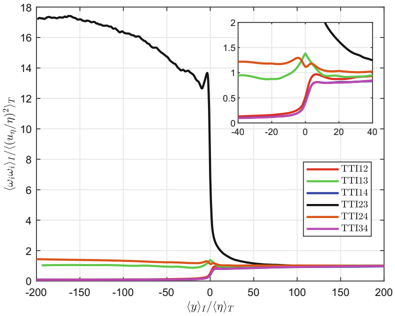

Fig. 6. Conditional profiles of mean enstrophy $\langle\omega_i\omega_i\rangle_I$ normalised by the values of the Kolmogorov velocity and length scale in the external turbulent region ($\langle u_\eta\rangle_T$ and $\langle\eta\rangle_T$), as function of the distance from the TTI, for all the temporal DNSs of TTIs. The inset shows a zoom of the profiles near the TTI.

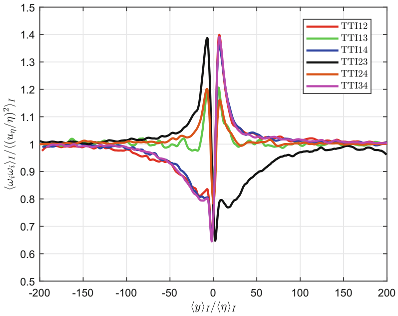

Fig. 7. Conditional profiles of enstrophy $\langle\omega_i\omega_i\rangle_I$ normalised by the values of the local mean Kolmogorov velocity and length scale ($\langle u_\eta\rangle_I$ and $\langle\eta\rangle_I$), as function of the distance from the TTI, for all the temporal DNSs of TTIs.

3.3 Turbulent/Turbulent Interfaces: Spatial Simulations

Similarly, the conditional statistics of the spatially-developing TTIs were analysed. In this case, an additional variable has to be considered because the flow is spatially evolving: the non-homogeneous streamwise coordinate direction (x). The conditional profiles of any flow quantity of interest have to computed as function of x, and we do these statistics by taking small sections, of size $H/2$ (H is the size of the inner turbulent region at the inlet).

If we take the normalised enstrophy profiles averaged over a section close to the inlet, $x/H \in [0.1; 0.5]$, one observes the results depicted in Fig. 8. For TTI14 and TTI34, the peak adjacent to the outermost layer ($y_I < 0$, which presents a low level of fluctuating vorticity) has a magnitude inferior to the peak closer to the innermost layer. This is reminiscent of the aforementioned temporal profiles, as the effects of spatial evolution are not strong.

However, as we move downstream, the curves seem to tend to a more universal profile (Fig. 9). Indeed, with the spatial decay of enstrophy, as well as the existent diffusion processes, the domain tends to be a homogeneous state. Therefore, the peaks with lower magnitude get increased. In the end, the curves resemble the ones that had similar initial levels of vorticity.

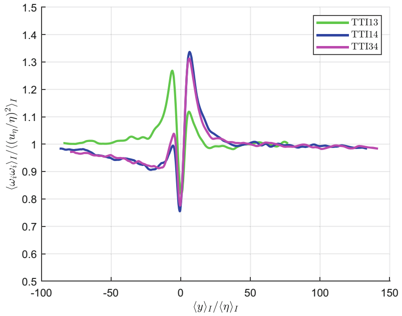

Fig. 8. Conditional profiles of enstrophy $\langle \omega_i \omega_i \rangle_I$ normalised by the values of the local mean Kolmogorov velocity and length scale ($\langle u_\eta \rangle_I$ and $\langle \eta \rangle_I$), as function of the distance from the TTI, for all the spatial DNSs of TTI13, TTI14 and TTI34. The profiles are taken from a section close to the inlet, $x/H \in [0.1; 0.5]$.

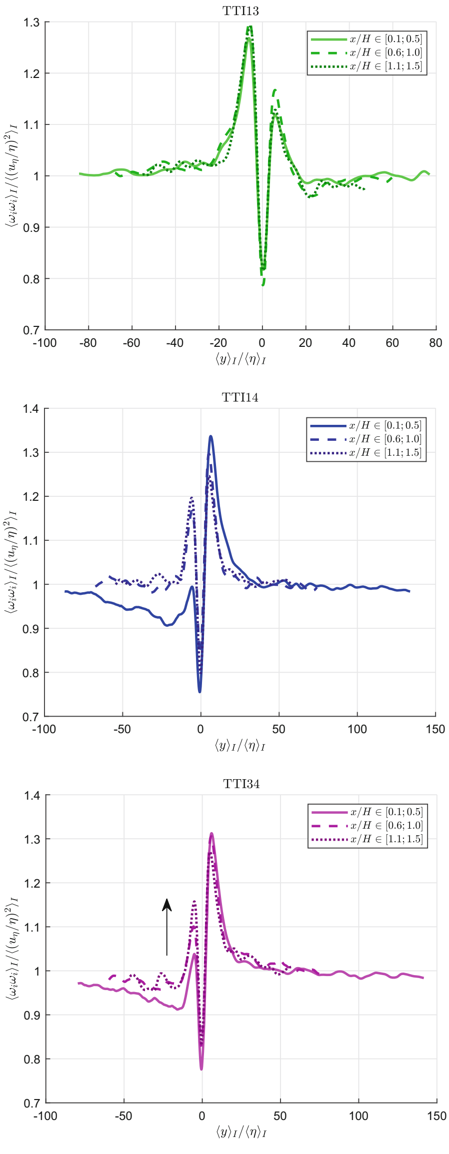

(a)

(b)

(c)

Fig. 9. Conditional enstrophy profiles for the DNS spatial simulations TTI13 (a), TTI14 (b), and TTI34 (c) obtained at three different locations: $x/H \in [0.1; 0.5], [0.6; 1.0], [1.1; 1.5]$.

4 Conclusions

This paper discuses some aspects of the conditional enstrophy profiles observed for turbulent/non-turbulent interfaces (TNTI) and turbulent/turbulent interfaces (TTI). The investigation uses TNTI generated from previous studies and new carefully designed DNS allowing the investigation of TTIs in temporal and spatial configuration.

Several different methods used to obtain conditional mean profiles of enstrophy in relation to the distance from the irrotational boundary present in TNTIs are compared and discussed. The methods employing the 3D normal distance and the 3D signed distance are virtually equivalent in the vorticity jump region, and differ only at a certain distance from the IB location. The 2D normal distance method is inaccurate at this location and should be avoided. When normalising the enstrophy by the local Kolmogorov velocity and length scales, all the profiles collapse, using either the 3D normal and the 3D signed methods, the higher value of the enstrophy peak is attributed to using either the interface or the envelope.

Conditional mean enstrophy profiles in temporal evolving TTIs typically exhibit an asymmetrical double peak structure, with the higher peak located in the region of stronger vorticity fluctuations, and show no effect of the integral scale of turbulence. The profiles can be divided into two sets and suggest that the conditional enstrophy profiles are universal, when normalised with the local Kolmogorov velocity and length scales.

Preliminary results from TTIs obtained for the spatial simulations seem to suggest a similar result, and the effects of the spatial flow development will be assessed in the near future.

References

1. Kankanwadi, K.S., Buxton, O.R.H.: Turbulent entrainment into a cylinder wake from a turbulent background. J. Fluid Mech. **905**, A35 (2020)
2. Kankanwadi, K.S., Buxton, O.R.H.: On the physical nature of the turbulent/turbulent interface. J. Fluid Mech. **942**, A31 (2022)
3. da Silva, C.B., Hunt, J., Eames, I., Westerweel, J.: Interfacial layers between regions of different turbulent intensity. Annu. Rev. Fluid Mech. **46**, 567–590 (2014)
4. Bisset, D.K., Hunt, J.C.R., Rogers, M.M.: The turbulent/non-turbulent interface bounding a far wake. J. Fluid Mech. **451**, 383–410 (2002)
5. Holzner, M., Luthi, B.: Laminar superlayer at the turbulence boundary. Phys. Review Lett. **106**, 134503 (2011)
6. Mistry, J., Philip, J., Dawson, J.R., Marusic, I.: Entrainment at multi-scales across the turbulent/non-turbulent interface in an axisymmetric jet. J. Fluid Mech. **802**, 690 (2016)
7. Mistry, D., Philip, J., Dawson, J.R.: Kinematics of local entrainment and detrainment in a turbulent jet. J. Fluid Mech. **871**, 896–924 (2019)
8. Breda, M., Buxton, O.R.H.: Behaviour of small-scale turbulence in the turbulent/non-turbulent interface region of developing turbulent jets 879
9. Westerweel, J., Fukushima, C., Pedersen, J.M., Hunt, J.C.R.: Momentum and scalar transport at the turbulent/non-turbulent interface of a jet. J. Fluid Mech. **631**, 199–230 (2009)
10. Westerweel, J., Fukushima, C., Pedersen, J.M., Hunt, J.C.R.: Mechanics of the turbulent-nonturbulent interface of a jet. Phys. Review Lett. **95**, 174501 (2005)

11. Attili, A., Cristancho, J.C., Bisetti, F.: Statistics of the turbulent/non-turbulent interface in a spatially developing mixing layer. J. Turbul. **15**, 555–568 (2014)
12. Borrell, G., Jiménez, J.: Properties of the turbulent/non-turbulent interface in boundary layers. J. Fluid Mech. **801**, 554–596 (2016)
13. Taveira, R.R., da Silva, C.B.: Characteristics of the viscous superlayer in free shear turbulence and in planar turbulent jets. Phys. Fluids **26**, 021702 (2014)
14. Watanabe, T., da Silva, C.B., Sakai, Y., Nagata, K., Hayase, T.: Lagrangian properties of the entrainment across turbulent/non-turbulent interface layers. Phys. Fluids **28**, 031701 (2016)
15. Watanabe, T., Jaulino, R., Taveira, R., da Silva, C., Nagata, K., Sakai, Y.: Role of an isolated eddy near the turbulent/non-turbulent interface layer. Phys. Rev. Fluids **2**, 094607 (2017)
16. Zecchetto, M., da Silva, C.B.: Universality of small-scale motions within the turbulent/non-turbulent interface layer. J. Fluid Mech. **916**, A9 (2021)
17. Silva, T.S., Zecchetto, M., da Silva, C.B.: The scaling of the turbulent/non-turbulent interface at high reynolds numbers. J. Fluid Mech. **843**, 156–179 (2018)
18. Kohan, F., Gaskin, S.: The effect of the geometric features of the turbulent/non-turbulent interface on the entrainment of a passive scalar into a jet **32**, 095114 (2020)
19. Kohan, F., Gaskin, S.: On the scalar turbulent/turbulent interface of axisymmetric jets. J. Fluid Mech. **950**, A32 (2022)
20. Nakamura, K., Watanabe, T., Nagata, K.: Turbulent/turbulent interfacial layers of a shearless turbulent mixing layer in temporally evolving grid turbulence. Phys. Fluids **35**, 045117 (2023)
21. Canuto, C., Hussaini, M.Y., Quarteroni, A., Zang, T.A.: Spectral Methods in Fluid Dynamics. Springer-Verlag (1987)
22. Williamson, J.H.: Low-storage Runge-Kutta schemes. J. Comp. Phys. **35**, 48–56 (1980)
23. Stanley, S., Sarkar, S., Mellado, J.P.: A study of the flowfield evolution and mixing in a planar turbulent jet using direct numerical simulation. J. Fluid Mech. **450**, 377–407 (2002)
24. da Silva, C.B., Pereira, J.C.F.: Invariants of the velocity-gradient, rate-of-strain, and rate-of-rotation tensors across the turbulent/nonturbulent interface in jets. Phys. Fluids **20**, 055101 (2008)
25. Lesieur, M., Ossia, S., Métais, O.: Infrared pressure spectra in 3D and 2D isotropic incompressible turbulence. Phys. Fluids **11**, 1535–1543 (1999)
26. Ghira, A.A., Elsinga, G., da Silva, C.B.: Characteristics of the intense vorticity structures in isotropic turbulence at high reynolds numbers. Phys. Rev. Fluids **7**, 104605 (2022)
27. Pope, S.B.: Turbulent Flows. Cambridge University Press, Cambridge (2000)
28. Lele, S.K.: Compact finite difference schemes with spectral-like resolution. J. Comput. Phys. Acad. Press **103**, 16–42 (1992)
29. Kim, J., Moin, P.: Application of a fractional-step method to incompressible navier-stokes equations. J. Comp. Phys. **59**, 308–323 (1985)
30. Guimaraes, M.C., Pimentel, N., Pinho, F.T., da Silva, C.B.: Direct numerical simulations of turbulent viscoelastic jets. J. Fluid Mech. **899**, 11–37 (2020)
31. Guimaraes, M.C., Pinho, F.T., da Silva, C.B.: Turbulent planar wakes of viscoelastic fluids analysed by direct numerical simulations. J. Fluid Mech. **946**, A26 (2022)
32. Watanabe, T., Sakai, Y., Nagata, K., Ito, Y., Hayase, T.: Vortex stretching and compression near the turbulent/non-turbulent interface in a planar jet. J. Fluid Mech. **758**, 754–784 (2014)

33. Watanabe, T., Sakai, Y., Nagata, K., Ito, Y., Hayase, T.: Reactive scalar field near the turbulent/non-turbulent interface in a planar jet with a second-order chemical reaction. Phys. Fluids **26**, 105111 (2014)
34. Watanabe, T., Riley, J.J., de Bruyn Kops, S.M., Diamessis, P.J., Zhou, Q.: Turbulent/non-turbulent interfaces in wakes in stably stratified fluids. J. Fluid Mech. **797**, 1–11 (2016)
35. Sakai, T.: On Riemannian manifolds admitting a function whose gradient is of constant norm. Kodai Math. J. **19**(1), 39–51 (1996)
36. Evans, L.: Partial Differential Equations. American Mathematical Society (2010)
37. Hassouna, M.S., Farag, A.A.: Multistencils fast marching methods: a highly accurate solution to the Eikonal equation on cartesian domains. IEEE Trans. Pattern Anal. Mach. Intell. **29**(9), 1563–1574 (2007)

Entrainment Across a Turbulent/Turbulent Interface: Points of Distinction from the Turbulent/Non-turbulent Interface

Oliver R. H. Buxton(✉)

Department of Aeronautics, Imperial College London, London, UK
`o.buxton@imperial.ac.uk`

Abstract. We show that the physics of a turbulent/turbulent interface (TTI) are different from those of a turbulent/non-turbulent interface (TNTI), with inertial vorticity stretching being wholly responsible for creating the enstrophy discontinuity in the former, whilst viscous diffusion dominates in the outermost region of the latter. We show how the entrainment velocity evolves spatially across a TTI formed between a planar-wake and turbulent backgrounds of various characteristic turbulence intensities and length scales. Background turbulence is shown to enhance entrainment in the near-wake where both nibbling and engulfment are active, whilst it suppresses entrainment in the far-wake where nibbling is the predominant entrainment mechanism. Finally, we consider the entrainment of streamwise momentum and kinetic energy and show that the presence of background turbulence can modify the efficiency with which these quantities are entrained with respect to mass but these effects are only important in the near-wake.

Keywords: entrainment velocity · turbulent/turbulent interface · turbulent wake

1 Introduction

The layer that demarcates a turbulent flow from a non-turbulent background is known as the turbulent/non-turbulent interface (TNTI). Across a TNTI there is a rapid change in flow physics as the flow adjusts from being irrotational in the background to vortical, i.e. $\omega^2 = |\nabla \times \boldsymbol{u}|^2 \neq 0$, within the turbulent bulk, governed by the enstrophy ($\frac{1}{2}\omega^2$) budget equation,

$$\frac{\mathrm{D}}{\mathrm{D}t}\frac{\omega^2}{2} = \underbrace{\omega_i s_{ij} \omega_j}_{\text{vorticity stretching}} + \underbrace{\nu \frac{\partial^2(\omega^2/2)}{\partial x_j \partial x_j}}_{\text{viscous diffusion}} - \underbrace{\nu \left(\frac{\partial \omega_i}{\partial x_j}\right)^2}_{\text{viscous dissipation}} . \tag{1}$$

J. Wang and I. Marusic (Eds.): IUTAM-TNTI 2024, IUTAM Bookseries 45, pp. 110–125, 2025.
https://doi.org/10.1007/978-3-031-78151-3_8

Accordingly, the outermost surface of a TNTI, known as the irrotational boundary, is an iso-surface of $\omega^2 = 0$ thereby requiring that the jump in enstrophy over a short distance, that is characteristic of a TNTI, is produced at this surface through viscous diffusion only since the inertial vorticity stretching term ($\omega_i s_{ij} \omega_j$) disappears at such a zero-vorticity surface. This intuition led Corrsin and Kistler [6] to predict the existence of a viscous layer in the outermost region of a TNTI, a result that has been subsequently verified many years later. The growth, through entrainment, of a turbulent flow into a non-turbulent background is thus driven by viscous action.

Nevertheless, the TNTI has been shown to be thicker than simply the outermost viscous layer [15,17, e.g.] and also encompasses a layer in which the enstrophy adjusts from close to zero (in the viscous layer) to the value within the bulk of the turbulent flow in a conditional mean sense. The dominant physics within this inner layer, termed the turbulent buffer layer [17], are inertial; once the enstrophy level within the TNTI becomes non-negligible then inertial vorticity stretching ($\omega_i s_{ij} \omega_j$) primarily yields the enstrophy production [15,18]. Viscous dissipation acts only as a sink of enstrophy throughout the TNTI.

In most turbulent geophysical or industrial flows the background is also turbulent, however, in which case the interface demarcating the primary flow from the turbulent background is the turbulent/turbulent interface (TTI), which is the more general case of which a TNTI is a special example. Despite their ubiquity in nature, due to the difficulty of distinguishing one adjacent stream of turbulence from another it is only recently that TTIs have been proven to exist even in scenarios where both streams of turbulence have a similar turbulent intensity to one another [8]. Similarly to TNTIs, TTIs were found to manifest as an enstrophy discontinuity characterised by a small length scale, with the exception that within the free-stream $\omega^2 > 0$ [8,9]. TTIs have subsequently been shown to be more contorted, i.e. they exhibit a greater tortuosity $\tau = \ell/L$ where ℓ is the interface length over streamwise distance L, than TNTIs [4,8,11].

The nature of a TTI is still not understood given that $\omega^2 \neq 0$ on both sides of a TTI meaning that its outermost surface is manifestly not an iso-surface of zero vorticity magnitude. This means that the inertial vorticity stretching term is no longer constrained to zero at the outermost surface and hence it is unknown what, if any, role viscous diffusion plays in a TTI since in homogeneous turbulence at sufficiently high Reynolds number $\omega_i s_{ij} \omega_j$ typically dwarfs the viscous contribution to (1). Since entrainment is governed by the small-scale turbulent physics within the interface the different flow physics for a TTI in comparison to a TNTI are also likely to lead to different entrainment behaviour. Earlier work has shown that free-stream turbulence (FST) leads to a suppression of entrainment mass flux in comparison to entrainment across a TNTI in a fully-developed turbulent wake [8]. In such fully-developed flows small-scale “nibbling” is expected to be the dominant entrainment mechanism. Contrastingly, in the near wake (where “engulfment” is a significant entrainment mechanism) FST has been shown to increase the entrainment mass flux with respect to that across a TNTI [10].

In this chapter we shall examine TTIs formed between a planar turbulent wake, generated by a circular cylinder, and various (decaying) turbulent free-streams produced by turbulence-generating grids placed upstream of the cylinder. We will identify the relevance of viscous diffusion to TTIs, since the presence of vortical fluid on both sides of a TTI renders the phenomenology described by Corrsin and Kistler [6] for TNTIs void. Subsequently, we will explore the spatial evolution of the entrainment fluxes across TTIs as the wake develops. Previous work has focused almost exclusively on the entrainment flux of mass ($\dot{M}$) across TNTIs but we will also consider the entrainment fluxes of streamwise momentum ($\dot{P}_x$) and kinetic energy ($\dot{K}$) across TTIs. These two entrainment fluxes have practical applications, for example the entrainment of momentum into a wake relates to the drag acting on the wake-producing body whilst the entrainment of kinetic energy from geostrophic wind into the atmospheric boundary layer is important in several meteorological phenomena.

2 Methodologies

This chapter reports on two campaigns of experiments conducted over several years [2,9] but both combine particle image velocimetry (PIV) and planar laser induced fluorescence (PLIF) to interrogate the wake of a circular cylinder of diameter $D = 10$ mm exposed to free-stream turbulence produced by a series of turbulence-generating grids within the hydrodynamics flume of the Department of Aeronautics at Imperial College London. The water speed was set to yield a Reynolds number based off the cylinder diameter of $Re_D \approx 3.8 \times 10^3$. Various "flavours" of FST were introduced as characterised by the length-scale – intensity $\{\mathcal{L}, k\}$ parameter space. $\mathcal{L}$ is computed by integrating the correlation function between the streamwise velocity fluctuations u' offset by distance r to the first zero-crossing, r_0, whilst $k \equiv \sqrt{\overline{(u'^2 + v'^2)/2}}/U_\infty$ based off our two-dimensional data. Each flavour is referred to as a "run" for the campaign of experiments pertinent to Figs. 2 and 3 (the three-dimensional experiments) and as a "case" for the two-dimensional experimental campaign (all other figures). Different grids, incorporating both regular and fractal geometries, were used and the streamwise separation between the grid and cylinder was varied in order to generate the various flavours of FST illustrated in Fig. 1(a), similarly to our previous work [8]. The explored $\{\mathcal{L}, k\}$ parameter space for the FST for the two-dimensional experimental campaign at the $x/D = 20$ measurement station (without the cylinder present) is depicted in Fig. 1(b). The flavours of FST were divided into three groups that were defined based off their FST intensities, k, with group 3 having the most intense background turbulence and group 1 the least. Note that group 1 also includes the no-grid case, which is our closest experimental approximation to a TNTI.

For the three-dimensional experiments cinematographic stereoscopic PIV and planar PLIF were conducted at a measurement station approximately $40D$ downstream. Measurement of all terms of (1) requires access to all nine components of the velocity-gradient tensor. The in-plane velocity gradients could readily be computed from the stereoscopic PIV data whilst the streamwise velocity gradients were extracted after invoking Taylor's hypothesis between consecutive velocity fields to produce a quasi three-dimensional, three-component (of the velocity vector) data set. Very high spatial (3.6η, where η is the Kolmogorov length scale) and temporal ($0.03\tau_\eta$, where τ_η is the Kolmogorov time scale) resolution was necessary for these experiments to capture the fine-scale velocity-gradient information and adequately apply Taylor's hypothesis. For the results of Sect. 4 the entrainment fluxes of mass, momentum, and kinetic energy were measured at five different locations whose fields-of-view were centred on $x/D = (6.5, 10, 20, 30, 40)$ downstream of the rear face of the cylinder. The fields-of-view of all measurement stations extended for a fixed distance of $L_x = 3D$ in the streamwise direction; their positions are illustrated in Fig. 1(c) showing that near-wake effects extend to $x/D \approx 15$. The PIV spatial resolution ranged from 1.7η to 3.2η, which was necessary to adequately resolve the fine-scale phenomenology of the interfacial turbulence.

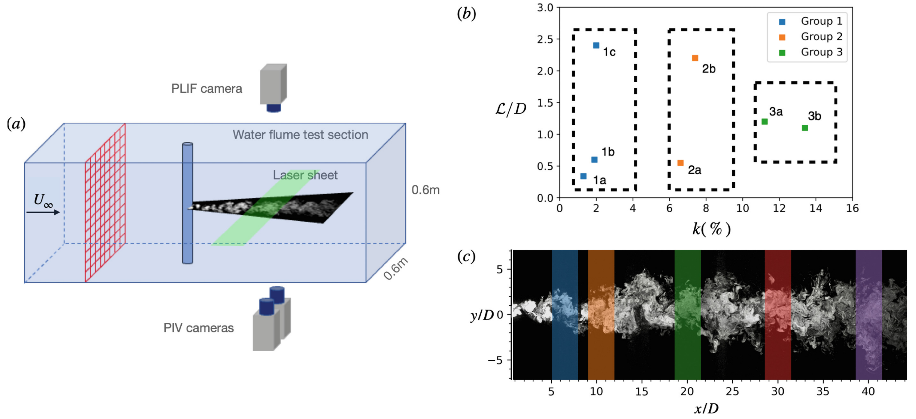

Fig. 1. (a) Schematic for the experiments. (b) $\{\mathcal{L}, k\}$ parameter space of the FST for the two-dimensional test cases. (c) Illustrative position of the various measurement stations where the colours of the strips are matched to the symbols in Figs. 6(a), 8, and 9. A PLIF image (from [4]) in the background illustrates the spatial evolution of the wake exposed to case 2a FST.

Classical interface-identification methods, such as placing a threshold on the enstrophy value [1] or turbulent kinetic energy (TKE) [3], are not suitable for TTIs due to the fact that $\omega^2 \neq 0$ on both sides of the interface and no discernible discontinuity in TKE was identified for TTIs [8]. Instead, we rely upon a high Schmidt number (Sc) passive scalar to ensure that molecular diffusion takes place only over a negligibly small length scale. Rhodamine 6G ($Sc \approx 2{,}500$ in water) was thus released isokinetically from a single hole on the rear face of the cylinder using a micro-dosing pump connected via a tube that was sufficiently long to ensure that the discrete nature of the pump was filtered out (2 m length). The data from the PLIF camera was used to capture the location of the TNTI/TTI by using a threshold on the magnitude of the light-intensity gradient, $|\nabla\phi|$. Our previous work has shown that in the absence of a turbulence-generating grid upstream of the cylinder (representative of a TNTI) the interface as identified by $|\nabla\phi|$ and a classical vorticity-magnitude threshold coincided, meaning that the scalar was well stirred and faithfully marked the wake-fluid [8]. A spatio-temporally evolving interface coordinate system is defined (ξ_s, ξ_n) where ξ_n is the interface-normal direction (hence $\xi_n = 0$ corresponds to the outermost boundary of the TTI/TNTI) and ξ_s is the interface-tangential direction.

3 The Underlying Physics of the Turbulent/Turbulent Interface

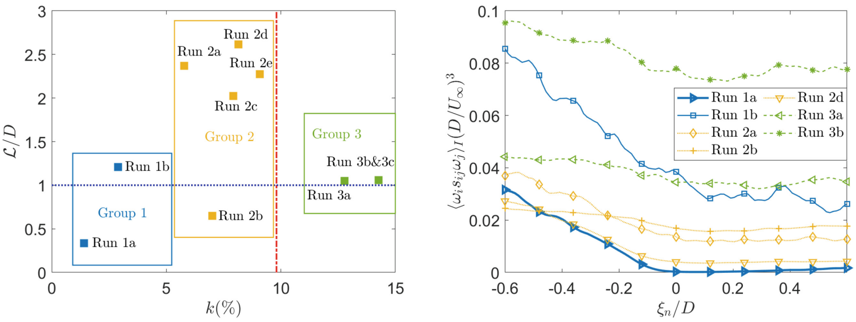

(a) (b)

Fig. 2. (a) $\{\mathcal{L}, k\}$ parameter space of the background turbulence parameter space for the three-dimensional experiments. (b) conditionally-averaged $\omega_i s_{ij}\omega_j$, the inertial term from (1), as a function of normal-distance from the outermost surface of the interface.

In this section we seek to determine whether the direct influence of viscosity is significant in producing the discontinuity in enstrophy that is characteristic of TTIs. We show the conditionally-averaged terms of (1) in Figs. 2(b) ($\omega_i s_{ij}\omega_j$, the inertial vorticity-stretching term) and 3 (the viscous diffusion term for runs in groups 1 and 2 in subfigure (a), and group 3 in subfigure (b)). The "flavours" of the FST in the various runs are presented in Fig. 2(a). For all figures the no-grid case, our closest experimental representation of a TNTI, is plotted with a thick blue line. The behaviour of the viscous diffusion term (Fig. 3) for the TNTI-run compares extremely well to previous studies conducted using DNS [15,18, e.g.]: there is a peak in production in the outermost region of the TNTI (the viscous superlayer) which transitions to sink-like behaviour in the innermost region of the TNTI (turbulent sublayer), with zero contribution in the free-stream and deep into the turbulent core. Figure 3(a) shows that there is similar behaviour for TTIs when there is moderate turbulence intensity in the free-stream (i.e. groups 1 and 2). This is not the case, however, when the free-stream turbulence is intense (i.e. group 3, Fig. 3(b)) where there is no discernible change in the behaviour of the diffusion term from the free-stream into the turbulent core, at least to within the experimental noise.

Importantly, however, when considering the conditional mean inertial vorticity stretching term in Fig. 2(b) we see that the magnitude of $\omega_i s_{ij} \omega_j$ dwarfs that of the diffusion term for TTIs, regardless of the turbulence intensity of the FST (i.e. across runs in groups 1, 2, and 3). By virtue of the fact that, in contrast to a TNTI, there is vorticity present on both sides of a TTI $\omega_i s_{ij} \omega_j > 0$ in both the free-stream and in the wake although there is a sharp rise coincident with $\xi_n = 0$. Contrastingly, $\omega_i s_{ij} \omega_j = 0$ for $\xi_n > 0$ (the free-stream) for the TNTI run 1a in keeping with the intuition of Corrsin and Kistler [6]. The severity of the increase in $\omega_i s_{ij} \omega_j$ as $\xi_n = 0$ is crossed for TTIs diminishes as the intensity of the FST increases but it still exists even for runs in group 3. We can thus conclude that viscous diffusion plays a negligible role in yielding the discontinuity in enstrophy that is characteristic of a TTI [8] which is instead produced inertially through the vorticity stretching term of (1). This is a point of distinction from a TNTI where the enstrophy discontinuity is initially created through viscous diffusion across the outermost surface, the irrotational boundary.

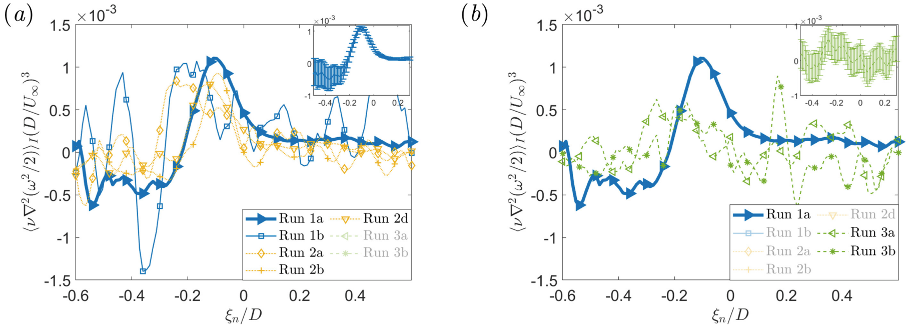

Fig. 3. The conditional mean viscous diffusion term from (1) as a function of normal distance from the outermost surface of the interface for runs in *(a)* groups 1 and 2 & *(b)* group 3. 95% confidence intervals are presented for the no-grid run *(a)* and run 3a *(b)* in the insets.

It is known that TNTIs and TTIs introduce a strong small-scale anisotropy such that the interface-normal strain-rate is enhanced, thereby increasing the $\omega_i s_{ij} \omega_j$ term [9]. The spatial evolution of the small-scale anisotropy adjacent to the interface is explored in Fig. 4 through consideration of the conditionally-averaged anisotropy metric $\langle \varXi \rangle_I = \langle \overline{(\mathrm{d}u_n/\mathrm{d}\xi_n)^2} / \overline{(\mathrm{d}u_s/\mathrm{d}\xi_s)^2} \rangle_I$ in which the velocity vector is written in the local interface coordinate system i.e. $\boldsymbol{u} = (u_s, u_n)$. It is evident that indeed TTIs do introduce a small-scale anisotropy

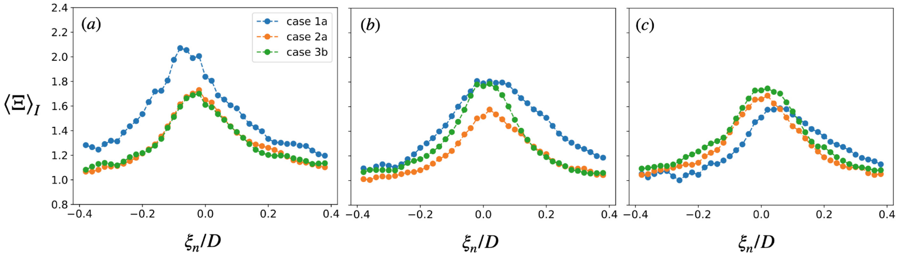

Fig. 4. Small-scale turbulence anisotropy ratio as a function of interface-normal distance at (a) $x/D = 6.5$, (b) $x/D = 20$, and (c) $x/D = 40$. Note FST cases are defined in Fig. 1(b) (case 1a is the no-grid, TNTI case; cases 2a and 3b are TTIs).

driven by enhanced interface-normal velocity gradients ($\varXi > 1$), but that $\varXi$ diminishes with downstream distance. However, the rate at which this happens is slower for a TTI than for a TNTI which sees a much more rapid decline in peak $\varXi$ from $x/D = 6.5$, where the TNTI shows the largest anisotropy, to $x/D = 40$. For a comparable $\mathcal{L}$ the figure shows that larger k increases the anisotropy in a TTI in the mid and near wake, although both TTIs show a similar degree of anisotropy in the near wake.

4 The Spatial Evolution of Entrainment Across the Turbulent/Turbulent Interface

4.1 The Entrainment Velocity

Having seen that the physics governing the TTI are different from the TNTI in Sect. 3 we now explore how this affects the rate at which mass, and other quantities, are entrained into the primary flow (wake) from the background. This requires computation of the entrainment velocity. To obtain the local entrainment velocity, we have adopted a method similar to that used in previous studies [8, 19, e.g.] by tracking the defined interface position at times t and $t + \varDelta, t$ where $\varDelta t = T_{ac} = 5$ ms is the time interval between two consecutive velocity fields, an illustration of which is depicted in Fig. 5. The position of the interface at $t + \varDelta t$ is a result of both fluid advection and entrainment, see Fig. 5(a), (b). Accordingly, when the interface at time $t + \varDelta t$ is advected backwards in time by the local fluid velocity at $\xi_n = 0$, i.e. $(u, v) \cdot \varDelta t$, then the difference between the interface position at time t and the backwards-advected interface from time $t + \varDelta t$ is equal to $v_e \cdot \varDelta t$ where $v_e(\xi_s, \xi_n = 0, t)$ is the entrainment velocity. This process is illustrated in Figs. 5(b) to (d). Note that we define positive v_e to mean that the interface is moving outwards (towards the background) and hence corresponds to entrainment whilst $v_e < 0$ corresponds to detrainment.

With v_e obtained at the examined streamwise positions for the various cases, the first question is *how does the mean entrainment velocity* $\overline{v_e}$ *evolve from the near- to far-fields for different "flavours" of background turbulence*?

Fig. 6 shows the mean entrainment velocity $\overline{v_e}$ normalised with the free-stream velocity U_∞ and the local Kolmogorov velocity at the outermost surface of the interface $u_{\eta,I} = u_\eta(\xi_n = 0)$ at the various measurement locations. Consistent with previous reports [8, 12, e.g.], the background turbulence intensity is a more important factor in affecting $\overline{v_e}$ than the integral length scale; the integral length scale of each case can be inferred from Fig. 1(b) with the turbulence intensity in Fig. 6(a). In the near-field at $x/D = 6.5$ and 10, the background turbulence intensity does not appreciably affect $\overline{v_e}/U_\infty$; however, as x/D increases to 20 and even further downstream, $\overline{v_e}/U_\infty$ is attenuated as the turbulence intensity increases. For instance, $\overline{v_e}/U_\infty$ in the two cases of group 3 is about one third the magnitude of those of group 1 at $x/D = 40$. Interestingly, for all cases, $\overline{v_e}$ in the near-field (e.g. $x/D = 6.5$) is much larger than those further downstream, Fig. 6(a), and this difference is particularly evident when the background turbulence intensity is high: in group 3, $\overline{v_e}/U_\infty$ at $x/D = 6.5$ is about 4 times that at $x/D = 40$.

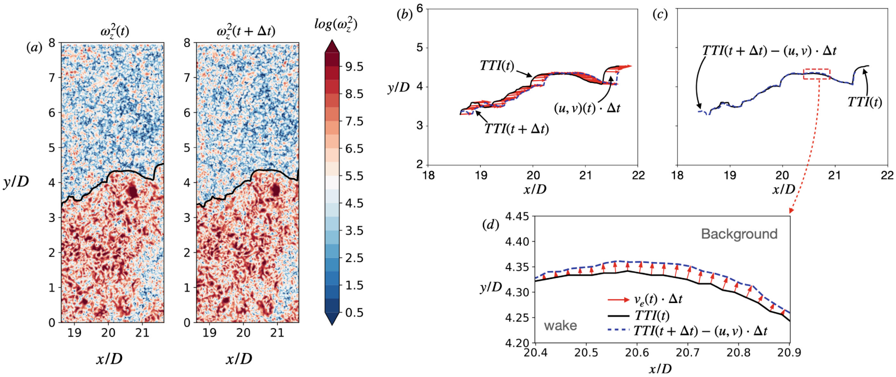

Fig. 5. Calculation of the entrainment velocity, v_e, presented for case 2b. (a) The black lines denote TTIs identified from the PLIF data in two consecutive snapshots, times t and $t' = t + \Delta t$, superimposed onto the out-of-plane vorticity magnitude field (ω_z^2) from the PIV data. (b) The local fluid velocity along the TTI-positions at times t (black line) and t' (blue dashed line) denoted with red arrows. (c) The TTI-position at time t' advanced backwards in time by the local fluid velocity (blue dashed line) and the TTI-position at time t (black line). (d) Magnification of the red box in (c) illustrating the displacement between the TTI-position at time t and the backwards-advected TTI-position at time t', $\delta = v_e \cdot \Delta t$, depicted with red arrows.

We can now paint a more complete picture of the role that background turbulence has on the mean entrainment velocity, i.e. the distinction between entrainment across a TTI versus a TNTI. In the far-field, where the coherent motions embedded into the wake have decayed, free-stream turbulence suppresses entrainment with the turbulence intensity of the free-stream turbulence being the dominant parameter. The near-wake, where the coherent motions are energetic, is a more complicated picture where both the intensity and the length scale of the background turbulence are significant. The presence of free-stream turbulence may, in fact, enhance entrainment rate (slightly) across a TTI relative to a TNTI but the difference between the two is not as significant as in the far-wake.

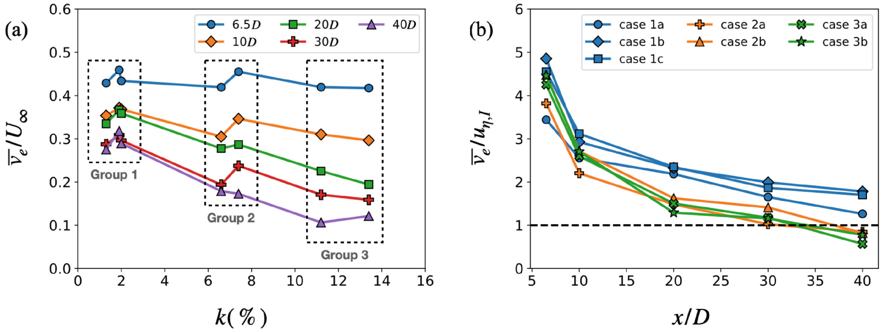

Fig. 6. (a) Distribution of mean entrainment velocity $\overline{v_e}$ with respect to the background turbulence intensity at different streamwise positions, normalised with incoming velocity U_∞. The division of the FST cases into three groups refers to Fig. 1(b). (b) The scaling of $\overline{v_e}$ on $u_{\eta,I}$ in the streamwise direction.

Along with its absolute magnitude, the streamwise scaling of $\overline{v_e}$ also varies spatially, see Fig. 6(b). In the near-field at $x/D = 6.5$ (and also 10), $\overline{v_e}/u_{\eta,I}$ decreases rapidly in the streamwise direction, suggesting that $\overline{v_e}$ does not in fact scale with the Kolmogorov velocity at the outermost boundary of the TTI/TNTI $u_{\eta,I} = u_\eta(\xi_n = 0)$ in this region of the flow. Beyond $x/D = 20$, however, $\overline{v_e}/u_{\eta,I}$ seems to approach a plateaued value between one and two, implying that $\overline{v_e}$ starts to evolve at roughly the same pace as $u_{\eta,I}$ with x (as the turbulent wake begins to develop fully). The distinct behaviour of the scaling of $\overline{v_e}$ in the two x/D ranges again reminds us that the wake's spreading rate transitions at $x/D = 15$ in the same flow [4].

Given the evidently larger $\overline{v_e}$ in the near-field of the wake and the attenuation of $\overline{v_e}$ in the far-field, especially with large background turbulence intensities, one may ponder the spatial evolution of the statistical distributions of v_e. Figure 7 displays the probability density functions (PDFs) of v_e for all cases from $x/D =$ 6.5 to 40. For all cases, the PDFs are skewed in favour of entrainment ($v_e > 0$), which as we saw previously yields $\overline{v_e} > 0$ (Fig. 6). At $x/D = 6.5$, Fig. 7(a), the modal peaks of the PDFs are located at larger positive values of v_e than farther downstream, Figs. 7(b)-(d). This corresponds well with the observation that $\overline{v_e}$ at $x/D = 6.5$ is substantially larger than at the farther downstream locations (Fig. 6). We postulate that the large modal value of $v_e/u_{\eta,I}$ in the near-field is associated with the dynamics of the large-scale coherent vortices. Their intense vortical motion gives rise to high shear (or strain rate) close to the interface (see our related work [5]) and thus high vorticity production.

A second noteworthy observation pertains to the altered effect of the background turbulence on the PDFs as the flow develops spatially. At $x/D = 6.5$, the effect of the background turbulence is reflected in the evidently heavier positive tails of the PDFs for the TTI-cases than for the TNTI-PDF (Fig. 7a). This reveals that the ambient turbulence acts to promote the probability of strong entrainment events (large v_e). However, as x/D increases the cases with higher background turbulence intensity tend to have heavier negative tails of their PDFs implying that farther downstream there is an increased likelihood of intermittent detrainment events when the background turbulence intensity is high (e.g. Fig. 7d). This is entirely consistent with the opposite effect of the background turbulence in affecting the turbulent entrainment in the near- and far-fields we reported previously, however we may now explain the effect of free-stream turbulence in suppressing entrainment rate in the far-field by highlighting the promotion of intermittent, powerful detrainment events.

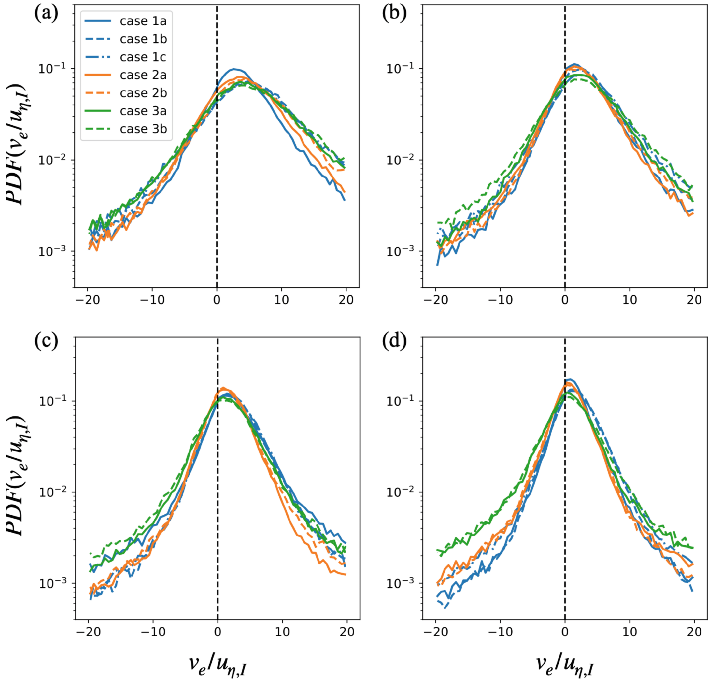

Fig. 7. PDFs of v_e for all cases at $x/D =$ (a) 6.5, (b) 10, (c) 20, and (d) 40.

4.2 Entrainment of Mass, Streamwise Momentum, and Kinetic Energy

Having seen that free-stream turbulence affects the entrainment velocity across TTIs, let us now consider how this affects the various entrainment fluxes of mass, streamwise momentum, and kinetic energy.

Re-introducing the local interface-tangential - interface-normal coordinate system (ξ_s, ξ_n) we may define the time-averaged entrained mass flux into the wake as follows

$$\dot{M} = \frac{1}{T}\int_0^T \left(\int_{\ell'(t)} \rho v_e(\xi_s)\mathrm{d}\xi_s\right)\mathrm{d}t =: \rho\overline{\int_{\ell'} v_e \mathrm{d}.\xi_s}. \tag{2}$$

This is obtained by interrogating a portion of the TTI/TNTI in a planar/two-dimensional domain with streamwise extent L_x. Within this domain the interface has a temporally fluctuating length of $\ell'(t)$ and v_e is the entrainment velocity (defined to be positive for mass flux entrained into the wake). Taking $\ell = \overline{\ell'}$ we approximate (2) as $\dot{M} \approx \rho\ell\langle v_e\rangle$ where $\langle\cdot\rangle$ denotes ensemble averaging (in both time and space) over the outermost boundary, $\xi_n = 0$, of the interface (TNTI or TTI) within the interrogated domain of streamwise extent L_x. This approximation is an *a priori* assumption, although evidence for its validity is presented later on in this section.

Let us now consider an idealised non-turbulent background where the streamwise velocity is a constant U_∞ everywhere in which case we may write the entrained flux of streamwise momentum into the wake as

$$\dot{P}_x \approx \rho\ell U_\infty\langle v_e\rangle = U_\infty\dot{M}. \tag{3}$$

Similarly, we obtain $\dot{K} = \frac{1}{2}U_\infty^2\dot{M}$ for the entrained kinetic energy flux into a wake exposed to an idealised non-turbulent background. The presence of FST however complicates this analysis since the velocity at $\xi_n = 0$ for a TTI is $u = U_I + u'$. Here U_I is the conditional mean velocity at the outermost surface of the TTI ($\xi_n = 0$) and u' is a turbulent fluctuation about U_I. Accordingly

$$\dot{P}_x = \rho\overline{\int_{\ell'}(U_I + u')v_e\mathrm{d}\xi_s} \approx \rho\ell U_I\langle v_e\rangle + \rho\ell\langle u'v_e\rangle = U_I\dot{M} + \rho\ell\langle u'v_e\rangle \tag{4}$$

highlighting the fact that should there exist a correlation between v_e and u' then $\langle u'v_e\rangle \neq 0$ ensures that the ratio between the entrained momentum flux to the entrained mass flux is different to that for an idealised non-turbulent background, and a simple relationship such as $\dot{P}_x = U_I\dot{M}$ does not exist. For simplicity we shall henceforth refer to the ratio $\dot{P}_x/\dot{M}$ as the "efficiency" with which momentum is entrained with respect to mass. Consideration of the efficiency with which kinetic energy is entrained with respect to mass reveals that there is a sum of three terms containing correlations between the entrainment velocity and the turbulent velocity fluctuations at the outermost surface of the TTI

$$\dot{K} = \frac{1}{2}U_I^2\dot{M} + \frac{\rho\ell}{2}\left[2U_I\langle u'v_e\rangle + \langle {u'}^2 v_e\rangle + \langle {v'}^2 v_e\rangle\right]. \tag{5}$$

The entrainment mass flux was computed by integrating v_e over the length of the defined interface within the PIV interrogation domain of streamwise extent L_x, c.f. (2). An illustration of this process, similar to previous work [8,14], is given in Fig. 5, although the entrainment velocity is multiplied by the local streamwise component u of the fluid velocity at $\xi_n = 0$ to compute $\dot{P}_x$ and $\frac{1}{2}(u^2 + v^2)$ at $\xi_n = 0$ to compute $\dot{K}$, c.f. (4) and (5) respectively. The data acquisition period $T = 25$ s, corresponding to the averaging-period of (2)–(5), encompassed c. 200 vortex-shedding cycles at a measurement frequency of 200 Hz. Whilst $L_x = 3D$ was fixed in absolute terms this varied from $147\eta_I$ (case 1a, $x/D = 40$) to $326\eta_I$ (case 3a, $x/D = 6.5$). Here η_I is the Kolmogorov length scale computed from the conditionally-averaged dissipation rate at $\xi_n = 0$ (the outermost surface of the identified TTI) for the various flavours of FST at each specific measurement station. In terms of integral scales of the various flavours of FST at the various measurement stations $L_x/\mathcal{L}$ thus varied between 1.25 and 8.8.

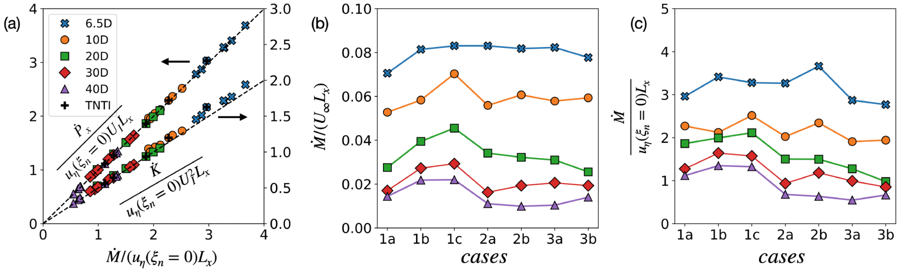

Fig. 8. (a) $\dot{P}_x$ and $\dot{K}$ plotted as a function of $\dot{M}$ for all FST cases at all measurement stations. (b) $\dot{M}$ normalised with fixed velocity scale U_∞ and (c) $\dot{M}$ normalised with $u_{\eta,I} = u_\eta(\xi_n = 0)$, the local Kolmogorov velocity scale at the outermost surface of the TTIs/TNTI; this can be cross referenced against (a) to identify the various FST cases/measurement stations.

The entrained momentum and kinetic energy fluxes as a function of the entrained mass flux are presented in Fig. 8(a), whilst Figs. 8(b) and (c) show $\dot{M}$ normalised with U_∞ (b) and $u_{\eta,I}$ (c) for the various flavours of FST studied. For a given FST flavour, including the no-grid TNTI case, the entrainment fluxes decrease monotonically with x in agreement with our mean entrainment velocity results in Sect. 4.1. However, when comparing across different FST flavours the picture is more complicated since for some cases the absolute entrainment fluxes at $x/D = 40$ are similar to the fluxes at $x/D = 20$ for other cases, see Fig. 8(b).

The large-scale coherent motions embedded within the wake diminish in energy content with x (see Fig. 1(c)) and the turbulent wake approaches a "fully-developed" state. The fractal dimension, and hence tortuosity, of a TNTI/TTI have been previously shown to approach a constant value for fully-developed turbulence, i.e. $\tau \to$ const. such that $\ell = \tau L_x \sim L_x$. Combining this observation with our earlier result $v_e \sim u_\eta$ for the fully-developed wake we may deduce

$\dot{M} \sim L_x u_\eta$ within the interrogated domain once the wake is fully-developed. This deduction is supported by the observation that for all FST flavours at the two farthest downstream measurement stations ($x/D = 30, 40$), where the wake is approaching a fully-developed state, the values of $\dot{M}/L_x u_{\eta,I}$ are similar in Fig. 8(c).

Adopting this scaling, Fig. 8(c) shows that in the intermediate and far wake ($x/D \geq 20$) there is a clear trend that increasing the intensity of the FST reduces $\dot{M}/u_{\eta,I} L_x$ such that group 3 < group 2 < group 1. This agrees with our previous results in the far wake [8] but also shows that $\dot{M}$ closely follows our results for $\overline{v_e}$ from Sect. 4.1, i.e. the entrainment velocity maps pretty well to the entrainment flux in the far-wake implying that the varying tortuosity $\tau(\mathcal{L}, k)$ is either small in comparison to the variation in $\overline{v_e}$ or they vary in a similar way to each other. Contrastingly, in the near-wake $\mathcal{L}$ also appears to play a role, with cases 1c and in particular 2b (those with the highest $\mathcal{L}$) seeing enhanced entrainment fluxes.

Most importantly, we see that for all measurement stations and for all FST flavours (including the TNTI case) there is minimal scatter from the line $\dot{P}_x = U_I \dot{M}$ and hence the idealised entrainment efficiency for momentum relative to mass is preserved for both turbulent backgrounds and real (non-idealised) non-turbulent backgrounds. This empirically validates our previous assumption that ℓ may be taken outside of the spatio-temporal averaging operation $\langle u' v_e \rangle$ in e.g. (3). Similarly, for $x/D \geq 20$ there is very little scatter from the idealised entrainment efficiency of kinetic energy $\dot{K} = \frac{1}{2} U_I^2 \dot{M}$. We thus conclude that the efficiency with which kinetic energy is entrained with respect to mass from an idealised non-turbulent background is preserved for a turbulent free-stream in the intermediate/far wake. Since Figs. 8(b) and (c) show that the entrained mass flux is spatially developing and varies across the different flavours of FST, i.e. $\dot{M} = \dot{M}(\mathcal{L}, k, x/D)$ then we may further conclude that $\dot{P}_x = \dot{P}_x(\mathcal{L}, k, x/D)$ and $\dot{K} = \dot{K}(\mathcal{L}, k, x/D)$ through being "slaved" to the entrainment mass flux.

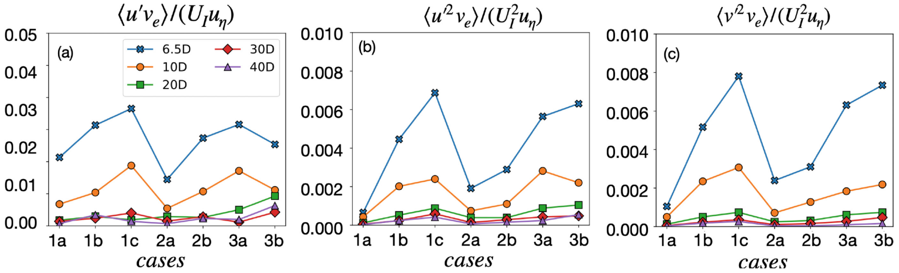

Fig. 9. The various correlations that appear in (5) between the entrainment velocity v_e and the fluctuating velocities (u', v') at the outermost surface of the TTIs/TNTI.

Contrastingly, in the near wake ($x/D = 6.5, 10$) a systematic departure is observed from the idealised efficiency for the entrainment of kinetic energy, including the TNTI case. Increasing the idealised efficiency with which kinetic energy is entrained relative to mass requires the existence of positive correlations between v_e and (u', v'), as dictated by (5), yet the preservation of $\dot{P} = U_I \dot{M}$ behaviour requires $\langle u' v_e \rangle \approx 0$. The spatial evolution of the correlations contained within the terms of (5) for all FST cases is presented in Fig. 9. As expected from the entrainment flux results of Fig. 8(a) vanishingly-small correlations are confirmed for all measurement stations $x/D \geq 20$ and for all FST flavours. In the near wake ($x/D = 6.5, 10$), however, where the large-scale coherent motions are at their most energetic (see Fig. 1(c)) these correlations are still small, although not negligible, and take positive values. This explains the observation that only the kinetic energy, and not the momentum, has an enhanced entrainment efficiency in relation to an idealised non-turbulent background due to the sum of three terms containing small-valued correlations leading to an entrainment flux that is greater than $\dot{K} = \frac{1}{2} U_I^2 \dot{M}$. Conversely, a single small contribution from $\langle u' v_e \rangle$ is insufficient to enhance the entrainment efficiency of momentum, $\dot{P}_x$. The increased efficiency of $\dot{K}$ in the near wake for the TNTI case results from correlations between v_e and the velocity fluctuations in the free-stream which are characteristic of a real (non-idealised) TNTI. These are either potential velocity fluctuations, that are known to exist in a non-turbulent free-stream and are driven by the irregular motion of the TNTI [7], or from the unavoidable non-zero background turbulence that is inherent to a water facility. Our final observation relating to TTIs is that these correlations are smallest for moderate FST-intensity, group 2 cases, whilst those for groups 1 and 3 are largest. The fluctuating velocities (u', v') can be sustained through either the free-stream turbulence intensity itself (largest in group 3) or the irregular motion of the TTI that causes accelerations/decelerations in the free-stream (comparable to the potential free-stream fluctuations induced by a TNTI). Previous work showed that this irregular motion was least suppressed in comparison to a TNTI by FST cases with low background turbulence intensity, i.e. group 1 [4,10].

5 Summary and Conclusions

We have shown that the physics governing TTIs are fundamentally different to those governing TNTIs; the fact that the outermost surface of a TTI is no longer an iso-surface of zero vorticity-magnitude means that there is no longer a constraint for $\omega_i s_{ij} \omega_j = 0$. Since this inertial vorticity stretching term is typically much larger than any viscous diffusion in a turbulent flow then TTIs seemingly have no requirement for a viscous sublayer. In fact, we show in related work [5] that TTIs have a thickness that is characteristic of the thickness of the turbulent sublayer of a TNTI at sufficiently high Reynolds number, i.e. $\delta \approx 13\eta_I$ [16]. Both TTIs and TNTIs introduce a small-scale anisotropy, driven by enhanced velocity gradients normal to the interface, and this enhanced interface-normal strain rate contributes to $\omega_i s_{ij} \omega_j$ in the interface. TNTIs seemingly show a larger anisotropy than TTIs in the near wake, but this decays more quickly such that TTIs show a greater anisotropy in the far wake. Increasing k in the FST seemingly yields slightly more anisotropic turbulence in the TTI.

The fact that the physics of a TTI are no longer constrained by viscosity affects the entrainment physics across a TTI. We observe that the mean entrainment velocity diminishes as the wake fully develops until eventually, when the wake becomes fully-developed, it seems to scale with the Kolmogorov velocity scale extracted from the outermost surface of the interface. Further, the presence of background turbulence has the tendency to suppress the mean entrainment velocity in the fully-developed region of the wake, seemingly driven by the promotion of intermittent, powerful detrainment events, with higher turbulence intensity in the background turbulence correlating to increasingly suppressed mean entrainment velocity. In the near-wake the picture is more complicated with both the turbulence intensity and length scale affecting the mean entrainment velocity, but to a lesser extent than in the far-wake.

When the free-stream is turbulent there is no longer the requirement that there is a direct proportionality between the entrainment rates of streamwise momentum $\dot{P}_x$ and kinetic energy $\dot{K}$ with mass $\dot{M}$ since the existence of velocity fluctuations in the background and their potential correlation with the entrainment velocity is seen to break this relationship. Nevertheless, we observe that other than in the very near-wake this proportionality is preserved, which is good news from the perspective of modelling the entrainment of e.g. momentum using the entrainment hypothesis in a turbulent environment; something that is gaining prominence in e.g. the modelling of wind-turbine wakes [13]. $\dot{P}_x$ and $\dot{K}$ are thus observed to be slaved to $\dot{M}$ across TTIs in the mid and far wake such that the dependences of $\dot{P}_x$ and $\dot{K}$ on the turbulence intensity and length scale of the free-stream turbulence (and their spatial evolution) are determined solely by $\dot{M}$. In the very near wake (which is of great significance for typical spacings of wind turbines within a farm, for example) then the presence of background turbulence is observed to mean that kinetic energy is entrained more efficiently, relative to mass, than from an idealised non-turbulent background.

References

1. Bisset, D.K., Hunt, J.C.R., Rogers, M.M.: The turbulent/non-turbulent interface bounding a far wake. J. Fluid Mech. **451**, 383–410 (2002)
2. Buxton, O.R.H., Chen, J.: The relative efficiencies of the entrainment of mass, momentum and kinetic energy from a turbulent background. J. Fluid Mech. **977**, R2 (2023)
3. Chauhan, K., Philip, J., De Silva, C.M., Hutchins, N., Marusic, I.: The turbulent/non-turbulent interface and entrainment in a boundary layer. J. Fluid Mech. **742**, 119–151 (2014)
4. Chen, J., Buxton, O.R.H.: Spatial evolution of the turbulent/turbulent interface geometry in a cylinder wake. J. Fluid Mech. **969**, A4 (2023)
5. Chen, J., Buxton, O.R.H.: Conditional mean velocity and vorticity fields in the vicinity of the turbulent/turbulent interface of a planar wake. In: Wang, J., Marusic, I. (eds.) IUTAM-TNTI 2024, pp. xx–yy. Springer, Cham (2024)
6. Corrsin, S., Kistler, A.L.: Free-stream boundaries of turbulent flows. NACA technical report (1244) (1955)

7. Holzner, M., Lüthi, B., Tsinober, A., Kinzelbach, W.: Acceleration, pressure and related quantities in the proximity of the turbulent/non-turbulent interface. J. Fluid Mech. **639**, 153–165 (2009)
8. Kankanwadi, K.S., Buxton, O.R.H.: Turbulent entrainment into a cylinder wake from a turbulent background. J. Fluid Mech. **905**, A35 (2020)
9. Kankanwadi, K.S., Buxton, O.R.H.: On the physical nature of the turbulent/turbulent interface. J. Fluid Mech. **942**, A31 (2022)
10. Kankanwadi, K.S., Buxton, O.R.H.: Influence of freestream turbulence on the near-field growth of a turbulent cylinder wake: turbulent entrainment and wake meandering. Phys. Rev. Fluids **8**(3), 034 603 (2023)
11. Kohan, K.F., Gaskin, S.J.: On the scalar turbulent/turbulent interface of axisymmetric jets. J. Fluid Mech. **950**, A32 (2022)
12. Kohan, K.F., Gaskin, S.J.: Scalar mixing and entrainment in an axisymmetric jet subjected to external turbulence (2023). arXiv preprint arXiv:2310.19086
13. Luzzatto-Fegiz, P., Caulfield, C.C.P.: Entrainment model for fully-developed wind farms: effects of atmospheric stability and an ideal limit for wind farm performance. Phys. Rev. Fluids **3**(9), 093 802 (2018)
14. Mistry, D., Philip, J., Dawson, J.R., Marusic, I.: Entrainment at multi-scales across the turbulent/non-turbulent interface in an axisymmetric jet. J. Fluid Mech. **802**, 690–725 (2016)
15. da Silva, C.B., Hunt, J.C.R., Eames, I., Westerweel, J.: Interfacial layers between regions of different turbulence intensity. Annu. Rev. Fluid Mech. **46**(1), 567–590 (2014)
16. Silva, T.S., Zecchetto, M., Da Silva, C.B.: The scaling of the turbulent/non-turbulent interface at high Reynolds numbers. J. Fluid Mech. **843**, 156–179 (2018)
17. Van Reeuwijk, M., Holzner, M.: The turbulence boundary of a temporal jet. J. Fluid Mech. **739**, 254–275 (2013)
18. Watanabe, T., Sakai, Y., Nagata, K., Ito, Y., Hayase, T.: Vortex stretching and compression near the turbulent/non-turbulent interface in a planar jet. J. Fluid Mech. **758**, 754–785 (2014)
19. Wolf, M., Lüthi, B., Holzner, M., Krug, D., Kinzelbach, W., Tsinober, A.: Investigations on the local entrainment velocity in a turbulent jet. Phys. Fluids **24**(10), 105–110 (2012)

Regular Papers

Entrainment Mechanism Analysis of Oblique Shock-Wave/Boundary-Layer Interactions

Fanzhao Meng(✉), Wang Han, and Lijun Yang

School of Astronautics, Beihang University, Beijing 100083, China
`{mengfanzhao,drwanghan}@buaa.edu.cn`

Abstract. The interaction between shock waves and boundary layers impacts hypersonic vehicles' aerodynamic structure, internal turbulent mixing, and combustion processes. Direct numerical simulations (DNSs) of the hypersonic boundary layer have been performed to study the turbulent/non-turbulent interface (TNTI) entrainment mechanism and the impact of shock waves. Two cases are analyzed with and without the shock-wave and boundary layer interaction. A novel approach is proposed to identify TNTI by integrating the vorticity threshold and fuzzy clustering method. To account for the influence of increasing Reynolds number in the flow direction on the vorticity threshold analysis, vorticity is normalized using the local boundary layer thickness and friction velocity. Two entrainment mechanisms are quantitatively described and compared using TNTI local entrainment velocity and the mass conservation equation. The results demonstrate that the entrainment process within the hypersonic boundary layer TNTI is predominantly governed by large-scale engulfment, and under the influence of shock waves, the dominance of large-scale ingestion is notably enhanced.

Keywords: Entrainment · Hypersonic boundary · Shock waves

1 Introduction

The interaction between shock waves and boundary layers (SBLI) is critical for hypersonic vehicle performance. In fluid dynamics, SBLI leads to various flow instability issues such as flow separation, vortex fragmentation and recombination, flow distortion, and localized heat transfer amplification. These effects result in increased drag, reduced combustion efficiency, and aerodynamic thermal protection challenges. Consequently, SBLI has been a significant research focus [1–4]. The instabilities from SBLI depend on parameters like Mach number, Reynolds number, shock wave intensity, and wall temperature. Research has primarily focused on understanding these interactions. Dolling's seminal work highlighted key early 21st-century SBLI issues, especially instability and heat transport rate [5]. Subsequent advancements have addressed these areas, with notable contributions from Clemens, Gaitonde, and Sandham [6–8].

J. Wang and I. Marusic (Eds.): IUTAM-TNTI 2024, IUTAM Bookseries 45, pp. 129–140, 2025.
https://doi.org/10.1007/978-3-031-78151-3_9

The turbulent boundary layer is typically divided into two regions: the non-turbulent region (without rotation) and the turbulent region (with rotational motion), separated by the TNTI. Significant exchanges of mass, momentum, energy, and chemical species occur within the TNTI, and flow properties change markedly across this interface. Recent research has focused on the flow characteristics near the TNTI, especially in incompressible turbulent flows [12–21].

Beyond geometric and flow characteristics, significant attention has been given to energy transport phenomena, particularly the entrainment mechanism governing boundary layer evolution. Previous studies indicated that engulfment is the primary entrainment mechanism in low Mach number flows [24–28], while recent findings on turbulent jets suggest nibbling predominates [22,23]. A key challenge in entrainment studies is establishing an objective methodology to quantify these mechanisms. Much research has focused on small-scale entrainment via local entrainment velocity. Holzner and Lüthi introduced this concept for turbulent shear layers [29], later extending it to boundary layers. However, there is no direct physical measure for large-scale engulfment, leading to reliance on indirect methods for analysis. Chauhan examined entrained mass flux [31], and Philip studied the rate of change of kinetic energy within a control volume bounded by the TNTI [32], showing large-scale vortex structures dominate overall entrainment. Eisma and Jahanbakhshi further explored TNTI properties and entrainment, indicating the dominance of large-scale mechanisms but noting the proportion changes with the vorticity threshold [28,33].

Most research has focused on incompressible flows, leaving uncertainty about the applicability of theoretical models to hypersonic boundary layers. No direct physical quantity exists for analyzing large-scale engulfment quantitatively, and indirect calculations show that the contributions of the two mechanisms vary with the vorticity threshold. This study aims to analyze the entrainment mechanism in hypersonic boundary layers and the impact of shock waves on this process.

2 DNSs of Hypersonic Boundary Layers with and Without Shock Waves

2.1 Simulation Details

The STREAmS solver is used to perform DNSs for two cases: the hypersonic boundary layer with and without a shock wave. This section provides a brief overview of the numerical simulations, with detailed validations of the STREAmS solver available in previous work [34].

The computational domain of $Lx \times Ly \times Lz = [70 \times 12 \times 6.5]\delta_{\text{in}}$ is discretized using the grid of $Nx \times Ny \times Nz = [2048 \times 384 \times 256]$, where δ_{in} represents the thickness of the initial boundary layer of the incoming flow. The spatial discretization relies on a hybrid sixth-order central/fifth-order WENO discretization. Non-reflecting boundary conditions are enforced at the upper and outflow boundaries, utilizing characteristic decomposition in the direction perpendicular to the boundary [35]. Likewise, a characteristic wave treatment is employed at the no-slip wall boundary, setting the wall temperature to its nominal recovery value, $T_r/T_\infty = 1+(\gamma-1)2rM_\infty^2$, with $r = Pr^{1/3}$. The flow is assumed to possess statistical homogeneity in the spanwise direction, enabling periodic boundary conditions to be applied. The free flow Mach number $M_\infty = 5.86$, the inlet friction Reynolds number $Re_\tau = 375$, and the wall temperature ratio $T_\mathrm{w}/T_r = 0.76$. Meanwhile, the shock-wave/boundary-layer interaction(SBLI) case is conducted. The boundary conditions are specified following the same setup as the boundary layer case, with the shock being artificially introduced through strict enforcement of the inviscid oblique shock solution that corresponds to the selected flow deflection angle. The interaction position between the shock wave and the boundary layer is at $x = 60\delta_\mathrm{in}$, and the incident angle is adjusted to 8°. The flow organization in the investigated SBLI is given in Figure. 1, where the contours of the density field are shown.

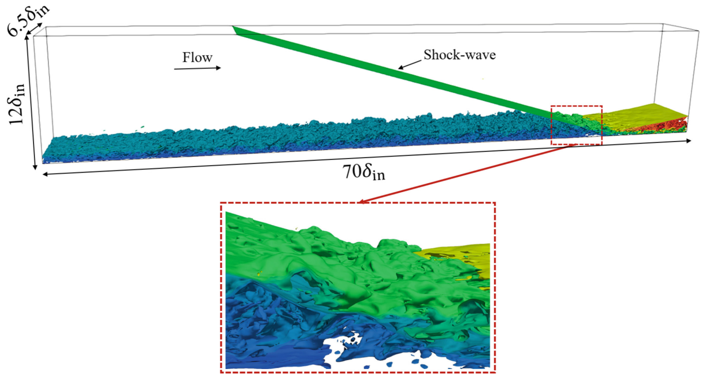

Fig. 1. Schematic diagram of the shock/boundary layer interaction case.

2.2 Detecting TNTI

The most commonly used method remains the vorticity threshold-based approach. However, for the problems related to hypersonic boundary layers, the higher Reynolds numbers and more complex flow conditions, often involving shock-wave interactions with the boundary layer, make detecting the TNTI more challenging. Multiple factors need to be considered, especially during the vorticity threshold selection. It is not sufficient to rely solely on vorticity for a simple analysis. Variations in local boundary layer thickness, friction velocity, and other influences must also be taken into account. Moreover, vorticity threshold methods tend to extract numerous noise points near the TNTI, resulting in unclear TNTI extraction and potentially affecting subsequent computation results. To address these issues, recently, some researchers have proposed using fuzzy clustering methods for TNTI detection [45,46]. In comparison to vorticity threshold methods and others, the approach detects clearer results with fewer noise points. However, since the results are obtained through fuzzy clustering of the velocity field, it becomes difficult to precisely determine the specific location of the TNTI, such as the viscous superlayer or turbulent sublayer.

Based on the aforementioned issues, normalizing the vorticity using local parameters [28] to account for the boundary layer's streamwise growth and provide a Reynolds-number independent threshold. Subsequently, A novel approach is proposed to identify TNTI by integrating the vorticity threshold and fuzzy clustering method to achieve more accurate detection of the TNTI. The vorticity magnitude, $\omega = \sqrt{\omega_i \omega_i}$, is normalized using the local boundary-layer thickness δ and the friction velocity u_τ. The normalized vorticity is defined as:

$$\omega^* = \omega \frac{\nu\sqrt{\delta^+}}{u_\tau^2} \tag{1}$$

where ν is the kinematic viscosity and the superscript "+" denotes wall units.

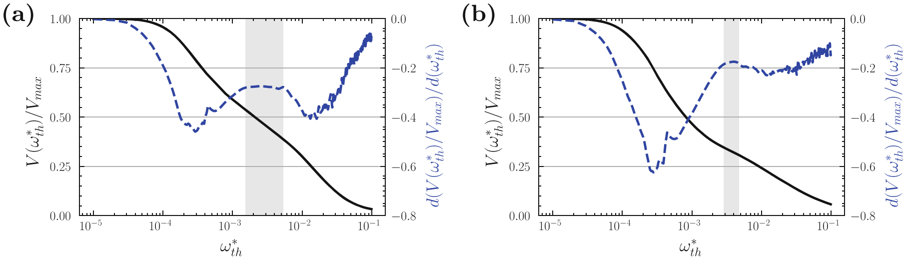

Fig. 2. The variation of the volume fraction of the turbulent region $V(\omega^*_{\text{th}})/V_{\max}$ (solid black line) and the change of volume fraction $d(V(\omega^*_{\text{th}})/V_{\max})/d(\omega^*_{\text{th}})$, with the normalized vorticity threshold ω^*_{th}:(a) boundary layer case, (b) SBLI case, the gray area represents the interval where the volume fraction of the turbulent region changes gradually with varying vorticity thresholds.

The volume fraction of the turbulent region decreases monotonically with increasing vorticity threshold. However, there is an interval where the change in volume fraction is minimal and nearly constant, corresponding to the TNTI. The TNTI is further divided into the viscous superlayer (VSL) and the turbulent sublayer (TSL). Regardless of the threshold choice, an isosurface that separates the turbulent and irrotational regions can be identified. Typically, the left boundary of the threshold range is considered the VSL, and the right boundary is the TSL. For comprehensive TNTI analysis, the entire threshold plateau range is used. As shown in Fig. 2, the vorticity threshold analysis for the two cases reveals that the plateau region is less distinct at hypersonic speeds due to compressibility effects, confirming previous findings [47]. The presence of a shock wave further narrows this plateau, increasing the vorticity threshold for the VSL outside the TNTI. This indicates that the shock wave lowers the TNTI's position and reduces its thickness, altering the transport characteristics of enstrophy and the entrainment mechanism at the TNTI.

The standard vorticity threshold method often introduces noise near the TNTI, resulting in unclear extraction, especially with shock waves. To address this, a new approach combines the vorticity threshold and fuzzy clustering methods. After selecting an appropriate threshold interval, the flow field is divided into regions of 0 and 1, with areas below the threshold as 0 and those above as 1. This generates sets of 0 and 1 combinations for different thresholds within the interval. The fuzzy clustering algorithm is then applied to these combinations through multiple iterations, yielding the fuzzy clustering results for each set. The complete TNTI is obtained by combining the clustering results from these threshold intervals. This method allows for selecting interfaces at different positions within the TNTI for analysis, providing insights into the characteristics of viscous and non-viscous areas based on different threshold results.

2.3 Entrainment Mechanism

Entrainment is the process where non-rotational fluid becomes part of the turbulent region [48]. There are two mechanisms in the entrainment process: one dominated by large-scale vortex structures, known as engulfment, and another by small-scale vortex structures through viscous diffusion, known as nibbling. Nibbling is considered to be a process of viscous diffusion of vortices on TNTI. The associated mass flow rate is calculated by multiplying the local entrainment velocity by the surface area of TNTI. Thus, analyzing the key to the small-scale entrainment mechanism lies in calculating the local entrainment velocity. Drawing on the theoretical framework of local entrainment velocity by [29], the local entrainment velocity in the hypersonic boundary layer is theoretically analyzed. As indicated in Eq. 2, considering that the magnitudes of $\varOmega_{II}$, $\varOmega_{III}$, and $\varOmega_{VI}$ significantly surpass the rest of the terms, a simplification of the compressible boundary layer's vorticity transport equation can be performed. The simplified outcome is presented below Eq. 3, where the summation of $\varOmega_{II}$ and $\varOmega_{III}$ corresponds to the non-viscous terms in the incompressible formulation, while $\varOmega_{VI}$ corresponds to the viscous term. Therefore, in subsequent analyses, the methodology proposed by Holzner to derive the local entrainment velocity can be adopted.

$$\begin{aligned}\underbrace{\frac{\mathrm{D}\varOmega}{\mathrm{D}t}}_{\varOmega_I} =& \underbrace{2\omega_i\omega_j\frac{\partial u_i}{\partial x_j}}_{\varOmega_{II}} \underbrace{-2\varOmega\frac{\partial u_j}{\partial x_j}}_{\varOmega_{III}} + \underbrace{\frac{2\omega_i\epsilon_{ijk}}{\rho^2}\frac{\partial \rho}{\partial x_j}\frac{\partial p}{\partial x_k}}_{\varOmega_{IV}} \\ & \underbrace{+v\frac{\partial^2\varOmega}{\partial x_j\partial x_j}}_{\varOmega_V} \underbrace{-2v\frac{\partial \omega_i}{\partial x_j}\frac{\partial \omega_i}{\partial x_j}}_{\varOmega_{VI}} \underbrace{-\frac{2\omega_i\epsilon_{ijk}}{\rho^2}\frac{\partial \rho}{\partial x_j}\frac{\partial \tau_{km}}{\partial x_m}}_{\varOmega_{VII}}.\end{aligned} \tag{2}$$

$$\frac{\mathrm{D}\varOmega}{\mathrm{D}t} = \omega_i\omega_j S_{ij} - 2v\frac{\partial \omega_i}{\partial x_j}\frac{\partial \omega_i}{\partial x_j}. \tag{3}$$

After simplifying the vorticity transport equation, analyzing equivalent surfaces using the same vorticity threshold, and considering the temporal evolution of these surfaces, the fluid velocity u^s on TNTI can be divided into two components. The first component is the velocity induced by the flow field, denoted as u, and the second component is the velocity relative to TNTI $\mathrm{V} = v_n \cdot \hat{n}$, where $\hat{n} = \nabla\omega^2 / \left|\nabla\omega^2\right|$, $u^s = u + V$. Because different instants are considered on the same isosurface, the rate of change of enstrophy with time is zero, which can be expressed as:

$$\frac{D\Omega}{Dt} = \frac{\partial\omega^2}{\partial t} + u_j^s \frac{\partial\omega^2}{\partial x_j} = \frac{\partial\omega^2}{\partial t} + \left(u_j + V_j\right) \frac{\partial\omega^2}{\partial x_j} = 0. \tag{4}$$

Combining the simplified enstrophy transport equation yields:

$$v_n = -\frac{\omega_i \omega_j s_{ij}}{\left|\nabla\omega^2\right|} + \frac{2v \frac{\partial\omega_i}{\partial x_j} \frac{\partial\omega_i}{\partial x_j}}{\left|\nabla\omega^2\right|}. \tag{5}$$

The mass flux of small-scale entrainment at the TNTI location can be expressed as:

$$\phi_n = \int_{\mathscr{S}_t} \rho \left(\overrightarrow{\mathbf{v}}_n \cdot \hat{n}_n\right) d\mathscr{S}. \tag{6}$$

Nibbling is denoted as ϕ_n and is the entrained mass flow rate into the turbulent region through the TNTI due to viscous diffusion. Where $\mathscr{S}_t$ is the surface of the moving TNTI.

Quantifying the mass flux of large-scale engulfment in the entrainment mechanism is challenging. Therefore, an indirect calculation is initially employed using mass conservation and local entrainment velocity. The Reynolds transport theorem and the continuity equation are used to determine the temporal variations in mass within the control volume [28].

$$\frac{d\mathscr{M}}{dt} = \int \frac{\partial\rho}{\partial t} d\mathscr{V} + \oint \rho \left(\overrightarrow{\mathbf{u}}_s \cdot \hat{n}\right) d\mathscr{S} = \oint \rho (\overrightarrow{\mathbf{v}} \cdot \hat{n}) d\mathscr{S}. \tag{7}$$

where ρ is the fluid density, $\mathscr{V}$ is the control volume, and $\mathscr{S}$ are its time-dependent control surfaces. The mass conservation equation within the computational domain is given as follows:

$$\begin{aligned} \left\langle \frac{d\mathscr{M}}{dt} \right\rangle = & \underbrace{\left\langle \int_{\mathscr{S}_i} \rho u d\mathscr{S} \right\rangle}_{\phi_i} - \underbrace{\left\langle \int_{\mathscr{S}_o} \rho u d\mathscr{S} \right\rangle}_{\phi_o} \\ & + \underbrace{\left\langle \int_{\mathscr{S}_t} \rho \left(\overrightarrow{\mathbf{v}}_n \cdot \hat{n}_n\right) d\mathscr{S} \right\rangle}_{\phi_n} + \underbrace{\left\langle \int_{\mathscr{S}_h} \rho \left(\overrightarrow{\mathbf{v}}_e \cdot \hat{n}_e\right) d\mathscr{S} \right\rangle}_{\phi_e}. \end{aligned} \tag{8}$$

where $< . >$ represents temporal averaging, $\mathscr{S}_i$ and $\mathscr{S}_o$ are the surface areas of turbulence at the inlet and outlet of the control volume. $\mathscr{S}_t$ is the surface of the moving TNTI, while the remaining boundaries of the turbulent region (holes) are referred to as $\mathscr{S}_h$. The streamwise component of fluid velocity is represented by u.

ϕ_n represents the mass flux associated with the small-scale nibbling mechanism, while ϕ_e characterizes the mass flux involved in the engulfment process. The overall mass change in the turbulent region is calculated by determining the total mass change within the region that conforms to a given vorticity threshold. The mass flux from the small-scale nibbling mechanism is computed based on previous analysis. The streamwise mass flux is obtained from the streamwise velocity. The remaining portion represents the mass flux associated with the large-scale engulfment mechanism.

3 Results and Discussion

The TNTI detection results are shown in Fig. 3. In part (a), representing the hypersonic boundary layer case, the new method provides clearer extraction at the TNTI edge, facilitating the distinction of engulfment effects. Previously, using the vorticity threshold method involved selecting a single threshold within a range to characterize the entire TNTI, which included noise points and affected quantitative analysis. The new method allows for analyzing different positions within the TNTI based on various vorticity thresholds, improving the accuracy of pseudo-vortex energy transport and entrainment mechanism analysis in the viscous superlayer and turbulent sublayer. Part (b) shows the results of the interaction between the shock wave and the boundary layer. In the presence of a shock wave, more error points appear at the TNTI edge, and vorticity changes caused by compression and expansion waves are mistakenly identified. This significantly affects the accuracy of the final entrainment mechanism calculations.

Figure 4 shows the variations in local entrainment velocity along the TNTI for two scenarios. The trends are consistent: local entrainment velocity rapidly increases near the TNTI, peaks around 5η, and then stabilizes. Under shock wave influence, local entrainment velocity slightly increases and fluctuates after the peak, likely due to compression and expansion wave interference within the boundary layer. However, the average values remain similar to those in the hypersonic boundary layer case, indicating a minor impact of shock waves on local entrainment velocity. The primary influences on the mass flux of small-scale entrainment are likely due to the TNTI's geometric interface and flow density variations.

Figure 5 illustrates the ratio of mass flux between large-scale engulfment and small-scale entrainment along the distance to TNTI. Initially, this ratio rapidly increases to a peak value, then quickly decreases, and finally stabilizes. The peak is likely due to the presence of the viscous sublayer within the TNTI, which causes a sharp change in the proportion between the two mechanisms. This observation aligns with previous studies [28]. Deeper within the TNTI, the ratio stabilizes. In the high-speed boundary layer case, large-scale engulfment constitutes about 94% near the TNTI's outer side and about 88% within the turbulent

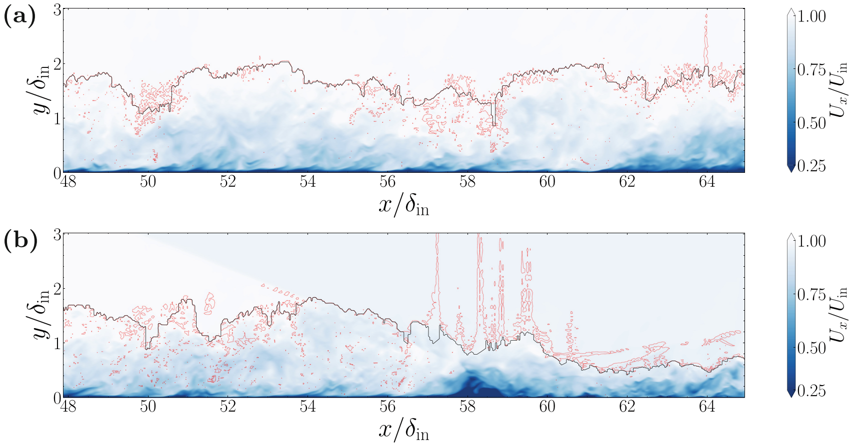

Fig. 3. TNTI extraction results, with red lines representing the vorticity threshold method and black lines representing the new method. (a) Hypersonic boundary layer case. (b) Shock wave/hypersonic boundary layer interaction case.

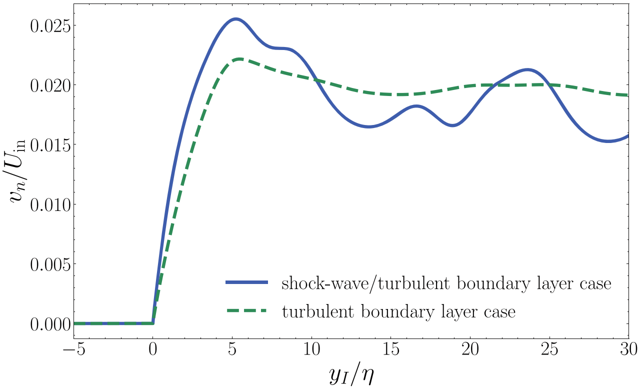

Fig. 4. With and without shock waves, local entrainment velocity variation along TNTI.

sublayer. Under shock wave influence, the variation trend is similar, with initial peaks followed by stabilization. However, the proportion of large-scale engulfment increases, and the peaks are more pronounced, with some fluctuations in the stable range. Near the outer edge of the hypersonic boundary layer, the large-scale engulfment proportion is around 98%, and within the TNTI's turbulent sublayer, it is about 96%. These findings indicate a significant amplification of the large-scale engulfment mechanism due to shock waves. To further analyze this amplification, a direct physical quantity is needed to characterize the large-scale engulfment mechanism. Therefore, establishing a simplified model for large-scale engulfment in the shock-wave/hypersonic boundary layer is necessary to understand the amplified effects of shock waves on this mechanism.

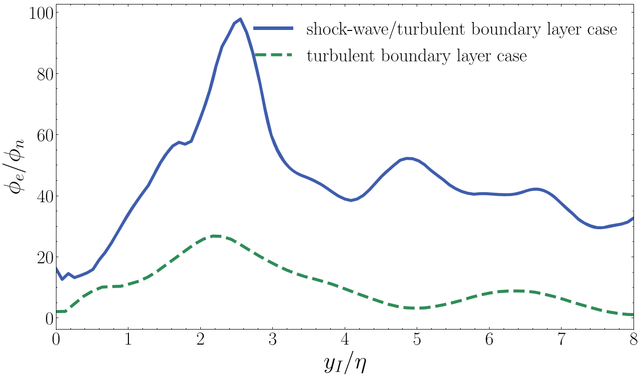

Fig. 5. With and without shock waves, the ratio of mass flux generated by the large-scale engulfment and small-scale nibbling mechanisms.

4 Conclusions

DNSs are conducted for hypersonic boundary layers with and without shock waves to investigate vortex entrainment mechanisms for non-rotating flows entering the turbulent region at the TNTI and the impact of shock waves. A novel method combining vorticity thresholding and fuzzy clustering is developed for more accurate TNTI extraction. Building on small-scale mechanism analysis, the mass flux of large-scale entrainment is indirectly calculated through mass conservation. The ratio of mass flux between large-scale and small-scale entrainment shows that the large-scale process dominates, with proportions exceeding 90%, especially in the viscous superlayer. Under shock wave influence, the proportion of large-scale entrainment increases further, indicating that shock waves enhance this process.

Acknowledgement. This work is supported by the National Natural Science Foundation of China.

References

1. Padmanabhan, S., Maldonado, J.C., Threadgill, J.A.S., Little, J.C.: Experimental study of swept impinging oblique shock/boundary-layer interactions. AIAA J. **59**(1), 140–149 (2021)
2. Adler, M.C., Gaitonde, D.V.: Unsteadiness in shock/turbulent-boundary-layer interactions with open flow separation. In: Proceedings of the Conference (2018)

3. Adler, M.C., Gaitonde, D.V.: Influence of separation structure on the dynamics of shock/turbulent-boundary-layer interactions. Theoret. Comput. Fluid Dyn. **36**, 303–326 (2021)
4. Adler, M.C., Gaitonde, D.V.: Flow similarity in strong swept-shock/turbulent-boundary-layer interactions. AIAA J. (2019)
5. Dolling, D.S.: Fifty years of shock-wave/boundary-layer interaction research: what next? AIAA J. **39**(8), 1517–1531 (2001)
6. Clemens, N.T., Narayanaswamy, V.: Low-frequency unsteadiness of shock wave/turbulent boundary layer interactions. Annu. Rev. Fluid Mech. **46**(1), 469–492 (2014)
7. Gaitonde, D.V.: Progress in shock wave/boundary layer interactions. Prog. Aerosp. Sci. **72**, 80–99 (2015)
8. Sandham, N.D.: Effects of compressibility and shock-wave interactions on turbulent shear flows. Flow Turbul. Combust. **97**(1), 1–25 (2016)
9. Eagle, W.E., Driscoll, J.F.: Shock wave-boundary layer interactions in rectangular inlets: three-dimensional separation topology and critical points. J. Fluid Mech. **756**, 328–353 (2014)
10. Grossman, I.J., Bruce, P.J.K.: Confinement effects on regular-irregular transition in shock-wave-boundary-layer interactions. J. Fluid Mech. **853**, 171–204 (2018)
11. Lusher, D.J., Sandham, N.D.: The effect of flow confinement on laminar shock-wave/boundary-layer interactions. J. Fluid Mech. **897** (2020)
12. Westerweel, J., Fukushima, C., Pedersen, J.M., Hunt, J.C.R.: Momentum and scalar transport at the turbulent/non-turbulent interface of a jet. J. Fluid Mech. **631**, 199–230 (2009)
13. da Silva, C.B., dos Reis, R.J.N.: The role of coherent vortices near the turbulent/non-turbulent interface in a planar jet. Philos. Trans. Roy. Soc. A Math. Phys. Eng. Sci. **369**, 738–753 (2011)
14. da Silva, C.B., Taveira, R.R.: The thickness of the turbulent/nonturbulent interface is equal to the radius of the large vorticity structures near the edge of the shear layer. Phys. Fluids **22**, 121702 (2010)
15. da Silva, C.B., dos Reis, R.J.N., Pereira, J.C.F.: The intense vorticity structures near the turbulent/non-turbulent interface in a jet. J. Fluid Mech. **685**, 165–190 (2011)
16. da Silva, C.B., Hunt, J.C.R., Eames, I.W., Westerweel, J.: Interfacial layers between regions of different turbulence intensity. Annu. Rev. Fluid Mech. **46**, 567–590 (2014)
17. Holzner, M., Liberzon, A., Nikitin, N., Lüthi, B., Kinzelbach, W., Tsinober, A.: A Lagrangian investigation of the small-scale features of turbulent entrainment through particle tracking and direct numerical simulation. J. Fluid Mech. **598**, 465–475 (2008)
18. Taveira, R.R., da Silva, C.B.: Kinetic energy budgets near the turbulent/nonturbulent interface in jets. Phys. Fluids **25**, 015114 (2013)
19. Taveira, R.R., da Silva, C.B.: Characteristics of the viscous superlayer in shear free turbulence and in planar turbulent jets. Phys. Fluids **26**, 021702 (2014)
20. Silva, T.S., Zecchetto, M., da Silva, C.B.: The scaling of the turbulent/non-turbulent interface at high Reynolds numbers. J. Fluid Mech. **843**, 156–179 (2018)
21. Watanabe, T., Sakai, Y., Nagata, K., Ito, Y., Hayase, T.: Vortex stretching and compression near the turbulent/non-turbulent interface in a planar jet. J. Fluid Mech. **758**, 754–785 (2014)
22. Mathew, J., Basu, A.: Some characteristics of entrainment at a cylindrical turbulence boundary. Phys. Fluids **14**(7), 2065–2072 (2002)

23. Westerweel, J., Pedersen, J.M., Fukushima, C., Hunt, J.C.R.: Mechanics of the turbulent/non-turbulent interface of a jet. Phys. Rev. Lett. **95**(17) (2005)
24. Dahm, P.E., Dimotakis, P.: Measurements of entrainment and mixing in turbulent jets. AIAA J. **25**(9), 1216 (1987)
25. Ferré, J.A., Mumford, J.C., Savill, A.M., Giralt, F.: Three-dimensional large-eddy motions and fine-scale activity in a plane turbulent wake. J. Fluid Mech. **210**, 371–414 (1990)
26. Mungal, M.G., Karasso, P.S., Lozano, A.: The visible structure of turbulent jet diffusion flames (1991)
27. Dimotakis, P.E.: The mixing transition in turbulent flows. J. Fluid Mech. **409**, 69–98 (2000)
28. Jahanbakhshi, R.: Mechanisms of entrainment in a turbulent boundary layer. Phys. Fluids **33**, 035105 (2021)
29. Holzner, M., Luthi, B.: Laminar superlayer at the turbulence boundary. Phys. Rev. Lett. **106**(13), 134503 (2011)
30. Wolf, M., Lüthi, B., Holzner, M., Krug, D., Kinzelbach, W., Tsinober, A.: Investigations on the local entrainment velocity in a turbulent jet. Phys. Fluids **24**(10), 105110 (2013)
31. Chauhan, K., Philip, J., Hutchins, N., Silva, C.D., Marusic, I.: The turbulent/non-turbulent interface and entrainment in a boundary layer. Am. Phys. Soc. (2012)
32. Philip, J., Meneveau, C., De Silva, C.M., Marusic, I.: Multiscale analysis of fluxes at the turbulent/non-turbulent interface in high Reynolds number boundary layers. Phys. Fluids **26**(1), 015105 (2014)
33. Eisma, J., Westerweel, J., Ooms, G., Elsinga, G.E.: Interfaces and internal layers in a turbulent boundary layer. Phys. Fluids **27**(5), 055105 (2015)
34. Bernardini, M., Modesti, D., Salvadore, F., Pirozzoli, S.: STREAmS: a high-fidelity accelerated solver for direct numerical simulation of compressible turbulent flows. Comput. Phys. Commun. **263**, 107906 (2021)
35. Poinsot, T.J., Lelef, S.K.: Boundary conditions for direct simulations of compressible viscous flows. J. Comput. Phys. (1992)
36. Klein, M., Sadiki, A., Janicka, J.: A digital filter based generation of inflow data for spatially developing direct numerical or large eddy simulations. J. Comput. Phys. **186**(2), 652–665 (2003)
37. Touber, E., Sandham, N.D.: Large-eddy simulation of low-frequency unsteadiness in a turbulent shock-induced separation bubble. Theoret. Comput. Fluid Dyn. **23**(2), 79–107 (2009)
38. Kempf, A.M., Wysocki, S., Pettit, M.: An efficient, parallel low-storage implementation of Klein's turbulence generator for LES and DNS. Comput. Fluids **60**, 58–60 (2012)
39. Pirozzoli, S., Bernardini, M.: Turbulence in supersonic boundary layers at moderate Reynolds number. J. Fluid Mech. **688**, 120–168 (2011)
40. Smits, A.J., Dussauge, J.-P.: Turbulent Shear Layers in Supersonic Flow. Springer, New York (2006). https://doi.org/10.1007/b137383
41. Musker, A.J.: Explicit expression for the smooth wall velocity distribution in a turbulent boundary layer. AIAA J. **17**(6), 655–657 (2012)
42. Bisset, D.K., Hunt, J.C.R., Rogers, M.M.: The turbulent/non-turbulent interface bounding a far wake. J. Fluid Mech. **451**, 383–410 (2002)
43. Holzner, M., Liberzon, A., Nikitin, N., Kinzelbach, W., Tsinober, A.: Small-scale aspects of flows in proximity of the turbulent/nonturbulent interface. Phys. Fluids **19**, 071702 (2007)

44. Jiménez, J., Hoyas, S., Simens, M.P., Mizuno, Y.: Turbulent boundary layers and channels at moderate Reynolds numbers. J. Fluid Mech. **657**(12), 335–360 (2010)
45. Younes, K., Gibeau, B., Ghaemi, S., Hickey, J.-P.: A fuzzy cluster method for turbulent/non-turbulent interface detection. Exp. Fluids **62**, 1–4 (2021)
46. Fan, D., Xu, J., Yao, M.X., Hickey, J.P.: On the detection of internal interfacial layers in turbulent flows. J. Fluid Mech. **872**, 198–217 (2019)
47. Madnia, C.K., Jahanbakhshi, R.: Entrainment in a compressible turbulent shear layer. J. Fluid Mech. (2016)
48. Townsend, A.A.: The Structure of Turbulent Shear Flow (1980)
49. Turner, J.S.: Turbulent entrainment - the development of the entrainment assumption, and its application to geophysical flows. J. Fluid Mech. **173**, 431–471 (1986)
50. Chapman, D.R., Kuehn, D.M., Larson, H.K.: Investigation of separated flows in supersonic and subsonic streams with emphasis on the effect of transition. NACA report (1957)
51. Dimotakis, P.E.: Entrainment into a fully developed, two-dimensional shear layer. In: AIAA, Aerospace Sciences Meeting (1983)

Baroclinic Vorticity Generation Near the Turbulent/Non-turbulent Interface of a Boundary Layer with Combustion

Chuhan Wang(✉) and Chunxiao Xu

AML, Department of Engineering Mechanics, Tsinghua University, Beijing 100084, People's Republic of China
chuhan_wang@mail.tsinghua.edu.cn, xucx@tsinghua.edu.cn

Abstract. Enstrophy transport is examined in a recent direct numerical simulation database of compressible turbulent boundary layer featuring non-premixed hydrogen-air combustion. The inlet flow profile combines a cold, sonic hydrogen stream near the wall with a preheated, supersonic air mainstream, resulting in downstream transition and ignition phenomena, using a detailed chemistry scheme. Unlike reacting mixing layers or jets where the flame surface typically develops at regions of maximum shear intensity, in this configuration, the flame surface region is found beneath the boundary layer edge within one Taylor micro-scale of the turbulent/non-turbulent interface. While classical enstrophy budget analyses along the wall-normal direction reveal no significant deviation from non-reacting boundary layers, conditional budget analyses in the direction normal to the turbulent/non-turbulent interface unveil baroclinic torque production of comparable magnitude to vortex stretching in the turbulent sublayer. The relationship between local chemical heat release and baroclinic torque generation is investigated by evaluation of the integrand linked to the enstrophy variation from baroclinic torque at different heat release levels. The findings suggest that net torque variations are skewed towards positive values in the local flow regions of sufficiently high chemical heat release.

Keywords: non-premixed combustion · turbulent boundary layer · compressible flow

1 Introduction

Enstrophy transport is an important research subject in general flame configurations encompassing both premixed and non-premixed flames. While several studies in isotropic turbulence flames concluded that the generation of baroclinic torque is unimportant at high turbulence intensity [1,3], Kazbekov *et al.* showed that the generation of baroclinic torque is comparable in magnitude to vortex stretching and viscous effects, in an experimental swirl combustor operating across a wide range of Reynolds number [10]. The study highlights the importance of specific flow field in the baroclinic enstrophy generation.

J. Wang and I. Marusic (Eds.): IUTAM-TNTI 2024, IUTAM Bookseries 45, pp. 141–152, 2025.
https://doi.org/10.1007/978-3-031-78151-3_10

The turbulent/non-turbulent interface (TNTI) plays a crucial role in the dynamics of non-premixed reacting flow, characterized by an abrupt change of transport scalars such as temperature and multi-species concentrations. Watanabe *et al.* conducted numerical investigations into scalar transport near the TNTI of an incompressible planar jet involving non-premixed reactant streams with an isothermal one-step chemical reaction [12]. The TNTI delineates the turbulent region where the mixing of two reactants are prominent. A similar observation was made in an experiment of a liquid jet with an isothermal reaction [11]. Jahanbakhashi and Madnia examined the influence of chemical heat release on entrainment in compressible turbulent mixing layers across subsonic and supersonic regimes using an infinitely fast chemistry [7]. They found that at high levels of heat release, the inviscid terms in the compressible enstrophy transport equations, encompassing thermal dilation and baroclinic torque, play a significant role in the entrained mass flow rate into the core of the mixing layer, whereas the contribution of these terms vanishes in a non-reacting setting [8]. A scalar-gradient transport equation was derived to analyse the mixing mechanisms near the TNTI, revealing, akin to the enstrophy transport, a laminar superlayer and a turbulent sublayer for scalar gradient transport within the TNTI [9]. Gauding *et al.* investigated the effect of external intermittency on small-scale turbulent mixing in a non-premixed jet flame by using high-order structure functions near the TNTI [6].

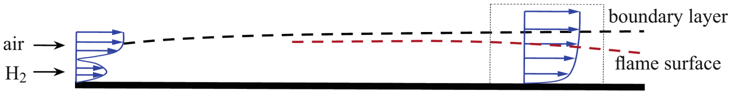

Fig. 1. Diagram of the simulated flow configuration. The area within the dotted rectangle represents the fully developed reacting boundary layer flow, investigated in the present paper.

While most studies of TNTI with chemical reactions focus on the reacting mixing layer or jet flames, TNTI in non-reacting boundary layers has been exclusively investigated over the past decade [2,4,15]. In high-speed boundary layers, chemical reactions may inevitably occur either in the scenario of high-enthalpy flow with thermochemical nonequilibrium or in supersonic combustion. Recently we conducted a direct numerical simulation (DNS) of a supersonic non-premixed wall jet with hydrogen-air combustion over a flat plate. The configuration simulated is schematized in Fig. 1. Our first attempt of investigating the DNS database focused on classical turbulence closure strategies, including diffusive gradient formulation using turbulent Prandtl and Schmidt numbers, and the strong Reynolds analogy associating local velocity and temperature fluctuations [16]. An interesting observation was that the strong Reynolds analogy is satisfied in the near-wall region, akin to non-reacting boundary layers, whereas the correlation between temperature and velocity fluctuations is lost in the outer region where chemical heat release is prominent. To better understand the dynamics in the outer layer, this paper focuses on exploiting enstrophy transport near the boundary-layer TNTI.

The paper is structured as follows. Section 2 outlines the computational setup and flow configuration. In Sect. 3, the statistics in the wall-normal direction are briefly described. In Sect. 4, conditional statistics at varying distances normal to the identified TNTI are given. In Sect. 5, the relationship between local baroclinic torque generation and chemical heat release is examined. Conclusions and perspectives are provided in Sect. 6.

2 Flow Configuration

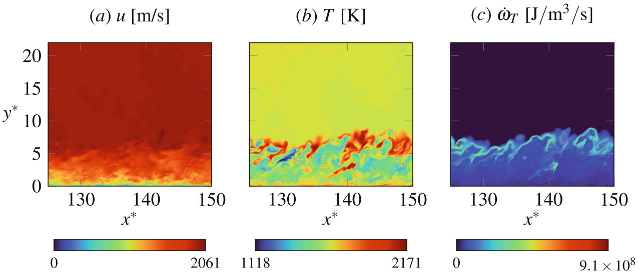

Fig. 2. Spanwise snapshots in the streamwise range $125 < x^* < 150$. (a) Streamwise velocity u. (b) Temperature T. (c) Chemical heat release rate $\dot{\omega}_T$.

A non-premixed hydrogen-air flame is ignited in a three-dimensional turbulent flat-plate boundary layer with a mainstream Mach number of 2.33 and streamwise velocity $U_\infty = 1987$ m/s. A model wall jet profile is specified at the laminar inlet featuring a Poiseuille flow profile close to the wall for the sonic hydrogen stream, and a similarity boundary layer profile for the preheated air mainstream farther away from the wall surface, as illustrated in Fig. 1. The inflow mainstream air temperature is set to $T_\infty = 1700$ K and the hydrogen gas temperature is set to 300 K. The mixing of the hydrogen and air stream triggers auto-ignition and sustained turbulent combustion in the boundary layer flow. Non-reflecting characteristic conditions are applied at all other boundaries.

The multi-species compressible reacting Navier-Stokes equations are solved in Cartesian coordinates, with (x, y, z) representing the streamwise, wall-normal and spanwise directions, respectively. The hydrogen-air chemical reaction is modeled using a 9-species 19-step detailed reaction scheme. These equations are resolved in time and space using the OpenCFD-Comb code, which has been used in the DNSs of reacting jet flows [5] and interface instabilities with hydrogen combustion [13].

The size of the effective computation domain is $L_x^* \times L_y^* \times L_z^* = 150 \times 22 \times 10$, with dimensionless lengths normalised by the inflow hydrogen stream height $h_0 =$

4 mm. This study concentrates on the downstream region $125 < x^* < 150$, which is discretised by $N_x \times N_y \times N_z = 477 \times 585 \times 356$ grids. Snapshots of streamwise velocity u, temperature T and chemical heat release rate $\dot{\omega}_T$ are presented in Fig. 2. The flame surface, distinguished by high levels of chemical heat release rate and temperature, predominantly forms in the outer layer adjacent to the edge.

3 Wall-Normal Statistics

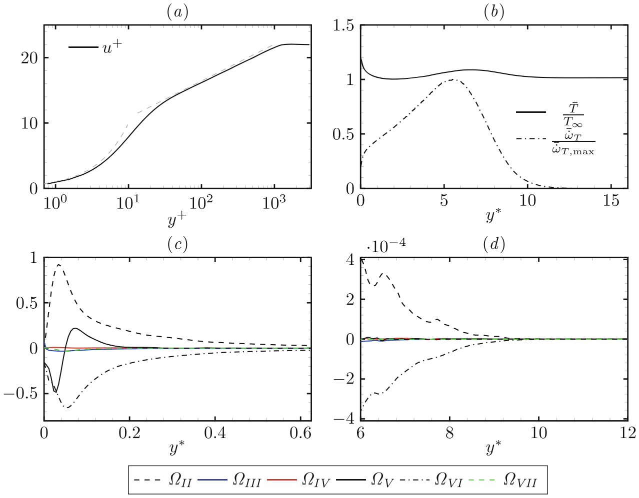

Fig. 3. Statistics in the wall-normal direction in the range $125 < x^* < 150$. (*a*) Inner-scale velocity u^+ against inner-scale wall-normal coordinate y^+. (*b*) Mean temperature $\bar{T}$ normalised by the inflow mainstream temperature $T_\infty = 1700$ K, and mean chemical heat release rate $\dot{\omega}_T$ normalised by its maximum value $\bar{\dot{\omega}}_{T,\max} = 1.53 \times 10^8$ J/m^3/s. (*c,d*) Enstrophy transport budget in the near-wall region and outer layer, respectively. $y^* = y/h_0$ is used as the wall-normal coordinate in (*b*-*d*).

Assuming that the streamwise variation of the boundary-layer thickness is relatively small within the region of interest, $125 < x^* < 150$, the statistics averaged both in the streamwise and spanwise directions, yield a boundary-layer thickness of $\delta_{99} = 8.2h_0$, a Reynolds number based on the momentum thickness of $Re_\theta = 6092$, and a frictional Reynolds number of $Re_\tau = 1044$. In this region, the velocity statistics nearly resemble those of a canonical turbulent boundary layer, as evidenced by the mean velocity profile u^+ in wall inner scale following the linear ($u^+ = y^+$) and logarithm laws ($u^+ = \frac{1}{\kappa}\ln(y^+) + B$, where $\kappa = 0.41$ and $B = 5.2$), shown in Fig. 3(*a*). The mean temperature profile shows one peak at the wall surface due to the adiabatic condition and another less prominent peak in the outer layer in the proximity of the peak associated with the chemical heat release rate.

Our previous paper provides a detailed analysis of first- and second-order statistics related to the flow, species and elementary chemical reactions for the current configuration, and those results are not duplicated here. In the following, we examine the contribution to enstrophy transport from various physical mechanisms. Enstrophy transport is defined as $\varOmega = \omega_i \omega_i$, and its transport equation in a compressible flow is formulated in accordance with [7,8], as follows:

$$\begin{aligned}\underbrace{\frac{\mathrm{D}\varOmega}{\mathrm{D}t}}_{\varOmega_I} = \underbrace{2\omega_i\omega_j\frac{\partial u_i}{\partial x_j}}_{\varOmega_{II}} \underbrace{-2\varOmega\frac{\partial u_j}{\partial x_j}}_{\varOmega_{III}} + \underbrace{\frac{2\omega_i\epsilon_{ijk}}{\rho^2}\frac{\partial \rho}{\partial x_j}\frac{\partial p}{\partial x_k}}_{\varOmega_{IV}} \\ \underbrace{+\frac{\nu}{Re}\frac{\partial^2\varOmega}{\partial x_j \partial x_j}}_{\varOmega_V} \underbrace{-\frac{2\nu}{Re}\frac{\partial \omega_i}{\partial x_j}\frac{\partial \omega_i}{\partial x_j}}_{\varOmega_{VI}} \underbrace{-\frac{2\omega_i}{\rho^2}\frac{\epsilon_{ijk}}{Re}\frac{\partial \rho}{\partial x_j}\frac{\partial \tau_{km}}{\partial x_m}}_{\varOmega_{VII}}.\end{aligned} \tag{1}$$

The left-hand-side term $\varOmega_I$ is the unstationary term. The right-hand-side terms $\varOmega_{II}$, $\varOmega_V$ and $\varOmega_{VI}$ correspond to the enstrophy contribution from the stretching or compression of vortex lines, viscous diffusion and viscous dissipation, respectively; these terms are also present in incompressible flows. The term $\varOmega_{III}$ accounts for the expansion or compression of the fluid, which is vanished in incompressible flows. The baroclinic enstrophy generation, represented by $\varOmega_{IV}$, arises from the local misalignment of density and pressure gradients and can be significant in swirling flows and flames [8,10]. The term $\varOmega_{VII}$ represents the torque generated by the misalignment of the density gradient and the shear stress gradient.

Figure 3(c) shows the right-hand-side of the enstrophy transport equation in the near-wall region, revealing that the enstrophy transport is primarily influenced by the incompressible terms $\varOmega_{II}$, $\varOmega_V$ and $\varOmega_{VI}$. The magnitudes of those terms are normalised by $(U_\infty/h_0)^3$. The enstrophy is primarily produced by vortex stretching and dissipated by viscous effects, with high enstrophy near the wall surface being diffused away from the wall surface. The terms $\varOmega_{III}$, $\varOmega_{IV}$ and $\varOmega_{VII}$, which are specific to compressible flows, have relatively minor significance in the near-wall region. Figure 3(d) further shows that these terms are also insignificant in the outer layer when compared to vortex stretching and viscous dissipation. However, it is crucial to note that the boundary layer edge exhibits highly irregular spatial characteristics, and a budget analysis based solely on wall-normal statistics may result in ambiguity in the outer layer near the edge. Consequently, conditional statistics across the TNTI are adopted in the next section.

4 Conditional Statistics in the Local Coordinates of Turbulent/Non-turbulent Interface

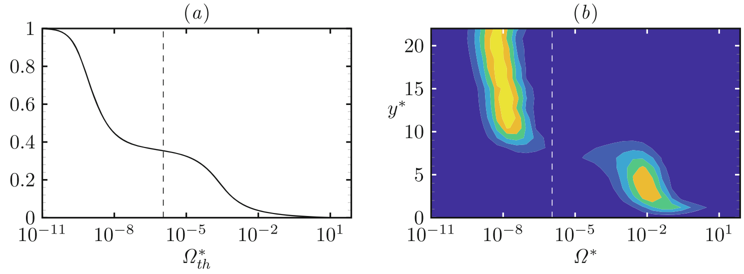

Fig. 4. (a) Volume fraction of turbulent region determined by different values of enstrophy threshold $\Omega_{th}*$. (b) jPDF of enstrophy Ω^* and wall-normal coordinate y^*. The vertical dashed lines represent the chosen enstrophy threshold $\Omega^*_{th} = 1.1 \times 10^{-6}$.

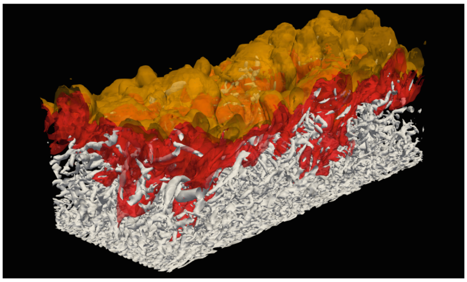

Fig. 5. Three-dimensional visualisation in the streamwise range $125 < x^* < 150$: TNTI (yellow), flame surface (red) and vortex structures identified by the $\lambda_{c,i}$ criterion (white).

The TNTI is detected by an isosurface corresponding to the enstrophy threshold Ω_{th}, identified from standard volume fraction methods [4]. The volume fraction of turbulent region determined by different enstrophy threshold is shown in Fig. 4(a). A dimensionless threshold of $\Omega_{th}* = \Omega_{th}/(U_\infty/h_0)^2 = 1.1 \times 10^{-6}$ is selected within the plateau range, corresponding to a slow change of turbulent volume fraction with the enstrophy threshold. Figure 4(b) displays the joint probability density function (jPDF) of enstrophy and the wall-normal coordinate y^*. The jPDF is computed by multiplying the occurrence by the associated local mesh quadrature, thereby accounting for the inhomogeneity in spatial discretisation. Consistent with results from compressible boundary layers [14], two peak regions are evident: one at the bottom right, corresponding to the strong shear region near the wall, and another at the top left corner, associated with enstrophy of very small magnitude, which may originate from pressure wave radiations or numerical errors. It is shown that the selected threshold effectively separates these two peak regions. A three-dimensional visualisation for the streamwise range $125 < x^* < 150$ is presented in Fig. 5. This visualisation includes the TNTI identified by an enstrophy isosurface at $\Omega_{th}* = 1.1 \times 10^{-6}$, the flame surface represented by a chemical heat release isosurface at $\dot{\omega}_T = \bar{\dot{\omega}}_{T,\max}$ and the vortex structures using the $\lambda_{c,i}$ criterion. The flame surface (red) is identified in close proximity to the TNTI, located around $7 < y^* < 8$, which is relatively far from the wall surface where vortex structures (white) are prominent. The depicted scenario differs from the three-dimensional visualisation of a reacting mixing layer with chemical heat release (see Fig. 5 in [8]), where the flame surface is identified within the mixing layer, corresponding to the strong shear region. Conversely, the TNTI therein is identified outside the mixing layer, separated from the flame surface region.

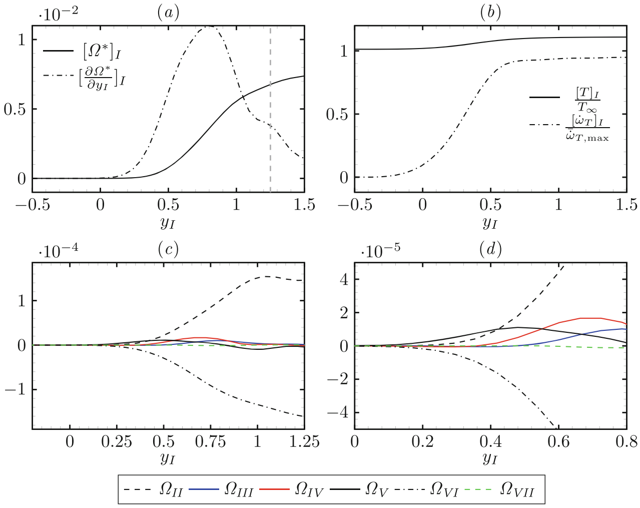

Fig. 6. Conditional statistics in the local coordinates of TNTI y_I. y_I is normalised by the Talyor micro-scale at the distance twice of the TNTI thickness. (a) Enstrophy and its derivative with respect to y_I. The vertical line (grey) denotes the identified TNTI thickness $\delta_{TNTI} \approx 1.25\lambda_I$. ($b$) Temperature and chemical heat release rate. (c,d) Enstrophy transport budget at $-0.2 < y_I < 1.25$ and $0 < y_I < 0.8$, respectively.

Conditional statistics in the local coordinates y_I are analysed using the procedure in [12], under the assumption that the normal direction to the interface envelops is contained within each two-dimensional spanwise section. The conditional average of a flow variable ϕ with respect to a certain distance y_I from the TNTI is denoted as $[\phi]_I(y_I)$. The positive direction of y_I indicates the direction towards the turbulent region, while the negative values correspond to the irrotational flow. Figure 6(a) shows the conditional average of enstrophy and its derivative with respect to the local coordinates. The thickness of the TNTI layer, δ_{TNTI}, is determined at the distance that corresponds to 30% of the maximum peak value of enstrophy derivative, as indicated by the vertical dashed line in grey. The reference length scales are obtained at a distance twice that of the TNTI thickness following [15]. The Taylor micro-scale, λ_I, is expressed as $\lambda_I = ([u_i'^2]_I/[\partial u_i'/\partial x_i]_I^2)^{1/2} = \delta_{99}/14.6$, and a Kolmogorov scale η_I, is expressed as $\eta_I = \nu^{3/4}[\epsilon]_I^{-1/4} = \delta_{99}/92.4$. The coordinate y_I is normalised by the Taylor micro-scale λ_I, so $y_I = 1$ represents a distance of one λ_I normal to the TNTI inside the turbulent flow region. It is found that the local mesh resolution at the TNTI is below the local Kolmogorov scale, with $\Delta x/\eta_I = 0.53$, $\Delta y/\eta_I = 0.59$ and $\Delta y/\eta_I = 0.32$, based on the local resolution (Δx, Δy, Δz) taken at a wall-normal distance of $y^* = 7.5$.

Figure 6(b)s shows a sudden transition of temperature and chemical heat release rate inside the TNTI, with the chemical heat release rate reaching a plateau at $y_I \approx 0.7$. The enstrophy transport budget calculated in local coordinates y_I is presented in Fig. 6(c,d), indicating classical contribution from incompressible terms, as well as significant magnitudes of baroclinic torque and thermal dilation inside the TNTI. In the range $0 < y_I < 0.41$, enstrophy generation is primarily due to viscous diffusion, with the magnitude of diffusion term Ω_V exceeding the vortex stretching term Ω_{II}, suggesting the presence of a viscous superlayer with a thickness of $\delta_{VSL} \approx 0.41\lambda_I$. In the range $y^* > 0.41$, the stretching term Ω_{II} undergoes rapid growth as it enters the turbulent region, accompanied by a notable increase of the baroclinic torque generation, represented by term Ω_{IV}. Between $0.5 < y_I < 0.55$, the magnitude of the baroclinic torque generation (red) is approximately 30% of the magnitude of the vortex stretching generation (black dashed line), as depicted in Fig. 6(d). As y^* increases beyond 0.8, the rate of increase of Ω_{II} accelerates, and the relative contribution from Ω_{IV} diminishes to less than 10% of Ω_{II}. The term Ω_{III} associated with the thermal dilation (blue) tunes in at around $y^* > 0.6$, but its relative contribution remains minor in comparison to that of Ω_{II}.

5 Local Influence of Chemical Heat Release on the Baroclinic Torque Generation

In reacting mixing layers, the contribution from baroclinic torque generation to entrainment was found to increase with the level of heat release [8]. In the current reacting boundary layer, the flame surface region, which exhibits significant chemical heat release, coincides with the TNTI, and the local influence of chemical heat release on baroclinic torque generation may be particularly significant. This local influence is examined in the range $0.5 < y_I < 0.55$ where the relative contribution of Ω_{IV} is at its peak. Our initial approach is to compute the jPDF of the local heat release rate $\dot{\omega}_T$ and the term Ω_{IV} within that distance range. However, as shown in Fig. 7, a visually symmetric distribution along the axis $\Omega_{IV} = 0$ is obtained, indicating that the two variables are not correlated. At the flame surface with a given level of heat release, both positive and negative variations of Ω_{IV} can coexist.

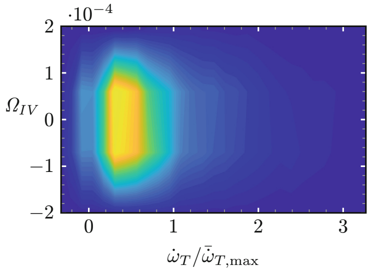

Fig. 7. jPDF of local heat release rate $\dot{\omega}_T$ and local baroclinic torque generation term Ω_{IV} in the range $0.5 < y_I < 0.55$.

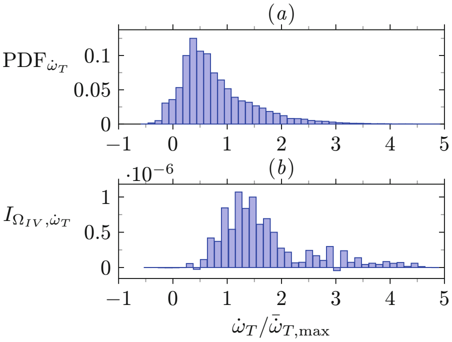

Fig. 8. (*a*) PDF of chemical heat release rate in $0.5 < y_I < 0.55$. (*b*) Integrand $I_{\Omega_{IV},\dot{\omega}_T}$ representing the enstrophy budget from baroclinic torque at each heat release level in $0.5 < y_I < 0.55$. The chemical heat rate is normalised with $\bar{\dot{\omega}}_{T,\max} = 1.53 \times 10^8$ J/m^3/s.

We further assess the budget of Ω_{IV} at various levels of chemical heat release. The cumulative baroclinic torque variation in the range $y_{I,\min} < y_I < y_{I,\max}$ can be represented as $\Omega_{IV,y_I\in[y_{I,\min},y_{I,\max}]}$. This quantity can be expressed as follows:

$$\Omega_{IV,y_I\in[y_{I,\min},y_{I,\max}]} = \int_{y_{I,\min}}^{y_{I,\max}} I_{\Omega_{IV},y_I} dy_I = \int_{\dot{\omega}_{T,\min}}^{\dot{\omega}_{T,\max}} I_{\Omega_{IV},\dot{\omega}_T} d\dot{\omega}_T, \qquad (2)$$

where I_{Ω_{IV},y_I} and $I_{\Omega_{IV},\dot{\omega}_T}$ denote the integrand of Ω_{IV} at each y_I and at each level of $\dot{\omega}_T$, respectively. To calculate the integrand I_{Ω_{IV},y_I}, in practice, a one-dimensional uniform grid is used to discretise $[y_{I,\min}, y_{I,\max}]$ into N intervals $[y_{I,n} - \delta/2, y_{I,n} + \delta/2]$, where $\delta y_I = (y_{I,\max} - y_{I,\min})/N$ is the distance between two grid points and $n = 1, \ldots, N$. The integrand at $y_{I,n}$ is expressed as $I_{\Omega_{IV},y_{I,n}} = \sum_{y_I\in[y_{I,n}-\delta/2,y_{I,n}+\delta/2]} \Omega_{IV,y_I}$, corresponding to the sum of baroclinic torque contribution from all the grids points whose local coordinates y_I fall inside the interval $[y_{I,n} - \delta/2, y_{I,n} + \delta/2]$. The integrand $I_{\Omega_{IV},\dot{\omega}_T}$ is calculated in the same manner, representing the contribution from grid points at the heat release rate level $\dot{\omega}_T$. The distribution of $I_{\Omega_{IV},\dot{\omega}_T}$ is depicted in Fig. 8(*b*). For reference, the probability density function (PDF) of $\dot{\omega}_T$ is shown in Fig. 8(*a*).

The PDF is centered around $\bar{\dot{\omega}}_{T,\max} = 0.5$, extending to the upper limit around $\bar{\dot{\omega}}_{T,\max} = 5$, but also includes local heat release rate of zero and slightly negative values around $\bar{\dot{\omega}}_{T,\max} = -0.5$, corresponding to local non-reacting flow and endothermic reactions. A mismatch is observed between the distribution of $I_{\Omega_{IV},\dot{\omega}_T}$ and the PDF of heat release rate. The distribution of the integrand is centered around $\bar{\dot{\omega}}_{T,\max} = 1.3$, which indicates a significant net generation of baroclinic torque corresponding to local regions of relatively strong heat release. For $\bar{\dot{\omega}}_{T,\max} < 0.5$, the integrand nearly vanishes, suggesting little generation of baroclinic torque in regions without chemical reaction or with endothermic reactions. Note that the presence of local endothermic reactions is possible due to the detailed chemistry scheme employed.

6 Conclusion

Enstrophy generation is investigated in a turbulent boundary layer with hydrogen combustion, which exhibits an intense shear region near the wall and a spatially-separated flame surface region located close to the TNTI at the outer edge. The enstrophy budgets in the outer layer are quantified by employing a conditional average in the normal directions relative to the TNTI. The effect of baroclinic torque emerges at around 0.5–0.55 Taylor micro-scale distances from the TNTI. The enstrophy budget due to baroclinic torque accounts for approximately 30% of the budget associated with vortex stretching within this distance range, before vortex stretching becomes the predominant mechanism for enstrophy generation as one moves further from the TNTI into the turbulent flow region. Given the proximity of the flame surface to the TNTI, we examine the local relationship between the chemical heat release rate and the enstrophy variations resulting from baroclinic torque. It is found there is no local correlation between these variables; however, the enstrophy budget is biased towards the net production of baroclinic vorticity in local regions with a sufficiently high chemical heat release rate. Theses results provide new evidence supporting previous studies that identified little contribution from baroclinic generation in non-reacting compressible shear layers [7] and boundary layers [14], but a significant contribution in compressible mixing layers with chemical heat release [8]. Further analysis will focus on the species transport in the vicinity of the TNTI using the current database.

Acknowledgements. The authors express their gratitude to Xinliang LI for providing the OpenCFD-Comb code. The work is supported by the National Natural Science of China (grant nos 12302286, 12388101). C.-H. Wang is supported by the Shuimu postdoc fellowship from Tsinghua University.

References

1. Bobbitt, B., Lapointe, S., Blanquart, G.: Vorticity transformation in high Karlovitz number premixed flames. Phys. Fluids **28**(1) (2016)
2. Borrell, G., Jiménez, J.: Properties of the turbulent/non-turbulent interface in boundary layers. J. Fluid Mech. **801**, 554–596 (2016)
3. Chakraborty, N.: Statistics of vorticity alignment with local strain rates in turbulent premixed flames. Eur. J. Mech.-B/Fluids **46**, 201–220 (2014)
4. da Silva, C.B., Hunt, J.C.R., Eames, I., Westerweel, J.: Interfacial layers between regions of different turbulence intensity. Ann. Rev. Fluid Mech. **46**, 567–590 (2014)
5. Fu, Y., Yu, C., Yan, Z., Li, X.: DNS analysis of the effects of combustion on turbulence in a supersonic H_2/air jet flow. Aerospace Sci. Technol. **93**, 105362 (2019)
6. Gauding, M., Bode, M., Denker, D., Brahami, Y., Danaila, L., Varea, E.: On the combined effect of internal and external intermittency in turbulent non-premixed jet flames. Proc. Combust. Inst. **38**(2), 2767–2774 (2021)
7. Jahanbakhshi, R., Madnia, C.K.: Entrainment in a compressible turbulent shear layer. J. Fluid Mech. **797**, 564–603 (2016)
8. Jahanbakhshi, R., Madnia, C.K.: The effect of heat release on the entrainment in a turbulent mixing layer. J. Fluid Mech. **844**, 92–126 (2018)
9. Jahanbakhshi, R., Madnia, C.K.: Scalar transport near the turbulent/non-turbulent interface in reacting compressible mixing layers. In: Livescu, D., Nouri, A.G., Battaglia, F., Givi, P. (eds.) Modeling and Simulation of Turbulent Mixing and Reaction. HMT, pp. 25–46. Springer, Singapore (2020). https://doi.org/10.1007/978-981-15-2643-5_2
10. Kazbekov, A., Kumashiro, K., Steinberg, A.: Enstrophy transport in swirl combustion. J. Fluid Mech. **876**, 715–732 (2019)
11. Watanabe, T., Naito, T., Sakai, Y., Nagata, K., Ito, Y.: Mixing and chemical reaction at high Schmidt number near turbulent/nonturbulent interface in planar liquid jet. Phys. Fluids **27**(3) (2015)
12. Watanabe, T., Sakai, Y., Nagata, K., Ito, Y., Hayase, T.: Reactive scalar field near the turbulent/non-turbulent interface in a planar jet with a second-order chemical reaction. Phys. Fluids **26**(10) (2014)
13. Yan, Z., Fu, Y., Wang, L., Yu, C., Li, X.: Effect of chemical reaction on mixing transition and turbulent statistics of cylindrical Richtmyer-Meshkov instability. J. Fluid Mech. **941**, A55 (2022)
14. Zhang, X., Watanabe, T., Nagata, K.: Turbulent/nonturbulent interfaces in high-resolution direct numerical simulation of temporally evolving compressible turbulent boundary layers. Phys. Rev. Fluids **3**(9), 094605 (2018)
15. Zhang, X., Watanabe, T., Nagata, K.: Reynolds number dependence of the turbulent/non-turbulent interface in temporally developing turbulent boundary layers. J. Fluid Mech. **964**, A8 (2023)
16. Wang, C., Xu, C.: Direct numerical simulation of a supersonic turbulent boundary layer with hydrogen combustion. J. Fluid Mech. **998**, A1 (2024)

On the Correlation Between Large-Scale Structures in the Vicinity of Turbulent/Non-turbulent Interface and Wall Pressure Within the Turbulent Boundary Layer

Langsheng Chen and Qingqing Ye(✉)

Key Laboratory of Fluid Power and Mechatronic Systems, Department of Mechanics,
Zhejiang University, Hangzhou 310027, China
qingqing_ye@zju.edu.cn

Abstract. The present work investigates the relation between large-scale coherent structures in the vicinity of turbulent/non-turbulent interface and corresponding pressure fluctuations within the turbulent boundary layer (TBL) close to the trailing edge of the NACA0012 airfoil. The planar particle image velocimetry (PIV) measurements were conducted to capture the instantaneous velocity fields, with simultaneous wall-pressure fluctuation measurement obtained by miniature transducers. Based on the identifications of high amplitude pressure peaks (HAPPs) in the pressure signal, the corresponding simultaneous measured velocity fields are conditionally averaged, revealing the dominance of high-speed large-scale motions (LSMs). The simultaneously measured pressure fluctuations are conditionally extracted based on the occurrence of low- and high-speed LSMs. Results show that high-speed LSMs induce high-energy positive pressure fluctuations, especially when located upstream of the reference wall pressure transducer. The correlation analysis between various scale velocities acquired by empirical modal decomposition (EMD) and the reference pressure signal is conducted. It is demonstrated that upstream high-speed motions with sweeps accompanied by downstream low-speed motions with ejections are responsible for the positive pressure fluctuations, while the negative pressure fluctuations are attributed to the adverse arrangement. It is also observed that the sourced coherent structures of pressure fluctuations can expand outside the TBL, with significant momentum exchange across the turbulent/non-turbulent interface (TNTI).

Keywords: Turbulent Boundary Layer · Coherent Structures · Wall Pressure Fluctuations · Velocity – Pressure Correlation

1 Introduction

The wall-pressure fluctuations in the turbulent boundary layer (TBL) play a key role in noise generation and structure vibrations (Seongkyu Lee et al. 2021). Especially for a trailing edge turbulent boundary layer, the scattering of wall pressure fluctuation at the

J. Wang and I. Marusic (Eds.): IUTAM-TNTI 2024, IUTAM Bookseries 45, pp. 153–163, 2025.
https://doi.org/10.1007/978-3-031-78151-3_11

trailing edge due to sudden changes in boundary conditions causes the prominent turbulent boundary layer trailing edge noise (Brooks et al. 1989). Amiet (1976) considered Schwartzschild's solution and simplified the scattering problem of the trailing edge as a semi-infinite flat plate to establish the classical model to predict the trailing edge noise, indicating the wall pressure yields a positive correlation with noise.

For the incompressible Navier-Stokes equation, the velocity gradient introduced by the coherent structures is the major contributor to the generation of pressure fluctuations. Besides the near-wall small-scale motions, recent studies indicate that coherent structures of very-large- and large-scale motions (VLSMs and LSMs) contribute significantly to the wall pressure fluctuations. For the zeros pressure gradient TBL, Ghaemi and Scarano (2013) use the methods of PIV-based pressure reconstruction and conditional averaging (Antonia 1981) to link the positive and negative high amplitude pressure peaks (HAPPs) to the coherent structures like shear layer between high- and low-speed LSMs, and spanwise and quasi-streamwise vortices, respectively. However, the error propagating from velocity into the pressure field limits the precision of the pressure detected. Naka et al. (2015) conducted a spatial-temporal correlation analysis between velocity and pressure based on simultaneous stereo-PIV and pressure fluctuation measurement, considering the Taylor hypothesis. They conclude that positive pressure fluctuations are responsible for large sweeping motions appearing upstream, while negative ones correspond to large ejection upstream. Gibeau and Ghaemi (2021) divided the wall pressure into various scales and conducted a correlation analysis of the simultaneously measured velocity. They found that high- and low-speed VLSMs cause positive and negative pressure fluctuations, respectively. The higher-frequency pressure fluctuation emerging in the signal is associated primarily with hairpin packets. Not only do LSMs dominate inside the TBL, but they also facilitate momentum exchange between the non-turbulent free-stream and the near-wall turbulent flow, crossing the turbulent/non-turbulent interface (TNTI). Long et al. (2022) demonstrated that the high-speed LSMs could enhance the engulfment and nibbling effects through sweeps and distorting the TNTI, thereby modifying flow structures inside the TBL. Meanwhile, the high-speed LSMs can lower the height of TNTI (Jin Lee et al. 2017). Therefore, flow structures in the vicinity of the TNTI or even outside the TBL also influence the wall pressure fluctuation due to the existence of LSMs, which requires detailed explanation and analysis.

With multiple investigations about the relationship between coherent structures and wall pressure in zero pressure gradient TBL, limited investigation has been conducted on TBL with adverse pressure gradient, which is the main source of airfoil trailing edge noise. Therefore, the present paper proposes a method of conditional extraction of pressure fluctuations based on the identification of the large-scale coherent structures in the vicinity of TNTI, which satisfies the specific predetermined spatial distribution.

2 Experimental Set-Up

The experiments were conducted in the anechoic wind tunnel of the Institute of Fluids Engineering at Zhejiang University. The test section of the wind tunnel has a cross-sectional area of $0.4 \times 0.5\ \mathrm{m}^2$ with a turbulence intensity of less than 0.5% and a maximum operation speed of 60 m/s. The NACA0012 airfoil with a chord of 200 mm and spanwise length of 400 mm was installed in the middle plane of the test section as shown in Fig. 1 (a). The experiments were performed at the free-stream velocity of $u_\infty = 10$ m/s, corresponding Reynolds number based on the chord ($Re_c = u_\infty c/v$) equal to 1.35×10^5. The x, y, and z axes of the coordinate system correspond to the streamwise, wall-normal, and spanwise directions, respectively, with the origin located at the middle span of the trailing edge (Fig. 1 (a) and (c)).

The two-dimensional velocity fields of the larger streamwise and wall-normal domain were captured by planar PIV in the $x - y$ cross-plane. A high-speed CMOS camera (phantom VEO E-340L, 2560 × 1600 pixels, 10 μm/pixel) equipped with a Nikkor 105 mm prime objective was used to capture the particle images. The flow was seeded with water-glycol droplets of approximately 1 μm diameter, with illumination provided by a high-speed laser (Nd: YLF, 527 nm Beamtech Vlite-Hi-527-50K, 2 × 50 mJ per pulse @ 1 kHz). The aperture was set as $f_\# = 5.6$. The sampling frequency of $fs = 10$ kHz was obtained by cropping the sensor into 512 × 480 pixels. Images are acquired throughout 1 s with an ensemble size of 10 000. The field of view (FOV) is expanded from $x = -39.5- -17.8$ mm (-19.8% c ~ -8.9% c), with a size of 21.7×19.5 mm^2 (Fig. 1 (b)). The digital image resolution is 23.62 pixels/mm. The velocity fields are calculated with sliding-averaged correlation with 3 sliding images in DaVis 10, with a final window size of 16 × 16 pixels and an overlap of 75%, resulting in a vector pitch of 0.17 mm.

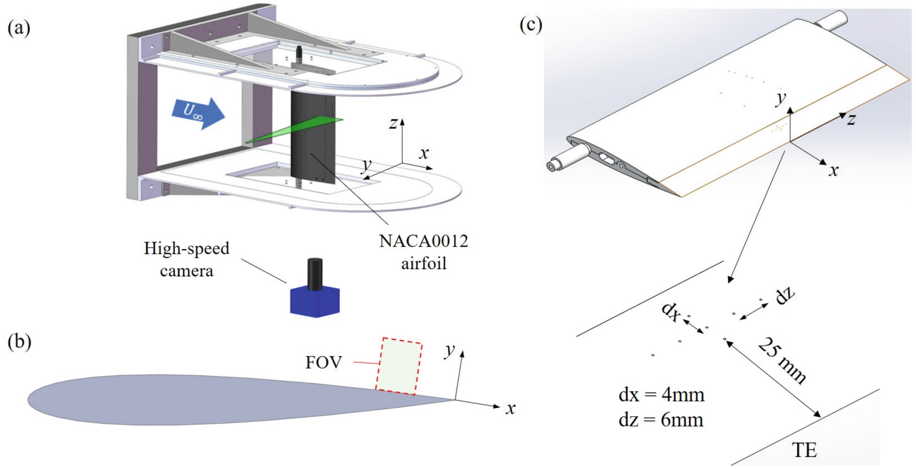

Fig. 1. Conceptual sketch of simultaneous measurement of PIV and wall pressure. (a) installation of airfoil and set-up for PIV, (b) FOV for planar PIV, and (c) the distributions of seven wall pressure transducers.

Wall pressure fluctuation signals were simultaneously sampled by 7 miniature Knowles FG-23329-P07 transducers. Three of the transducers are flash-mounted at x = –25, –29, and –33 mm (–16.5% c, –14.5% c, and –12.5% c) along the mid-span (z = 0) of the airfoil. The other four are flash-mounted at x = –14.5% c with a spanwise shit of –12, –6, 6, and 12 mm, the detailed distributions of all seven transducers are illustrated in Fig. 1 (c). The data were acquired using a National Instrument PXle-4499, with a sampling frequency of 40 kHz and an acquisition time of 10 s.

3 Results

3.1 High Amplitude Pressure Peaks

Although the HAPPs occur infrequently over time, they contribute to over half of the overall disturbance energy of the wall pressure fluctuations (Karangelen et al. 1993). Conditional averaging of the simultaneous flow fields based on HAPPs helps detect the coherent structures responsible for them. The time-series of wall pressure fluctuation (p_f) signal simultaneously measured with PIV are shown in Fig. 2. The threshold for detecting HAPPs is two times the root mean square of the wall pressure fluctuations (p_{rms}) as suggested by Ghaemi and Scarano (2013). The positive and negative HAPPs are marked with red circle and blue asterisk in Fig. 2, respectively, performing low-frequency occurrences and significant deviation from zeros.

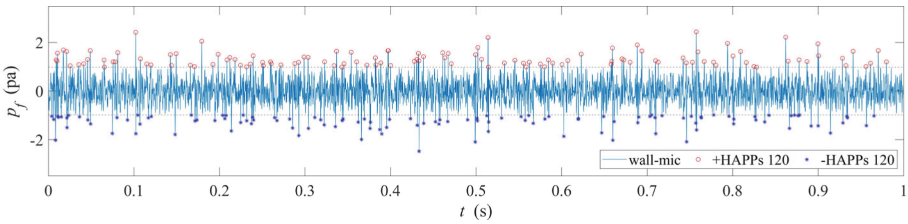

Fig. 2. HAPPs detected from pressure fluctuation signal measured simultaneously with PIV.

Based on the detected time instants when HAPPs occur, the corresponding coherent structures can be acquired through conditional averaging of these velocity fields, with the results shown in Fig. 3. A high-speed LSM emerges on top of the wall pressure transducer for both positive and negative HAPPs. This indicates that high-speed LSMs are more responsible for the HAPPs, consistent with the results of Naka and Osawa (2022). For the positive HAPPs, the high-speed LSM arises upstream of the reference transducer and attaches to the wall, resembling the attached eddies. Whereas for the negative HAPPs, the corresponding LSM manifests downstream, detaching from the wall with a large inclination angle with respect to the streamwise direction.

3.2 Conditional Extraction of Wall Pressure Based on Coherent Structures

Regarding the high- and low-speed LSMs convecting across a reference wall pressure transducer, four conditions arise, including LSMs located at the upstream, center, and downstream of the reference point, with additional consideration for detaching. To determine these conditions for the specific instants, the LSMs should be detected first. The LSMs are extracted based on detecting clusters of streamwise velocity fluctuation u (Hwang and Sung 2018). Setting the length limitation of the cluster of $L_{\text{th}} \geq 3\delta^*$ (δ^*

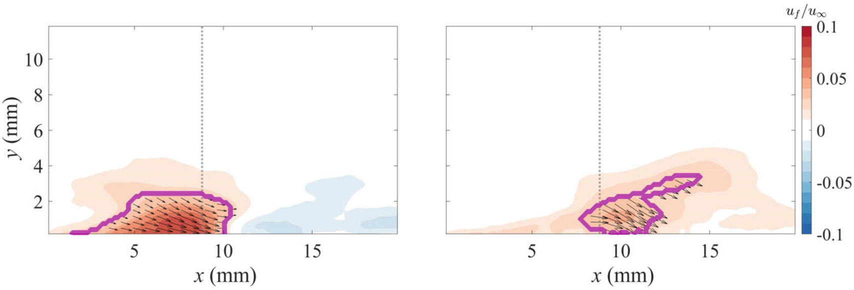

Fig. 3. Coherent structures of conditional averaging based on (a) positive HAPPs for planar PIV, (b) negative HAPPs for planar PIV. The gray dash line in (a) and (b) refer to the location of the reference wall pressure transducer.

= 1.46 mm, is the displacement thickness), and a velocity limitation of $|u_{\mathrm{th}}| > 0.1u_\infty$, the low- and high-speed LSMs are detected. LSMs detection is performed over 10 000 planar PIV instantaneous fields. The instances that satisfy the four conditions for both LSMs are averaged, with the resulting conditional averaged flow fields depicted in Fig. 4. In addition to illustrating the spatial distributions of LSMs, Fig. 4 also demonstrates that high-speed LSMs exhibit a sweep, while low-speed LSMs correspond to ejection. These phenomena arise from the downward and upward motions induced by the quasi-streamwise vortex (QSV) between low- and high-speed LSMs (Marusic et al., 2010).

The pressure fluctuations corresponding to the four conditions of the flow field are conditionally extracted from the 1-s simultaneous wall pressure signal. The averaged value ($<p>$) and root mean square (p_{rms}) of pressure fluctuation, along with the detected number (num) are summarized in Table 1. All conditions have similar detected numbers for high- and low-speed LSMs. High-speed LSMs exhibit positive averaged pressure fluctuations, while low-speed LSMs correspond to the negative (only expected for the downstream condition of low-speed LSMs, with small positive pressure fluctuation). Moreover, when the LSMs are upstream of the reference transducer, the pressure fluctuations deviate maximumly from zero, indicating high-energy disturbance. These results are consistent with the findings of the correlation analysis between pressure and velocity in TBL conducted by Gibeau and Ghaemi (2021) and Naka et al. (2015). Due to the convecting direction, the LSMs for detaching conditions emerge upstream of the reference transducer (Fig. 4 (g) and (h)). The pressure fluctuations for both LSMs are greatly weaker than the attaching upstream cases. The high-speed LSMs exhibit larger p_{rms}, indicating higher energy content of pressure fluctuations compared to the low-speed ones.

The probability density function (PDF) of pressure fluctuations of four conditions for both LSMs are shown in Fig. 5. The PDF curves of high-speed LSMs (Fig. 5 (a)) exhibit a much lower peak and wider span compared to the low-speed LSMs (Fig. 5 (b)), suggesting higher occurrences of high-energy large pressure fluctuations for high-speed LSMs. For the attached upstream and center conditions, the high-speed LSMs perform a positive deviation from zero, while the low-speed ones correspond to negative ones. For

Table 1. The properties of wall pressure fluctuation extracted for four conditions of high- and low-speed LSMs.

	parameter	upstream	center	downstream	detached
high-speed LSMs	$< p >$	+0.19	+0.16	+0.03	+0.01
	p_{rms}	0.63	0.55	0.53	0.52
	num	574	296	1250	499
low-speed LSMs	$< p >$	–0.13	–0.09	+0.01	–0.06
	p_{rms}	0.41	0.43	0.41	0.40
	num	589	281	1124	376

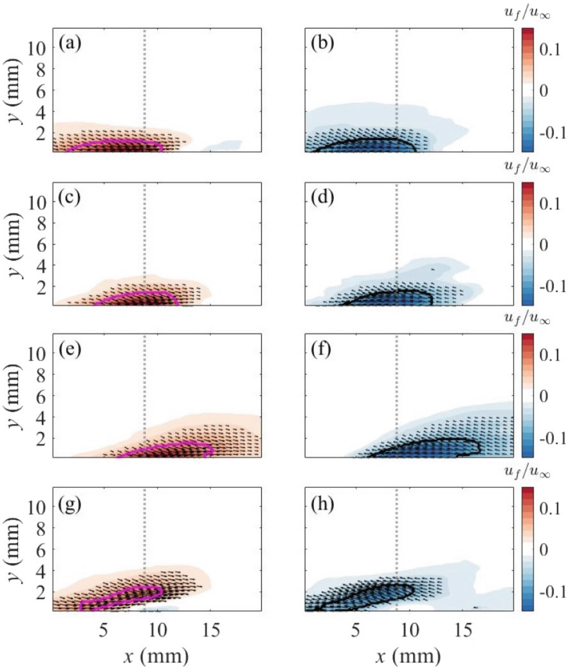

Fig. 4. Conditions for (a, c, e, g) high-speed and (b, d, f, h) low-speed LSMs locate at various positions relative to the reference transducer. Four conditions represent LSMs located at (a, b) upstream, (c, d) center, and (e, f) downstream. (g, h) refer to the detaching cases.

upstream condition, the high-speed LSMs perform high content at large positive pressure fluctuation (red dashed line in Fig. 5 (a)), while the low-speed LSMs demonstrate significant negative pressure fluctuations (red solid line in Fig. 5 (b)).

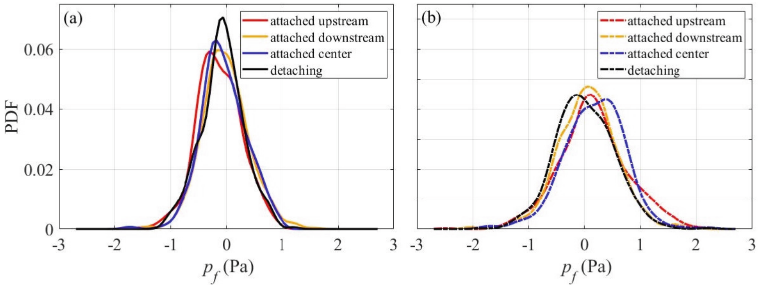

Fig. 5. PDF of pressure fluctuations of each condition for (a) high-speed and (b) low-speed LSMs, respectively.

3.3 Multi-Scale Analysis of Pressure and Velocity Correlations

Huang et al. (1998) first proposed the empirical mode decomposition (EMD) to process the nonlinear one-dimensional signal in a physically meaningful manner. The one-dimensional signal can be decomposed into intrinsic mode functions (IMFs), extracting various inherent spatial or temporal scales from the original data. For the temporal signal at each PIV grid node, the streamwise and wall-normal velocity fluctuations are processed with one-dimensional EMD and decomposed into 10 IMFs. To determine the scale of the raw velocity and IMFs, the streamwise premultiplied power spectrum density (PSD) is calculated, with results shown in Fig. 6. The premultiplied PSD of raw streamwise velocity peaks at approximately ${\lambda_x}^+ = 1000$ and $y^+ < 20$, with good agreement of the first region corresponding to near-wall streaks in previous study by Hutchins and Marusic (2007). Although expanding to the interface of TBL, the second and third regions, corresponding to LSMs and VLSMs respectively, are not identified in the premultiplied spectrum. For the IMFs, the peaks of premultiplied PSD shift to larger (${\lambda_x}^+ = 300$, 600, 900, 3000, and 4600) characteristic scale from IMF 1 to IMF 5 (Fig. 6 (b) – (f)), with the second region related to LSMs detected in the large-scale IMFs 2–4 (Fig. 6 (c) – (e)). However, VLSMs are not identified due to the low Reynolds number ($Re_\tau = 350$).

To assess how the coherent structures with various scales contribute to the wall pressure, the correlation between the velocity of various IMFs and wall pressure can be estimated following Gibeau and Ghaemi (2021):

$$R_{pu_i}(x, y) = \overline{\frac{1}{\rho u_\infty^3} p_f(t) u_i(t, x, y)} \tag{1}$$

where $u_i = u$ or v, denoting the streamwise and wall-normal components measured by PIV and $p_f(t)$ is the simultaneously measured pressure fluctuation. To consider the sourced coherent structures to the positive or negative wall pressure fluctuation, respectively, pressure signals with $p_f > 0$ and $p_f < 0$ are separately applied in Eq. (1) for estimating the correlation (Rp^+u_i and Rp^-u_i).

According to Naka et al. (2015) and Gibeau and Ghaemi (2021), Rpu_i can be used to visualize coherent structures. Figure 7 shows the Rp^+u and -Rp^-u corresponding to IMF 1 to IMF 4. Since p_f for estimating Rp^-u has a negative sign, contours of Rp^-u

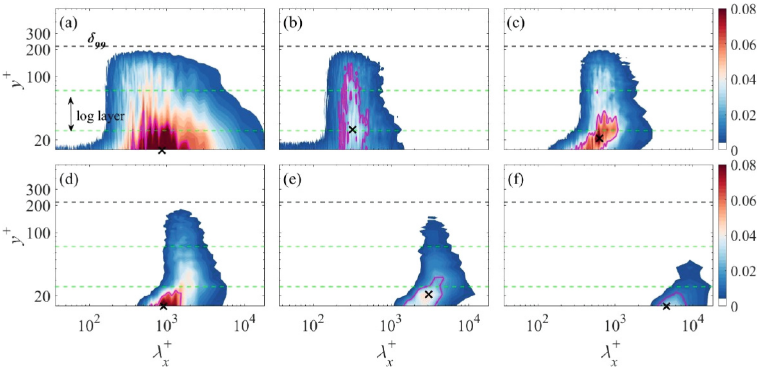

Fig. 6. Streamwise premultiplied PSD Φ_{uu}/λ_x of (a) raw streamwise velocity fluctuations, and (b) – (f) the 1st – 5th streamwise IMFs. The velocity profile selected for calculating the spectrum is above the reference pressure transducer (x = –33 mm). The black dashed line represents the boundary layer thickness, and the range between the two green dashed lines represents the log layer. The magenta contour corresponds to 50% of the maximum Φ_{uu}/λ_x.

are displayed by multiplying –1 to represent the true direction of u. Results exhibit good agreement with the former conditional extraction of pressure fluctuations in Sect. 3.2. For small or middle scale (IMF 1 to IMF 3, $\lambda_x{}^+ = 300, 600, 900$), the positive pressure fluctuations are related to the upstream high-speed motions (Fig. 7 (a) – (c)), while negative ones correspond to upstream positive ones (Fig. 7 (e)–(g)). However, for larger scale (IMF 4, $\lambda_x{}^+ = 3000$), Rp^+u shows a slender high-speed structure, extending across the whole streamwise range below the upper limit of the log layer (Fig. 7 (d)). While large-scale structures are not identified by -Rp^-u, performing chaotic (Fig. 7 (h)). Meanwhile, the high-speed LSMs visualized through -Rp^-u indicate structures responsible for negative pressure fluctuations can expand to the interface between the TBL and non-turbulent free-stream, namely turbulent/non-turbulent interface (TNTI) (Fig. 7 (e) and (f)). They exhibit significant tortuosity, indicating stronger nibbling flux (Long et al. 2022), which in turn causes momentum exchange along the TNTI. On the contrary, the coherent structures responsible for positive pressure perform more regularly, especially for the IMF with larger scales (Fig. 7 (c), (d)).

Similarly, results of Rp^+v and -Rp^-v, corresponding to IMF 1 to IMF 4, are shown in Fig. 8. For the small to middle scale (IMF 1 to IMF 3, $\lambda_x{}^+ = 300, 600, 900$), upstream sweeps combined with downstream ejections are responsible for the positive pressure fluctuations (Fig. 8 (a), (b), and (c)). In contrast, negative pressure fluctuations are associated with the inverse arrangement: upstream ejections and downstream sweeps (Fig. 8 (e), (f), and (g)). The wall-normal motions identified by Rp^+v and -Rp^-v also suggest that the sweeps can be traced from the inside to the outside of TBL for small- to middle-scale coherent structures (Fig. 8 (a), (b), (e), and (f)), indicating the corresponding wall pressure fluctuations accompanied by significant momentum exchanged across the TNTI. Meanwhile, the sweeps extend more broadly compared with the ejections. It attributes that the high-speed LSMs lower the TNTI, resulting in a valley at the interface (Jin Lee et al. 2017). Therefore, outer free-stream flow trending into the valley with substantial engulfment across the interface towards the near wall. For the larger scale

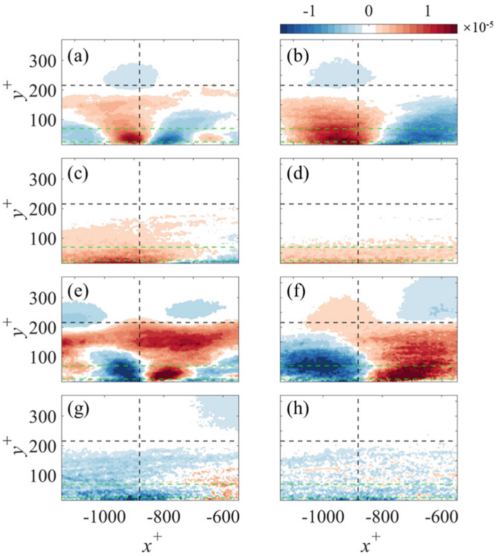

Fig. 7. Correlation between wall pressure and streamwise velocity of various IMFs. Rp^+u: (a)–(d) IMF 1–4. -Rp^-u: (e) - (h) IMF 1 – 4. The vertical black dashed line corresponds to the streamwise location of the reference transducer.

(IMF 4, $\lambda_x{}^+ = 3000$), Rp^+v shows a global sweep along the whole streamwise range of measurement domain in the near-wall region, and no momentum exchange across the TNTI is observed, while the coherent structures corresponding to negative pressure distribute chaotically (Fig. 8 (h)).

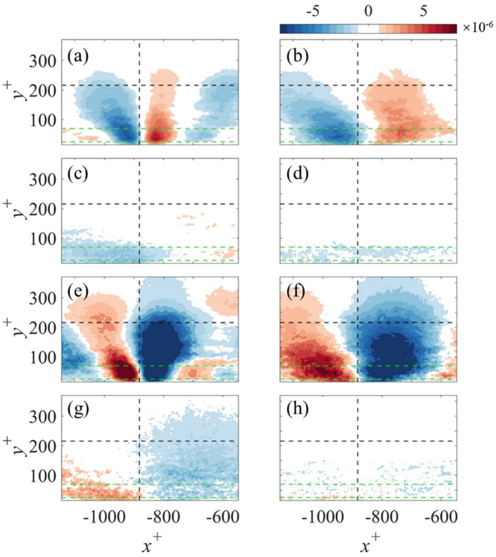

Fig. 8. Correlation between wall pressure and wall-normal velocity of various IMFs. Rp^+v: (a)–(d) IMF 1–4. -Rp^-v: (e) - (h) IMF 1–4. The vertical black dashed line corresponds to the streamwise location of the reference transducer.

4 Conclusion

The relationship between coherent structure and wall pressure fluctuations in the vicinity of TNTI in the turbulent boundary layer under adverse pressure gradient is investigated based on the simultaneous measurement of PIV and wall pressure transducers.

The HAPPs of the pressure signals from the transducer are identified with a detected threshold of $2p_{rms}$. The instantaneous velocity fields corresponding to these HAPPs are conditionally averaged. The results indicate the presence of an attaching upstream high-speed LSM for positive HAPPs and a detaching downstream high-speed LSM for negative HAPPs.

For the simultaneous measurement of planar PIV and wall pressure transducer, the pressure fluctuations are conditionally extracted by considering the relative streamwise location of LSMs to the reference wall pressure transducer. Results show that high-speed LSMs result in positive pressure fluctuations, while low-speed LSMs are responsible for negative ones. Meanwhile, when the LSMs are located upstream of the reference wall pressure transducer, it leads to large pressure fluctuations. Pressure fluctuations caused by high-speed LSMs perform greater p_{rms}, indicating higher energy contents.

Then, the velocity fields are decomposed into various scales with one-dimensional emd, and correlation analysis between velocity with various scales and reference pressure signal is conducted. When considering only positive or negative pressure fluctuations, results of small to middle scales show that upstream high-speed motions with sweeps accompanied by downstream low-speed motions with ejections are responsible for positive pressure fluctuations, whereas the opposite pattern leads to negative pressure fluctuations. The streamwise motions detected by $Rp^{+}u$ and -$Rp^{-}u$ indicate greater tortuosity near the TNTI for high-speed LSMs, corresponding to a stronger nibbling flux along the interface. The wall-normal motions visualized by $Rp^{+}v$ and -$Rp^{-}v$ suggest that small- to mid-scale coherent structures accountable for wall pressure are accompanied by significant momentum exchange across the TNTI, corresponding to the engulfment, especially for the high-speed sweeps. Results of large-scale velocity suggest a slender high-speed motion with global sweeps, emerging near-wall, is attributed to the positive pressure fluctuations. However, no large-scale coherent structure corresponding to negative pressure fluctuations is identified.

Acknowledgments. This research has been supported by the National Key R&D Program of China (Grant No: 2020YFA0405700), National Natural Science Foundation of China (Grant No: 12372280).

References

Amiet, R.K.: Noise due to turbulent flow past a trailing edge. J. Sound Vib. **47**(3), 387–393 (1976)

Antonia, R.: Conditional sampling in turbulence measurement. Annu. Rev. Fluid Mech. **13**(1), 131–156 (1981)

Brooks, T. F., Pope, D.S., Marcolini, M.A.: Airfoil self-noise and prediction (1989)

Ghaemi, S., Scarano, F.: Turbulent structure of high-amplitude pressure peaks within the turbulent boundary layer. J. Fluid Mech. **735**, 381–426 (2013). https://doi.org/10.1017/jfm.2013.501

Gibeau, B., Ghaemi, S.: Low- and mid-frequency wall-pressure sources in a turbulent boundary layer. J. Fluid Mech. **918** (2021). https://doi.org/10.1017/jfm.2021.339

Huang, N.E., Shen, Z., Long, S.R., Wu, M.C., Shih, H.H., Zheng, Q., et al.: The empirical mode decomposition and the Hilbert spectrum for nonlinear and non-stationary time series analysis. Proc. R. Soc. London. Series A Math. Phys. Eng. Sci. **454**(1971), 903–995 (1998)

Hutchins, N., Marusic, I.: Evidence of very long meandering features in the logarithmic region of turbulent boundary layers. J. Fluid Mech. **579**, 1–28 (2007). https://doi.org/10.1017/s0022112006003946

Hwang, J., Sung, H.J.: Wall-attached structures of velocity fluctuations in a turbulent boundary layer. J. Fluid Mech. **856**, 958–983 (2018). https://doi.org/10.1017/jfm.2018.727

Karangelen, C.C., Wilczynski, V., Casarella, M.J.: Large amplitude wall pressure events beneath a turbulent boundary layer (1993)

Lee, J., Sung, H.J., Zaki, T.A.: Signature of large-scale motions on turbulent/non-turbulent interface in boundary layers. J. Fluid Mech. **819**, 165–187 (2017). https://doi.org/10.1017/jfm.2017.170

Lee, S., Ayton, L., Bertagnolio, F., Moreau, S., Chong, T.P., Joseph, P.: Turbulent boundary layer trailing-edge noise: theory, computation, experiment, and application. Prog. Aerosp. Sci. **126**,(2021). https://doi.org/10.1016/j.paerosci.2021.100737

Long, Y., Wang, J., Pan, C.: Universal modulations of large-scale motions on entrainment of turbulent boundary layers. J. Fluid Mech. **941**,(2022). https://doi.org/10.1017/jfm.2022.355

Marusic, I., Mathis, R., Hutchins, N.: Predictive model for wall-bounded turbulent flow. Science **329**(5988), 193–196 (2010)

Naka, Y., Osawa, K.: Pressure Source contribution and near wall flow structures related to high amplitude wall pressure peaks. In: 12th International Symposium on Turbulence and Shear Flow Phenomena, TSFP 2022 (2022)

Naka, Y., Stanislas, M., Foucaut, J.-M., Coudert, S., Laval, J.-P., Obi, S.: Space–time pressure–velocity correlations in a turbulent boundary layer. J. Fluid Mech. **771**, 624–675 (2015). https://doi.org/10.1017/jfm.2015.158

Speed of the Downstream Turbulent Front in Pipe Flow

Baofang Song[1(✉)] and Duo Xu[2,3]

[1] State Key Laboratory for Turbulence and Complex Systems, College of Engineering, Peking University, Beijing 100871, China
`baofang.song@pku.edu.cn`
[2] The State Key Laboratory of Nonlinear Mechanics, Institute of Mechanics, Chinese Academy of Sciences, Beijing 100190, China
[3] School of Engineering Science, University of Chinese Academy of Sciences, Beijing 100049, China

Abstract. The mechanism that determines the propagation speed of the upstream turbulent front of pipe flow turbulence has been proposed recently in our earlier work. It states that the local flow speed at the most upstream tip of the front, where transition to turbulence takes place, determines the global propagation speed of the front. The key was shown to be determining the radial position of the transition point, which can be approximated by the radial position of low-speed streaks at the front tip. In this paper, we will verify whether or not this mechanism also applies to the downstream front. However, the transition is not through near wall streaks, but takes place near the pipe center at the downstream front tip. Through an energy budget analysis in the front region, we managed to determine the position of the transition point, and our results suggest that the mechanism indeed also applies to the downstream front.

Keywords: turbulent front · pipe flow · transition

1 Introduction

Given a localized perturbation, turbulence in pipe flow can form a localized state (with a nearly constant streamwise extension) or expanding state depending on the Reynolds number [1–3]. These forms of turbulence have been the subject of extensive studies in the past decades. In either flow state, turbulence coexists and competes with the neighboring laminar flow, a typical characteristic of subcritical transition in shear flows. An important feature of the flow is the formation and propagation of the laminar-turbulent interface, which is referred to as turbulent front when discussing its global characteristics such as the global propagation speed. As the speed difference between the upstream and downstream fronts determines how fast the turbulent region and consequently the wall friction grows, studying front speed is of both fundamental and application importance. Following the seminal work of [1], many studies have been devoted

J. Wang and I. Marusic (Eds.): IUTAM-TNTI 2024, IUTAM Bookseries 45, pp. 164–173, 2025.
https://doi.org/10.1007/978-3-031-78151-3_12

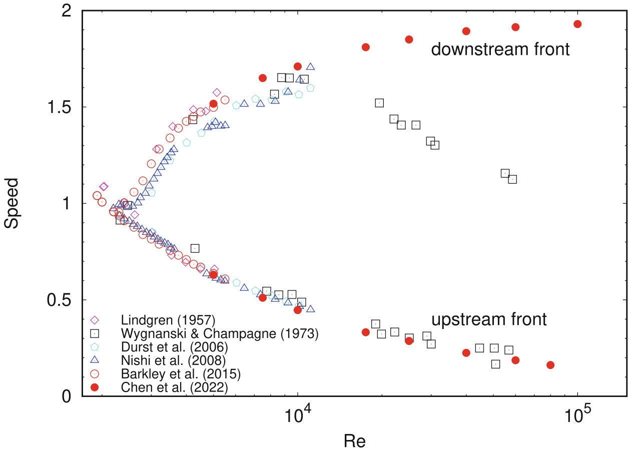

Fig. 1. Front speed of pipe flow turbulence. Some major data sets from the literature are included. The lower branch represents the upstream front and the upper one represents the downstream front. The unit of the speed is the bulk flow speed.

to this matter in the past decades, including experiments [2–7], direct numerical simulations (DNS) [7–12] and theoretical modeling [7, 13–15].

Figure 1 shows the existing measurement data in the literature. It can be seen that different data sets approximately agree with each other for the upstream front. Results showed that this speed decreases monotonically as the Reynolds number increases. Lesser agreement was obtained for the downstream front speed, showing much larger scattering than the data for the upstream front. Particularly, the two data sets at high Reynolds numbers showed distinct trends. The experiments of [3] showed a decreasing trend and the authors concluded that the speed would approach the bulk speed at infinitely large Reynolds number in their experimental setup. In contrast, the direct numerical simulation of [12] up to $Re = 10^5$ gave an increasing trend with the speed seemingly approaching the centerline velocity of the basic laminar flow. In this paper, the Reynolds number is based on pipe diameter D and the bulk flow speed U. Ref [12] argued that the decreasing trend of [3] is attributed to the undeveloped basic laminar flow at high Reynolds numbers in the 500-diameter-long pipe in the experiment. In fact, the Fig. 9 of [3] indeed showed a velocity profile that was far from being fully developed, and showed that the higher the Reynolds number, the less developed the velocity profile. This is in fact a well known fact that the development length of the inlet flow for a pipe is proportional to the Reynolds number, $L \approx 0.06Re$ in unit of pipe diameter. For example, it takes $3000D$ for the parabolic velocity profile to develop at $Re = 5\times10^4$, and the pipe should be further longer for the front speed measurement. The $500D$ pipe of [3] was not sufficient for the Reynolds number they considered, which was up to $Re \approx 6 \times 10^4$. It was proposed that, if the pipe is long enough such that the basic laminar flow is fully developed, the speed of the downstream front would monotonically increase as Re increases, based on the changing trend of the front structure and the transition process as Re increases [12]. However, so far, there has been no laboratory experiment performed in a sufficiently long pipe at comparable Reynolds numbers to finally confirm this point.

These studies either measured the front speed by tracking the front over time or modeled the front as a highly simplified one-dimensional dynamical system which allows theoretical treatment of the front dynamics [7,13–15]. But an explicit relationship between the front speed and Re has not been derived for decades, due to the limited understanding of the transition mechanism at the front and the mechanism determining the front speed.

Recently, Ref. [16] proposed a mechanism for the upstream front speed and derived an explicit relationship between the front speed and Re. The authors showed that the local speed of flow structures on the laminar-turbulent interface changes with the local radial position, i.e. the structures close to the pipe center travel at a higher streamwise speed than those close to the pipe wall. This reflects the dominance of the advection by the local mean flow on the motion of velocity fluctuations. Therefore, the interface is continuously distorted by the shear. Nevertheless, there is certainly a characteristic structure and global propagation speed of the front as a whole. This is attributed to the continuous transition at the tip, i.e., the most upstream point of the upstream front, which generates turbulence and reform the interface against the distortion of the shear. Thus, the authors inferred that the traveling speed of this transition point determines the front speed. They further assumed that this traveling speed is approximately determined by the advection of the local mean flow at the transition point, and approximated the radial position of the transition point by the radial position of the low-speed streaks at the front tip, whose instabilities were considered to be responsible for the transition [6,8,17,18]. Based on these assumptions, the authors measured the wall-distance of the low-speed streaks and found it nearly a constant in the local wall units, and derived an explicit relationship between the front speed and Re, $c_{UF} = 2\sqrt{2}ARe^{-0.5} - A^2Re^{-1}$, which was shown to agree well with DNS measurement by front tracking up to $Re = 8 \times 10^4$ (see Fig. 5 of [16]). The formula only contains a single parameter A, which denotes the wall-distance of the transition point. The good agreement strongly supports the proposed mechanism.

However, the mechanism underlying the downstream front speed and the scaling law with Re still remain to be explained. A fit of the DNS measurement gives $c_{DF} = 1.971 - (Re/1925)^{-0.825}$ [12], however, no physical understanding was given so far. As pointed out by [12], the downstream front is different from the upstream one in that the transition to turbulence takes place near the pipe center, where no near-wall low speed streaks exist. In other words, the transition is likely through a different route other than the well-known one through streak instabilities. Although the transition mechanism cannot be elucidated in this work, we aim to verify if the downstream-front speed is also determined by the local flow speed at the tip of the downstream front.

2 Methods

The methods used for simulating turbulent fronts at high Reynolds numbers were reported and verified in our earlier work [12]. Here, a brief introduction is given for the ease of understanding.

As turbulent region expands at high Reynolds numbers with the front propagating into the laminar region, a long pipe is needed if the whole flow should be simulated. However, DNS of a long pipe at high Reynolds numbers is very expensive. A technique used in Ref. [12] is to track and simulate the front region only in a relatively short pipe, which was achieved by using a frame of reference co-moving with the front and damping out the turbulence sufficiently far from the important region of the front, where transition to turbulence takes place, see Fig. 2. This assumes that turbulence far away does not affect the transition at the front, and the agreement between the measured front speed with the speed measured in a long pipe where the whole flow was simulated verified the technique [12].

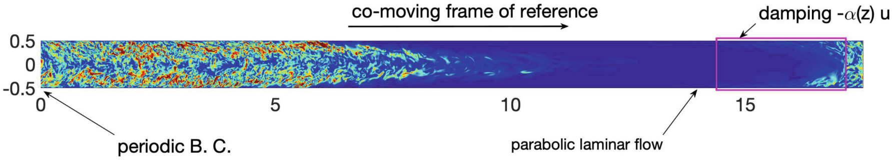

Fig. 2. Schematic of the simulation technique. Periodic boundary condition in the streamwise direction is imposed. The frame co-moves with the front (moving to the right in the figure). A damping term $-\alpha(z)\boldsymbol{u}$ is added to the Navier-Stokes equations to damp out the velocity perturbations $\boldsymbol{u}$ so that a parabolic laminar flow region can be maintained on the downstream side of the front. The damping coefficient $\alpha(z)$ is a function of axial position z and is positive so that the term is purely damping, and it is localized in an axial region marked by the magenta rectangle. A similar plot was shown in [12].

The total pipe length can be selected based on the need. If the whole front region should be simulated, the pipe should be long enough to contain the front, the laminar flow on the downstream, and the turbulent region on the upstream side, connecting the fully developed bulk turbulence and the front, as the case shown in Fig. 2. One can either simulate only the most downstream part of the front by using a much shorter pipe length, which was necessary at high Reynolds numbers for reducing the computation cost. For this study, the pipe length of $L = 17.5D$ is used for $Re = 10000$ and 25000, and the length $L = 5D$ is used for $Re = 40000$, and 10^5. The details of the front speed measurements are summarized in Table 2 and 3 of Ref. [12] and the grid resolution can be found in Table 4 and 5 there also.

3 Results

As proposed by [16], for the upstream front, the key of determining the front speed is to find the radial position of the transition point at the front tip. For this purpose, we will first show the structure of the downstream front. Some aspects of the front structure were already reported in [3] and our earlier work [12,16], but we will still show some of them here for the ease of discussion.

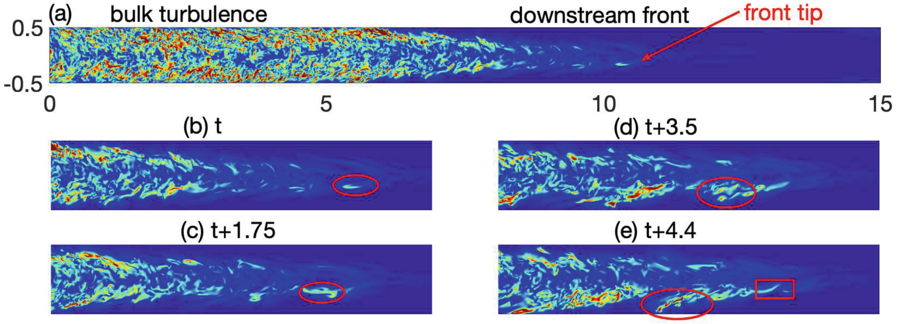

Fig. 3. Structure of the downstream turbulent front in the axial-radial cross-section at $Re = 25000$. The magnitude of the velocity fluctuations is color-coded, with blue showing the low-magnitude region and red showing the high-amplitude region. (a) The flow is from left to right, with the bulk turbulence on the left and the downstream front on the right. Further downstream of the front is the laminar flow region. The front tip refers to the most downstream point of the front where transition takes place, see the arrow. (b-e) Depiction of the transition process at the downstream front in the frame of reference co-moving with the front. The elipse marks a flow structure, which moves toward the pipe wall and intensifies meanwhile. The data is taken from [12].

Figure 3 shows the structure of the downstream turbulent front in the cross-section along the pipe axis. It can be seen that the front region is an arrow-head like structure reaching into the laminar flow on the downstream. By observing the dynamics at the front tip, i.e. the most downstream point of the front, one can find that transition continuously takes place at the front tip. The flow structure is generated at the tip, which is near the pipe center, and strengthens and slows down while moving toward the pipe wall, see the red elipses (the slowing-down is reflected by the shift to the left in the co-moving frame). Meanwhile, new flow structures are generated at the front tip, see the red rectangular. This process has been reported in our earlier work also [12]. We proposed that this continuous transition enables the front to maintain a characteristic shape and global speed as a whole under the continuous distortion by the shear.

Following [16], the front speed should be determined by the local mean flow at the radial position of the transition point. At the upstream front, it was shown that the radial position of the transition point can be approximated by that of the near-wall low-speed streaks. But this approach does not apply to the downstream front because the absence of streaks in the low-shear region near the pipe center. Ref [12] attempted to determine the position of the front tip by performing energy budget analysis but did not discuss about the quantitative relationship between the position of the front tip and the front speed. In the following, we will take this approach of energy budget analysis, see Fig. 4.

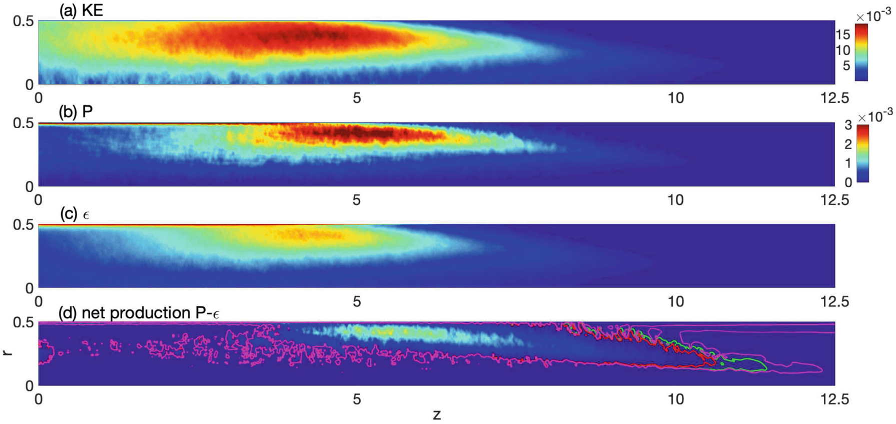

Fig. 4. Energy budget at the downstream front at $Re = 25000$. Panel (a) shows the contours of the turbulent kinetic energy KE, panels (b-d) show the production term P, the dissipation term ϵ, and the net production $P - \epsilon$, respectively. Panels (b-d) share the color scale as shown in (b). Note that only the upper half of the cross-section is shown. In (d), the contour lines with the level 1×10^{-5} (red), 1×10^{-6} (green) and 1×10^{-7} (magenta) are plotted.

Following [10, 12], the production rate P and dissipation rate ϵ of turbulent kinetic energy are defined as

$$P = -\overline{u_i' u_j'} \frac{\partial \overline{u_i}}{\partial x_j}, \qquad \epsilon = \frac{2}{Re} \overline{s_{ij} s_{ij}}, \tag{1}$$

where u denotes velocity, the overbar denotes the average over time and over the azimuthal direction in the co-moving frame of reference, the prime denotes the velocity fluctuation with respect to the average flow $\bar{\boldsymbol{u}}(r, z)$, x_j denotes the spatial coordinates and s_{ij} the fluctuating rate of strain defined as

$$s_{ij} = \frac{1}{2} \left(\frac{\partial u_i'}{\partial x_j} + \frac{\partial u_j'}{\partial x_i} \right). \tag{2}$$

Figure 4 shows the distribution of P, ϵ and their difference, i.e. the net energy production rate $P - \epsilon$, in the cross-section along the pipe axis. It can be seen that the distribution is very different at the front from that in the bulk region. In the bulk region, the two are largest in a very thin layer very close to the pipe wall, whereas in the front region, strong production appears in a much broader radial region, reaching much closer to the pipe center. There is similar distribution in the dissipation, which is significantly shifted toward upstream compared to P. This is reasonable since the kinetic energy should be first generated at the front and then dissipated, thus a time delay is expected, which is reflected in the spatial shift given that flow structures are advected toward the bulk relative to the front tip.

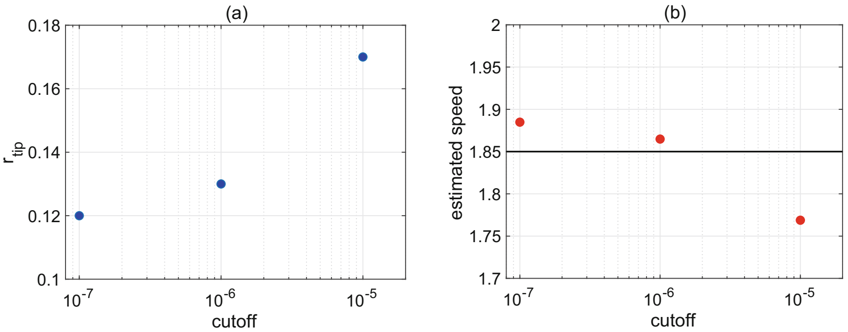

Fig. 5. Panel (a) shows the radial position of the front tip determined using the contour levels shown in Fig. 4(d). Panel (b) shows the front speed estimated by the local flow speed at the respective radial position. Parabolic velocity profile is used to calculate the speed based on the radial position, because the velocity profile at the front tip was shown to be nearly parabolic [12,16].

To determine the position of the front tip, we plot the contour of $P - \epsilon$ in Fig. 4(d). Our key hypothesis is that P should outweigh ϵ in the region where transition to turbulence takes place and, naturally, the contour level of zero should separate the transitioning region and the turbulence-decaying/laminar region at the front tip. Based on this hypothesis, we can approximate the position of the front tip by the position of the nose of the contour line (see the part between $z = 10$ and 12.5 in Fig. 4d) with the contour level of zero. However, in energy budget analysis, the contour of zero or a very small level may be contaminated by numerical noise or other error sources. For example, see the magenta curve with level 1×10^{-7} in Fig. 4(d). The contour line also appears in the near wall region (see the right top corner of this panel where the flow in fact should be laminar), which is due to numerical errors and the non-vanishing fluctuations that have not been completely damped by the damping technique we used in our simulations [12]. In a word, we cannot use a too low contour level to determine the front position, which will be prone to numerical contamination. Larger levels can cleanly separate the transitioning region and the decaying/laminar region, but on the other hand may overestimate the radial position of the front tip because the higher $P - \epsilon$, the farther from the pipe center. For example, see the contour levels of 1×10^{-5} and 1×10^{-6} plotted as red and green contour lines, respectively, in Fig. 4(d). Although being non-zero, they are still two and three orders of magnitude, respectively, smaller than the peak value of $P - \epsilon$ of the front region (about 2×10^{-3}), see the bright region between $z = 5$ and 6 in panel (d).

Figure 5(a) shows the radial position of the front tip for $Re = 25000$ using the three contour levels of $P - \epsilon$ as shown in Fig. 4(d). It can be seen that a higher level gives a larger radial position, which is expected. Panel (b) shows the average flow speed at the radial position by assuming a parabolic velocity profile, which is reasonable as shown by [12,16]. The horizontal line shows the front speed measured by front tracking in DNS. It can be seen that all three estimated speeds are close to the measured front speed, with errors of about a few percent (up to 6%). The contour level 1×10^{-6} gives the closest estimation for this Re (error below 1%), therefore, we use this criterion to a few different Reynolds numbers to estimate the front speed, see the results shown in Fig. 6. The estimated speed agrees well with the DNS measurement for all the Reynolds numbers considered, with errors all below 3%. This good agreement supports our hypothesis that the local flow speed at the transition point of the front tip approximately determines the front speed.

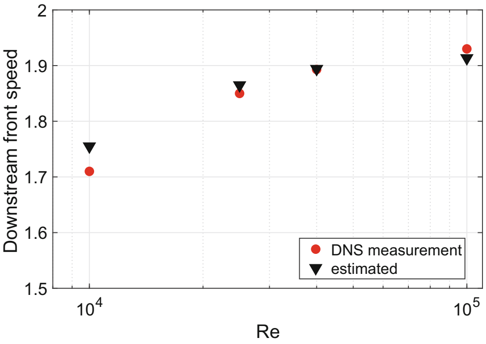

Fig. 6. Comparison between the front speed measured by DNS and the estimated speed using the contour level 1×10^{-6} of $P - \epsilon$. The DNS data is from [12] as also shown in Fig. 1.

4 Conclusion

In this paper, we determined the position of the front by assuming that the production rate and dissipation rate balance at the front tip where transition to turbulence is initiated. With the contour of the net production rate of the kinetic energy, the position of the front tip can be approximately determined. With the radial position of the front tip and nearly parabolic velocity profile, the estimated flow speed at the front tip is very close to the measured front speed by front tracking. This strongly supports the determining mechanism of the global propagation speed of a turbulent front proposed by [16], that is, the local flow speed at the front tip where the transition is initiated, for either the upstream or downstream front.

It can be expected that, as the Reynolds number increases further, the transition point would move toward the pipe center further. This trend would suggest that the front speed would increase monotonically as the Reynolds number increases further. However, future study is needed to explain the scaling law of the front speed with the Reynolds number more quantitatively, and the ideal is to derive an explicit scaling with the Reynolds number based on the transition mechanism. This requires to resolve the transition mechanism at the downstream front tip, where the transition is clearly not through near-wall low-speed streaks.

Acknowledgment. This work is supported by the Opening fund of State Key Laboratory of Nonlinear Mechanics and the National Natural Science Foundation of China (grant numbers 12322209 and 12272264).

References

1. Lindgren, E.R.: The transition process and other phenomena in viscous flow. Ark. Fys. **12**, 1–169 (1957)
2. Lindgren, E.R.: Propagation velocity of turbulent slugs and streaks in transition pipe flow. Phys. Fluids **12**, 418 (1969)
3. Wygnanski, I.J., Champagne, F.H.: On transition in a pipe. Part 1. The origin of puffs and slugs and the flow in a turbulent slug. J. Fluid Mech. **59**, 281–335 (1973)
4. Durst, F., Ünsal, B.: Forced laminar to turbulent transition in pipe flows. J. Fluid Mech. **560**, 449–464 (2006)
5. Nishi, M., Ünsal, B., Durst, F., Biswas, G.: Forced laminar to turbulent transition in pipe flows. J. Fluid Mech. **614**, 425–446 (2008)
6. van Doorne, C.W.H., Westerweel, J.: The flow structure of a puff. Phil. Trans. R. Soc. Lond. A **367**, 489–507 (2008)
7. Barkley, D., Song, B., Mukund, V., Lemoult, G., Avila, M., Hof, B.: The rise of fully turbulent flow. Nature **526**, 550–553 (2015)
8. Duguet, Y., Willis, A.P., Kerswell, R.R.: Slug genesis in cylindrical pipe flow. J. Fluid Mech. **663**, 180–208 (2010)
9. Holzner, M., Song, B., Avila, M., Hof, B.: Lagrangian approach to laminar-turbulent interfaces. J. Fluid Mech. **723**, 140–162 (2013)
10. Song, B., Barkley, D., Hof, B., Avila, M.: Speed and structure of turbulent fronts in pipe flow. J. Fluid Mech. **813**, 1045–1059 (2017)
11. Rinaldi, E., Canton, J., Schlatter, P.: The vanishing of strong turbulent fronts in bent pipes. J. Fluid Mech. **866**, 487–502 (2019)
12. Chen, K., Xu, D., Song, B.: Propagation speed of turbulent fronts in pipe flow at high Reynolds numbers. J. Fluid Mech. **935**, A11 (2022)
13. Barkley, D.: Simplifying the complexity of pipe flow. Phys. Rev. E **84**, 016309 (2011)
14. Barkley, D.: Theoretical perspective on the route to turbulence in a pipe. J. Fluid Mech. **803**, P1 (2016)

15. Wang, M., Goldenfeld, N.: Stochastic model for quasi-one-dimensional transitional turbulence with streamwise shear interactions. Phys. Rev. Lett. **129**, 034501 (2022)
16. Wu, H., Song, B.: Scaling and mechanism of the propagation speed of the upstream turbulent front in pipe flow. J. Fluid Mech. **977**, R4 (2023)
17. Shimizu, M., Kida, S.: A driving mechanism of a turbulent puff in pipe flow. Fluid Dyn. Res. **41**, 045501 (2009)
18. Hof, B., de Lozar, A., Avila, M., Tu, X., Schneider, T.M.: Eliminating turbulence in spatially intermittent flows. Science **327**, 1491–1494 (2010)

Connecting the Temporal Evolution of the Turbulence Interface to the Entrainment and Detrainment in a Turbulent Plane Jet

Yuanliang Xie[1](✉), Koji Nagata[2], and Yi Zhou[1]

[1] School of Energy and Power Engineering, Nanjing University of Science and Technology, Nanjing 210094, China
yizhou@njust.edu.cn
[2] Department of Mechanical Engineering and Science, Kyoto University, Kyoto 615-8540, Japan

Abstract. Direct numerical simulation is performed to investigate the connection between the evolution of the turbulent/non-turbulent interface (TNTI) and the entrainment and detrainment process in a temporally evolving turbulent plane jet with Taylor Reynolds number of about $Re_\lambda \approx 72$. For an accurate calculation of the surface area of the turbulent interface, a novel algorithm is used. On average, the stretching term and the curvature/propagation term counterbalance each other, maintaining a constant surface area of the TNTI. We show that regardless of the entrainment or detrainment process, the stretching term always contributes to the production of surface area. The curvature/propagation term contributes to the destruction of surface area in the entrainment process. In contrast, the curvature/propagation term is related to the production of surface area in the detrainment process.

Keywords: turbulence theory · jets · turbulence simulation

1 Introduction

Free shear turbulence (e.g., jet, wake, mixing layer, and shear free flow) can be segmented into two regions: a turbulent region and a non-turbulent region, separated by a sharp and highly contorted turbulent/non-turbulent interface layer (for the sake of simplicity, hereafter referred to as TNTI) [1]. The growth of free shear turbulence is caused by the turbulent entrainment process of surrounding environment fluid from the non-turbulent region into the turbulent region. In numerous environmental and industrial flows, free shear turbulence is a typical flow type, and accurate prediction and control of its development are of critical importance [2].

The entrainment process on the surface of TNTI causes the TNTI to propagate towards the non-turbulent region and enables the irrotational fluid across

J. Wang and I. Marusic (Eds.): IUTAM-TNTI 2024, IUTAM Bookseries 45, pp. 174–181, 2025.
https://doi.org/10.1007/978-3-031-78151-3_13

the interface layer to obtain the enstrophy. In contrast, the detrainment process refers to the transfer of fluid element from the turbulent region to the non-turbulent region [2]. Generally, the intensity of the entrainment and detrainment process are examined by the local entrainment velocity in the fully developed turbulence [3], namely, $\boldsymbol{V}_n = v_n \boldsymbol{n}$, where $\boldsymbol{n} = \nabla|\boldsymbol{\omega}|/|\nabla|\boldsymbol{\omega}||$ denotes the unit normal vector of the TNTI. The entrainment velocity v_n being positive (negative) represents the detrainment (entrainment) process. The evolution equation of the TNTI surface area has shown that the growth of the TNTI area exhibits some dependency on the turbulent entrainment [4]. However, it is not fully understood why the production/destruction of the TNTI surface area is coupled to the local entrainment and detrainment process. In this paper we investigate the relationship between the evolution of the TNTI and the entrainment and detrainment process.

2 Numerical Details and Simulation Validation

A highly parallelized open source solver 'Incompact3d' [6] with spectral-like resolution [7] is used to directly solve the Navier-Stokes equations (i.e. the continuity and momentum equations) of the incompressible flow to obtain a high-fidelity temporally evolving planar jet database. In the Cartesian coordinate system, a uniformly distributed grid is employed for discretizing the computational domain. Periodic boundary conditions are employed in the streamwise X and spanwise Z directions, and free slip boundary condition is employed in the vertical Y direction. For spatial discretization, the sixth-order central compact finite difference scheme is applied. Concerning the time advancement of unsteady term, a third-order Adams-Bashforth scheme is employed.

Following the previous studies, the initial streamwise mean velocity U_{in} of the turbulent plane jet is given by a hyperbolic tangent function [5]:

$$U_{in}(Y) = \frac{U_J}{2} + \frac{U_J}{2} \tanh\left[\frac{H_J}{4\theta_0}\left(1 - \frac{2|Y|}{H_J}\right)\right], \tag{1}$$

where $U_J = 1$ and $H_J/\theta_0 = 1/35$ with H_J being the width of the nozzle and initial momentum thickness, respectively. The initial mean velocity in the vertical and spanwise directions (i.e. V_{in} and W_{in}) is set to zero.

Table 1. Computational and geometric parameters.

Re_J	θ_0/H_J	L_X	L_Y	L_Z	N_X	N_Y	N_Z	$\Delta T/(H_J/U_J)$
4000	1/35	$8H_J$	$12H_J$	$8H_J$	768	1025	768	0.0015

The DNS of the turbulent plane jet is performed in a computational domain with sizes of $L_X \times L_Y \times L_Z = 8H_J \times 12H_J \times 8H_J$ in three directions, where the corresponding grid numbers are $N_X \times N_Y \times N_Z = 768 \times 1025 \times 768$. The global Reynolds number is set to $Re_J = 4000$. To ensure simulation stability, a time step of $\nabla T/T_{ref} = 0.0015$, where $T_{ref} = H_J/U_J$, is employed in the simulation. The calculation and geometric parameters are summarized in Table 1 as presented above. In order to induce a quick transition to a turbulent state, the perturbation fields in three directions generated by the diffusion method [8] are applied to the initial mean velocity field within the range of $-0.5 \leq Y/H_J \leq 0.5$.

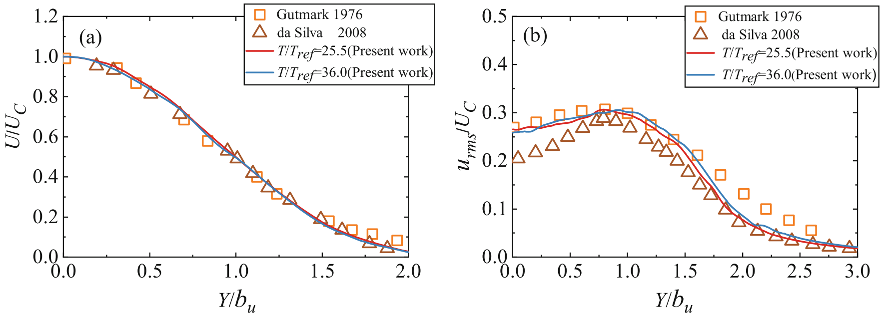

Fig. 1. The vertical distributions of the normalized mean streamwise velocity and streamwise rms velocity.

Figure 1 shows the profiles of normalized mean streamwise velocity and rms of velocity fluctuation along the normal direction at two time steps ($T/T_{ref} =$ 25.5 and 36.0). The accuracy of the turbulent plane jet field can be validated by comparing with previous experimental result [9] and numerical simulation result [5]. It is evident from Fig. 1 that our simulation results are in agreement with the results of previous studies. In this paper, U_C represents the centerline mean velocity and b_U denotes the jet half-width. The normalized spatial resolutions $(\Delta X \Delta Y \Delta Z)^{1/3}/\eta$ at the jet centerline for the two time steps are 1.1η and 0.9η, respectively, where η being the Kolmogorov scale, which can capture the small-scale turbulent motion well.

3 Results and Discussion

3.1 Detection of the TNTI and Surface Area of the TNTI

Following previous study by da Silva and Pereira [5], an isosurface of vorticity threshold $|\boldsymbol{\omega}|_{th}$ is used to detect the location of TNTI. Typically, the vorticity threshold $|\boldsymbol{\omega}|_{th}$ is determined by the dependence of turbulent volume V_T on vorticity magnitude $|\boldsymbol{\omega}|_{th}$. Figure 2(a) shows the profile of turbulent volume percent as a function of vorticity magnitude. There is a clearly defined plateau region within the range $1.0 \times 10^{-5} \leq |\boldsymbol{\omega}|_{th}(t)/|\boldsymbol{\omega}|_{max}(t) \leq 1.0 \times 10^{-3}$, where the turbulent volume fraction remains nearly unchanged with the variation in vorticity magnitude. Here, $|\boldsymbol{\omega}|_{max}(t)$ represents the maximum vorticity magnitude within the turbulent region at the current instantaneous time. This finding means that any value within this interval between $\left[1.0\times10^{-5}, 1.0\times10^{-3}\right]$ can be used to detect the position of TNTI. Hereafter, we choose $|\boldsymbol{\omega}|_{th}(t)/|\boldsymbol{\omega}|_{max}(t) = 1.6\times10^{-4}$ to determine the precise position of the TNTI isosurface. As seen in Fig. 2(b), the white solid line represents the position of the detected TNTI, clearly distinguishing the internal turbulent region from the external irrotational region.

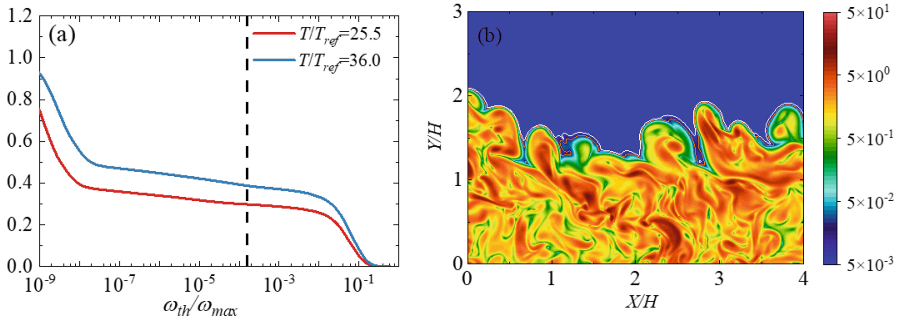

Fig. 2. (a) Volume fraction V_T of the turbulent region as a function of the vorticity threshold $|\boldsymbol{\omega}|_{th}$. (b) Contours of the instantaneous vorticity magnitude $|\boldsymbol{\omega}|$ in a $X-Y$ plane at $T/T_{ref} = 25.5$. The outer edges of the TNTI are included under two different thresholds, that is $|\boldsymbol{\omega}|_{th}(t)/|\boldsymbol{\omega}|_{max}(t) = 1.6\times10^{-4}$ and 1.0×10^{-3} (presented by the white and orange lines, respectively). Only a part of the computational domain is displayed.

A novel method derived by Yurtoglu et al. [10] utilizing grid-based integration has been introduced for the numerical evaluation of surface integrals (i.e. the surface area $A(t)$ and the instantaneous flux $Q(t)$), eliminating the stochastic nature of Monte Carlo methods and the need for problem-specific domain decompositions. The derivation of this method utilizes the divergence theorem and properties of surface normal vectors to transform challenging surface integral into volume integral based on grid data. For any arbitrary integrand function f, the instantaneous flux can be expressed as:

$$Q(t) = \int f(t)\mathrm{d}A(t) = -\sum_{I,J,K}(f)_{I,J,K}\frac{\nabla\boldsymbol{\chi}(|\boldsymbol{\omega}|)_{I,J,K}\cdot\nabla|\boldsymbol{\omega}|_{I,J,K}}{\sqrt{\nabla|\boldsymbol{\omega}|_{I,J,K}\cdot\nabla|\boldsymbol{\omega}|_{I,J,K}}}\Delta X\Delta Y\Delta Z, \tag{2}$$

where

$$\boldsymbol{\chi}(|\boldsymbol{\omega}|) = \begin{cases}1, & |\boldsymbol{\omega}| \geq |\boldsymbol{\omega}|_{th}\\ 0, & |\boldsymbol{\omega}| < |\boldsymbol{\omega}|_{th}\end{cases} \tag{3}$$

represents the occupancy function defined by using the detection threshold $|\boldsymbol{\omega}|_{th}$ of the TNTI. The indices I, J, and K represent the grid nodes along the three directions in the computational coordinate system. The occupancy function $\boldsymbol{\chi}(|\boldsymbol{\omega}|)$ is numerically computed using a fourth-order central finite difference scheme. Take for instance, $(\partial\boldsymbol{\chi}(|\boldsymbol{\omega}|)/\partial x)_{I,J,K} = \boldsymbol{\chi}(|\boldsymbol{\omega}|)_{I-2,J,K} - 8\boldsymbol{\chi}(|\boldsymbol{\omega}|)_{I-1,J,K} + 8\boldsymbol{\chi}(|\boldsymbol{\omega}|)_{I+1,J,K} - \boldsymbol{\chi}(|\boldsymbol{\omega}|)_{I+2,J,K})/12\Delta X$. This method significantly reduces the computational workload by eliminating the need to re-mesh the surface grid. If the integrand function f is equal to 1, the value of the surface integral equals the surface area $A(t)$, namely, $Q(t) = \int f(t)\mathrm{d}A(t) = A(t)$. Further detailed explanations can be referenced in Yurtoglu et al. [10].

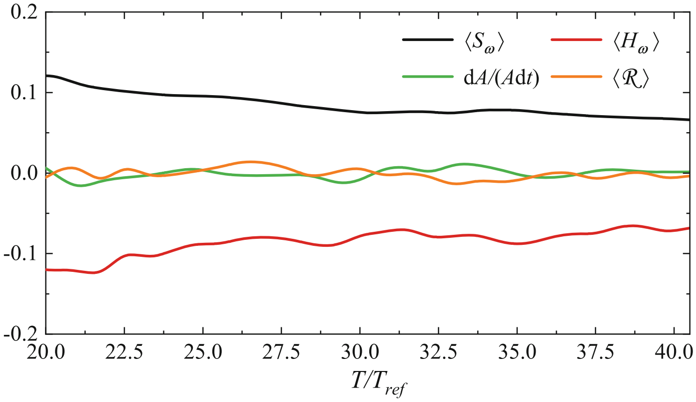

Fig. 3. Time evolution of the mean stretching term $\langle S_\omega \rangle$ and the mean curvature/propagation term $\langle H_\omega \rangle$ for $T/T_{ref} \geq 20$. For reference, the residual term $\langle \mathcal{R} \rangle = \langle S_\omega \rangle + \langle H_\omega \rangle - \mathrm{d}A(t)/(A(t)\mathrm{d}t)$ is also included.

3.2 Relationship Between the Interface Evolution and the Entrainment and Detrainment Process

The relationship between the production/destruction of TNTI and the entrainment and detrainment process is examined by the temporal evolution equation of non-material infinitesimal element of area δA, as deduced by Phillips [4].

$$\frac{1}{\delta A(t)}\frac{\mathrm{d}\delta A(t)}{\mathrm{d}t} = (\delta_{ij} - n_i n_j)\, S_{ij} + v_n \nabla \cdot \boldsymbol{n} = S_{\boldsymbol{\omega}} + H_{\boldsymbol{\omega}}, \tag{4}$$

where $S_{\boldsymbol{\omega}} = (\delta_{ij} - n_i n_j)\, S_{ij}$ represents the stretching term, which is related to the large-scale inhomogeneity of the turbulent flow. Here, δ_{ij} is the Kronecker delta, S_{ij} is the strain rate tensor, and n_i is the ith component of the surface unit normal vector $\boldsymbol{n}$. The curvature/propagation term $H_{\boldsymbol{\omega}} = v_n \nabla \cdot \boldsymbol{n}$ represents the combined influences of the local entrainment velocity v_n and the local mean curvature $\nabla \cdot \boldsymbol{n}$, which is associated with the small-scale turbulent motion.

When the spatial average of the non-material infinitesimal element of area δA on the surface of TNTI is taken, formula (4) can be expressed as [11]:

$$\frac{1}{A(t)}\frac{\mathrm{d}A(t)}{\mathrm{d}t} = \langle S_{\boldsymbol{\omega}} \rangle + \langle H_{\boldsymbol{\omega}} \rangle\,, \tag{5}$$

where the symbol $\langle\rangle$ denotes the average over the surface of TNTI. Therefore, the average production/destruction of the TNTI area $A(t)$ is observed to result from the combined effects of $\langle S_{\omega}\rangle$ and $\langle H_{\omega}\rangle$. Obviously, the term $\mathrm{d}A(t)/(A(t)\mathrm{d}t)$ being positive (negative) represents the production (destruction) region of the TNTI surface.

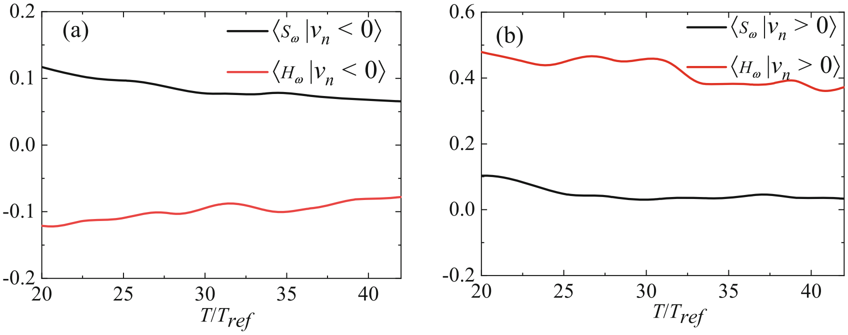

Fig. 4. Time evolution of the average stretching term $\langle S_{\omega}\rangle$ and the average curvature/propagation term $\langle H_{\omega}\rangle$ in the (a) entrainment and (b) detrainment process at $T/T_{ref} \geq 20.0$.

Figure 3 illustrates the time evolution of each term (i.e. the unsteady term $\mathrm{d}A(t)/(A(t)\mathrm{d}t)$, the stretching term $\langle S_{\omega}\rangle$ and the curvature/propagation term $\langle H_{\omega}\rangle$) in formula 5. For comparison, the unsteady term $\mathrm{d}A(t)/(A(t)\mathrm{d}t)$ is also included, as well as the residual term $\langle\mathcal{R}\rangle = \langle S_{\omega}\rangle + \langle H_{\omega}\rangle - \mathrm{d}A/(A\mathrm{d}t)$. It is worth mentioning that the surface area $A(t)$ of the TNTI is computed by formula 2. The term $\langle S_{\omega}\rangle$ roughly balances the term $\langle H_{\omega}\rangle$, implying that the surface area of TNTI remains approximately constant, i.e. $\mathrm{d}A/\mathrm{d}t \simeq 0$. This observation consistent with the TNTI surface theory in previous studies [1], as the Reynolds number is almost constant in self-similar states.

The expansion of the jet is caused by the imbalance between the entrainment and detrainment processes. Although the probability of the detrainment process is considerably lower compared to the entrainment process [2], the ratio of entrainment to detrainment is approximately 2:1, i.e., $\int_{-\infty}^{0} P(v_n)v_n dv_n : \int_{0}^{\infty} P(v_n)v_n dv_n \simeq 2 : 1$. The growth of the surface area is strongly influenced by the local entrainment velocity v_n, and the relationship between the entrainment and detrainment process and the area evolution is further investigated. The time evolution of the average stretching term $\langle S_{\omega}\rangle$ and the average curvature/propagation term $\langle H_{\omega}\rangle$ in the entrainment and detrainment regions at $T/T_{ref} \geq 20.0$ are plotted in Fig. 4. The stretching term $\langle S_{\omega}|v_n < 0\rangle$ contributes to the production of surface area, while the curvature propagation term $\langle H_{\omega}|v_n < 0\rangle$ contributes to the destruction of surface area in the entrainment process. For the detrainment process, the stretching term $\langle S_{\omega}|v_n > 0\rangle$ and curvature/propagation term $\langle S_{\boldsymbol{\omega}} | v_n > 0 \rangle$ contribute to the production of the surface area.

4 Conclusion

In this paper, we characterise the relationship between the entrainment and detrainment process and the evolution of the TNTI surface in a turbulent plane jet. In order to accurately assess the evolution of the TNTI, a fine grid partition is employed, along with a novel method for calculating the surface area of TNTI. We show that the evolution of the TNTI surface exhibits some dependence on the entrainment and detrainment process. On average, the effect of stretching term $\langle S_{\boldsymbol{\omega}} | v_n < 0 \rangle$ is responsible for the production of the surface area, whereas the effect of the curvature propagation term $\langle H_{\boldsymbol{\omega}} | v_n < 0 \rangle$ leads to a decrease of the surface area during the entrainment process. For the detrainment process, both the stretching and curvature propagation terms contribute to the production of the surface area. To understand the influence of turbulent structures on the growth of surface area, we will continue to investigate the relationship between the growth of surface area and local fluid dynamics in the future work.

References

1. da Silva, C.B., Hunt, J.C.R., Eames, I., Westerweel, J.: Interfacial layers between regions of different turbulence intensity. Annu. Rev. Fluid Mech. **46**, 567–590 (2014). https://doi.org/10.1146/annurev-fluid-010313-141357
2. Mistry, D., Jimmy, P., James, R.D.: Kinematics of local entrainment and detrainment in a turbulent jet. J. Fluid Mech. **871**, 896–924 (2019). https://doi.org/10.1017/jfm.2019.327
3. Holzner, M., Lüthi, B.: Laminar superlayer at the turbulence boundary. Phys. Rev. Lett. **106**(13), 134503 (2011). https://doi.org/10.1103/PhysRevLett.106.134503
4. Phillips, O.M.: The entrainment interface. J. Fluid Mech. **51**(1), 97–118 (1972). https://doi.org/10.1017/S0022112072001090
5. da Silva, C.B., Pereira, J.C.: Invariants of the velocity-gradient, rate-of-strain, and rate-of-rotation tensors across the turbulent/nonturbulent interface in jets. Phys. Fluids **20**(5) (2008). https://doi.org/10.1063/1.2912513
6. Laizet, S., Lamballais, E.: High-order compact schemes for incompressible flows: a simple and efficient method with quasi-spectral accuracy. J. Comput. **228**(16), 5989–6015 (2009). https://doi.org/10.1016/j.jcp.2009.05.010
7. Lele, S.K.: Compact finite difference schemes with spectral-like resolution. J. Comput. **103**(1), 16–42 (1992). https://doi.org/10.1016/0021-9991(92)90324-R
8. Kempf, A., Klein, M., Janicka, J.: Efficient generation of initial-and inflow-conditions for transient turbulent flows in arbitrary geometries. Flow Turbul. Combust. **74**(1), 67–84 (2005). https://doi.org/10.1007/s10494-005-3140-8
9. Gutmark, E., Wygnanski, I.: The planar turbulent jet. J. Fluid Mech. **73**(3), 465–495 (1976). https://doi.org/10.1017/S0022112076001468
10. Yurtoglu, M., Carton, M., Storti, D.: Treat all integrals as volume integrals: a unified, parallel, grid-based method for evaluation of volume, surface, and path integrals on implicitly defined domains. J. Inf. Sci. Engng. **18**(2), 021013 (2018). https://doi.org/10.1115/1.4039639

11. Neamtu-Halic, M.M., Krug, D., Mollicone, J.-P., van Reeuwijk, M., Haller, G., Holzner, M.: Connecting the time evolution of the turbulence interface to coherent structures. J. Fluid Mech. **898**, A3 (2020). https://doi.org/10.1017/jfm.2020.414

Frequency Effect on Properties of Turbulent/Non-turbulent Interface in Separated and Reattaching Flows Past an Oscillating Fence

Sicheng Li and Jinjun Wang(✉)

Fluid Mechanics Key Laboratory of Education Ministry, Beihang University,
Beijing 100191, China
`jjwang@buaa.edu.cn`

Abstract. The turbulent/non-turbulent interface (TNTI) in the separated and reattaching flows induced by an oscillating fence is experimentally study using particle image velocimetry in this paper. The oscillation frequency of fence is varied spanning subcritical, transitional, critical and supercritical flow regimes, respectively. In the subcritical case, the flow pattern and the TNTI properties are very similar to that in the static case, except in the vicinity of the fence where the actuated low-frequency flapping of the separated shear layer causes larger TNTI height fluctuations. The strongest conditional averaged vorticity is observed in the critical case. However, the faster transition to turbulence is induced by the higher oscillation frequency rather than the critical one. Higher oscillation frequency results in the slower decrease and less fluctuations in the TNTI height normalized by the boundary thickness. Additionally, the greatest TNTI height fluctuation in the recirculation zone is observed in the transitional case, where the vortex shedding frequency is locked to the oscillation frequency resulting in larger shedding vortices.

Keywords: flow separation · transition · turbulent intermittency

1 Introduction

In many turbulent flows, turbulent and non-turbulent regions are separated by a distorted interface, called the turbulent/non-turbulent interface (TNTI). The TNTI plays an important role in the entrainment process, by which fluids in the non-turbulent region gain vorticity and become part of the turbulent region [1]. Therefore, the TNTI is expected to be important in the evolution of turbulent flows and attracts a lot of attention.

With the improvement of experimental technologies and computational resources in recent years, the TNTI has been investigated in canonical free shear flows such as jets [2–5], wakes [6,7], mixing layers [8,9], and turbulent boundary

J. Wang and I. Marusic (Eds.): IUTAM-TNTI 2024, IUTAM Bookseries 45, pp. 182–193, 2025.
https://doi.org/10.1007/978-3-031-78151-3_14

layers [10,11]. Most of studies rely on conditional statistics computed as a function of the distance from the TNTI [5,6,11], which lead to a clearer picture of flow characteristics in the vicinity of the TNTI. The step change in conditional statistics across the TNTI is captured by this methodology and is a common feature among different types of turbulent flows [1]. The level of conditional statistics is matched between the turbulent core region and the non-turbulent region in a layer with a finite thickness, which is referred to as the TNTI layer. For fully developed turbulence (especially at high Reynolds numbers), these conditional statistics can collapse onto the same profile for the different flow types when properly normalized [12]. Some studies suggested that small-scale properties are universal at the TNTI layer for different flows and at different high Reynolds numbers. Nevertheless, different results were also reported when the flow is developing or at a lower Reynolds number [13–15], and more research is still needed in this regard for comprehensive knowledge of the TNTI.

To acquire more profound understanding of the TNTI, the influence of flow structures on the TNTI has attracted much attention. It is realized that geometric properties of the TNTI are closely associated with flow structures. The large-scale shape, spatial position and orientation of the TNTI are modulated by large-scale structures [8,16,17]. On the other hand, small-scale geometric properties of the TNTI is related to nearby vortex structures, e.g., the TNTI layer thickness is actually very close to the radius of the vortex near the TNTI [13]. In addition to the influence on geometric properties, flow structures also significantly modulates dynamical properties and entrainment at the TNTI [17–19].

Many studies have focused on the TNTI in fully developed canonical turbulence. However, only relatively few works have been devoted to the study of the TNTI in developing flows or complex flows, such as Refs. [15,20–22]. In our previous work [20], the evolution of geometric and dynamical properties of the TNTI in the shear layer separated from a wall-mounted fence was investigated. Characteristics of the TNTI show some distinct differences in each evolution stage of the shedding vortex, which reflects that the influence of developing vortices on the TNTI is not exactly the same with that in fully developed turbulence. On this basis, we further wonder how the TNTI will be affected if the flow is actively disturbed by oscillating the fence, as the oscillating fence was reported to have a significant regulating effect on the vortex shedding behavior [23–25]. With this motivation, the TNTI in the separated and reattaching flows induced by an oscillating fence is experimentally studied in this paper.

2 Approach

2.1 Experimental Setup

The time-resolved particle image velocimetry (PIV) experiment was conducted in the water channel at Beihang University. The schematic of the experimental device is illustrated in Fig. 1(a). A flat and smooth acrylic plate was vertically fixed in the center of the channel. The plate measures 200 cm in length, 1.5 cm in thickness, and 60 cm in height, protruding from the water with a depth of 50 cm.

An elliptic leading edge with the aspect ratio of 5:1 was adopted to avoid flow separation from the plate leading edge. At a distance of 30 cm downstream from the leading edge of the plate, a slot measuring 402 mm in length and 2 mm in width was reserved to allow for the free vertical movement of the fence through it. The 400 mm long and 1 mm thick stainless steel fence was actuated by an eccentric drive mechanism, which converted the rotary motion output from the servo motor (Yaskawa SGM7J) into a straight motion along the guide rail via the connecting rod (more clearly visualized in the bottom view).

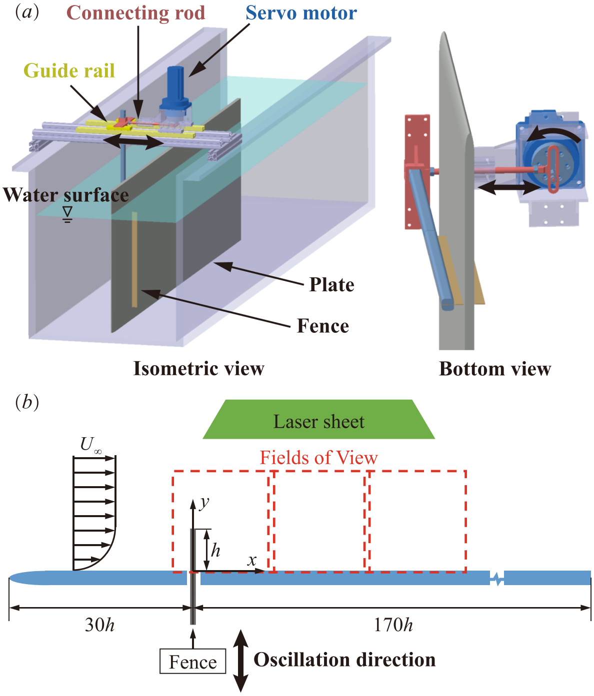

Fig. 1. (*a*) Three-dimensional diagram of the experimental device. (*b*) Schematic of the experiment setup and fields of view for PIV from the spanwise view.

A brief schematic of the experiment setup and fields of view (FoVs) for PIV from the spanwise view are shown in Fig. 1(*b*). Streamwise, vertical, and spanwise coordinates are denoted by x, y, and z, respectively. The x-axis originates at the slot center, and the y-axis origin is located on the plate surface. The two-dimensional PIV system was used to obtain the velocity field in x-y plane. FoVs were located in the central plane of the plate, which were far away from both the water surface and the bottom wall of the channel so as to neglect the end effect. Seeding particles were hollow glass beads with a diameter of 5–20 μm and a density of 1.05 g/cm^3, which were illuminated by a laser sheet approximately

1 mm thick generated by a high-frequency double-pulsed laser (Beamtech Vlite-Hi-527). Particle images were synchronously captured by three CMOS cameras (2048 × 2048 pixels) with a sampling frequency of 250 Hz. The multiple iterative Lucas–Kanade algorithm [26] was used to calculate the velocity field with an interrogation window of 32 × 32 pixels and an overlap of 75% for the final iteration. The FoV size for each camera was approximately 90 mm × 90 mm, with an overlap of at least 10 mm between adjacent FoVs. Calibration with a single long reference target covering the entire measurement area was used for stitching all velocity fields together.

The fence was carefully adjusted to fit through the slot. The stationary height of the fence (denoted by h) was 10 mm above the plate surface, which is also the mean position of the fence during its oscillation. The boundary layer thickness ratio h/δ_l is 1.20, where δ_l denotes the laminar boundary layer thickness before the installation of the fence. The Reynolds number is $Re_h = hU_\infty/\nu = 1274$, where ν is the kinematic viscosity and U_∞ is the freestream velocity equal to 105 mm/s. The oscillation direction of the fence was nearly perpendicular to the mean shear flow, which facilitates the roll-up of the shear layer, resulting in observable modulations on the vortex shedding [23,25]. The amplitude (A_o) and oscillation frequency (f_o) of fence oscillation can be controlled by adjusting the eccentric radius and motor speed, respectively. Thus, the instantaneous fence height can be expressed as:

$$y_h = A_o sin(2\pi f_o t + \varphi_0) + h, \tag{1}$$

where φ_0 is the initial phase. As we are interested in the effect of small perturbations, A_o is set to be only $0.1h$.

Furthermore, according to Singh *et al.* [25], the appropriate flow regime parameter was the ratio of the fence oscillation frequency to the natural shedding frequency of the corresponding stationary fence: $\phi_o = f_o/f_s$, which successfully characterizes the basic flow regimes. The natural shedding frequency f_s refers to the vortex shedding frequency when the fence is stationary, which is equal to 2.0 Hz in the present work. Different flow regimes exhibit distinct characteristics. Briefly, subcritical flows ($\phi_o \ll 1$) create vortices at the shedding frequency depending on the local fence height. Transitional flows ($\phi_o < 1$) generate unstable vortices locked at the oscillation frequency. In critical flows ($\phi_o \approx 1$), vortices shed at the natural shedding frequency and contain higher vorticity. Supercritical flows ($\phi_o > 1$) initially form vortices at the oscillation frequency, but subsequently, these vortices quickly pair and coalesce after shedding. More details can be found in Refs. [23,25]. Consequently, the oscillation frequency in the present work was designed to span all flow regimes, as shown in Table 1.

Table 1. Oscillation frequencies f_o and frequency ratios ϕ_o in each flow regime.

Flow regime [25]	static	subcritical	transitional	critical	supercritical	supercritical
f_o (Hz)	0	0.1	1.0	2.0	4.0	6.0
ϕ_o (f_o/f_s)	0	0.05	0.5	1	2	3

2.2 TNTI Detection Method

Generally, the vorticity of turbulent flows is much higher than that of non-turbulent flows, so the vorticity magnitude (or the enstrophy) is widely used to detect the TNTI between turbulent and non-turbulent regions [1]. In the present work, spanwise enstrophy $\omega_z^2 = (\partial v/\partial x - \partial u/\partial y)^2$ is used to detect the TNTI with a threshold $\omega_{z,th}^2$. The threshold is utilized to eliminate the noise, affected by which the measured enstrophy in the non-turbulent region is not completely zero. By specifying a threshold, the flow field is divided into two regions: the turbulent region where $\omega_z^2 > \omega_{z,th}^2$ and the non-turbulent region where $\omega_z^2 < \omega_{z,th}^2$. $\omega_{z,th}^2$ is usually determined following an empirical process in which the sensitivity of the result to the threshold is tested [1,11]. Herein, we examined A_{tur}/A against the threshold, where A_{tur} denotes the mean area of the turbulent region and A represents the total field area (A_{tur} is obtained by summing up the instantaneous areas of the turbulent region at every moment and dividing by the total number of instances). Subsequently, the threshold is selected where the gradient $A'_{tur} = |dA_{tur}/d\omega_{z,th}^2|$ is minimal, as marked by the hollow circles in Fig. 2(a). An instantaneous vorticity field superimposed with the TNTI is shown in Fig. 2(b). The result shows that the TNTI is well detected, effectively distinguishing the high-vorticity flow from the outer low-vorticity flow with clarity.

3 Results

3.1 Basic Characteristics of Flow Regimes

Since TNTI properties are related to flow structures, it is necessary to make clear basic characteristics of the flow first. Figure 3 shows the mean streamlines around the recirculation zone. An observable flow separation is induced by the fence. Isopleths of $U = 0$ and $\Phi = 0$ are superimposed to show the center and upper boundary of the recirculation zone, respectively [27], where U is the mean streamwise velocity and Φ is the integral of mean streamwise velocity along the vertical direction, i.e., $\Phi(x, y) = \int_0^y U(x, y)dy$. In the static case ($\phi_o = 0$), the mean large-scale vortex occupies the latter part of the separation bubble centered at approximately $8h$. It is attributed to the initially laminar nature of the separated shear layer, which develops gradually before the appearance of large-scale shedding vortices [20]. By contrast, when the fence oscillates faster, it prompts an accelerated instability, so that the vortex structure is formed from the earlier rolling up of the separated shear layer. Except the subcritical

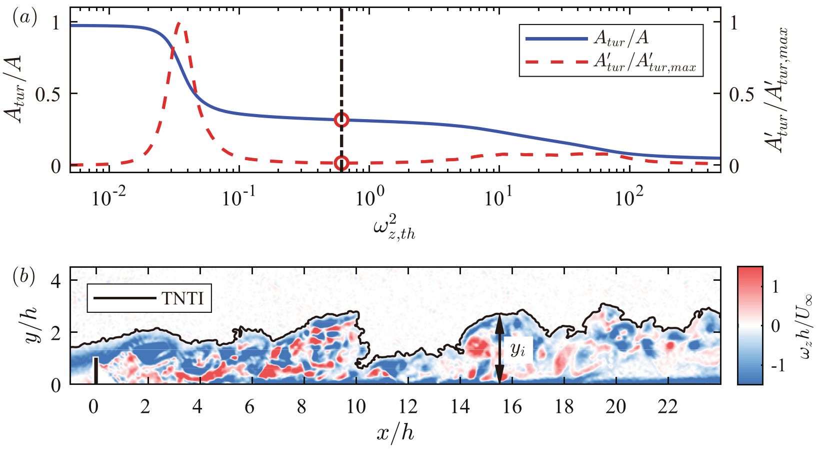

Fig. 2. (a) Area ratio A_{tur}/A as a function of the threshold $\omega^2_{z,th}$ and its normalized gradient $A'_{tur}/A'_{tur,max}$. (b) Visualization of the instantaneous vorticity field and the TNTI. For brevity, only the critical case ($\phi_o = 1$) is presented as an example.

case ($\phi_o = 0.05$) in which the mean flow characteristics is almost the same as that of the static case, other oscillatory cases ($\phi_o = 0.5, 2, 3$) exhibit a closer resemblance to the flow pattern presented in Fig. 3(b). The length (x_r) and height (y_r) of the recirculation zone are quantified by checking the peak and the intersection point with the wall on the isopleth of $\Phi = 0$, respectively. With the increase of oscillation frequency, the size of the recirculation zone decreases first and then increases with its minimum in the critical case both along streamwise and vertical directions. Furthermore, although the amplitude is much smaller, the vortex shedding dynamics still agrees well with observations of Singh *et al.* [25], that one vortex sheds per oscillation circle except subcritical cases. In the transitional case, the shedding frequency is locked to the oscillation frequency, while in supercritical cases, vortex shedding and pairing occur more frequently.

3.2 Characteristics of the TNTI

The TNTI height y_i is defined as the vertical distance from the wall (the plate surface) to the TNTI. Figure 4 shows the streamwise variation of the mean TNTI height (Y_i) and standard deviation (σ_i) normalized by the boundary layer thickness δ. In the subcritical case ($\phi_o = 0.05$), the evolution of (Y_i/δ) and (σ_i/δ) closely resemble that in the static case. Nevertheless, a deviation occurs in the behavior of σ_i/δ when $x < 0.7x_r$. This increase in σ_i/δ should be attributed to the stronger flapping of the separated shear layer induced by the low-frequency oscillation. In other oscillatory cases ($\phi_o = 0.5, 1, 2, 3$), the shedding vortex is generated in advance resulting in stronger disturbance. Consequently, the apparent decrease in Y_i/δ manifests earlier at $x = 0.2x_r$ compared to $x = 0.6$ in static

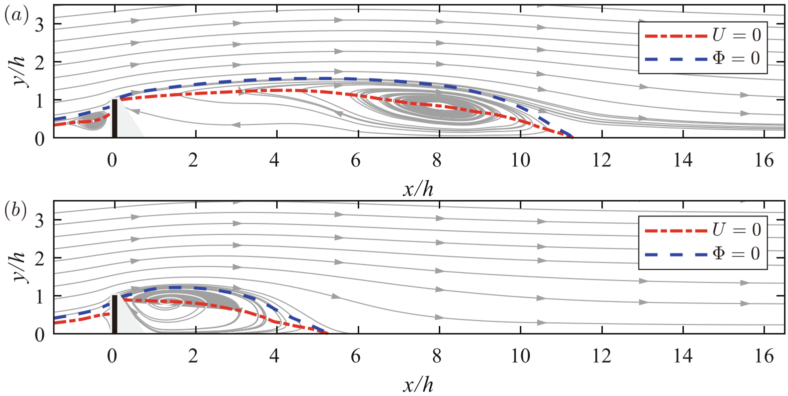

Fig. 3. Mean streamlines in cases: (*a*) $\phi_o = 0$ and (*b*) $\phi_o = 1$. Isopleths of $U = 0$ and $\varPhi = 0$ are superimposed to show the center and upper boundary of the recirculation zone, respectively.

and subcritical cases, with σ_i/δ also increasing sooner. Moreover, a higher oscillation frequency leads to the slower decrease of Y_i/δ and less increment in σ_i/δ.

The oscillation frequency not only affects the TNTI near the recirculation zone, but also influences the TNTI further downstream of the fence. In static, subcritical and transitional cases, Y_i eventually converges to 0.53δ while σ_i becomes 0.27δ when $x > 2x_r$. However, Y_i and σ_i in critical and supercritical cases converge to 0.65δ and 0.24δ, respectively. It indicates that the fluctuation of the TNTI height is weakened and the flow becomes more turbulent under higher oscillation frequencies. It is apparent that the TNTI position is in accordance with the spacial distribution of vortices as shown in Fig. 2(*b*). Although high-frequency perturbation leads to more vortex shedding [23], the strength and size of the shedding vortex are reduced resulting in a faster transition to turbulence. The transitional case bridges characteristics in subcritical case and higher-frequency cases. It exhibits a flow pattern similar to those in critical and supercritical cases where shedding vortices appear near the fence. However, the TNTI geometric properties further downstream gradually converge to that of static and subcritical cases. Remarkably, turbulence in the transitional case is significantly intermittent leading to the greatest fluctuation in the TNTI position.

The dynamic characteristics of the TNTI are investigated by the conditional statistics as a function of the distance from the TNTI. The local interface coordinate y_I is established with its origin on the instantaneous TNTI and its axis always aligned with the local unit normal vector $\boldsymbol{n} = \nabla\omega_z^2/|\nabla\omega_z^2|$, pointing toward the turbulent region. Subsequently, quantities situated on the local interface coordinate with an equal distance from the TNTI are re-collected and averaged. Further details of the computation of the conditional statistics can be found in our previous work [20]. The conditional averaged quantities are denoted by $\langle\cdot\rangle_I$ in this paper.

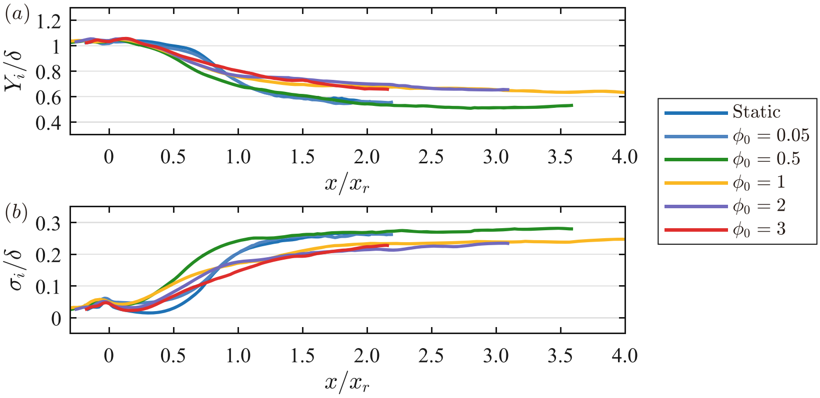

Fig. 4. Streamwise variation of (a) mean and (b) standard deviation of TNTI height.

An example of conditional averaged vorticity in Fig. 5(a). The step change in the conditional averaged profile is clearly demonstrated, which reconfirm the appropriateness of the detected TNTI. Following Zhang *et al.* [11], the TNTI thickness δ_ω is quantified as the distance from the TNTI to the position where the conditional averaged vorticity gradient $\langle|\omega_z|\rangle_I'$ equals 20% of its maximum. The Kolmogorov scale is also estimated using this conditional methodology. $\langle\eta\rangle_I$ is defined as $\langle\eta\rangle_I = (\nu^3/\langle\varepsilon\rangle_I)^{1/4}$, where $\langle\varepsilon\rangle_I$ is the conditional averaged dissipation rate estimated based on the assumption of local axisymmetry [21,28]. It is illustrated in Fig. 5(b) that out of the turbulent core region ($y_I < \delta_\omega$), $\langle\eta\rangle_I$ varies rapidly along the y_I coordinate. Conversely, $\langle\eta\rangle_I$ is almost independent of y_I in the turbulent core region ($y_I > \delta_\omega$), except for the region near the fence where the small-scale eddy is scarcely present. Therefore, the Kolmogorov scale η_I is defined at $y_I = \delta_\omega$, expressed as: $\eta_I(x) = \langle\eta\rangle_I(x, y_I = \delta_\omega)$. The Kolmogorov velocity scale u_{η_I} and time scale τ_I are defined in the same way.

The streamwise variation of the normalized conditional averaged vorticity $\langle|\omega_z|\rangle_I$ is shown in Fig. 6. Conspicuous peaks of $\langle|\omega_z|\rangle_I$ are discernible. These peaks correspond to the TNTI thickness, and accordingly, are associated with the vortex scale near the TNTI [13]. Near the fence, e.g. at $x = 0.2x_r$, peaks in critical and supercritical cases are located further from the TNTI, compared to peak in the static and subcritical cases, and the peak in the transitional case falls in between. However, as the flow evolves downstream, peaks in supercritical cases move closer to the TNTI, while peaks in transitional and critical cases behave in the opposite way. According to previous studies [23,25], the vortex structure grows in the rise period and sheds in the fall period of oscillation, respectively. The transitional and critical cases facilitate better vorticity accumulation. Conversely, in supercritical cases, the rapid oscillation leads to vortex shedding without sufficient growth in strength and size. As a result, it is not difficult to understand the situation that $\langle|\omega_z|\rangle_I$ in the turbulent core region is the greatest in the critical case, followed by the transitional case. In contrast,

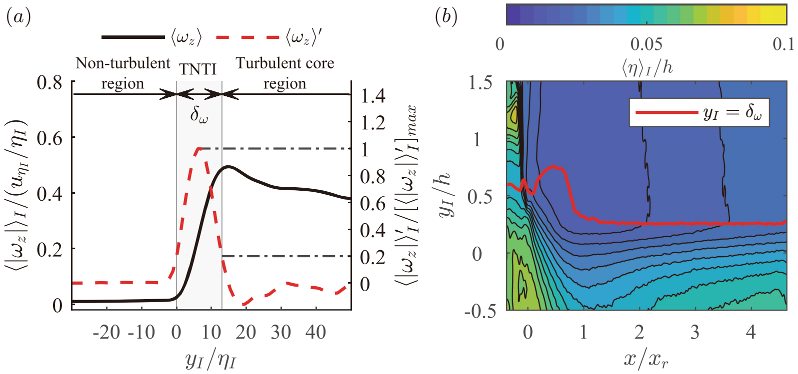

Fig. 5. (*a*) Conditional averaged vorticity $\langle|\omega_z|\rangle_I$ and vorticity gradient $\langle|\omega_z|\rangle'_I$ ($\langle|\omega_z|\rangle'_I = d\langle|\omega_z|\rangle_I/dy_I$) at $x = 2x_r$. (*b*) Conditionally computed Kolmogorov scale $\langle\eta\rangle_I$. The critical case ($\phi_o = 1$) is presented as an example.

the evolution of $\langle|\omega_z|\rangle_I$ converges more quickly as the flow becomes increasingly turbulent in supercritical cases.

Moreover, $\langle|\omega_z|\rangle_I$ is better normalized by the local Kolmogorov scale when $x \geq 1.4x_r$ as shown in the bottom of Fig. 6. It is consistent with the conclusion of Zecchetto and da Silva [12], despite the deviation that $\langle|\omega_z|\rangle_I/(u_{\eta_I}/\eta_I) \neq 1$, which might be attributed to the less homogeneousness of turbulence at the low Reynolds number. In the recirculation zone, the magnitude of $\langle|\omega_z|\rangle_I/(u_{\eta_I}/\eta_I)$ seems to exhibit a greater dependency on u_{η_I}/η_I which is equal to $1/\tau_I$, the inverse of the Kolmogorov time scale. Given the modulation effect on the vortex shedding in the transitional case where the shedding frequency is locked to the oscillation frequency [25], it is not difficult to consider that the characteristic time scale is enlarged compared to other cases. Therefore, $\langle|\omega_z|\rangle_I/(u_{\eta_I}/\eta_I)$ is observed to be larger than that in critical and supercritical cases, and it appears to be smaller as the fence oscillation frequency increases. Meanwhile, since the shedding vortex is growing regularly when $x \leq 0.6x_r$ [20], the computed u_{η_I}/η_I is much smaller. Consequently, peaks of $\langle|\omega_z|\rangle_I/(u_{\eta_I}/\eta_I)$ in static and subcritical cases is greater than that in other cases when $x \leq 0.6x_r$.

4 Conclusion

We performed the particle image velocimetry experiment to investigate the turbulent/non-turbulent interface in the separated and reattaching flows induced by an oscillating fence. The ratios of the fence oscillation frequency to the natural shedding frequency of the stationary fence were set corresponding to the subcritical, transitional, critical and supercritical flow regimes, respectively. Statistical properties of the TNTI in the subcritical case closely resemble that in the static case, except in the vicinity of the fence where the actuated low-frequency

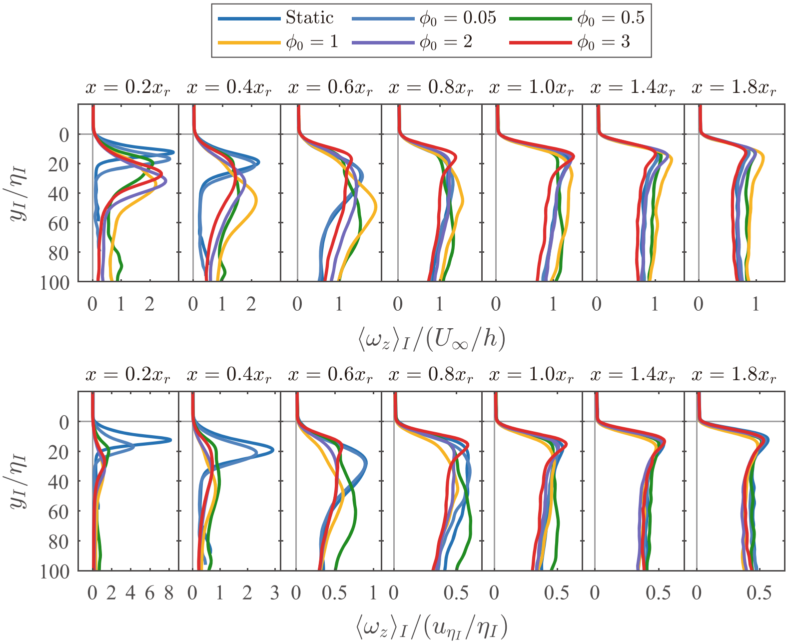

Fig. 6. Conditional averaged vorticity $\langle|\omega_z|\rangle_I$ at different streamwise stations normalized by (top) U_∞/h and (bottom) u_{η_I}/η_I, respectively.

flapping of the separated shear layer in the subcritical case leads to larger fluctuations in the TNTI position. In transitional, critical and supercritical cases, the disturbance is more intense, resulting in the earlier appearance of the shedding vortex near the fence. The strongest conditional averaged vorticity is observed in the critical case. However, the faster transition to turbulence is induced by the higher oscillation frequency rather than the critical one, because more low-vorticity and smaller shedding vortices, which is closer to the small-scale eddy in turbulence, are generated in the supercritical cases. Meanwhile, the higher oscillation frequency results in the slower decrease and less fluctuations of the TNTI height normalized by the boundary thickness, indicating that the turbulence is less intermittent. Besides, the greatest fluctuation in the TNTI height in the recirculation zone is observed in the transitional case where the vortex shedding frequency is locked to the oscillation frequency resulting in influential large-scale shedding vortices.

References

1. da Silva, C.B., Hunt, J.C.R., Eames, I., Westerweel, J.: Interfacial layers between regions of different turbulence intensity. Annu. Rev. Fluid Mech. **46**(1), 567–590 (2014). https://doi.org/10.1146/annurev-fluid-010313-141357

2. Breda, M., Buxton, O.R.H.: Behaviour of small-scale turbulence in the turbulent/non-turbulent interface region of developing turbulent jets. J. Fluid Mech. **879**, 187–216 (2019). https://doi.org/10.1017/jfm.2019.676
3. Er, S., Laval, J.P., Vassilicos, J.: Length scales and the turbulent/non-turbulent interface of a temporally developing turbulent jet. J. Fluid Mech. **970**, A33 (2023). https://doi.org/10.1017/jfm.2023.654
4. Kohan, K.F., Gaskin, S.J.: On the scalar turbulent/turbulent interface of axisymmetric jets. J. Fluid Mech. **950**, A32 (2022). https://doi.org/10.1017/jfm.2022.825
5. Westerweel, J., Fukushima, C., Pedersen, J.M., Hunt, J.C.R.: Momentum and scalar transport at the turbulent/non-turbulent interface of a jet. J. Fluid Mech. **631**, 199–230 (2009). https://doi.org/10.1017/S0022112009006600
6. Bisset, D.K., Hunt, J.C.R., Rogers, M.M.: The turbulent/non-turbulent interface bounding a far wake. J. Fluid Mech. **451**, 383–410 (2002). https://doi.org/10.1017/S0022112001006759
7. Li, B., Yang, Z., Zhang, X., He, G., Deng, B.Q., Shen, L.: Using machine learning to detect the turbulent region in flow past a circular cylinder. J. Fluid Mech. **905**, A10 (2020). https://doi.org/10.1017/jfm.2020.725
8. Balamurugan, G., Rodda, A., Philip, J., Mandal, A.: Characteristics of the turbulent non-turbulent interface in a spatially evolving turbulent mixing layer. J. Fluid Mech. **894**, A4 (2020). https://doi.org/10.1017/jfm.2020.241
9. Watanabe, T., Sakai, Y., Nagata, K., Ito, Y., Hayase, T.: Turbulent mixing of passive scalar near turbulent and non-turbulent interface in mixing layers. Phys. Fluids **27(8)**, 085,109 (2015). https://doi.org/10.1063/1.4928199
10. Chauhan, K., Philip, J., de Silva, C.M., Hutchins, N., Marusic, I.: The turbulent/non-turbulent interface and entrainment in a boundary layer. J. Fluid Mech. **742**, 119–151 (2014). https://doi.org/10.1017/jfm.2013.641
11. Zhang, X., Watanabe, T., Nagata, K.: Reynolds number dependence of the turbulent/non-turbulent interface in temporally developing turbulent boundary layers. J. Fluid Mech. **964**, A8 (2023). https://doi.org/10.1017/jfm.2023.329
12. Zecchetto, M., da Silva, C.B.: Universality of small-scale motions within the turbulent/non-turbulent interface layer. J. Fluid Mech. **916**, A9 (2021). https://doi.org/10.1017/jfm.2021.168
13. da Silva, C.B., Taveira, R.R.: The thickness of the turbulent/nonturbulent interface is equal to the radius of the large vorticity structures near the edge of the shear layer. Phys. Fluids **22**, 121,702 (2010). https://doi.org/10.1063/1.3527548
14. Wu, D., Wang, J., Cui, G., Pan, C.: Effects of surface shapes on properties of turbulent/non-turbulent interface in turbulent boundary layers. Sci. China Technol. Sci. **63**, 214–222 (2020). https://doi.org/10.1007/s11431-018-9434-5
15. Wu, X., Wallace, J.M., Hickey, J.P.: Boundary layer turbulence and freestream turbulence interface, turbulent spot and freestream turbulence interface, laminar boundary layer and freestream turbulence interface. Phys. Fluids **31**, 045,104 (2019). https://doi.org/10.1063/1.5093040
16. Lee, J., Sung, H.J., Zaki, T.A.: Signature of large-scale motions on turbulent/non-turbulent interface in boundary layers. J. Fluid Mech. **819**, 165–187 (2017). https://doi.org/10.1017/jfm.2017.170
17. Long, Y., Wang, J., Pan, C.: Universal modulations of large-scale motions on entrainment of turbulent boundary layers. J. Fluid Mech. **941**, A68 (2022). https://doi.org/10.1017/jfm.2022.355

18. Neamtu-Halic, M.M., Krug, D., Mollicone, J., van Reeuwijk, M., Haller, G., Holzner, M.: Connecting the time evolution of the turbulence interface to coherent structures. J. Fluid Mech. **898**, A3 (2020). https://doi.org/10.1017/jfm.2020.414
19. Yin, W., Tao, S., Nagata, K., Ito, Y., Sakai, Y., Zhou, Y.: Spatial distribution of coherent structures in a self-similar axisymmetric turbulent wake. Phys. Rev. Fluids **8**, 084,603 (2023). https://doi.org/10.1103/PhysRevFluids.8.084603
20. Li, S., Long, Y., Wang, J.: Turbulent/non-turbulent interface for laminar boundary flow over a wall-mounted fence. Phys. Fluids **34**, 125,113 (2022). https://doi.org/10.1063/5.0128609
21. Long, Y., Wang, J., Wang, J.: "turbulent/non-turbulent interface" in a low-reynolds-number transitional boundary layer over a multi-element airfoil. Phys. Fluids **34**, 102,111 (2022). https://doi.org/10.1063/5.0120934
22. Marxen, O., Zaki, T.: Turbulence in intermittent transitional boundary layers and in turbulence spots. J. Fluid Mech. **860**, 350–383 (2019). https://doi.org/10.1017/jfm.2018.822
23. Hind, M., Lindberg, W., Naughton, J.: Quantification of flow structures generated by an oscillating fence in a flat plate laminar boundary layer. In: 46th AIAA Aerospace Sciences Meeting and Exhibit (2008). https://doi.org/10.2514/6.2008-600
24. Miau, J.J., Chen, C., Chou, J.H.: A vertically oscillating plate disturbing the development of a boundary layer. J. Fluid Mech. **298**, 1–22 (1995). https://doi.org/10.1017/S0022112095003211
25. Singh, P., Lindberg, W., Naughton, J.: Flow structures generated by oscillating fences in boundary layer flows. In: 35th AIAA Fluid Dynamics Conference and Exhibit (2005). https://doi.org/10.2514/6.2005-4882
26. Pan, C., Xue, D., Xu, Y., Wang, J., Wei, R.: Evaluating the accuracy performance of Lucas-Kanade algorithm in the circumstance of PIV application. Sci. China Phys. Mech. Astron. **58**, 104,704 (2015). https://doi.org/10.1007/s11433-015-5719-y
27. Fang, X., Tachie, M.F.: On the unsteady characteristics of turbulent separations over a forward-backward-facing step. J. Fluid Mech. **863**, 994–1030 (2019). https://doi.org/10.1017/jfm.2018.962
28. George, W.K., Hussein, H.J.: Locally axisymmetric turbulence. J. Fluid Mech. **233**, 1–23 (1991). https://doi.org/10.1017/S0022112091000368

On Low-Scalar Patches in Turbulent Wakes with and Without Free-Stream Turbulence

Khashayar F. Kohan[1,2(✉)], Oliver R. H. Buxton[2], and Susan J. Gaskin[1]

[1] Department of Civil Engineering, McGill University, Montreal,
Québec H3A 0C3, Canada
khashayar.feizbakhshiankohan@mail.mcgill.ca, susan.gaskin@mcgill.ca
[2] Department of Aeronautics, Imperial College London, South Kensington Campus,
London SW7 2AZ, UK
o.buxton@imperial.ac.uk

Abstract. High-resolution, time-resolved, simultaneous particle image velocimetry and planar laser-induced fluorescence are performed to study the characteristics of the low-scalar 'holes' in a planar wake exposed to various cases of background turbulence as parameterized by the turbulence intensity and length scale. Several metrics are employed to distinguish the engulfed holes from those generated internally. It is found that beyond a transition distance of 18 Kolmogorov microscales from the wake boundary, holes exhibit comparable behaviour to the wake core, suggesting their generation by local turbulence. It is further revealed that engulfment constitutes less than 1% of the total mass flux in the far-field, regardless of the strength of incoming turbulence intensity.

Keywords: wakes · turbulent/turbulent interface · turbulent entrainment

1 Introduction

Entrainment refers to the incorporation of fluid from the background into a primary turbulent flow. Entrainment occurs due to large-scale inviscid 'engulfment' and small-scale viscous/molecular 'nibbling' across the convoluted turbulence/ambient interfacial layer, hereinafter referred to as the turbulent/non-turbulent interface (TNTI) and turbulent/turbulent interface (TTI) for quiescent and turbulent surroundings, respectively. Whilst engulfment is brought about by the large-scale eddies enveloping pockets of ambient fluid at the inward cusps of the interface [1], nibbling takes place due to the continuous action of small-scale intense vorticity structures across the boundary [2]. Early experimental studies in the far-field of turbulent shear layers [3] and jets [4] suggested engulfment as the dominant entrainment mechanism in the quiescent ambient. These studies relied on flow visualization to reveal unmixed ambient fluid

J. Wang and I. Marusic (Eds.): IUTAM-TNTI 2024, IUTAM Bookseries 45, pp. 194–202, 2025.
https://doi.org/10.1007/978-3-031-78151-3_15

('holes') deep inside the turbulent core, indicating large-scale engulfment. However, later numerical and experimental studies [5–8] found insignificant amounts of intact ambient fluid within the turbulent shear flow. Other studies showed that the probability density function (p.d.f.) of the characteristic size of the holes inside jets [9–11], boundary layers [12], and shear layers [13] obey a similar distribution to that of the holes in homogeneous isotropic turbulence (HIT), where large vorticity structures are essentially non-existent. This suggests that ambient holes are likely generated by the internal dynamics of the turbulence and are not engulfed into the turbulent core by large-scale motions. This evidence further refutes the notion that the contribution of engulfment surpasses that of nibbling, at least in the far-field of turbulent flows where the large-scale coherent structures have decayed. The maximum contribution of engulfment is assessed to be 7%-10% of the total entrained mass flux in jets [6] and shear layers [13] in the far-field. In these studies, the assessment of the contribution of engulfment considers all the holes present in the flow. Recent studies, however, show that only holes within the TNTI and TTI thickness are generated by engulfment, whereas the remainder of the holes originate from the small-scale turbulence within the flow [10–13]. This would decrease the contribution of engulfment even further, substantiating the dominant role of nibbling in the entrainment process in the far-field.

The aim of the current work is to explore the potential universality of the impact of external turbulence, regardless of its generation method, on the engulfment mechanism of jets and wakes in the far-field. This investigation is prompted by the resemblance of our previous findings concerning the effect of background turbulence on the geometry of the TTI outline (i.e. outer boundary) and the net entrainment rate for axisymmetric jets in zero-mean-flow external turbulence [11,14], compared to those of planar wakes in grid-generated turbulence [15,16].

2 Methodology

The data used in the present work are taken from [17], and, therefore, only an overview of the experimental configuration is described herein for brevity. High-resolution, time-resolved, simultaneous particle image velocimetry (PIV) and planar laser-induced fluorescence (PLIF) were performed to analyze the wake of a $d = 10$ mm diameter cylinder exposed to a range of turbulence intensity/length scale combinations of grid-generated external turbulence. The experiments were conducted in the hydraulic flume at the Department of Aeronautics at Imperial College London, where the free-stream velocity and Reynolds number were respectively $u_\infty = 0.38\,\mathrm{m\,s^{-1}}$ and $Re_W = 3800$. A total of 5000 instantaneous snapshots were captured in the far-wake ($38.6 \leqslant x/d \leqslant 41.6$ and $-0.6 \leqslant y/d \leqslant 8.1$) with a frequency of 200 Hz. A passive scalar, Rhodamine 6G with a Schmidt number of 2500 (in water), was isokinetically released into the wake through a small hole in the rear face of the cylinder (see Fig. 1a) to mark the outer boundary of the wake.

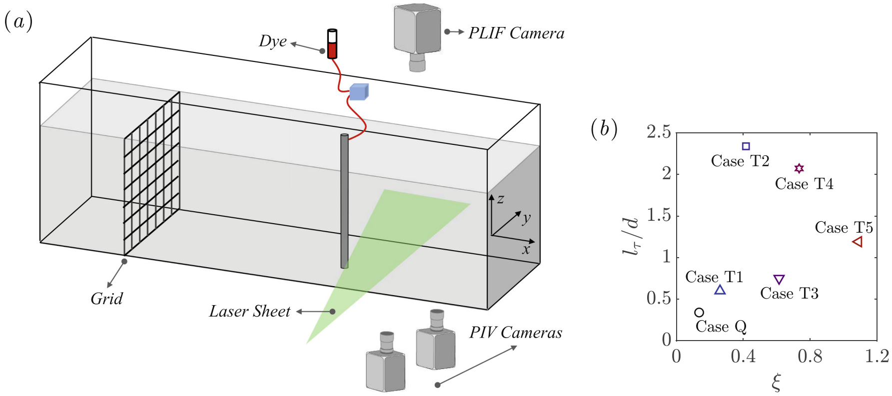

Fig. 1. (a) Illustration of the experimental set-up. Note that the origin of the laboratory coordinate system lies on the rear face of the cylinder. The figure is not to scale. (b) Parameter space (ξ, l_τ) of the free stream.

The intensity and length scale of the free stream were modified by employing four different grids with several grid-cylinder spacings. The integral length scale of the ambient, l_τ, is calculated from the lateral correlation of the streamwise velocity fluctuation [15]. The relative turbulence intensity is defined as

$$\xi = \left(\frac{u'^2_{grid} + v'^2_{grid}}{u'^2_{wake} + v'^2_{wake}} \right)^{1/2}, \qquad (1)$$

where u'_{wake} and v'_{wake} represent the streamwise and lateral components of velocity fluctuations near the wake centerline at $x/d = 40$ in the quiescent ambient (i.e. with no grid upstream), while u'_{grid} and v'_{grid} denote the fluctuating velocity of the grid turbulence along the said directions. The cases are named such that the letters Q and T signify the wake in quiescent and turbulent ambient conditions, respectively. The strength of the incoming turbulence intensity is indicated, in hierarchical order, by the number following the letter T. Figure 1(b) depicts the parametric envelope of this campaign in the absence of the cylinder. It is, however, worth noting that previous findings in jets [11,14] and wakes [15,16] showed relative insensitivity of the interfacial/entrainment behavior to the length scale of the ambient turbulence in the far-field, making the background intensity the only relevant parameter.

The detection of the interface outlines and holes was achieved by applying a threshold to the light intensity fields in the original PLIF images [14,16]. The scalar holes signify regions within the wake characterized by a local intensity value below the threshold. The coordinates of the outlines and the holes were subsequently interpolated onto a grid that matched the PIV vector spacing. This process is illustrated in Fig. 2, and shows the inability of a velocity/vorticity criterion to reliably detect the TTI outline for cases of intense external turbulence (see Fig. 2f). The spatial resolution of the PIV ranged from $0.9\,\eta_{|x_n=0}$ (case Q)

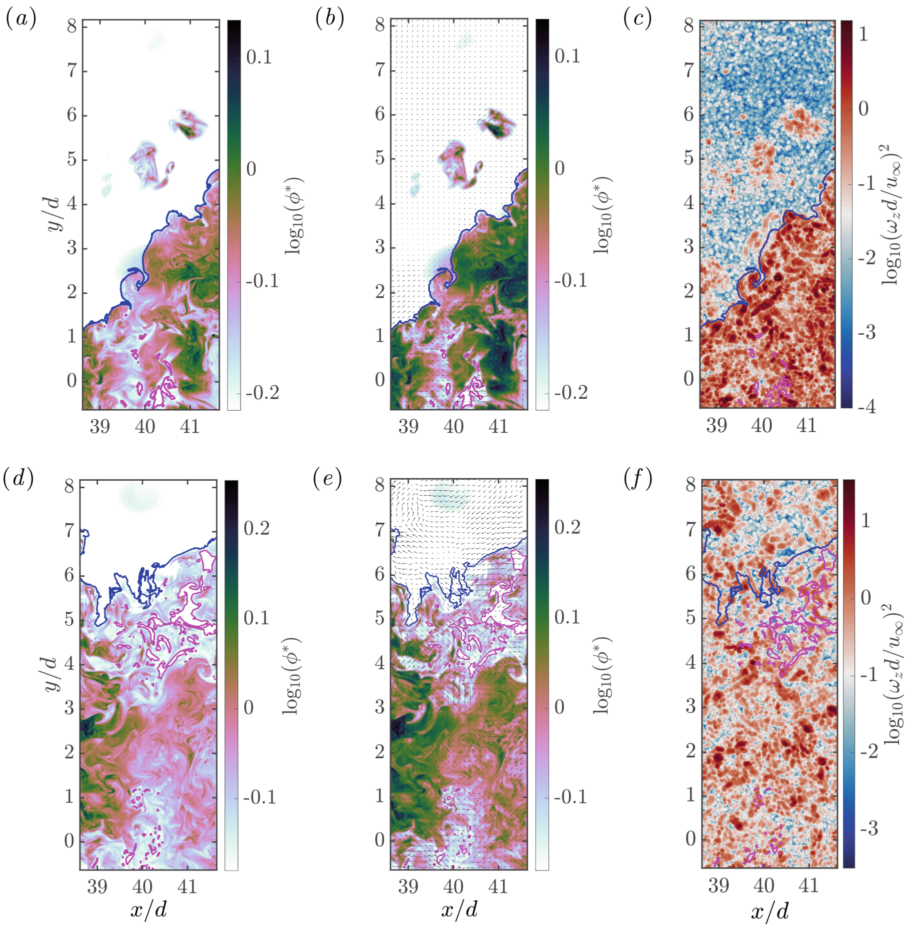

Fig. 2. (a,d) Instantaneous passive scalar fields in the original PLIF images. (b,e) Same fields as (a,d) but interpolated onto the PIV grids. The arrows are velocity fluctuations, displayed every five vectors for clarity. (c,f) Same data as (b,e) but with the vorticity fields, ω_z^2. The TTI outlines and holes are shown with the blue and magenta lines, respectively. Note that $\phi^*(x,y) = \phi(x,y)/\phi_c(x)$, where $\phi(x,y)$ represents the instantaneous intensity value at each (x,y), while $\phi_c(x)$ is the ensemble-averaged intensity value along the wake centerline, that is, $\phi_c(x) = \overline{\phi}(x, y = 0)$. The data are for cases (a–c) T2 and (d–f) T5.

to $1.2\,\eta_{|x_n=0}$ (case T5), where $\eta_{|x_n=0}$ is the averaged Kolmogorov microscale along the outline (see Sect. 3). Lastly, holes with an area smaller than 2×2 data points were discarded to avoid measurement error.

3 Results

The robustness of the interface identification algorithm is verified by examining the conditional average of flow variables in the interface-normal direction (denoted by x_n). Figure 3 reveals that the sharp jumps in velocity/vorticity statistics take place across the isocontours defined from the scalar fields. The values of the Kolmogorov velocity and length scales increase and decrease, respectively, by 40% between the wake boundary and the turbulent core in the quiescent ambient [18]. This variation gradually reduces with the introduction of free-stream turbulence, diminishing to $\sim 5\%$ in the most intense external turbulence case (T5). When normalized locally, the conditional vorticity profiles display two local peaks on either side of the interface outline (Fig. 3*c*). This region, depicted by the grey bars in Fig. 3, has an approximate thickness of $10\,\eta_{|x_n=0}$ regardless of the ambient condition and can be regarded as the interfacial layer demarcating the wake from the free stream. Overall, the presence of conditional jumps indicates that the wake and ambient regions are effectively separated.

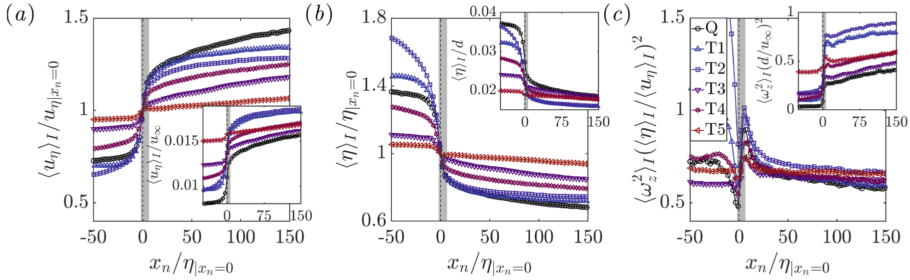

Fig. 3. Conditional profiles of (*a*) Kolmogorov velocity scale, (*b*) Kolmogorov length scale, and (*c*) spanwise enstrophy component. The location of the TNTI and TTI outlines ($x_n = 0$) are shown with the vertical dashed black line. The vertical grey bars denote the assessed thickness of the interfacial layer.

Both the dynamics [10–12] and geometric properties [13] of the holes have been utilized to infer their origin in an Eulerian approach. In the current study, the holes are categorized according to the homogeneity of their internal flow field and their vorticity magnitude. The root-mean-square (r.m.s.) of the streamwise and lateral velocity components within the hole (u_h^{rms} and v_h^{rms} respectively) are defined as

$$u_h^{rms} = \sqrt{\overline{(u-u_h)^2}}, \quad v_h^{rms} = \sqrt{\overline{(v-v_h)^2}}, \qquad (2a,b)$$

where u_h and v_h represent the mean streamwise and lateral velocity within the hole, respectively. Kohan and Gaskin [11] previously argued that engulfed holes, trapped by large-scale structures near the jet boundary, exhibit a uniform

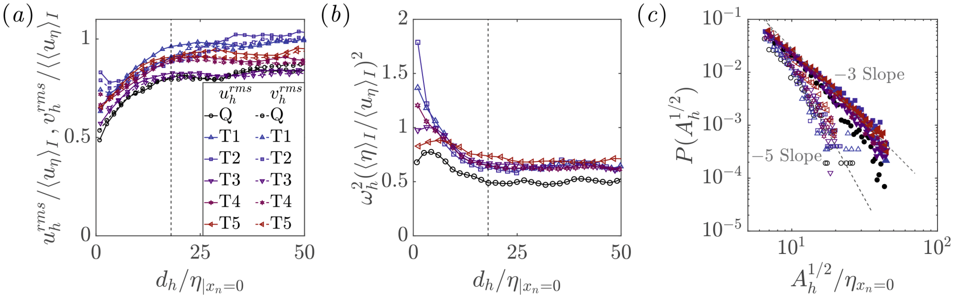

Fig. 4. Locally normalized (*a*) streamwise and lateral velocity r.m.s. and (*b*) vorticity magnitude inside the holes as functions of d_h. (*c*) P.d.f. of the characteristic size of the holes. Hollow and filled markers denote holes with $d_h < 18\,\eta_{|x_n=0}$ and $d_h > 18\,\eta_{|x_n=0}$, respectively.

scalar field, while the deeper-positioned, internally generated holes show high but identical levels of scalar fluctuations (see their Fig. 4*a*). Analogously, Fig. 4(*a*) presents the evolution of u_h^{rms} and v_h^{rms} as a function of the Euclidean distance of the hole centroid to the wake boundary (d_h), revealing a distinct separation of the holes into two regions at a distance of 18 $\eta_{|x_n=0}$, irrespective of the strength of free-stream turbulence intensity. This observed trend is consistent with that seen in Fig. 4(*b*), where the vorticity magnitude within the holes, ω_h, normalized by the local Kolmogorov scales, initially decreases until reaching its core value (see Fig. 3*c*) beyond a distance of 18 $\eta_{|x_n=0}$ from the TNTI and TTI outlines.

One may now surmise that holes with $d_h < 18\,\eta_{|x_n=0}$ are induced by engulfment, as the deeper holes exhibit identical (in)homogeneity in their velocity field regardless of their distance from the wake boundary. The p.d.f.s of the characteristic size of the holes, $A_h^{1/2}$, are thus examined to verify this notion. Indeed, the −3 power-law distribution of the anticipated core holes (filled markers in Fig. 4*c*) is analogous to that of holes in HIT [9], while the −5 power-law of the supposedly engulfed holes (hollow markers in Fig. 4*c*) resembles that of the interfacial holes in axisymmetric jets [11]. These findings suggest that holes with $d_h < 18\,\eta_{|x_n=0}$ are related to engulfment, whereas holes with $d_h > 18\,\eta_{|x_n=0}$ are likely generated in the turbulent core region of the wake. The subsequent engulfment analysis, therefore, only considers holes near the TNTI and TTI outlines, that is, those with $d_h < 18\,\eta_{|x_n=0}$.

The local contribution of engulfed to total mass flux is assessed as [11,13,19]

$$\frac{\dot{Q}_e}{\dot{Q}} = \frac{L_z \int_{y_{min}}^{y_{max}} \overline{u(y)}\,\mathcal{P}_e(y)\,\mathrm{d}y}{L_z \int_{y_{min}}^{y_{max}} \overline{u(y)}\mathcal{P}(y)\,\mathrm{d}y}, \tag{3}$$

which is averaged across the streamwise extent of the field of view (FOV). In the aforementioned relation, $\overline{u(y)}$ and L_z are the mean streamwise velocity and an arbitrary length along the vertical direction, respectively, while y_{min} and y_{max} are the lower and upper lateral bounds of the FOV. $\mathcal{P}(y)$ and $\mathcal{P}_e(y)$ rep-

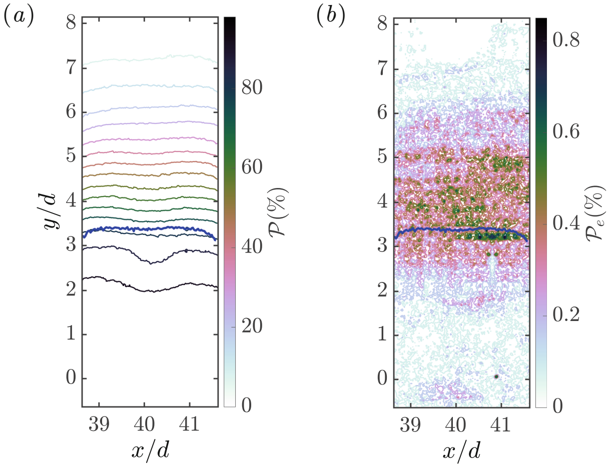

Fig. 5. Contour maps of (a) $\mathcal{P}$ and (b) $\mathcal{P}_e$ for case T5. The mean position of the TTI outline is shown with the blue line.

resent, respectively, the probability of a given fluid element at location y to be within the wake and to be within a hole with $d_h < 18\,\eta_{|x_n=0}$. As an example, Fig. 5 depicts the contour map of these two probabilities and the mean position of the TTI outline for case T5. The fact that both probabilities span the complete lateral extent of the FOV hints at the large-scale meandering of the wake in extreme free-stream turbulence. The value of $\dot{Q}_e/\dot{Q}$ never exceeds 1% in any of the cases, indicating the negligible role of local engulfment in the turbulent/turbulent entrainment paradigm.

4 Conclusions and Further Discussion

The findings of this study partially corroborates the possible universality of the effect of external turbulence on free shear flows. A simple visual inspection of Fig. 2 reveals that the wake boundary becomes more ‘jagged’ with increasing external turbulence intensity. This mirrors the result of [14–16], which established a positive correlation between the roughness of the jet/wake boundary and background intensity. Given that the p.d.f.s of the characteristic size of the engulfed holes follow the same power-law in both jets and wakes, irrespective of the background conditions (e.g. compare Fig. 4c to Fig. 4b of [11]), one can infer that the governing physics of engulfment across TTIs exhibit some universality in free shear flows. The same is true for the internally-generated holes which also follow a similar power-law in both jets and wakes. In the case of a round jet exposed to external turbulence with intensities $0.15 \leqslant \xi \leqslant 0.26$, large-scale engulfment was found to be secondary to nibbling and/or turbulent diffusion at the interface, notwithstanding the more significant role of engulfment in the turbulent ambient [11]. This result is reproduced herein, even when the intensity of the ambient surpasses that of the wake. These findings refute the hypothesis of [19], which regarded engulfment as the dominant entrainment mechanism in perturbed free shear flows in the far-field.

Acknowledgments. The authors would like to acknowledge Dr. Jiangang Chen for providing the dataset and for fruitful discussions during the preparation of this paper. This effort was supported by the Natural Sciences and Engineering Research Council of Canada discovery grant (RGPIN 2022-03438) and Mitacs Globalink research award (FR109660/IT36450).

References

1. Yule, A.J.: Large-scale structure in the mixing layer of a round jet. J. Fluid Mech. **210**, 413–432 (1978)
2. Corrsin, S., Kistler, A.L.: Free-stream boundaries of turbulent flows. NACA Technical report, 1244, 1033 (1955)
3. Brown, G.J., Roshko, A.: On density effects and large structure in turbulent mixing layers. J. Fluid Mech. **64**(4), 775–816 (1974)
4. Dahm, W.A., Dimotakis, P.E.: Measurements of entrainment and mixing in turbulent jets. AIAA J. **25**(9), 1216–1223 (1987)
5. Mathew, J., Basu, A.: Some characteristics of entrainment at a cylindrical turbulence boundary. Phys. Fluids **14**(7), 2065–2072 (2002)
6. Westerweel, J., Fukushima, C., Pedersen, J.M., Hunt, J.C.R.: Mechanics of the turbulent-nonturbulent interface of a jet. Phys. Rev. Lett. **95**(17), 174501 (2005)
7. Taveira, R.R., Diogo, J.S., Lopes, D.C., da Silva, C.B.: Lagrangian statistics across the turbulent-nonturbulent interface in a turbulent plane jet. Phys. Rev. E. **88**(4), 043001 (2013)
8. Kohan, K.F., Gaskin, S.: The effect of the geometric features of the turbulent/nonturbulent interface on the entrainment of a passive scalar into a jet. Phys. Fluids **32**(9), 095114 (2020)
9. da Silva, C.B., Taveira, R.R., Borrell, G.: Characteristics of the turbulent/nonturbulent interface in boundary layers, jets and shear-free turbulence. J. Phys.: Conf. Ser. **506**(1), 012015 (2014)
10. Xu, C., Long, Y., Wang, J.: Entrainment mechanism of turbulent synthetic jet flow. J. Fluid Mech. **958**, A31 (2023)
11. Kohan, K.F., Gaskin, S.J.: Scalar mixing and entrainment in an axisymmetric jet subjected to external turbulence. Phys. Fluids **36**(10), 105142 (2024)
12. Long, Y., Wang, J., Pan, C.: Universal modulations of large-scale motions on entrainment of turbulent boundary layers. J. Fluid Mech. **941**, A68 (2022)
13. Jahanbakhshi, R., Madnia, C.K.: Entrainment in a compressible turbulent shear layer. J. Fluid Mech. **797**, 564–603 (2016)
14. Kohan, K.F., Gaskin, S.J.: On the scalar turbulent/turbulent interface of axisymmetric jets. J. Fluid Mech. **950**, A32 (2022)
15. Kankanwadi, K., Buxton, O.R.H.: Turbulent entrainment into a cylinder wake from a turbulent background. J. Fluid Mech. **905**, A35 (2020)
16. Chen, J., Buxton, O.R.H.: Spatial evolution of the turbulent/turbulent interface geometry in a cylinder wake. J. Fluid Mech. **969**, A4 (2023)
17. Buxton, O.R.H., Chen, J.: The relative efficiencies of the entrainment of mass, momentum and kinetic energy from a turbulent background. J. Fluid Mech. **977**, R2 (2023)

18. Zecchetto, M., da Silva, C.B.: Universality of small-scale motions within the turbulent/non-turbulent interface layer. J. Fluid Mech. **914**, A9 (2021)
19. Westerweel, J., Fukushima, C., Pedersen, J.M., Hunt, J.C.R.: Momentum and scalar transport at the turbulent/non-turbulent interface of a jet. J. Fluid Mech. **631**, 199–230 (2009)

Conditional Mean Velocity and Vorticity Fields in the Vicinity of the Turbulent/Turbulent Interface of a Planar Wake

Jiangang Chen(✉) and Oliver R. H. Buxton

Department of Aeronautics, Imperial College London, South Kensington Campus,
London SW7 2AZ, UK
`jiangang-chen@outlook.com`, `o.buxton@imperial.ac.uk`

Abstract. This work reports an experimental investigation of the spatial evolution of the conditionally-averaged velocity and vorticity fields in the vicinity of the turbulent/turbulent interface (TTI) in the planar wake of a circular cylinder. The wake was exposed to various turbulent backgrounds featuring different turbulence intensities and integral length scales. Combined simultaneous particle image velocimetry (PIV) and planar laser induced fluorescence (PLIF) measurements were conducted at an inlet Reynolds number of 3800 to capture the velocity and vorticity fields close to the interface. The result implies that TTIs can establish two layers when the background turbulence is sufficiently intense, which distinguishes TTIs from the turbulent/non-turbulent interface (TNTI). The two layers in TTIs have equal thickness of about 13 local Kolmogorov length scales, which is approximately equal to the thickness of the turbulent sublayer in a TNTI at sufficiently high Reynolds number and suggests that there is no viscous superlayer in TTIs.

1 Introduction

In turbulent flows, there exists a thin layer demarcating the primary flow from the ambient fluid, which is usually referred to as the turbulent/non-turbulent interface (TNTI) when the background flow is non-turbulent and irrotational [6, 14]. More generally, when the background flow is turbulent, it has been confirmed that the bounding interface of the primary flow persists and is referred to as the turbulent/turbulent interface [10,12,13]. In contrast to the extensive studies on TNTIs in the past decades, the investigation of TTIs has only started to intensify in recent years, despite their widespread existence in many geophysical and industrial flows.

Due to the presence of turbulence on both sides of the interface, the physics of the TTI is quite different from the TNTI. For example, the essential feature of a TNTI is the existence of a sharp vorticity jump when the interfacial layer is traversed from the freestream to the primary flow. The initiation of the vorticity jump is understood as a reflection of the mechanism that vorticity can only

J. Wang and I. Marusic (Eds.): IUTAM-TNTI 2024, IUTAM Bookseries 45, pp. 203–214, 2025.
https://doi.org/10.1007/978-3-031-78151-3_16

spread into non-rotational freestream by local viscous diffusion [16]. However, in the situation of the TTI, Kankanwadi & Buxton [11] experimentally proved that the magnitude of viscous diffusion of vorticity is more than one order of magnitude smaller than that of the inertial vorticity stretching throughout the TTI. This observation suggests that vorticity stretching, by which vorticity in the vicinity of the interface is produced and amplified, overwhelms the effect of viscous diffusion in sustaining the vorticity jump across the interface.

Given the remarkable difference in the physics between TNTIs and TTIs, it would be intriguing to see how differently the velocity and vorticity fields in the vicinity of TTIs and TNTIs behave. In particular, in contrast to the dominant viscous diffusion in the outer-most portion of a TNTI giving rise to a viscous superlayer [14], the presence of freestream turbulent is expected to diminish the viscous superlayer in a TTI [9]. This could lead to a different scaling of the thickness of the two kinds of interfacial layers. Additionally, the behavior of both TNTIs and TTIs may also be affected by the large-scale motions in the bulk of the primary flow. Chen & Buxton [4] indeed observed that in a cylinder wake, there is a transition position of wake spreading rate for both TNTIs and TTIs at about 15 diameters downstream of the cylinder, where the organized von Kármán vortices weaken substantially. It would thus also be interesting to examine how the velocity and vorticity fields nearby the interface are affected by the bulk coherent motions and how this effect evolves as the coherent motions decay downstream, which has not been addressed in previous studies of TTIs.

2 Experimental Setup and Interface Detection

The experiments were similar to those in [3] and were conducted in the water flume of the hydrodynamics laboratory of the Department of Aeronautics at Imperial College London. A cylinder with a diameter $d = 1\,\text{cm}$ was vertically mounted in the middle of the test section (Fig. 1a). The Reynolds number based on the incoming velocity U_∞ and d was approximately 3800. There was a turbulence-generating grid installed upstream of the cylinder to generate the background turbulence. Four different grids (including two regular grids and two fractal grids, see [10] for details of the grids) were utilised and the distance between the grid and the cylinder was adjusted such that the integral length scale $\mathcal{L}(\equiv \int_0^{r_0} R_{12}(r)\mathrm{d}r$ where $R_{12}(r)$ is the correlation function between velocity fluctuations $u'(x, y)$ and $u'(x, y + r)$, and r_0 is the first zero-crossing of R_{12}) and the turbulence intensity $k(\equiv \sqrt{(u'^2 + v'^2)/2}/U_\infty)$ of the background turbulence are varied independently (Fig. 1c). The cases are divided into three groups based on the background turbulence intensity and case 1a is the case with no grid placed upstream which serves as the closest representation of a TNTI under our experimental conditions. The variation of TI and L with respect to their values at $x/d = 20$ within the field of view is about 2% and $0.1d$ for the cases of regular grids (cases 2a, 3a, 3b in Fig. 1c); for the cases of fractal grids (cases 1b, 1c and 2b), the variations are about 1% for TI and $0.5d$ for L, which do not affect the relative positions of the cases in Fig. 1(c).

Simultaneous measurements of combined PIV and PLIF were carried out with measurements centred at five streamwise positions, *i.e.* $x = 6.5d$, $10d$, $20d$, $30d$ and $40d$, where x is the streamwise coordinate (Fig. 1b). In the PIV system, two cameras (Phantom V641 with sensor resolution of 2560×1600 pixels) were arranged in the cross-stream (y) direction. They together formed a combined field of view (FoV) of $9d \times 3d$ with a $1d$ overlap in the y direction (Fig. 1b). The PLIF camera was located on the opposite side of the flume to the PIV cameras (Fig. 1a) with a field of view large enough to encompass that of the combined PIV FoV (Fig. 1d).

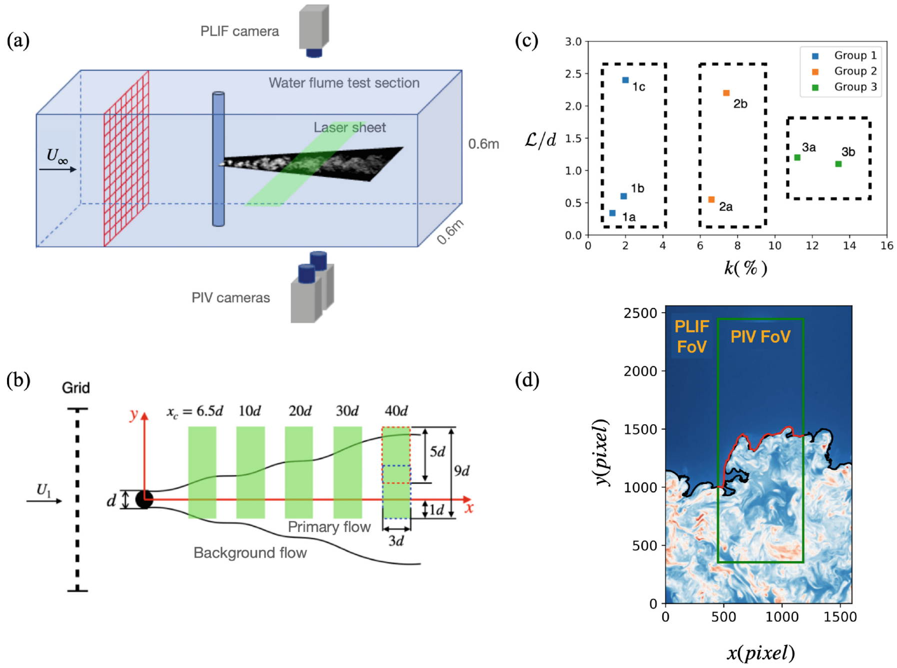

Fig. 1. (a) Conceptual sketch of the experimental setup. (b) Configuration of the measurement fields of view. (c) Parameter space (k, $\mathcal{L}$) of the background flow in the $x/d = 20$ measurement station. The dashed rectangles highlight the cases of the three groups. (d) The determined interface (black line) in a typical PLIF image and the resultant interface-envelope (red line) in the PIV field of view.

A high-speed Nd:YLF laser (Litron LDY304) was used to illuminate the flow which was seeded with hollow glass spheres with a mean diameter of 10μm. A fluorescent dye, Rhodamine 6G, was employed to demarcate the wake region of the cylinder from the background flow. The dye has a high Schmidt number (Sc, about 2500 in water) which ensures that the molecular diffusion of the dye is negligibly small compared to the turbulent motions. The dye was released into the wake from a hole in the rear surface of the cylinder with the

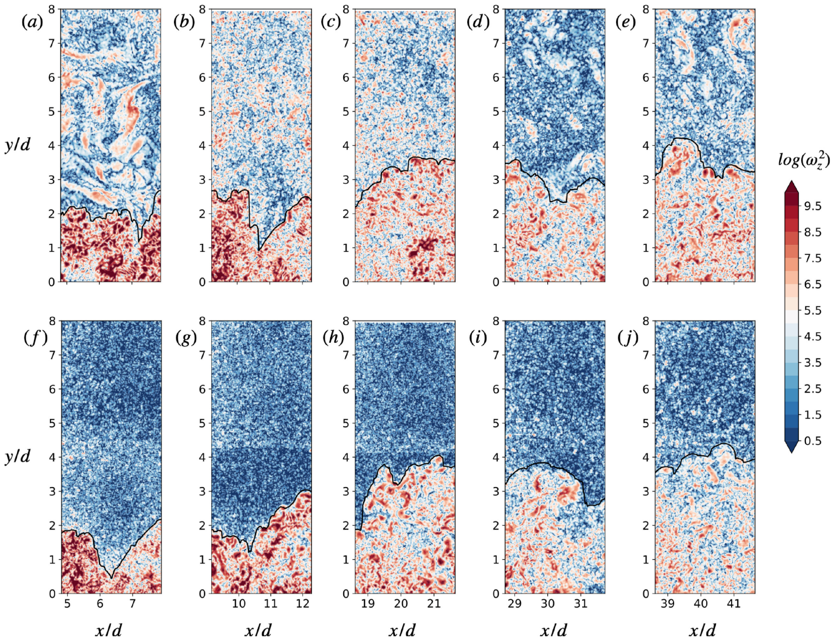

Fig. 2. Examples of a TTI (case 2b, (a)–(e)) and a TNTI (case 1a, (f)–(j)) at $x/d =$ 6.5 (a, f), 10(b, g), 20 (c, h), 30 (d, i), and 40 (e, j).

aid of a micro-dosing pump (Bürkert 7615). This method has been previously shown to faithfully mark the region occupied by the wake fluid from almost immediately downstream of the cylinder [10].

The acquisition frequency f_{ac} of both PIV and PLIF cameras was 200 Hz and 5000 velocity fields/concurrent PLIF images were captured for each measurement. The PIV processing was conducted via the programme PIVlab, an open-source toolbox of Matlab, which features multi-pass and multi-grid with image deformation [17]. Four passes were carried out during the analysis and the final interrogation window size was 24 × 24 pixels with 50% overlap, which corresponds to a $0.48 \times 0.48\,\mathrm{mm}^2$ interrogation window in physical space. The spatial resolution quantified with the ratio of interrogation window size L_{IW} to the Kolmogorov length scale on the interface η_I ranges from about 4–5 in the very near wake to about 2–4 in the farthest downstream position, and the temporal resolution, quantified with the ratio of the period of acquisition $T_{ac}(= 1/f_{ac})$ to the Kolmogorov time scale on the interface $\tau_{\eta,I}$ is always below 0.6 for all the cases at all measured positions.

The interface is identified from the boundary of the fluorescent dye captured by the PLIF camera [10]. In each PLIF image, the magnitude of the gradient of the normalised light intensity is calculated as $\Gamma^* \equiv |\nabla\phi^*|$ where ϕ^* is the light intensity normalized by the mean light intensity at the same x-location along the wake centerline. A threshold of Γ^* is determined in a similar way as in

[4]. In this work, envelope of the interface (red line in Fig. 1d) is employed to study the conditional mean of the velocity and vorticity fields. Typical examples of the determined interface position at each measured x/d location of one TTI case (case 2b in Fig. 1b) and the TNTI case (case 1a) are shown in Fig. 2. From $x/d = 6.5$ to $x/d = 40$, both the interfaces of the turbulent/turbulent case and the turbulent/non-turbulent case are effectively captured and agree well with those identified visually from the vorticity field.

3 Results and Discussion

In this work, conditional-averaging with respect to the position of the determined interface envelope, denoted with $\langle \cdot \rangle$, is conducted spatially over the streamwise extent of the identified interfaces in each PIV FoV, as well as temporally *i.e.* over all PIV velocity fields, on the condition of distance-to-the-interface along the interface-normal direction. The statistics are generated over the range $-0.4d \leq \xi_n \leq 0.4d$ with the origin set to the detected interface location. The direction pointing into the wake region is defined as being positive ($\xi_n > 0$).

Figure 3 shows the distributions of the conditionally-averaged streamwise and lateral velocities $\langle U \rangle$ and $\langle V \rangle$ for all seven cases denoted in Fig. 1c at various measurement stations from $x/d = 6.5$ to 40. $\langle U \rangle$ is normalized by the mean velocity at the interface $\langle U \rangle_I$, so that the mean shear $\mathrm{d}\langle U \rangle/\mathrm{d}\xi_n$ throughout the interfacial layer for different cases can be compared, which is of significance in affecting the vorticity jump across the interface[18]. Although the mean shear for all cases decays noticeably as the flow evolves downstream, freestream turbulence (FST) has a substantial effect on the mean shear strength, especially in the far

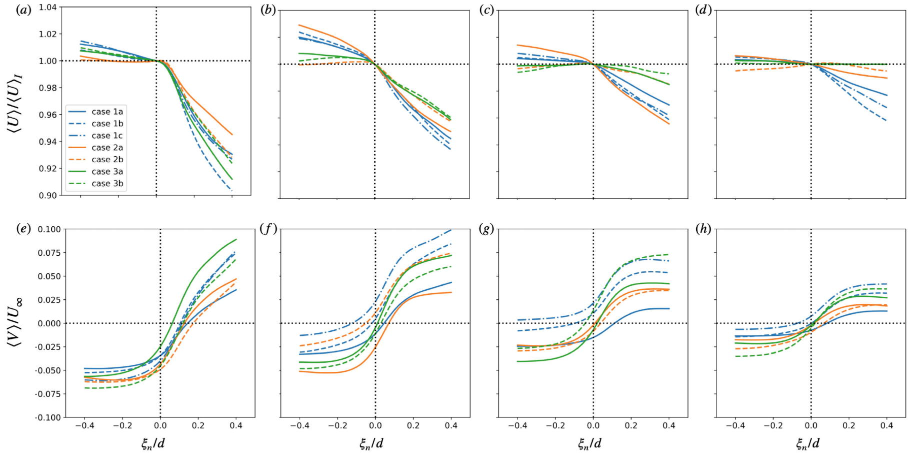

Fig. 3. Streamwise evolution of the conditionally-averaged velocity (a–d) $\langle U \rangle / \langle U \rangle_I$ and (e–h) $\langle V \rangle / U_\infty$ across the TNTI and TTIs for all cases at (a, e) $x/d = 6.5$, (b, f) 10, (c, g) 20 and (d, h) 40.

field of the wake. At $x/d = 6.5$ (Fig. 3a), $\langle U\rangle/\langle U\rangle_I$ for all cases drops at a similar rate nearby to the interface ($\xi_n \approx 0$) on the wake side. It implies that the large-scale forcing of the wake itself dictates the mean shear across the interfacial layer, such as the high strain rate near to the wake boundary enhanced by the strong rotational motion of the von Kármán vortices. Further downstream (Fig. 3b–d), the importance of the FST seems to increase. Note that the cases with higher freestream turbulence intensities (group 3 in Fig. 1c) generally degrade faster than those with lower ones (groups 1 or 2 in Fig. 1c). Especially at $x/d = 40$ (Fig. 3d), the mean shears of cases 3a and 3b are almost imperceptible, while the cases of group 1 still maintain a noticeable mean shear with cases in group 2 lying somewhere in between.

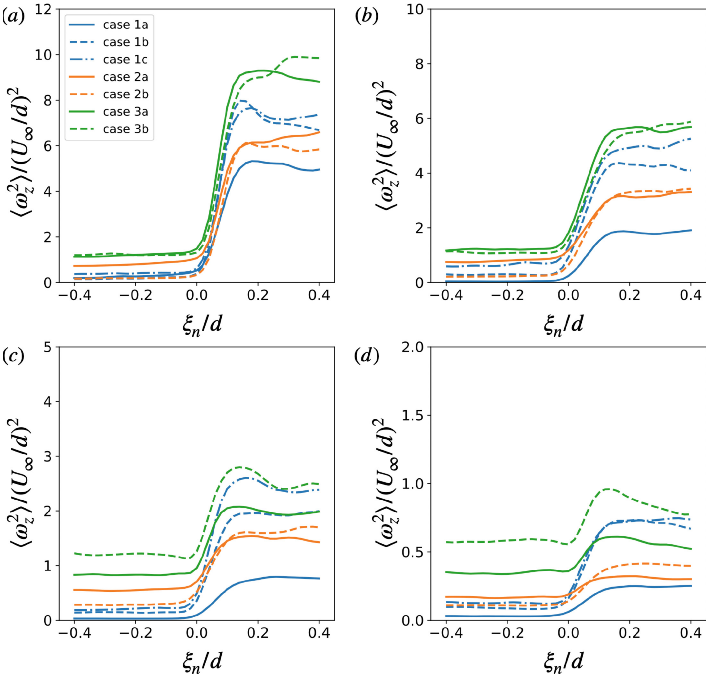

Fig. 4. Conditionally-averaged enstrophy $\omega_z^2/(U_\infty/d)^2$ at $x/d =$ (a) 6.5, (b) 10, (c) 20 and (d) 40 for all cases.

Compared to the rapid change of the streamwise velocity across the interfacial layer, the transverse velocity $\langle V\rangle/U_\infty$ crosses the layer more continuously (Fig. 3e-h). For all cases, $\langle V\rangle/U_\infty$ generally displays negative values on the freestream side of the interface ($\xi_n < 0$) and positive values on the wake side ($\xi_n > 0$), which indicates that the local velocity field tends to compress the TNTI/TTI. The positive $\langle V\rangle/U_\infty$ on the wake side reflects the transverse spreading of the wake towards the ambient freestream, and the negative $\langle V\rangle/U_\infty$ outside the interface manifests the ambient fluid moving toward the wake due to the entrainment into the wake [2]. Note that at $x/d = 6.5$ (Fig. 3e) $\langle V\rangle/U_\infty$ changes sign, for all cases, slightly towards the wake-side of the interface ($\xi_n \geq 0$). We confirmed that the zero-position of $\langle\ V\rangle(\xi_n)$ for each case coincides with the location of the maximum mean shear $\mathrm{d}\langle U\rangle/\mathrm{d}\xi_n$, particularly evident when the background turbulence is not intense. As x/d increases to 40 (Fig. 3h), in accordance with the reduced mean shear (Fig. 3d), the zero-position of $\langle V\rangle/U_\infty$ evolves gradually towards the defined-interface position ($\xi_n = 0$).

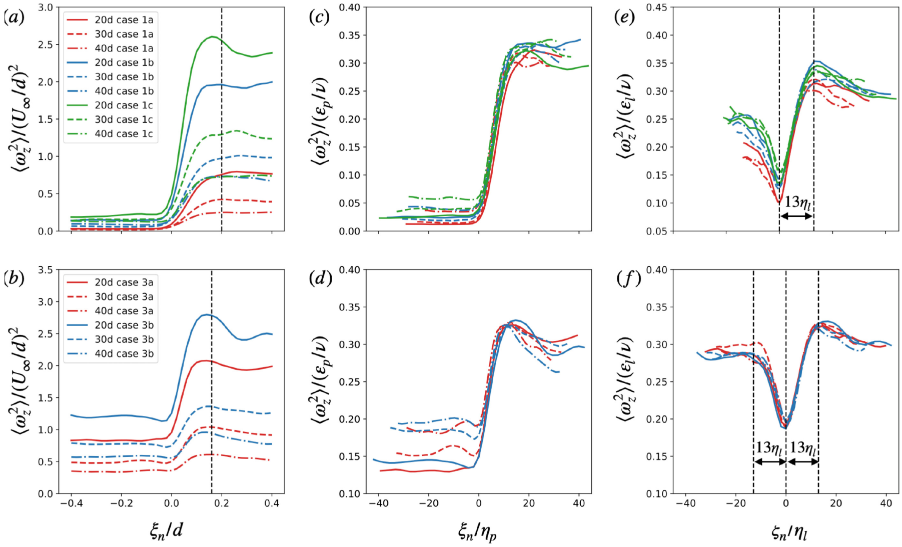

Fig. 5. Scaling of $\langle\omega_z^2\rangle$ in low (a, c, e) and high (b, d, f) background turbulence intensities. (a) and (b) show $\langle\omega_z^2\rangle$ and ξ_n normalised with invariant length/time scales d and U_∞. (c) and (d) show $\langle\omega_z^2\rangle$ normalised by the plateau value of the dissipation rate (c.f. the plateau within the wake-side of the TTIs for $\langle\omega_z^2\rangle$ in Fig. 5a, b) and ξ_n normalised by the Kolmogorov length scale formed from the plateau dissipation rate. (e) and (f) are normalised with the local dissipation rate $\varepsilon_l(\xi_n)$.

The strong streamwise evolution of the conditionally-averaged velocity field in proximity to the interface suggests that there is also an intense streamwise variation in the vorticity field, which could have a direct influence on the small-scale entrainment processes across the interface [7,19]. The conditionally-averaged vorticity $\langle\omega_z^2\rangle$ for the various cases of TTIs and the TNTI, from $x/d = 6.5$ to $x/d = 40$, is shown in Fig. 4. As expected, there is a clear jump of the vorticity initiating at the outermost surface of the interface ($\xi_n = 0$) for all cases, although the magnitude of the jump decays as the flow progresses downstream. For all measurement locations, the vorticity jump across the TTIs is generally larger than that across the TNTI, similar to the observation made in [10]. It is interesting to see that at the farthest downstream location $x/d = 40$ (Fig. 4d), for some TTI cases (e.g. cases 3a and 3b), even though the background vorticity level is comparable to that inside the wake and the mean shear of the interfacial layer is negligibly small (case 3a and 3b in Fig. 3d), the vorticity jump still exists.

In light of the evident decay of the magnitude of the vorticity jump across the TTIs as they evolve downstream, a particularly interesting question is whether the scaling of the vorticity varies in this process? We first examine the scaling of the vorticity from $x/d = 20$ to 40 in Fig. 5. In this figure, the jump of $\langle \omega_z^2 \rangle$ for the cases with low (Fig. 5a, c, e) and high (Fig. 5b, d, f) background turbulence intensities are presented separately. Consistent with Fig. 4, the vorticity jump for all cases decreases monotonically downstream when they are normalised by the invariant quantities of incoming velocity U_∞ and cylinder diameter d (Fig. 5a, b). As vorticity predominantly resides in the small scales, it is natural to expect the vorticity field close to the interface to scale with the Kolmogorov scales. Here we compare two possible choices of the Kolmogorov length scale, based on different dissipation rates. One possible choice is a dissipation rate representative of the turbulent core of the wake, but still in proximity to the interface. For this we select the dissipation rate ε_p at the ξ_n-position where the profile of $\langle \omega_z^2 \rangle$ plateaus on the wake-side of the interfaces, as indicated by the dashed line in Figs. 5(a) and (b). Here ε_p is estimated from the PIV measurements by using a locally axisymmetric assumption [5]. With such a normalisation, based on ε_p, the distributions of $\langle \omega_z^2 \rangle$ for the various cases with various background turbulence intensities from $x/d = 20$ to $x/d = 40$ follow each other fairly well on the wake-side of the interfaces ($\xi_n/\eta_p > 0$ in Fig. 5(c) and (d), where η_p is the Kolmogorov length scale based on ε_p).

However, it is clear that in the background-side of the TTI, outside of the wake ($\xi_n/\eta_p < 0$), the vorticity field does not scale with the Kolmogorov scale from the turbulent core of the wake, especially when the background turbulence intensity is high (Fig. 5d). This is not unexpected since the vorticity fields separated by the interface feature different organizations and magnitudes [11]. Zecchetto & da Silva [20] reported that the statistics of the enstrophy across TNTIs universally scale with the local Kolmogorov velocity and length scales for different free-shear flows. Following their method, we normalise $\langle \omega_z^2 \rangle$ of the examined cases using the local dissipation rate (ε_l) as a function of ξ_n-position in Figs. 5(e) and (f). It is interesting to see that the shape of $\langle \omega_z^2 \rangle$ for the various cases are quite different from those normalised by the dissipation rate from the wake core in Fig. 5(c) and (d), especially in the background-region outside of the wake ($\xi_n < 0$). When the background turbulence intensity is low (Fig. 5e), the distributions of $\langle \omega_z^2 \rangle$ for different cases diverge widely; on the contrary, for the cases with high background turbulence intensity (Fig. 5f), the distributions of $\langle \omega_z^2 \rangle$ outside the wake ($\xi_n < 0$) collapse, similarly to those within the wake ($\xi_n > 0$). A similar symmetric enstrophy profile of $\langle \omega^2 \rangle$ was also actually observed in a recent direct numerical simulation of a TTI in grid-generated shear-free turbulence [13].

In contrast to the distinct scaling of the vorticity distribution from $x/d = 20$ to $x/d = 40$, the scenario in the near wake, e.g. at $x/d = 6.5$ and $x/d = 10$, is quite different, as shown in Fig. 6. At these locations, the pro-

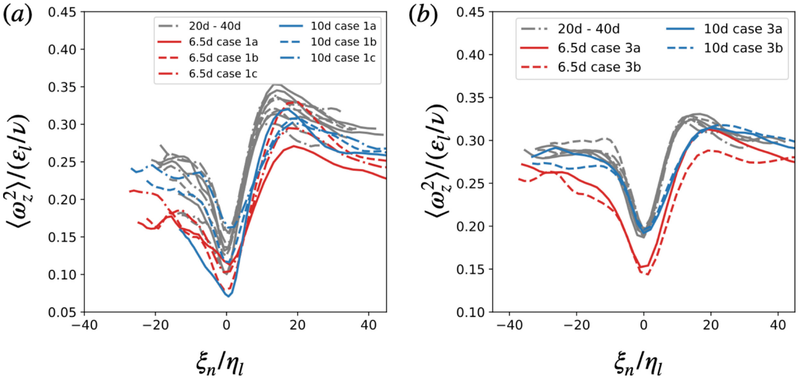

Fig. 6. Comparison of the scaling of $\langle\omega_z^2\rangle$ at $x = 6.5d$ and $10d$ with the measurement stations further downstream.

files of $\langle\omega_z^2\rangle/(\varepsilon_l/\nu)$ for cases with low (Fig. 6a) and high (Fig. 6b) background turbulence intensities evidently depart from their corresponding collapsed distributions further downstream ($20 \le x/d \le 40$), notwithstanding the profiles having a similar shape.

In summary, the structure of TTIs seems to be different from that of the TNTI in that there are two distinct layers established in the former (Fig. 5f) with one on each side of the defined-interface ($\xi_n = 0$) whereas contrastingly there is only one distinct layer formed in the latter (case 1a in Fig. 5e). The two layers of the TTIs seemingly arise from different physical mechanisms. The layer on the wake side ($\xi_n > 0$) is apparently a manifestation of the rapid vorticity jump from the ambient flow to the wake (Fig. 5a, b). As such a vorticity jump does not exist on the ambient-flow side of the layer ($\xi_n < 0$ in Fig. 5a, b), then the normalisation must be responsible. Indeed we have identified that the dissipation rate (ε_l) is highly inhomogeneous in the ambient flow immediately adjacent to the interface when the background turbulence is intense (not shown here for brevity, to be presented in the conference). Note that for an ideal TNTI, $\langle\omega_z^2\rangle/(\varepsilon_l/\nu)(\xi_n < 0) = 0$, as shown in the simulation of [20]. Each layer of the TTI has a thickness of approximately $13\eta_l$ where η_l is the local Kolmogorov length scale, as indicated by the dashed-lines in Fig. 5(e, f). This thickness seems to be the same for both the TNTI and the various TTIs at the measurement locations of $x/d = 20$, 30 and 40, at least for the current experimental configuration. Note that previous work has argued that the universal scaling for the thickness of the turbulent sublayer of a TNTI is about 12η [15] at sufficiently high Reynolds number, whilst our previous work showed that TTIs do not feature a viscous sublayer, *i.e.* they consist entirely of a turbulent sublayer where inertial vorticity stretching is the dominant term of the enstrophy transport equation [11]. This result thus suggests that TTIs in sufficiently intense turbulent backgrounds manifest as two adjacent turbulent sublayers that are driven by different mechanisms responsible for the smooth adjustment of the enstrophy and dissipation levels from the characteristic values within the core of the primary flow (wake) to the turbulent background.

4 Summary and Conclusions

In this work, we studied the conditionally averaged velocity and vorticity fields in the vicinity of the turbulent/turbulent interface of a cylinder wake in various streamwise positions at $x/d = 6.5$, 10, 20, 30 and 40. A combined measurement of PIV and PLIF was carried out to capture the velocity and vorticity fields of various TTIs and a TNTI.

The mean shear is strongest in the near wake and diminishes gradually downstream. It is interesting to see that the cases with higher background turbulence intensity attain a virtually-zero mean shear across the TTI earlier than those with lower background turbulence intensity (Fig. 3a–d). Similarly, the lateral velocity $\langle V \rangle$ (Fig. 3e–h), is notably larger in the near field ($x/d = 6.5$) than it is much farther downstream ($x/d = 40$). $\langle V \rangle$ changes sign as the interfacial layer is traversed, indicating that the velocity field in proximity to the interfaces tends to compress the interfacial layer. This could be partially attributed to the influence of vortices created by the mean shear forcing [1,8]. In the far-field of the wake at $x/d = 40$, the mean shear of the interfaces is greatly diminished (Fig. 3d) and accordingly $\langle V \rangle$ at the interface-position for all cases reduces to a value very close to zero (Fig. 3h).

The vorticity field in close proximity to the various interfaces, which has a direct influence on the entrainment velocity [7,18], also displays distinct features in the near and far fields of the wake. The distributions of $\langle \omega_z^2 \rangle$ start to scale with the local Kolmogorov scales from at $x/d = 20$ and beyond. It is intriguing to see that the non-dimensional conditionally-averaged enstrophy displays jumps on both the wake- and background-side of TTIs when the background turbulence intensity is sufficiently high (e.g. cases in group 3 in Fig. 5). The former is driven by a discontinuity of the vorticity field across the interfaces, while the latter is driven by the inhomogeneous dissipation field from the interface to the background turbulence. Such behaviour is clearly distinct from a TNTI. In this manifestation, the two layers of the TTIs have equal thicknesses of about 13 η_l which is roughly equal to the thickness noted for the turbulent sublayer of TNTIs at sufficiently high Reynolds number [15]; a finding that is in keeping with our previous observation that TTIs do not have a viscous sublayer [9] which is characteristic of the outermost, viscous-dominated portion of a TNTI. This conclusion should be tempered somewhat by the observation that our closest approximation to a TNTI, case 1a, has interface thickness about 13η (Fig. 5e), however this can potentially be explained by the fact that the background turbulence intensity in our hydrodynamics flume is around 1% (see Fig. 1c), *i.e.* it is non-zero.

References

1. Balamurugan, G., Rodda, A., Philip, J., Mandal, A.C.: Characteristics of the turbulent non-turbulent interface in a spatially evolving turbulent mixing layer. J. Fluid Mech. **894**, A4 (2020)
2. Bisset, D.K., Hunt, J.C.R., Rogers, M.M.: The turbulent/non-turbulent interface bounding a far wake. J. Fluid Mech. **451**, 383–410 (2002)
3. Buxton, O.R.H., Chen, J.G.: The relative efficiencies of the entrainment of mass, momentum and kinetic energy from a turbulent background. J. Fluid Mech. **977**, R2 (2023)
4. Chen, J.G., Buxton, O.R.H.: Spatial evolution of the turbulent/turbulent interface geometry in a cylinder wake. J. Fluid Mech. **969**, A4 (2023)
5. Chen, J.G., Cuvier, C., Foucaut, J.M., Ostovan, Y., Vassilicos, J.C.: A turbulence dissipation inhomogeneity scaling in the wake of two side-by-side square prisms. J. Fluid Mech. **924**, A4 (2021)
6. Corrsin, S., Kistler, A.L.: Free-stream boundaries of turbulent flows. NACA Tech. Rep. **1244** (1955)
7. Holzner, M., Lüthi, B.: Laminar superlayer at the turbulence boundary. Phys. Rev. Lett. **106**, 134,503 (2011)
8. Jahanbakhshi, R., Madnia, C.K.: The effect of heat release on the entrainment in a turbulent mixing layer. J. Fluid Mech. **844**, 92–126 (2018)
9. Kankanwadi, K.S.: Turbulent/turbulent entrainment: a detailed examination of entrainment, and the behaviour of the outer interface as affected by background turbulence. Ph.D. thesis, Imperial College London (2022)
10. Kankanwadi, K.S., Buxton, O.R.H.: Turbulent entrainment into a cylinder wake from a turbulent background. J. Fluid Mech. **905**, A35 (2020)
11. Kankanwadi, K.S., Buxton, O.R.H.: On the physical nature of the turbulent/turbulent interface. J. Fluid Mech. **942**, A31 (2022)
12. Kohan, K.F., Gaskin, S.J.: On the scalar turbulent/turbulent interface of axisymmetric jets. J. Fluid Mech. **950**, A32 (2022)
13. Nakamura, K., Watanabe, T., Nagata, K.: Turbulent/turbulent interfacial layers of a shearless turbulence mixing layer in temporally evolving grid turbulence. Phys. Fluids **35**, 045,117 (2023)
14. da Silva, C.B., Hunt, J.C.R., Eames, I., Westerweel, J.: Interfacial layers between regions of different turbulence intensity. Annu. Rev. Fluid Mech. **46**, 567–590 (2014)
15. Silva, T.S., Zecchetto, M., Da Silva, C.B.: The scaling of the turbulent/non-turbulent interface at high Reynolds numbers. J. Fluid Mech. **843**, 156–179 (2018)
16. Tennekes, H., Lumley, J.L.: A First Course in Turbulence. MIT Press, Cambridge (1972)
17. Thielicke, W., Sonntag, R.: Particle image velocimetry for matlab: accuracy and enhanced algorithms in pivlab. J. Open Res. Softw. **9**, 12 (2021)
18. Wolf, M., Holzner, M., Lüthi, B., Krug, D., Kinzelbach, W., Tsinober, A.: Effects of mean shear on the local turbulent entrainment process. J. Fluid Mech. **731**, 95–116 (2013)
19. Wolf, M., Lüthi, B., Holzner, M., Krug, D., Kinzelbach, W., Tsinober, A.: Investigations on the local entrainment velocity in a turbulent jet. Phys. Fluids **24**, 105,110 (2012)
20. Zecchetto, M., da Silva, C.B.: Universality of small-scale motions within the turbulent/non-turbulent interface layer. J. Fluid Mech. **916**, A9 (2021)

Turbulent/Non-turbulent Interface in a Spatially Developing Turbulent Boundary Layer Laden with Small Heavy Particle

Ping Wang[1], Qingqing Wei[1], and Xiaojing Zheng[2](✉)

[1] Department of Mechanics, Lanzhou University, Lanzhou 730000, People's Republic of China
[2] Research Center for Applied Mechanics, School of Mechano-Electronic Engineering, Xidian University, Xi'an 710071, People's Republic of China
xjzheng@lzu.edu.cn

Abstract. Direct numerical simulations of spatially developing turbulent boundary layer laden with small, heavy particles are performed at low Reynolds number. The effects of particle gravity settling on the turbulent/non-turbulent interface are discussed by comparing the new simulations with previous simulations laden with inertial particles. The results reveal that heavy particles reduced the height of the interface but increase the complexity of the interface by stretching the boundary downwards and generating extra small-scale structures. Different degrees and positions of particle accumulation beneath the interface, together the gravity settling of heavy particles, result in nonmonotonical changes of the thickness of the interface layer which is apparently different from inertia-particle cases.

Keywords: small heavy particle · two-phase boundary layer · turbulent/non-turbulent interface

1 Introduction

Particle-turbulence interaction is a topic which has attracted continual attentions over the years in the areas of industrial and the environmental flows. More often than not, the presence of particles will complicate the turbulent dynamics through direct and/or indirect modulation of turbulent statistics and structures. Previous investigations for wall-bounded turbulent shear flows have addressed that turbulent modulations by particles can occur at any wall-normal position, ranging from viscous sublayer to logarithmic region, and depend on an extensive set of parameters [1], of which the gravitational settling is essential because the gravity on particles is in any way inevitable in an actual multiphase flow [2, 3].

In a spatially developing turbulent boundary layer (TBL), the turbulent/non-turbulent interface (TNTI) is the thin layer of finite thickness that separates the turbulent and non-turbulent flow regions. This sharp irregular, wrinkled, irrotational boundary of the TNTI contributes significantly to the transfer of momentum, mass and energy between turbulent and potential regions [4–7]. Although the TNTI in a turbulent boundary layer

J. Wang and I. Marusic (Eds.): IUTAM-TNTI 2024, IUTAM Bookseries 45, pp. 215–225, 2025.
https://doi.org/10.1007/978-3-031-78151-3_17

was revealed to share many common features with jets, wakes and mixing layers [4], its geometry and nearby dynamics in the context of particle-laden turbulence are seldom concerned about. The only exception is Wei et al. [8] in which the effects of inertial particles (only governed by the drag force) on the TNTI were studied. It was found that the inertial particles interact with the large-scale vortices in the outer region of boundary layer turbulence, resulting in not only the accumulation of particles themselves beneath the interface but also the significantly changes in the geometric features of the TNTI.

The objective of the present study is to investigate the effect of heavy particle, whose motion is governed by both the drag force and gravity, on the features and dynamics of the TNTI. The remainder of the work is organized as follows. We introduce numerical procedures and parameters in Sect. 2. Detailed analysis of the modification of TNTI by settling heavy particles is provided in Sect. 3. The concluding remarks are given in Sect. 4.

2 Numerical Procedures and Parameters

We perform a new simulation for an incompressible two-phase boundary layer flow developing in streamwise direction over a flat, smooth no-slip wall, spatially periodic spanwise, but with non-periodic streamwise. The code uses a relatively classical fractional-step method with second-order computational accuracy [9]. Throughout the paper, x, y and z represent the streamwise, wall-normal and spanwise coordinate, u, v and w are the fluid velocity components in the three directions. t, ρ, p and ν are time, density, pressure and kinematic viscosity of the fluid, respectively. The average pressure gradient of the boundary layer flow is zero and the flow is driven by the inlet turbulence at momentum thickness Reynolds number of $Re_\theta = U_\infty \theta/\nu = 300$, where $\theta = \int_0^\infty U(1-U)dy$ is the momentum thickness, U_∞ and U are the upper free-stream velocity and the turbulent mean streamwise velocity at height y.

The computational domain (L_x, L_y, L_z) is set to be $(1536\theta_{in}, 60\theta_{in}, 80\theta_{in})$, where θ_{in} is the boundary-layer momentum thickness at the inlet plane. The mesh is (4096, 400, 256) and the corresponding grid spacing $(\Delta x^+, \Delta y^+(min), \Delta z^+)$ is $(5.0, 0.17, 4.19)$, where superscript " +" indicates the distance based on the wall unit, namely, the ratio of ν to the friction velocity,ν/u_τ, at $x/\theta_{in} = 1267.5$ where the boundary layer thick is $\delta = 30\theta_{in}$ and$Re_\tau = \delta u_\tau/\nu = 402$. One can refers to [8] for the details of turbulence calculation.

The new simulation differs from the older one mainly in particle tracking. The small (sub-Kolmogorov sized), heavy spherical particle is still simplified to mass point with a volume. Its motion is solved in the Lagrangian frame but governed by $d^2\boldsymbol{x_p}/dt^2 = d\boldsymbol{u_p}/dt = \boldsymbol{F_D}/m_p - \boldsymbol{F_G}/m_p$ in the new simulation. $\boldsymbol{F_D}/m_p = (1 + 0.15Re_p^{0.687})/\tau_p(\boldsymbol{u_{@p}} - \boldsymbol{u_p})$ and $\boldsymbol{F_G} = m_p\boldsymbol{g}$. $m_p = \rho_p \pi D_p^3/6$ is the mass of particle with diameter D_p and density ρ_p. $\tau_p = D_p^2\rho_p/18\rho\nu$ is the particle response time.$Re_p = \left|\boldsymbol{u_{@p}} - \boldsymbol{u_p}\right|D_p/\nu$ is the particle Reynolds number based on the modulus of slip velocity vector,$\left|\boldsymbol{u_{@p}} - \boldsymbol{u_p}\right|$, the difference between particle $\boldsymbol{u_p}$ and the fluid velocity $\boldsymbol{u_{@p}}$ at particle position $\boldsymbol{x_p}$ obtained by trilinear interpolation.

The particle Stokes numbers are $St = \tau_p/(\theta_{in}/U_\infty) = 2, 11, 53$. Initially, a total of 3.3×10^8 particles are randomly released within the region of $y/\theta_{in} \leq 36$ with zero-slip local velocities. The particle motion equation is solved by the third-order Runge-Kutta scheme with the same spanwise periodic condition as the fluid and similar inlet/outlet condition in the streamwise direction. For the latter, particles are continuously released from the inlet plane at a number rate the same as that exit the computational domain from the streamwise outlet plane. The feedback force of particles on the fluid is collected in each computation cell [10] to realize the two-way coupling.

A perfectly elastic collision is assumed when a particle contacts the bottom wall as in most previous direct numerical simulations. Due to the gravity settling, however, the particles are never re-entrained into the main flow in spite of experiencing rebound with lower and lower saltating trajectory. Finally, its velocity will asymptotically approach the mean fluid velocity at $\mathrm{y} = D_p/2$, contributing negligible feedback force to the fluid. This particle will be removed from the simulation after a certain time $t_p^+ = t_p/(\nu/u_\tau{}^2)$. We set $t_p^+ = 500\mathrm{St}^+\mathrm{g}^+ = 500(\tau_p/(\nu/u_\tau{}^2))(\ g/(u_\tau{}^3/\nu)$, which has been verified to be appropriate in channel turbulence [2, 3] at similar friction Reynolds number. Then, we release another particle from $y/\theta_{in} = 36$ with vertical velocity of $\tau_p g$ and zero horizontal slip velocity.

Note that the special treatments of particle boundary conditions in the streamwise and vertical direction is to keep a constant bulk particle volume fraction in the simulation domain. If the gravitational acceleration is $g = 9.8\,m/s^2$, the Froude numbers $\left(\mathrm{Fr_d} = \mathrm{u_\tau}/\tau_\mathrm{p}\mathrm{g}\right)$ for the three studied particles are 47,8.5 and 1.7, respectively.

3 Results

The direct numerical simulation database of incompressible spatially developing turbulent boundary layer laden with inertial particles [8] is used in this study for comparison. We will focus on the similarities and differences of the TNTI in the older inertial-particle simulation and the new heavy-particle simulation.

In [8], the isosurface of vorticity magnitude ω^* was used to identify the outer edge of the TNTI layer, where $\omega^* = \omega\nu\sqrt{\delta^+}/\mathrm{u}_\tau^2$ and $\omega = \sqrt{\omega_\mathrm{i}\omega_\mathrm{i}}$. The ω^* where the contours of the probability density functions (p.d.f.s) of $\log_{10}\omega^*$ interlock was selected as the vorticity threshold $\omega^*{}_\mathrm{th}$. And then the vorticity thresholds were validated by turbulent volume fraction ($\mathrm{V_T}$, the volume fraction of the turbulent region identified by $\omega^* > \omega^*{}_\mathrm{th}$) method. Although different thresholds can affect the identification of interfaces, $\omega^*{}_\mathrm{th}$ for particle-free TBL and TBLs laden with inertial particles all fall in the plateau region of $\mathrm{dV_T} \sim \mathrm{dlog}_{10}\omega^*{}_\mathrm{th}$ curves and therefore the identified interfaces are not sensitive to $\omega^*{}_\mathrm{th}$. Here we employ the same vorticity thresholds for the identification of interfaces. Figure 1 (a), (c) and (e) show the p.d.f.s of $\log_{10}\omega^*$ for turbulent boundary layer laden with heavy particles of varying inertia. Note that the plateau region of $\mathrm{dV_T} \sim \mathrm{dlog}_{10}\omega^*{}_\mathrm{th}$ curves cannot be observed (not shown here) because the interfaces are severely deformed by the settling particles. Whatever, the interlock point of the contours of the p.d.f.s of $\log_{10}\omega^*$ is still a reasonable choice since it represents the boundary between the near-wall high-vorticity region and the free flow with very low vorticity value. The same identification method can also ensure that discussions about the influence of particle gravity and inertia are based on the same foundation.

It is already known from [8] that ω^*_{th}=0.0093 for the unladen turbulent boundary layer, while those for particle-laden turbulent boundary layer are apparently increased. It is 0.011, 0.021 and 0.072 for inertial particle cases with St = 2, 11 and 53, respectively. Further, Fig. 1 shows that ω^*_{th}= 0.0525, 0.119, 0.179 for heavy particle case, indicating the significant shift of the interface into the deep turbulent region. As a matter of fact, the ordinates corresponding to ω^*_{th} are $\delta_i = 33.2\theta_{in}$, $32.5\theta_{in}$, $12.7\theta_{in}$. Figure 1(b), (d) and (f) show the two-dimensional snapshots of the spatially developing boundary layers on the x–y plane in the sub-domain of $1236 \leq x/\theta_{in} \leq 1299$ and the identified TNTI. The instantaneous distribution of particles are also presented with arrows indicating their velocity vectors ($\mathrm{v_p}$, $\mathrm{w_p}$). Several important features can be seen from this figure: the low- (St = 2) and moderate- (St = 11) inertia heavy particles distribute mainly in low-enstrophy (high-velocity) region due to the centrifugal effect of the large-scale vortex structures in the outer region of turbulent boundary layer despite that particles do not perfectly follow vortex structures any more due to the gravity settling and crossing-trajectory effect; high-inertia (St = 53) heavy particle move down almost vertically with very little spanwise motion in the potential flow region and the outer turbulent structures are apparently suppressed, as reported in previous heavy-particle-laden channel turbulence studies [3]; typical "banana-like" particle cluster can be observed beneath the TNTI which is accompanied by the distinct downward stretching of the irrotational boundary. Obviously, these features were not reported in TBL laden with inertial particles.

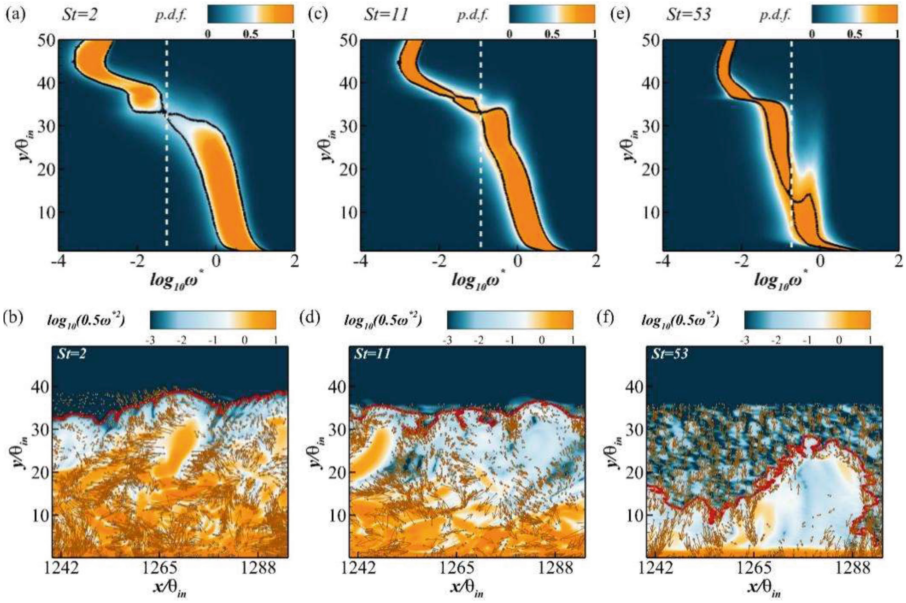

Fig. 1. The probability density functions (p.d.f.s) of $\log_{10}\omega^*$ for turbulent boundary layer laden with heavy particles (a) St = 2, (c) St = 11, (e) St = 53. (b), (d) and (f) show the enstrophy (background contours), the detected TNTI (red line) and instantaneous distribution of particles (yellow points, with arrow indicating their velocity vectors).

Figure 2 presents the conditionally averaged particle concentration $\langle C_v \rangle$ near the TNTI. Note that the conditional sampling is performed based on the TNTI local coordinate ζ which originates from the TNTI and the local direction is defined by $\mathbf{n} = -\nabla \omega^{*2} / \left| \nabla \omega^{*2} \right|$. The results from [8] for particle-free TBL and TBL laden with inertial particles are also shown for comparison. In the inertia-particle cases, particles with St = 53 displays the most significant accumulation in the region of $\zeta/\delta = -0.1 \sim 0$. It has been revealed that in this case the particle response time scale is closest to the Kolmogorov time scale of turbulence near the TNTI. Particles with high-speed vertical upward motion under the strong centrifugal effect in the turbulent side, as seen in Fig. 2(b) or Fig. 8 in [8], are blocked by the potential flow when crossing the interface. For St = 2, the particles relatively uniformly distribute in the turbulence side and their concentration monotonically decreases with ζ in the potential flow region near the TNTI. The moderate-inertia particles, St = 11, slightly accumulate beneath the TNTI. In the heavy-particle cases, however, particles with St = 11 ($\mathrm{Fr_d} = 8.5$) displays the most significant accumulation in the region of $\zeta/\delta = -0.1 \sim 0$, while the accumulation peak of particles with St = 53 ($\mathrm{Fr_d} = 1.7$) moves down to about $\zeta/\delta = -0.125(\zeta = 3.75\theta_{in})$. This is obviously attributed to the high, negative particle vertical velocity $\langle v_p \rangle$ across the TNTI, as shown in Fig. 2(b). In addition, the gravity settling effect also increase the concentration of low-inertia particles seen by the TNTI because of the decreased TNTI height. For this case, the upward centrifugal transport of particles in the turbulent region cannot be offset by gravity settling due to the large Froude number. Therefore, the conditional particle vertical velocity $\langle v_p \rangle$ is positive and a slight peak in the conditional concentration profile can be observed near $\zeta/\delta = 0$.

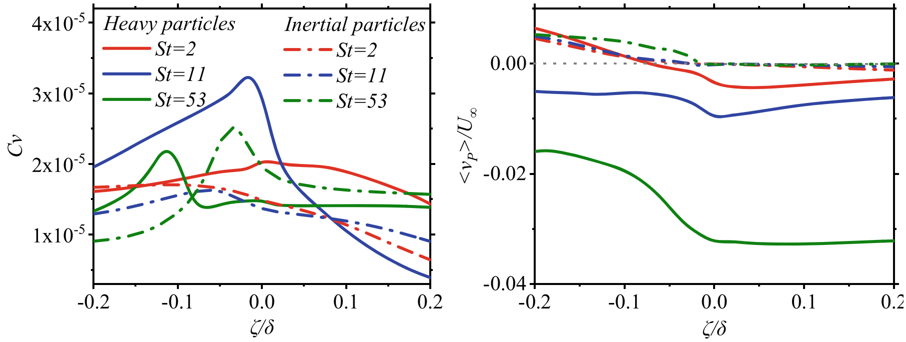

Fig. 2. Conditionally averaged (a) particle concentration and (b) particle vertical velocity.

Figure 3 presents the conditionally averaged vorticity $\langle \omega^* \rangle$ near the TNTI and its derivative $-\mathrm{d}\langle \omega^* \rangle / d\zeta$. Those for particle-free TBL and TBLs laden with inertia-particles are also selectively shown. We know from [8] that the vorticity jump is not significant in particle-free TBL because of the low turbulent Reynolds number and the presence of high-inertia particle makes the jump notable. As compared to inertia-particle cases, the sudden change in the derivatives of the conditional vorticity is more clearly visible, indicating much more significant jump in vorticity across the TNTI for heavy-particle cases. This is obviously related to the particle accumulation near the TNTI.

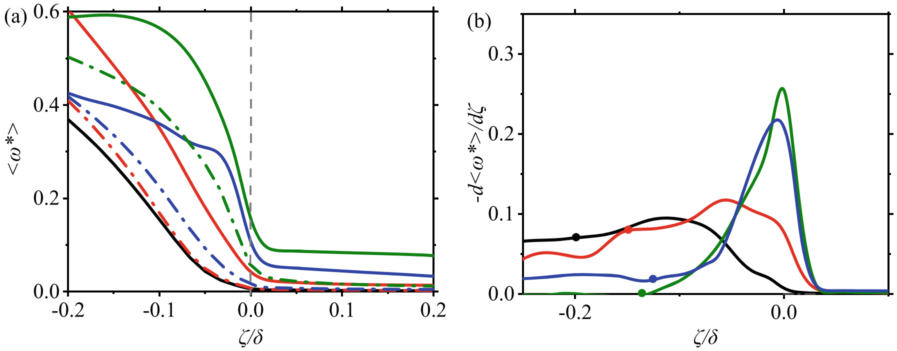

Fig. 3. (a) Conditionally averaged vorticity and (b) the vorticity derivative with respective to ζ/δ for particle-free (the black solid line) and particle-laden flow. The line colours represent the Stokes number and the line types represent particle type as Fig. 2.

As to the geometric features of the TNTI, we focus on the p.d.f.s of the height, the fractal dimension of the TNTI and the thickness of the TNTI layer. Before presenting the statistics, we first show the top view of the iso-surfaces (the irrotational boundary) obtained by applying the selected vorticity magnitude threshold in Fig. 4. The iso-surfaces are coloured by the instantaneous (local) values of the TNTI height, indicating its large- and small-scale undulation.

It is seen from Fig. 1 and Fig. 4 that for particle-free TBL, the most prominent characteristics are the streamwise-aligned structures that modulate the TNTI into bulges and valleys and the small-scale wrinkles sitting on large-scale indentations. Previous studies [8] about the effects of inertia particles on the TNTI found that particles obscure the wrinkles in particle-laden TBL. This effect becomes more pronounced as Stokes number increases. However, this is not true for heavy-particle case. Although the interface in Fig. 4 (b) show that the case with low-inertia heavy particles share similar features with particle-free TNTI, moderate- and high- inertia heavy particles modulate the interface in different way. In Fig. 4 (c), there are many small, isolated concavities located on the deformed small-scale wrinkles, which is more visible in Fig. 1(e). In Fig. 4 (d), the small-scale features on the interface become even more intricate. Note that the inertial particles result in less conspicuous wrinkles on the large-scale bulges of the TNTI in [8], while the introduction of heavy particles increases the visibility of the small-scale structures. This is obviously attributed to the gravity settling of particles frequently passing through the interface and disrupting the large-scale structures. The downward stretching of the irrotational boundary shown in Fig. 1(f) emphasizes the dominance of fine-scale dynamics under the influence of gravity.

From Fig. 5, in which the p.d.f.s of the interface height y_i are presented, we see the non-Gaussian and even asymmetric distribution of y_i for TBL laden with moderate- and high-inertia heavy particles. There is a lower peak at about $y_i/\delta_i \approx 0.9$ for case St = 11, which may be attributed to the "banana-like" stretching effect of gravity settling on the TNTI as shown in Fig. 1(e). The asymmetric distribution for case St = 53 is likely the result of the suppressed turbulent structures in the outer layer of TBL, as seen from Fig. 1(f). Under the influence of gravity, high-inertia (low Froude number) particles

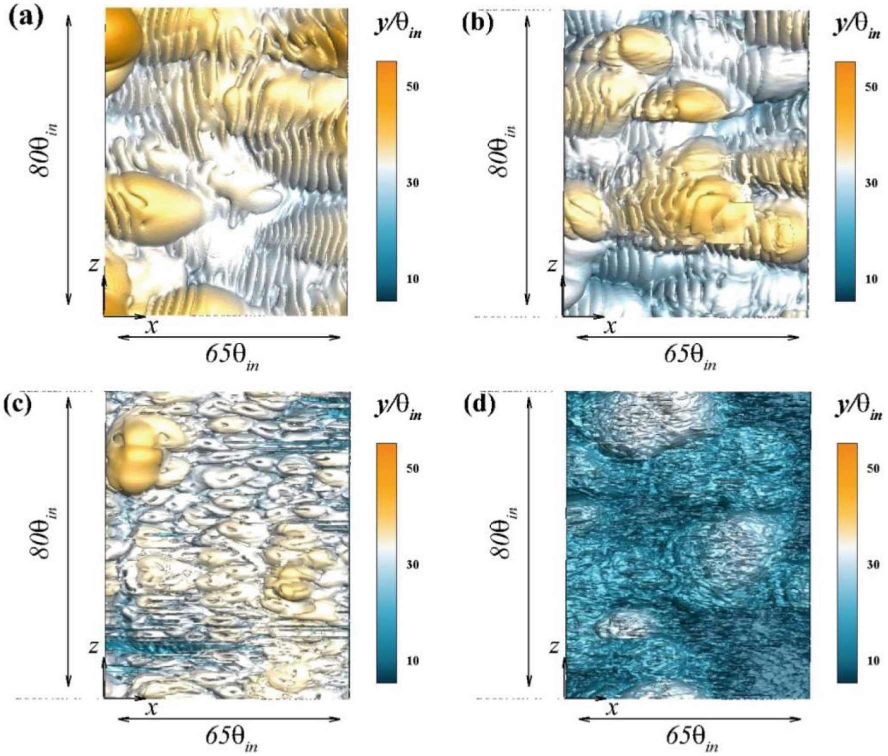

Fig. 4. Top view of the iso-surfaces corresponding to (a) ω^*_{th}=0.0093 for particle-free TBL and (b)$\omega^*_{\mathrm{th}} = 0.0525$ for heavy-particle case St = 2 (c)$\omega^*_{\mathrm{th}} = 0.119$ for heavy-particle case St = 11 and (d) $\omega^*_{\mathrm{th}} = 0.179$ for heavy-particle case St = 53.

more readily penetrate the interface and carry high-velocity fluid rapidly towards the wall, thereby accelerating the fluid beneath the interface. This process results in the shift of the interface height towards the wall, as shown in Fig. 1. Meanwhile, the turbulent structures in turbulent region beneath the interface seen by the particles are significantly suppressed, that is, one cannot observe alternating high-/low- vorticity structures in Fig. 1(f) as those in Fig. 1(d) and (e). Since the undulation of the TNTI is strongly related to the large-scale structures [5–8] in the turbulent side, the suppressed turbulent structures leads to a broader probability density function (PDF) distribution for the height of the TNTI. Accordingly, the mean interface height $\overline{y}_i$ for heavy-particle cases decrease but the variance σ_{yi} increases as compared to inertia-particle cases.

The classical box-counting method [11] is used to obtain the fractal dimension D_f of the TNTI within the range of 0.032δ < b < 0.4δ (this range is similar to that adopted by [12], which spans from $b/\delta = 0.04$ to $b/\delta = 0.3$) as shown in Fig. 6. That is, D_f is estimated with a power law $N \sim b^{D_f}$, where N is the minimum number of boxes with size b required to cover the whole instantaneous irrotational boundary. Due to the increase of small-scale structures in the boundary with increasing St (decreasing $\mathrm{Fr_d}$),

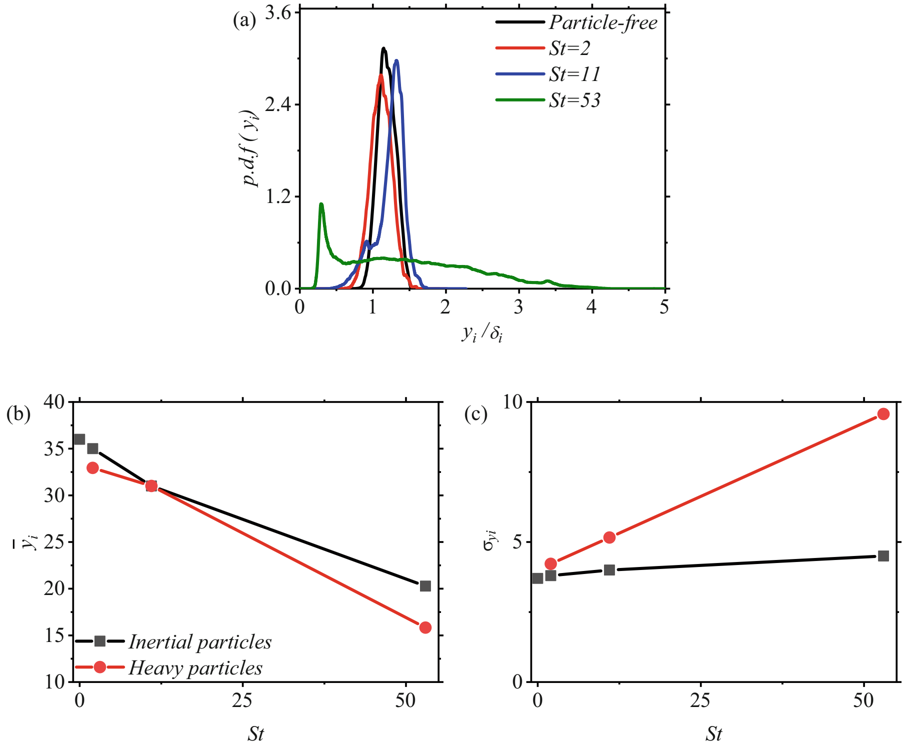

Fig. 5. (a) The p.d.f.s of the interface height scaled by the mean height of δ_i. The mean $\bar{y}_i$ (b) and (c) variance σ_{yi} of y_i as a function of Stokes number. In the latter subfigures, the particle-free TBL is represented by $\mathrm{St} = 0$.

see Fig. 1 and Fig. 4, the fractal dimension increases remarkably in heavy-particle cases, which is contrast to that in inertia-particle cases.

Finally, we show in Fig. 7(a) the thickness of the TNTI layer δ_{TNTI} corresponding to a small threshold of $\mathrm{d}^2 < \omega^* > /\mathrm{d}\zeta^2 = 0.008$ for particle-free TBL and TBL laden with inertial and heavy particles. The positions for TBL laden with heavy particles and particle-free TBL are indicated in Fig. 3 by the solid circles of different colours. We just discussed the change resulted from inertia particles with $\mathrm{St} = 53$ in [8] but present the δ_{TNTI} for all three inertia here. It is clear that the presence of the inertial particles will reduce the thickness of the TNTI layer because the accumulated particle beneath the TNTI will limit the free development of the interface layer through two-phase interactions. This effect becomes more pronounced as St increases. For heavy particle with low- and moderate-inertia, δ_{TNTI} becomes thinner because the settling particles further compress the TNTI layer the from above, as well as the accumulation of particles just beneath the TNTI. With the increase of St and the decrease of $\mathrm{Fr_d}$, the heavy particles tend to stretch downwards the TNTI layer. The peak of conditional concentration of particles moves down to about $\zeta/\delta = -0.125$, as shown in Fig. 2(a), is one of the manifestation of stretching effect. Consequently, the thickness of the TNTI

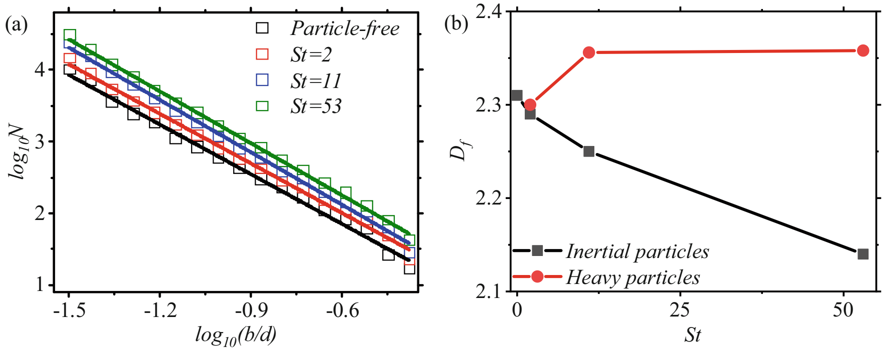

Fig. 6. (a) Plots of $log_{10}N$ against $log_{10}b$ for different cases, where b is the box size and N is the minimum number of boxes with size b for covering the whole instantaneous irrotational boundary. (b) The fractal dimension D_f for TBL laden with inertial and heavy particles.

layer δ_{TNTI} in TBL laden with high-inertia heavy particles is slightly higher than that inertia-particle case.

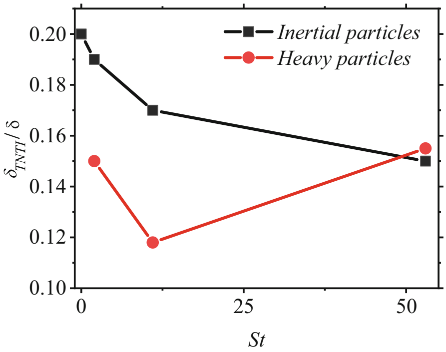

Fig. 7. The thickness of the TNTI layer δ_{TNTI} scaled by the boundary layer thickness of particle-free TBL δ.

4 Conclusions

Direct numerical simulations of a spatially developing turbulent boundary layer laden with small, heavy particles are performed to investigate the particle dynamics near the TNTI and the geometric properties of the TNTI. The results are compared against inertia-particle cases to address the effect of the gravitational settling of particles.

It is revealed that the heavy particles are more easily accumulated beneath the TNTI because the gravity settling will result in a downward particle velocity. The smaller the particle Froude numbers, the lower they accumulate. As compared to inertia-particle cases, the stronger accumulation of heavy particles results in more significant jump of the conditionally averaged vorticity. When heavy particles settle across the irrotational boundary between turbulent and potential flow, they will generate many small, "banana-like" concavities located on the deformed small-scale wrinkles and stretch the boundary into the turbulent region. As a result, the mean height of the boundary decreases but the variance increases as compared to inertia-particle cases. The generated small-scale structures further complicate the TNTI geometry, leading to increased fractal dimension. However, the thickness of the TNTI layer varies nonmonotonically with St (and $\mathrm{Fr_d}$) for heavy particle. Low-inertia and high $\mathrm{Fr_d}$ particles reduce the thickness of the TNTI layer because the near-TNTI accumulation and the compression of settling particles, instead, high-inertia and low $\mathrm{Fr_d}$ particles thicken the TNTI layer through the stretching effect.

References

1. Balachandar, S., Eaton, J.K.: Turbulent dispersed multiphase flow. Annu. Rev. Fluid Mech. **42**, 111–133 (2010)
2. Lee, J., Lee, C.: The effect of wall-normal gravity on particle-laden near-wall turbulence. J. Fluid Mech. **873**, 475–507 (2019)
3. Wang, P., Li, J.C., Zheng, X.J.: The effect of gravity on turbulence modulation in particle-laden horizontal open channel flow. Phys. Fluids **33**, 083315 (2021)
4. Da Silva, C.B., Hunt, J.C.R., Eames, I., Westerweel, J.: Interfacial layers between regions of different turbulence intensity. Ann. Rev. Fluid Mech. **46**, 567–590 (2014)
5. Zhang, X., Watanabe, T., Nagata, K.: Reynolds number dependence of the turbulent/non-turbulent interface in temporally developing turbulent boundary layers. J. Fluid Mech. **964**, A8 (2023)
6. Chauhan, K., Philip, J., Marusic, I.: Scaling of the turbulent/non-turbulent interface in boundary layers. J. Fluid Mech. **751**, 298–328 (2014)
7. Chauhan, K., Philip, J.D., Silva, C., Hutchins, N., Marusic, I.: The turbulent/non-turbulent interface and entrainment in a boundary layer. J. Fluid Mech. **742**, 119–151 (2014)
8. Wei, Q.Q., Wang, P.P., Zheng, X.J.: Modulations of turbulent/non-turbulent interfaces by particles in turbulent boundary layers. J. Fluid Mech. **983**, A15 (2024)
9. Kim, K., Baek, S.J., Sung, H.J.: An implicit velocity decoupling procedure for the incompressible Navier-Stokes equations. Intl J. Numer. Meth. Fluids **38**(2), 125–138 (2002)
10. Li, D., Luo, K., Fan, J.: Modulation of turbulence by dispersed solid particles in a spatially developing flat-plate boundary layer. J. Fluid Mech. **802**, 359–394 (2016)
11. Borrell, G., Jiménez, J.: Properties of the turbulent/non-turbulent interface in boundary layers. J. Fluid Mech. **801**, 554–596 (2016)
12. Wu, D., Wang, J., Cui, G., et al.: Effects of surface shapes on properties of turbulent/non-turbulent interface in turbulent boundary layers. Sci. China Technol. Sci. **63**(2), 214–222 (2020)

Turbulent/Non-turbulent Interface in Water Jet with Polymer Additives

Heng-Dong Xi[1(✉)], Sheng-Hong Peng[1], and Yi-Bao Zhang[1,2]

[1] Institute of Extreme Mechanics and School of Aeronautics, Northwestern Polytechnical University, Xi'an 710072, China
`hengdongxi@nwpu.edu.cn`
[2] Center for Combustion Energy, Key Laboratory for Thermal Science and Power Engineering of Ministry of Education, Department of Energy and Power Engineering, Tsinghua University, Beijing 100084, China
`https://teacher.nwpu.edu.cn/m/en/2014010143.html`

Abstract. The effect of polymer additives on the global entrainment of a turbulent round jet was found to show two distinct regimes: the reduction and enhancement regimes in the near and far fields, respectively. Using time-resolved simultaneous particle image velocimetry and laser-induced fluorescence measurements, we hereby present an experimental study on the local entrainment and engulfment process along the turbulent/non-turbulent interface (TNTI). We find that the local entrainment velocity is augmented in both regimes, due to the contribution from polymer elastic stress and a higher probability for TNTI to visit jet centreline region where the entrainment velocity is larger. In the entrainment reduction regime, the fractal dimension and length of TNTI are smaller compared to the Newtonian case; while those in the enhancement regime are nearly not changed. The difference between the two regimes results from the fact the jet flow decays in the streamwise direction. In the near field, the flow is intense enough to substantially stretch polymers, which results in a redistribution of energy among different scales and a steeper decay of energy in the inertial range. However, in the far field, the stretching of the polymer and in turn the feedback of polymers is not strong enough to alter the inertial range scaling of the energy spectrum. Moreover, our study reveals although more ambient fluid is engulfed into the turbulent region due to the augmented large scale motion by polymers, engulfment is still not the major contribution to the entrainment in polymer-laden jet, which is similar to the case in Newtonian jet.

Keywords: Jets · Viscoelasticity · Entrainment

1 Introduction

The addition of minute amounts of long-chain flexible polymers to fluid flow can drastically change the flow behaviour, such as reducing the drag in pipe/channel

J. Wang and I. Marusic (Eds.): IUTAM-TNTI 2024, IUTAM Bookseries 45, pp. 226–237, 2025.
https://doi.org/10.1007/978-3-031-78151-3_18

flow [1–3], attenuating flow-induced noise in underwater vehicles [4], reducing the risk of explosion when the oil tank is impacted during an air crash event [5], and inhibiting the energy transfer from the large to small scales [6–8]. The unique properties of polymer-laden flows are related to the fact that polymer chains can be stretched under a velocity gradient [9], and the stretched polymers in turn affect the local flow behaviour. Compared with polymer drag reduction, the effects of polymers on the turbulent transport and mixing are less studied. [10,11], and [12] reported that, depending on the boundary conditions, polymers can either enhance or inhibit heat transfer in Rayleigh-Bénard convection. [13] studied the effects of polymers on the Rayleigh-Taylor turbulence, and they found that mixing is enhanced at large scales while depleted at small scales. Recently, there is growing interest in investigating the effects of polymers on the jet flow [14–19], which is a canonical flow configuration for studying turbulent transport and mixing.

In jet flow, the turbulent core is surrounded by the ambient non-turbulent fluid, and the two regions are separated by a sharp and highly convoluted boundary, known as the turbulent/non-turbulent interface (TNTI) [20]. The non-turbulent fluid is transported across the TNTI and becomes part of the turbulent core region, resulting in an increase of mass flux with downstream distance. There are a host of studies debating whether this entrainment process is dominated by large-scale processes through the energy-containing eddies (engulfment), or whether it is due to small-scale diffusive processes occurring along the TNTI (viscous nibbling) [21–24]. However, it is realized later that the entrainment is a multi-scale process, and the mean mass flux across the TNTI is scale-independent [25–27]. The entrainment velocity at small scales is small but is balanced by a large surface area, while the entrainment velocity at large scales is large but is balanced by a smoother surface area [27,28]. Therefore, the local entrainment velocity along the TNTI and the interface area are combined to determine the entrainment rate.

Turbulence is characterized by a wide spectrum of eddies with different sizes. These eddies imprint on the TNTI, and hence deform the TNTI, affecting its surface area and local entrainment velocity [29–32]. In previous study, we observed that in homogeneous isotropic turbulence polymers alter the distribution of energy among different scales: a new elastic range emerges between the inertial and dissipation ranges, and its scaling exponent is about -2.38, which means that the energy content decays more rapidly with wavenumber in the elastic range than in the inertial range [8]. In a turbulent round jet, it is found that the polymers' effects can be divided into two distinct regimes: the entrainment reduction regime in the near field and the entrainment enhancement regime in the far field [17]. How the energy distributes among different scales and how the surface area and local entrainment velocity vary to accommodate these two regimes are the key to the understanding of the entrainment process in viscoelastic fluid.

In previous studies, the entrainment in jet flow was investigated from the global view, i.e., the jet half-width and mean centerline velocity (see [14,17] and references therein). Only in recent years, with the advancement of numerical simulation and experimental measurement technique, it is possible to study the local entrainment process by tracking the interface in various flow configurations. [33] investigated the impact of polymer additives on oscillating grid turbulence. They found that the flow drew more energy from the oscillating grid, resulting in increased large-scale fluctuations. They also found that polymer additives alter the shape of TNTI and enhance the propagation velocity of the turbulent front. In Rayleigh-Taylor turbulence, [34] reported that polymers increase the growth rate of the turbulent mixing layer, while the small scale mixing is depressed. The above phenomena are related to the different effects of polymers on the large and small scales: polymers increase the energy content of large scale motions, while the small scale fluctuations are inhibited. [14,16] numerically simulated the Navier-Stokes equation coupled with finitely extensible nonlinear elastic with Peterlin closure model in planar jet and wake flows. They found that the entrainment rate is suppressed in the near field, and developed a new scaling theory in this entrainment reduction regime. [35] numerically studied the turbulent entrainment in a shear-free turbulence by inserting a developed homogeneous isotropic turbulence into the center of a quiescent flow. They found that the contributions of vortex stretching, viscous diffusion, and viscous dissipation to the entrainment velocity are strongly depressed by polymers, while polymer elastic stress itself accelerate the propagation of TNTI. The above mentioned combined effects of polymers are to increase the mean entrainment velocity. Besides, the interface area in the viscoelastic case is much smaller than that in the Newtonian case due to the suppression of small scale structures. Although the entrainment velocity is enhanced, the surface area is depressed more such that the entrainment rate is reduced in the viscoelastic fluid [35].

From the above discussion, it is clear that experimental study of the local entrainment process in a viscoelastic jet is seldomly reported. Now with the development of the "graphical" approach to track the TNTI [36], investigation of local entrainment in experiments is possible [27,32]. This paper aims to experimentally elucidate the entrainment mechanism of the polymer-laden jet from the perspective of TNTI, especially in the entrainment enhancement regime, which helps to understand the transition between the entrainment reduction and enhancement regimes.

2 Experimental Setup and Methods

2.1 Apparatus

The jet facility used in the current study has been described in detail in [17], here we only show the key features of the setup. The jet was generated in a 1.7 m long plexiglass rectangular tank with a cross-section of 0.3 m × 0.4 m, filled with 178 liters of deionized water or premixed aqueous polymer solution to a depth of 0.35 m. The jet fluid was introduced into the tank via a small circular pipe (nozzle) with an inner diameter (D) of 3 mm and a length of 200 mm. A separate reservoir, containing dyed deionized water/polymer solution, was utilized to supply the jet, hereafter referred to as pure water jet and polymer-laden jet, respectively. For the experiments using polymer solution, both the jet and the fluid in the tank are premixed aqueous polymer solutions with the same concentration. The mean velocity at the nozzle exit U_e (volume flow rate divided by the cross-sectional area of the nozzle) is 2.36 m/s, and the corresponding Reynolds number is $Re = U_e D/\nu = 7075$, where ν is the kinematic viscosity of the fluid. We note that at this Re the pipe flow is turbulent. The pipe was positioned $500D$ away from the tank's end wall, and no backflow was observed during the simultaneous PIV (particle image velocimetry) and LIF (laser induced fluorescence) measurements, which lasted approximately eight seconds.

For polymeric fluid flows, two additional control parameters are relevant: polymer concentration ϕ and Weissenberg number Wi. The polymer solution was prepared to a given concentration following the same protocol as in [8,17]. In a polymer-laden jet, the exit Weissenberg number is defined as $Wi = 2U_e\tau_p/D$, which is the ratio of the polymer's longest relaxation time τ_p to the characteristic time of the jet at the exit $D/2U_e$. The polymer used in this study is polyethylene oxide (PEO, Sigma-Aldrich) with different molecular weight M_w. We here take PEO with $M_w = 5 \times 10^6$ for an example, it consists of $N = 113637$ monomers, with a radius of gyration $R_g = N^{3/5}a = 475\,\text{nm}$. In fully stretched state, the maximum length of the macromolecular is about $R_{max} = Na \approx 50,000\,\text{nm}$, which is 100 times larger than that in the coiled state.

2.2 Detection of the Turbulent/Non-turbulent Interface

The detection of TNTI necessitates a threshold of scalar concentration [37]. Across the TNTI, there is a sharp jump in flow properties, including scalar concentration, kinetic energy, vorticity, and energy dissipation rate, etc. This feature can be utilized to determine the scalar concentration threshold [27,37–39], which is achieved by a conditional average process. Given a scalar concentration threshold $\phi_{R,th}$ and a variable f, the mean value of f is calculated using all points sampled on the FOV where the local concentration exceeds $\phi_{R,th}$ (Fig. 1),

$$\widetilde{f}(\phi_{R,th}) = \langle f\ |_{\phi_R > \phi_{R,th}} \rangle. \tag{1}$$

Then the threshold is chosen at the value where $\widetilde{f}(\phi_{R,th})$ exhibits a slope change. Since the jet decays along the streamwise direction, both $\phi_{R,th}$ and f need to be normalized by their centerline mean values $\phi_{R,c}$ at the specific streamwise position during the conditional average. Besides, islands in the ambient fluid are not considered in this procedure [27].

In Figs. 2(*a*,*b*), the green curve depicts the TNTI of the polymer-laden jet ($Wi = 85.6$) determined by the scalar concentration contour $\phi_R/\phi_{R,c} = 0.18$. This green curve effectively demarcates the turbulent and non-turbulent regions. Figure 2(*b*) shows the corresponding vorticity field computed from our measured velocity field. It can be seen that the TNTI determined from the scalar concentration field closely encloses the vorticity field, confirming that the scalar concentration is a reliable surrogate of vorticity in detecting TNTI even in the polymer-laden jet. Furthermore, unlike Newtonian flows, the vortex in the polymer-laden

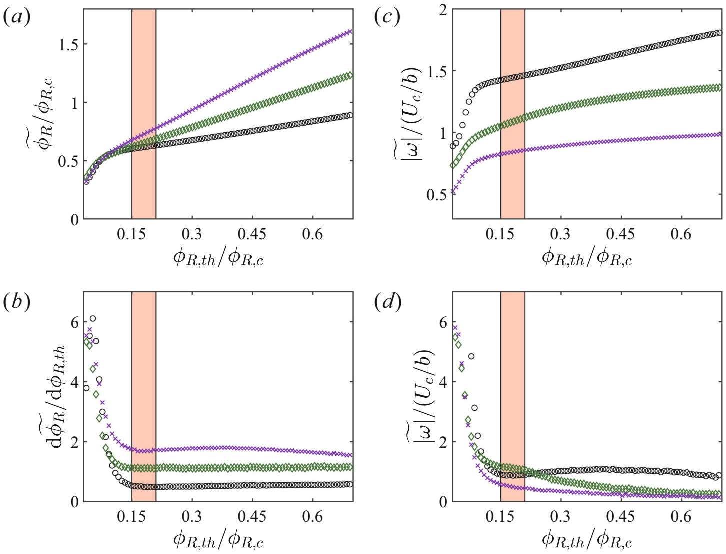

Fig. 1. (a) The conditional averaged scalar concentration $\widetilde{\phi_R}/\phi_{R,c}$ which is averaged across all positions where $\phi_R/\phi_{R,c} > \phi_{R,th}/\phi_{R,c}$ and over the entire duration of the experiment. (c) Similarly, calculated conditional average of the normalized out-of-plane vorticity magnitude $|\omega|/(U_c/b)$. The derivatives of the data in panels (a) and (c) are shown in panels (b) and (d). The red filled rectangles denote the range of TNTI concentration threshold.

jet predominantly exhibits sheet-like structures, a finding consistent with [17] and the numerical simulation of the viscoelastic jet [14]. These elongated structures are attributed to the local stretching of the polymers along the streamwise direction, which generate local nonlinear elastic stresses and induce elasto-inertial instabilities [40]. The vortex-sheet structure typically appears where the local scalar concentration is high, suggesting a strong correlation between passive scalar mixing and the coherent structures in turbulent flows.

As depicted in Fig. 2(a), once the TNTI is determined, a local coordinate system along the TNTI can be established. The applicability of scalar concentration contours for detecting the TNTI of a polymer-laden jet is further demonstrated by the conditionally averaged profiles along this local coordinate system. Here, the conditional average $\langle \bullet\ |_I \rangle$ is denoted as $\langle \bullet \rangle_I$, where the subscript $_I$ refers to the TNTI. Please note that $s_n < 0$ and $s_n > 0$ correspond to the non-turbulent and turbulent regions, respectively. Following the approach of [27,39], points pertaining to low scalar concentration bubbles within the turbulent region and high concentration islands distant from the turbulent region are excluded from the conditional average process. Furthermore, instances where the normal direction $\boldsymbol{s_n}$ intersects the TNTI, causing a transition from turbulent to non-turbulent regions or vice versa, are also omitted from the conditional statistics [27]. In the pure water case, both the $\langle \phi_R \rangle_I/\phi_{R,c}$ and $\langle |\omega| \rangle_I/(U_c/b)$ are virtually small in the

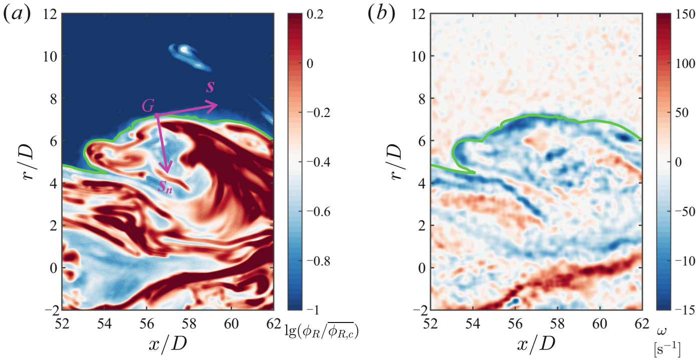

Fig. 2. (a) The instantaneous scalar concentration $\phi_R/\overline{\phi_{R,c}}$ of the polymer solution jet at $Re = 7075$, $\phi = 20\,\text{ppm}$, and $Wi = 85.6$. The TNTI is represented by the green curve. A local coordinate system, indicated by the pink arrow $\boldsymbol{s}$, is established at point G on the TNTI, with the normal direction $\boldsymbol{s_n}$ oriented towards the turbulent region. (b) The corresponding vorticity field.

non-turbulent region ($s_n < 0$), then experience a sharp jump across the TNTI ($s_n = 0$), and finally increase slowly in the turbulent core region ($s_n > 0$). Similar conditional profiles have been reported in other shear flows [20,27,41,42]. The non-zero vorticity in $s_n < 0$ is attributed to PIV noise [38]. In the non-turbulent region, polymers are in a coiled state and have no effect on the flow, consistent with the observations that $\langle\phi_R\rangle_I/\phi_{R,c}$ and $\langle|\omega|\rangle_I/(U_c/b)$ of pure water and polymer-laden jets almost overlap with each other in $s_n < 0$. In the turbulent region, the local Weissenberg number Wi_{local} exceeds 1, and polymers thus suppress the small scale fluctuations, leading to smaller vorticity compared to pure water jet. The suppressed small scales inhibit the mixing of scalar [34]. Lots of high scalar concentration clumps are observed in the turbulent region, resulting in higher $\langle\phi_R\rangle_I/\phi_{R,c}$ in $s_n > 0$.

3 Results

Recent study showed that the entrainment is a multi-scale process along the TNTI [25,27], with the entrainment rate depending on the surface area S and entrainment velocity V_n. At the smallest length scale (of order of η), V_n is small but is balanced by a large S since the surface is convoluted. While at large scales, V_n is large but is balanced by a small S since the surface is smooth. Hence, the entrainment rate, $S(\varDelta)\,V_n(\varDelta)$, estimated at different scale $\varDelta$ is scale-invariant. In the inertial range of scales, the TNTI is multi-fractal, i.e. $S(\varDelta) \sim \varDelta^{-D_3}$ with the scaling exponent $2.3 < D_3 < 2.4$ [27]. Accordingly, $V_n(\varDelta) \sim \varDelta^{D_3}$ in the inertial range. In this section, we will delve into the effects of polymers on the entrainment rate from those two perspectives: $S(\varDelta)$ and $V_n(\varDelta)$.

In our experiment, two dimensional velocity and scalar concentration fields are available, from which TNTI length L_{TNTI} and local entrainment velocity v_n

projected on the $x - r$ plane can be estimated. Given the axisymmetric nature of the jet, the mean entrainment velocity can be formulated as follows:

$$V_n = \overline{\left[\frac{\int_0^{L_{TNTI}} (-v_n) r_I \mathrm{d}s}{\int_0^{L_{TNTI}} r_I \mathrm{d}s} \right]}, \tag{2}$$

which is integrated on the local coordinate along the TNTI. In the Newtonian case, $L_{TNTI}(\varDelta) \sim \varDelta^{2-D_3}$ and $V_n(\varDelta) \sim \varDelta^{D_3-2}$.

In Figs. 3(*a,b*), we compare L_{TNTI} and V_n of the pure water case with those of the $Wi = 36.7$ case at $x/D = [35, 47]$ and $x/D = [50, 62]$. For the pure water case, L_{TNTI} scales with the filter size $\varDelta$ in the log-log plot between λ and b (we take jet half-width as the integral length scale), i.e. $L_{TNTI} \sim \varDelta^{2-D_3}$ with $D_3 \approx 2.31$. V_n increases with $\varDelta$ and follows a power-law scaling in the inertial range with an exponent $D_3 - 2 \approx 0.31$. Those two scaling –$L_{TNTI} \sim \varDelta^{-0.31}$ and $V_n \sim \varDelta^{0.31}$– together make the entrainment rate, $L_{TNTI}(\varDelta)\, V_n(\varDelta)$, independent of scales, which was first corroborated in experiment by [27]. We also note that the scaling range of V_n is shorter than that of L_{TNTI}, probably due to the small Reynolds number ($Re_\lambda = 106$ at $x/D = 56$) in our study [27].

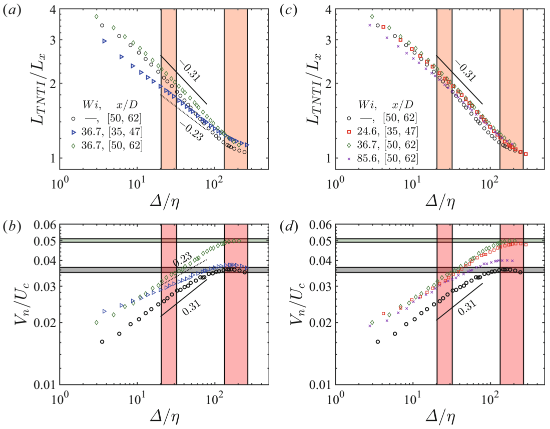

Fig. 3. The TNTI length, L_{TNTI} (normalized by L_x), (*a,c*) and the mean entrainment velocity, V_n (normalized by the mean centerline axial velocity U_c), (*b,d*) as a function of the filter size $\varDelta$ (normalized by the Kolmogorov length scale η). $L_x = 12D$ represents the length of the measurement region along the flow direction. The two vertical bars represent the Taylor scale λ (left) and the jet half-width b (right) within the measurement range. The black horizontal bar denotes the large scale entrainment coefficient of the pure water case in the self-similar regime. The green horizontal bar denotes the large scale entrainment coefficient of the polymer-laden case in the entrainment enhancement regime.

For the $Wi = 36.7$ case at $x/D = [35, 47]$, the scaling exponent of L_{TNTI} is altered by polymers, with a least-square fit yielding $2 - D_3 \approx -0.23$. The corresponding $D_3 \approx 2.23$, indicating that the interface is smoother than that of the pure water case at small scales, in line with the numerical simulation [35]. The scaling exponent of V_n changes accordingly, i.e. $V_n \sim \Delta^{0.23}$ despite the short scaling range. The multi-scale nature of the entrainment velocity in the viscoelastic case has not been investigated in previous study. We have shown that the small-scale end of the inertial range will be modified with the addition of polymers and a new scaling range, coined as elastic range, will emerge between the inertial and dissipation ranges at high polymer concentration [8]. The elastic scaling is also observed when Wi is larger than a critical value in numerical simulations [43,44]. In turbulent jet flow, the scaling of the power spectrum of fluctuating velocity is altered. The change in the energy content among different scales will then modulate the scaling of L_{TNTI} and V_n in the polymer-laden jet. At the small length scale ($\Delta < \lambda$), the inertial force can be neglected and the viscous diffusion becomes dominated. Hence the viscous nibbling is the dominating mechanism of entrainment at small scales. By incorporating the elastic stress term into the enstrophy transport equation and considering the evolution of the enstrophy isosurface [32,35,36,45,46], one can decompose the nibbling velocity of viscoelastic turbulence into the following components:

$$v_n = \underbrace{-\frac{\omega_i \omega_j S_{ij}}{\left|\nabla(\frac{\omega_i \omega_i}{2})\right|}}_{V_P} \underbrace{-\frac{\nu \frac{\partial^2}{\partial x_j \partial x_j}(\frac{\omega_i \omega_i}{2})}{\left|\nabla(\frac{\omega_i \omega_i}{2})\right|}}_{V_D} \underbrace{+\frac{\nu(\frac{\partial \omega_i}{\partial x_j}\frac{\partial \omega_i}{\partial x_j})}{\left|\nabla(\frac{\omega_i \omega_i}{2})\right|}}_{V_\varepsilon} \underbrace{-\frac{\omega_i \epsilon_{nji} \frac{\partial^2 T_{p,mj}}{\partial x_m \partial x_n}}{\left|\nabla(\frac{\omega_i \omega_i}{2})\right|}}_{V_V} . \qquad (3)$$

Here, ω_i is the component of vorticity in the i direction, and ϵ_{nji} denotes the Levi-Cevita symbol. The first three terms on the right side of equation (3), namely the enstrophy production term (V_P), the viscous diffusion term (V_D), and the viscous dissipation term (V_ε), contribute to the nibbling velocity of the Newtonian fluid. The last term on the right side corresponds to the vorticity diffusion induced by the elastic stress of the polymer (V_V, viscoelastic production term). In the Newtonian case, V_P, V_D, and V_ε all contribute to the nibbling process [35]. However, the small scale fluctuation is suppressed [8,43,47], and the enstrophy production is also inhibited by polymers [48,49]. We would then expect that the contributions from V_P, V_D, and V_ε will be depressed accordingly, as being observed in [35]. At the smallest scale we resolved here ($\Delta \approx 3\eta$), we find that V_n, however, is larger than that of the pure water case, implying that polymer elastic stress will contribute to increase the entrainment velocity, i.e. V_V plays an important role on the local entrainment at small scales in the polymer-laden jet. In their simulation, [35] reported that most part of V_n is contributed by V_V at high Wi.

4 Discussion and Conclusions

In our previous study, we reported that polymer-laden jet can be divided into two regimes: the entrainment reduction regime in the near field and the entrainment enhancement regime in the far field [17]. The former one has been extensively studied in planar jet and shear-free turbulence [14,35]. The reduced entrainment rate is caused by the smoother turbulent/non-turbulent interface (TNTI), which results in a small surface area, although polymers increase the mean entrainment velocity. The local entrainment process in the entrainment enhancement regime remains elusive and is the focus of this study.

We here present an experimental study on the effects of polymer additives on the entrainment process of non-turbulent fluid across the TNTI into the turbulent region in a turbulent round jet. We employ time-resolved simultaneous PIV and LIF to measure the velocity and scalar concentration fields. From the scalar concentration field, we can detect the TNTI and engulfed "bubbles". The entrainment velocity along the TNTI is determined using an interface-tracking method [27]. By applying the spatial-filtering to the velocity and scalar concentration fields, we also analyze the geometric feature of the TNTI and the entrainment velocity at multi-scales.

Observation of the instantaneous scalar field reveals that more unmixed ambient fluids are engulfed into the turbulent region, with some bubbles even appearing in the center of the jet at high Wi. The engulfment is a large scale inviscous process. The augmented large scale motion by polymers directly leads to more bubbles being engulfed into the turbulent core region. The bubbles, once engulfed into the turbulent core region, are then mixed with the surrounding turbulent fluid to acquire vorticity. This process is primarily dominated by small scales. Polymers suppress the small scale fluctuations, which in turn make the bubbles unable to mix with the turbulent core flow timely, resulting in a longer residence time of bubbles. Though the engulfment is enhanced, the conditional mean velocity and vorticity inside the bubbles are not affected by polymers due to the fact that those fluid parcels are from the ambient quiescent fluid, where polymers cannot be stretched. Moreover, we note that the engulfment is still not the major entrainment mechanism in polymer-laden jet.

In the transition range, which is between the entrainment reduction and enhancement regimes, we found that the behavior of local entrainment is similar to that in the entrainment reduction regime, as reported in [35]. In the turbulent region, polymers change the distribution of energy among different scales. More importantly, the scaling exponent of the energy spectra in the inertial range is also modified, which leads to smaller scaling exponent of the TNTI length and a smoother interface at small scales. In the pure water jet, the enstrophy production, viscous diffusion, and viscous dissipation all contribute to the nibbling velocity. In polymer-laden jet, however, these terms are inhibited. The increased mean entrainment velocity at small scales thus comes from the polymer elastic stress. We also note another mechanism that contribute to the increased mean entrainment velocity. It is found that TNTI in polymer-laden jet experiences higher fluctuation in the radial direction, and it has larger probability to locate near the centerline, where the local entrainment velocity is faster than that near the non-turbulent region [27]. This mechanism is due to the inhomogeneity of the jet in the radial direction, and is not present in [35]'s simulation.

In the entrainment enhancement regime, the small scale fluctuations are suppressed by polymers. However, since the flow decays in the streamwise direction, the scaling exponent of the energy spectra is altered for flow near the centerline ($0 \leq r/b < 0.5$), it remains nearly unchanged for $r/b \geq 1$. Note that TNTI seldom excursus to region with $r/b < 1$. Hence, the interface will mostly visit flow whose small scales are depressed while the scaling exponent is unaffected. The scaling exponent of the TNTI length is thus the same as that in the pure water jet. We conclude that the unaffected interface surface and augmented entrainment velocity result in the enhanced entrainment rate. Our results also show that, in the entrainment enhancement regime, the TNTI length and mean entrainment velocity, when properly normalized, are independent of the Weissenberg number, demonstrating the universal nature of polymer-laden jet.

Acknowledgements. We are grateful to stimulating discussions with Jin-Jun Wang and acknowledge Chao Sun for the rheology measurement. This work is financially supported by the National Natural Science Foundation of China (NSFC) through Grant Nos. 12125204 and 11472094, the China Postdoctoral Science Foundation through Grant No. 2022M721853, and the 111 Project of China through Grant No. B17037.

References

1. Bailey, F.E., Koleske, J.V.: Poly (Ethylene Oxide). Academic Press, New York (1976)
2. White, C.M., Mungal, M.G.: Annu. Rev. Fluid Mech. **40**, 235 (2008)
3. Xi, L.: Phys. Fluids **31**(12), 121302 (2019)
4. Polmar, N., Moore, K.J.: Cold War Submarines: The Design and Construction of US and Soviet Submarines. Potomac Books, Inc., Williamsport (2004)
5. Wei, M.H., et al.: Science **350**(6256), 72 (2015)
6. Ouellette, N.T., Xu, H.T., Bodenschatz, E.: J. Fluid Mech. **629**, 375 (2009)
7. Xi, H.D., Bodenschatz, E., Xu, H.T.: Phys. Rev. Lett. **111**(2), 024501 (2013)
8. Zhang, Y.B., Bodenschatz, E., Xu, H., Xi, H.D.: Sci. Adv. **7**(14), eabd3525 (2021)
9. Perkins, T.T., Smith, D.E., Chu, S.: Science **276**(5321), 2016 (1997)
10. Ahlers, G., Nikolaenko, A.: Phys. Rev. Lett. **104**(3), 034503 (2010)
11. Benzi, R., Ching, E.S.C., De Angelis, E.: Phys. Rev. Lett. **104**(2), 024502 (2010)
12. Xie, Y.C., Huang, S.D., Funfschilling, D., Li, X.M., Ni, R., Xia, K.Q.: J. Fluid Mech. **784**, R3 (2015)
13. Boffetta, G., Mazzino, A., Musacchio, S., Vozella, L.: Phys. Rev. Lett. **104**(18), 184501 (2010)
14. Guimarães, M.C., Pimentel, N., Pinho, F.T., da Silva, C.B.: J. Fluid Mech. **899**, A11 (2020)
15. Yamani, S., Keshavarz, B., Raj, Y., Zaki, T.A., McKinley, G.H., Bischofberger, I.: Phys. Rev. Lett. **127**(7), 074501 (2021)
16. Guimarães, M.C., Pinho, F.T., da Silva, C.B.: J. Fluid Mech. **946**, A26 (2022)
17. Peng, S.H., Zhang, Y.B., Xi, H.D:, Phys. Fluids **35**(4) (2023)
18. Soligo, G., Rosti, M.E.: Int. J. Multiph. Flow 104546 (2023)

19. Yamani, S., Raj, Y., Zaki, T.A., McKinley, G.H., Bischofberger, I.: Phys. Rev. Fluids **8**(6), 064610 (2023)
20. da Silva, C.B., Hunt, J.C.R., Eames, I., Westerweel, J.: Annu. Rev. Fluid Mech. **46**, 567 (2014)
21. Roshko, A.: AIAA J. **14**(10), 1349 (1976)
22. Mathew, J., Basu, A.J.: Phys. Fluids **14**(7), 2065 (2002)
23. Holzner, M., Liberzon, A., Nikitin, N., Lüthi, B., Kinzelbach, W., Tsinober, A.: J. Fluid Mech. **598**, 465 (2008)
24. Jahanbakhshi, R., Madnia, C.K.: J. Fluid Mech. **797**, 564 (2016)
25. Meneveau, C., Sreenivasan, K.R.: Phys. Rev. A **41**(4), 2246 (1990)
26. de Silva, C.M., Philip, J., Chauhan, K., Meneveau, C., Marusic, I.: Phys. Rev. Lett. **111**(4), 044501 (2013)
27. Mistry, D., Philip, J., Dawson, J.R., Marusic, I.: J. Fluid Mech. **802**, 690 (2016)
28. Philip, J., Meneveau, C., de Silva, C.M., Marusic, I.: Phys. Fluids **26**(1), 015105 (2014)
29. Krug, D., Holzner, M., Marusic, I., van Reeuwijk, M.: J. Fluid Mech. **820**, R3 (2017)
30. Mistry, D., Philip, J., Dawson, J.R.: J. Fluid Mech. **871**, 896 (2019)
31. Balamurugan, G., Rodda, A., Philip, J., Mandal, A.C.: J. Fluid Mech. **894** (2020)
32. Long, Y.G., Wang, J.J., Pan, C.: J. Fluid Mech. **941**, A68 (2022)
33. Liberzon, A., Holzner, M., Lüthi, B., Guala, M., Kinzelbach, W.: Phys. Fluids **21**(3), 035107 (2009)
34. Boffetta, G., Mazzino, A., Musacchio, S.: Phys. Rev. E **83**(5), 056318 (2011)
35. Abreu, H., Pinho, F.T., da Silva, C.B.: J. Fluid Mech. **934** (2022)
36. Wolf, M., Lüthi, B., Holzner, M., Krug, D., Kinzelbach, W., Tsinober, A.: Phys. Fluids **24**(10), 105110 (2012)
37. Prasad, R.R., Sreenivasan, K.R.: Exp. Fluids **7**(4), 259 (1989)
38. Westerweel, J., Fukushima, C., Pedersen, J.M., Hunt, J.C.R.: J. Fluid Mech. **631**, 199 (2009)
39. Kohan, K.F., Gaskin, S.: Phys. Fluids **32**(9), 095114 (2020)
40. Datta, S.S., et al.: Phys. Rev. Fluids **7**(8), 080701 (2022)
41. Holzner, M., Liberzon, A., Nikitin, N., Kinzelbach, W., Tsinober, A.: Phys. Fluids **19**(7), 071702 (2007)
42. Westerweel, J., Fukushima, C., Pedersen, J.M., Hunt, J.C.R.: Phys. Rev. Lett. **95**(17), 174501 (2005)
43. Valente, P.C., da Silva, C.B., Pinho, F.T.: Phys. Fluids **28**(7), 075108 (2016)
44. Rosti, M.E., Perlekar, P., Mitra, D.: Sci. Adv. **9**(11), eadd3831 (2023)
45. Holzner, M., Lüthi, B.: Phys. Rev. Lett. **106**(13), 134503 (2011)
46. Watanabe, T., Sakai, Y., Nagata, K., Ito, Y., Hayase, T.: Phys. Fluids **26**(10), 105103 (2014)
47. Zhang, Y.B., Xi, H.D.: Phys. Fluids **34**(7), 075114 (2022)
48. Cai, W.H., Li, F.C., Zhang, H.N.: J. Fluid Mech. **665**, 334 (2010)
49. ur Rehman, S., Lee, J., Lee, C.: Phys. Rev. Fluids **7**(6), 064303 (2022)

Interfacial Morphology of a Bubble Moving in Confined Channel Filled with Viscoelastic Fluid

Yidi Zhang, Xubo Cao, and Zhenzhen Li(✉)

School of Aerospace Engineering, Beijing Institute of Technology, Beijing 100081, China
zhenzhenli@bit.edu.cn

Abstract. Bubble motion in confined channels find applications ranging from carbon oxide sequestration to cardio-vascular embolism, and is ubiquitous in nature and industry. The confinement of bubbles in the channel causes the formation of a thin liquid film between gas and solid wall, whose flow field has been studied theoretically and especially for Newtonian fluids. Steadily moving bubbles in Newtonian fluids exhibits saddle shape. However, since a large amount of industrial and biological fluids are complex fluids, the motion of morphology of moving bubbles can be affected by non-Newtonian effect such as viscoelasticity. The purpose of this work is to explore the thickness distribution of liquid film between gas and solid wall during the motion of bubbles in a confined channel filled with viscoelastic fluid. In this study, bubbles are formed with flow focusing method of droplet microfluidics, bubbles move steadily through a long channel, and the film thickness is measured by an experimental method based on light interference. The relative optical interference intensity (ROII) method was used to obtain the thickness distribution of liquid film by analyzing the fringes. The thickness distribution of the liquid film within the bubble's reference frame exhibits a different pattern compared to that in Newtonian fluids, and the symmetry of the spherical bubble is violated. This study provides experimental data for theoretical and computational research on bubble dynamics in confined channels.

Keywords: Microfluidic · Bubble Dynamics · Liquid Film · Flow Focusing · Light Interferometry

1 Introduction

The motion of bubbles is ubiquitous in nature and industry [1], the application ranges from energy extraction to drug delivery. For instance, in the process of carbon dioxide sequestration, CO_2 is injected into the underground porous media where it dissolves and diffuses, it helps displacement of the crude oil, and involves the motion of gas bubbles in complex fluids [2]. In vascular flow, stagnant bubbles can cause embolisms, which may lead to serious cardiovascular disease [3].

When a confined bubble is moving in a hydrophilic channel, a liquid film is forms between the gas and the solid wall. The lubrication film directly affects the motion of

J. Wang and I. Marusic (Eds.): IUTAM-TNTI 2024, IUTAM Bookseries 45, pp. 238–246, 2025.
https://doi.org/10.1007/978-3-031-78151-3_19

the bubbles and the transport of fluids [4]. Gas and liquid flow rate, physical properties such as the liquid viscosity and density also regulate the flow field [5]. In the analysis of film profile squeezed by long bubbles in a square-section capillary, Wong et al. [6] found that the thickness of the liquid film follows a power-law with the capillary number. For slowly moving bubbles with a lower capillary number (Ca), the thinnest region of the liquid film along the flow direction is located at the rear of the bubble, and the bubbles lower interface exhibits a saddle shape. Magnini et al. [7] found that the liquid film thickness and flow field in square channels differ from situations in circular capillaries as the capillary number increases. Chen et al. [8] used dual-wavelength interferometry to measure the distribution of liquid film thickness around steadily moving long bubbles in a square glass tube, validating Wong et al.'s [6] theory. The bubbles were formed with microfluidics, which has become a common method for generating evenly distributed bubbles, micro-bubbles can be produced within channels formed by capillary assemblies [9]. The combination of microfluidics and light interference provides an effective technique for studying the morphology and dynamics of bubbles under the effect of confinement.

The rheological properties of the fluid significantly affect the interface morphology of bubbles moving in viscoelastic fluids [10]. Li [11] discovered that viscoelasticity has a beneficial effect on the lubrication properties of liquid films in viscoelastic fluids. Ma et al. [12] compared the Marangoni effect in viscoelastic and Newtonian fluids, highlighting that shear thinning and viscoelasticity accentuate the instability of liquid films. Seminal work in confined channel revealed that viscoelasticity regulates the gas filament width in the Saffman-Taylor instability [13], indicating the role of elastic effect on the liquid film thickness. However, detailed measurements are still lacking regarding the evolution of liquid film thickness caused by bubble motion in viscoelastic fluids.

This paper aims to study the thickness distribution of the thin liquid film of steadily moving bubbles in a viscoelastic fluid within confined channel, and to compare with that in Newtonian fluids. It shows the coupling phenomena between the viscoelastic effect under strong shear and the bubble interfacial morphology. For this purpose, the study utilizes the flow focusing method to generate bubbles, employs optical interference experimental techniques for the measurement of liquid film thickness. This is intended to provide references for the study of bubble morphology near the channel wall.

2 Materials and Methods

2.1 Materials

The viscoelastic fluid used is a mixed solution of polyethylene glycol (PEG, Merck) with a molecular weight of 8 kDa and polyethylene oxide (PEO, Merck) with a molecular weight of 5000 kDa, both dissolved in distilled water (Shanghai Titan Scientific Co.), with the gas being air. PEG is soluble in water at 20 °C with a solubility of 630 mg/ml; PEO is soluble in water at 25 °C with a solubility of 1.21 g/ml. In this experiment, the mixed solution contains 16.7 wt% PEG and 0.08 wt% PEO. The viscosity measurements were conducted using an Anton-Paar MCR302 rheometer with a CP50–1 rotor (50 mm diameter and 1° cone angle) at 20 °C. The viscosity of the viscoelastic solution was 22.7 mPa·s [12].

2.2 Device and Equipment

The microfluidic chip used in the experiment is based on polydimethylsiloxane (PDMS). The mold of the chip is made of acrylic material. First, draw a plan view of the channel. The mold with convex channel geometry is obtained by the manufacturer through milling process. The acrylic plate mold is cleaned with a mixture of alcohol and detergent. During this process, a layer of surface-active molecules is covered on the acrylic plate to avoid the adhesion of subsequent PDMS. Dry the treated acrylic board and prevent it from falling ash. The PDMS material covering the mold is prepared by dimethylsiloxane and curing agent (Sylgard), which were mixed at a mass ratio of 9:1, after being thoroughly stirred, centrifuged to remove bubbles, is poured into the acrylic plate mold wrapped in a bowl of aluminum foil, and then placed in a vacuum drying oven at 70 °C for 1 h, demolded PDMS blocks with concave channels were obtained. Drill holes at the inlet of the fluid injection and cut with a knife at the outlet of the channel on the PDMS block. The PDMS block and slide are bonded with a plasma cleaning machine (HarrickPDC-32G-2) to obtain the required microfluidic chip. The channel wall was hydrophilic after plasma treatment, which facilitates the formation of bubbles in aqueous solution.

The length, width and height of the molds used in the experiment were 125 mm, 2 mm and 0.5 mm respectively, and bubbles were generated by flow focusing method. The channel comprises a viscoelastic fluid injection port, an air injection port and a flow focusing part. The width of the flow focusing tube mouth is 0.4 mm, and the accuracy error of the washing machine is ± 0.2 mm. The channel downstream of the flow-focusing tube mouth is a horizontal and shows a serpentine shape.

A syringe pump (LanGe LSP02) was used for the liquid injection at a constant flow rate, mercury lamp (Nikon INTENSILIGHT C-HGFI) sends full-frequency light into a fluorescent transmission microscope (Nikon Ti2-U), as shown in Fig. 1(a), the light passes through a filter of green light (wavelength 537−552 nm), and a semi-transparent and semi-reflective filter. The microfluidic chip was fixed on the microscope platform. The lights are reflected at the interface of glass-liquid, and that of liquid-gas, as shown in Fig. 1(b), the fringes of interference were captured by a high-speed camera (Photron Fastcam mini).

2.3 Experimental Methods

In the experiment, air was firstly injected and then the fluid. Bubbles are formed by flow focusing, as shown in Fig. 1(c). The flow rate of the air is at 100 µl/min and that for the solution is at 300 µl/min. The bubbles move steadily (with constant velocity) in the serpentine channel. The high-speed camera is used to capture images at a rate of 2500 fps as shown in Fig. 1(d), that are for further analysis. During the recording process, a suitable objective was chosen to ensure the bubble was of moderate size. We take the position of the bubble's leading edge every one second, and calculate the bubble's velocity by differentiation.

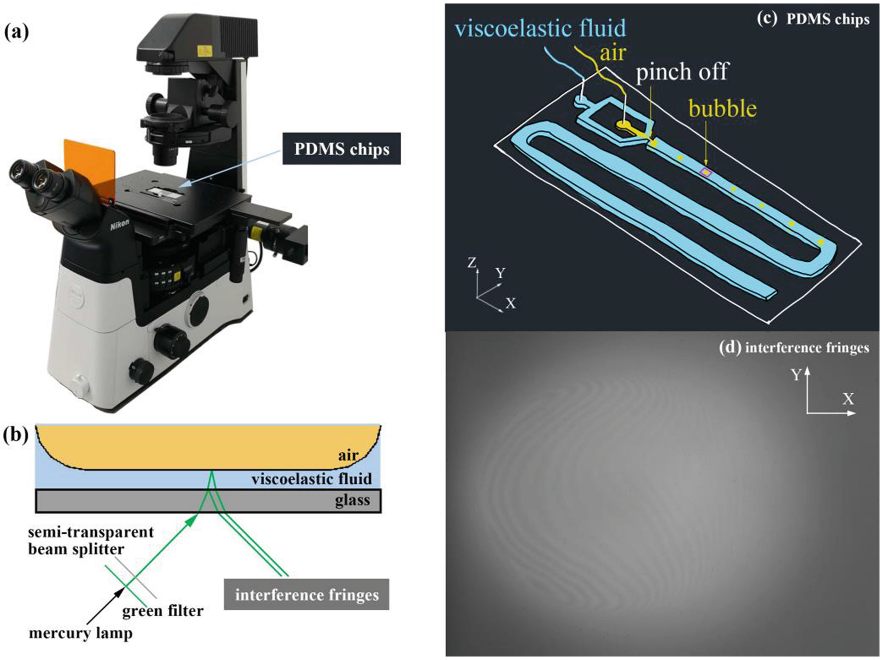

Fig. 1. Experimental setup. (a) Microfluidic platform; (b) Optical path of interference lights; (c) The snaking channel, and flow focusing for bubble generation. (d) Interference fringe pattern.

2.4 Interference Fringe Analysis and Liquid Film Thickness Calculation

During image analysis, the first step involves using ImageJ software to adjust the photo's contrast, thereby highlighting the interference fringes; the noise was reduced, and an adaptive threshold binarization helps transforming the photo into black and white, facilitating the distinction of fringe boundaries. The second step involves image processing, where grayscale value ranges are defined as different levels of characteristic color cards, which are then filled into the corresponding fringe areas. The third step involves importing the original and pre-processed images into a custom program, calculating the thickness values for each pixel, and plotting the relative thickness image of the liquid film. The calculation of film thickness is based on the Relative optical interference intensity (ROII) method [8]:

$$h = \frac{\lambda}{4\pi k}\left[\left(n + \left|\sin\frac{n\pi}{2}\right|\right)\pi + \arccos(I)\cos n\pi - \arccos(I_0)\right] \tag{1}$$

$$H = \frac{h}{h'} \tag{2}$$

in which λ is the wavelength of light, n is the order of the fringe, k is the refractive index of the liquid (1.333 for water solution), I is the light intensity of the interference fringe, and I_0 is the light intensity of the zero-order fringe at the dewetting point where the thickness of the liquid film is zero.

Due to the high speed of the bubbles in the experiment, the dewetting part cannot be tracked in our field of view, so the 0-order bright fringe at the zero liquid film could not be found. We considered the lowest order of the fringes at order 2, this results in the film thickness data obtained in this study being relative thicknesses. In Eq. 2, $h\prime$ represents the minimum liquid film thickness calculated from the initial image within the same video using the ROII method. The thicknesses at other positions are normalized based on this minimum thickness.

3 Results and Discussion

The experiment captured interference fringes induced by shear in thin films, which were formed by bubbles moving with constant velocity through a serpentine tube filled with a viscoelastic fluid. A single bubble was selected for measurement, continuous variation of interference fringes and corresponding calculated relative thickness of the liquid film are shown in Supplemental Information Video 1. The position of the leading edge of the bubble was recorded, and its average velocity was determined to be 4.8 mm/s by differentiation, as shown in Fig. 2(a). At four arbitrarily chosen moments in the figure (marked with stars), the relative thickness morphology of the liquid film was calculated from the captured interference fringe images, as shown in Figs. 2(b–e). The results indicate that the bubble moving in the X-direction, exhibits asymmetry in the thickness of the compressed liquid film relative to its central axis ($Y = 318.7$ μm), this is on the contrary with bubbles moving steadily in Newtonian fluids. From the observed movement pattern of the fringes in the experiments, there was a significant distortion and change at the front edge of the bubble, indicating substantial deformation of the bubble front during its steady motion in the viscoelastic fluid. Near both ends of the bubble's central axis parallel to the X-axis, around the areas at $Y = 118.5$ μm and $Y = 475.1$ μm, and near the edge close to the bubble's tail, the regions connect to form a semi-circular arc. This arc is the thinnest region of the bubble film. The liquid film thickens at positions approaching to the edge of the bubble, and exhibits a larger thickness gradient.

Over time, in the moving reference frame attached to the bubble, the thickness distribution at most of the liquid film exhibits steady characteristic, except at the front edge. The complementary part of the liquid film thickness determines the morphology of the bubble's lower surface. It is apparent that bubbles moving steadily in a viscoelastic fluid also display a morphology that is slightly thinner in the middle and thicker at the ends, and this configuration does not change significantly over time. However, unlike in Newtonian fluids, where the bubble is only thicker at the ends along the Y-axis and the thickness at the tail is as thin as in the middle, bubble moving in viscoelastic fluid also shows a thicker tail. Furthermore, the thickness at the front end of the bubble changes over time during steady motion in a viscoelastic fluid, indicating that the bubble undergoes some deformation at the front.

To conduct a quantitative study on the thickness of the liquid film, profiles were selected along the X-axis and two different distances along the Y-axis within the bubble's reference frame for height measurements and compare changes over time. The profile along the X-axis was chosen at $Y = 318.7$ μm, while the profiles along the Y-axis were chosen at distances of 267.9 μm and 438.3 μm from the tail of the bubble where visible

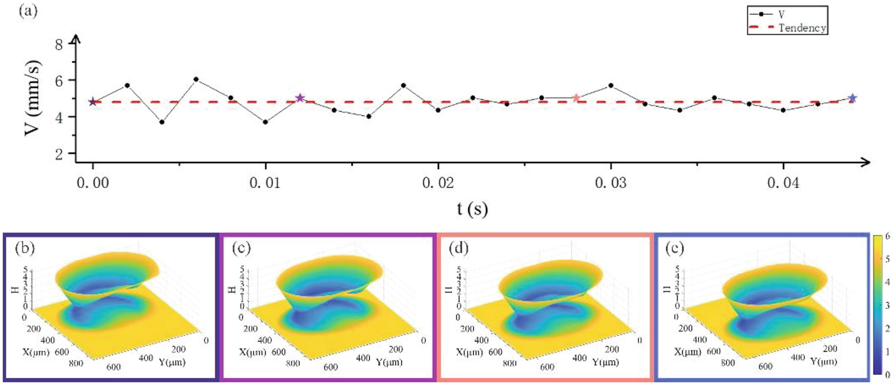

Fig. 2. The film thickness of steadily moving bubbles in viscoelastic fluid. (a) Velocity of steadily moving bubble; (b-e) Relative thickness of liquid film at time 0, 12 ms, 28 ms, and 44 ms.

stripes occur, as shown in Fig. 3(a). The height distribution of the liquid film on the profile along the X-axis is shown in Fig. 3(b), and that along the Y-axis are displayed in Figs. 3(c) and 3(d). It can be seen that when the bubble moves steadily in a viscoelastic fluid, the profile of the liquid film at both ends of the bubble in the profile parallel to the X-axis remain largely unchanged over time, while noticeable differences develop over time in the center of the bubble. In the profiles parallel to the Y-axis, the central region of the bubble continues to show a morphology that is thicker in the middle and thinner at the sides. At the front of the bubble, the middle film thickness gradually thins from the distal end to the proximal end along the Y-axis over time. In viscoelastic fluids, the morphology of bubbles evolves over time and displays asymmetrical shapes primarily due to the nonlinear behavior exhibited by viscoelasticity under strong shear forces [12]. This instability leads to an uneven distribution of the film thickness. In contrast, in Newtonian fluids, bubbles maintain a symmetrical and steady shape during motion [8].

According to the above experimental observation, comparing with bubbles moving in Newtonian fluids, the bubble moving steadily in a viscoelastic fluid possesses an asymmetric shape, with thinner head and thicker tail, and the interfacial morphology no longer shows a saddle shape as for Newtonian fluid. Viscoelastic fluid under strong shear may exhibit interfacial instability, where the interface appears shape perturbation with certain wavelength [12], the first normal stress difference representing the elastic property is induced by high shear rate. The asymmetric shape of the bubble may be caused by the nonlinear shear effects in the liquid film. Further experimental and theoretical work are perusing for the purpose of elucidating the dominant effect of bubble shape in viscoelastic fluids.

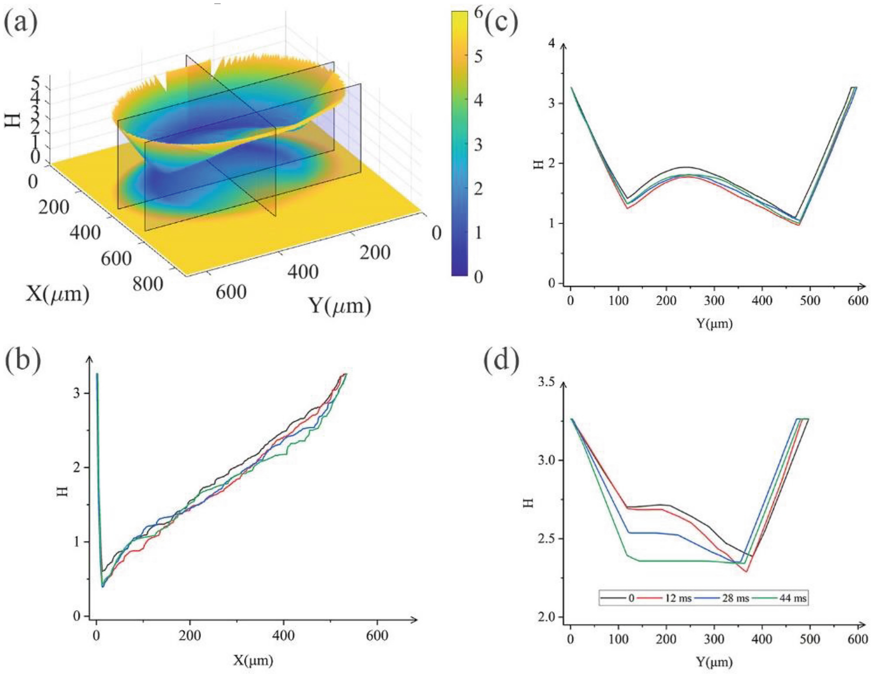

Fig. 3. Profile of liquid film relative thickness of a bubble moving steadily in viscoelastic fluids. (a) Location of the profiles; (b-d) Profile of liquid film relative thickness in the plane at Y = 318.7 μm, X = 267.9 μm and X = 438.3 μm over time.

4 Conclusion

This paper studies the thickness of the liquid film and its variations during the steady motion of confined bubbles in a Hele-Shaw cell using optical interference experimental methods. It compares the formation of liquid film thicknesses of bubbles in Newtonian fluids and viscoelastic fluids.

In viscoelastic fluids, bubbles moving at a constant speed exhibit a liquid film morphology that is thinner in the middle and thicker at the ends, which remains relatively stable during movement. However, unlike the saddle-shaped bubble morphology in Newtonian fluids, bubbles in viscoelastic fluids exhibit an asymmetric shape with a thinner front and a thicker tail. Additionally, as the bubble moves steadily in a viscoelastic fluid, the changing thickness of the liquid film at the front of the bubble indicates deformation occurring at the front. This demonstrates that the interfacial morphology of the bubble in viscoelastic fluids changes in real-time as it moves.

Accurately measuring the liquid film thickness between bubbles and solid walls through experimental methods helps to gain a deeper understanding of the evolution of liquid films, particularly the bubble dynamics in viscoelastic fluids. Further experimental and theoretical work will be conducted to elucidate the dominant effect of bubble shape in viscoelastic fluids.

Appendix

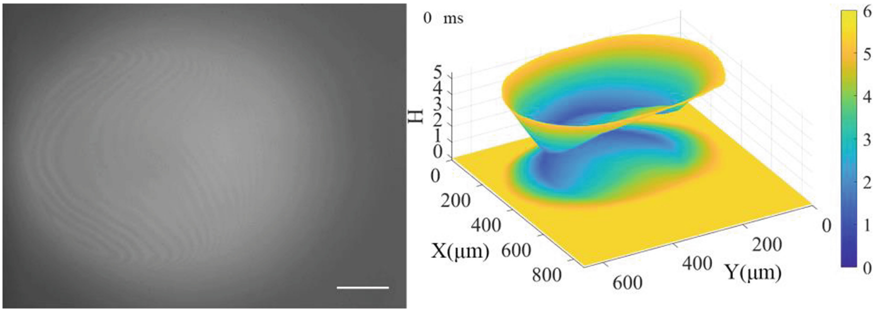

Movie 1 Dynamic video of interference fringe diagram and calculation diagram of moving bubble liquid film in viscoelastic fluid.

References

1. Ajaev, V.S., Homsy, G.M.: Modeling shapes and dynamics of confined bubbles. Ann. Rev. Fluid Mech. **38**(1), 277–307 (2006)
2. Sambo, C., Liu, N., Shaibu, R., et al.: A technical review of CO2 for enhanced oil recovery in unconventional oil reservoirs. Geoenergy Sci. Eng. **221**(11), 111185 (2023)
3. Li, Z., Li, G., Li, Y., et al.: Flow field around bubbles on formation of air embolism in small vessels. Proc. Natl. Acad. Sci. **118**(26), 1–6 (2021)
4. Qin, J.: Hydrodynamic theory of liquid film and moving contact line on solid wall. [PhD Thesis]. Hefei: University of Science and Technology of China 1−160 (2021). (in Chinese)
5. Zhang, A.M., Li, S.M., Cui, P., et al.: A unified theory for bubble dynamics. Phys. Fluids **35**(03), 033323 (2023)
6. Wong, H., Radke, C.J., Morris, S.: The motion of long bubbles in polygonal capillaries. part 1. Thin films. J. Fluid Mech. **292**, 71–94 (1995)
7. Magnini, M., Matar, O.K.: Morphology of long gas bubbles propagating in square capillaries. Int. J. Multiph. Flow **129**(10), 103353 (2020)
8. Chen, H., Meng, Q., Li, J.: Thin lubrication film around moving bubbles measured in square microchannels. Appl. Phys. Lett. **107**(14), 141608 (2015)
9. Lu, W., Li, E.Q., Gao, P.: Generation of microbubbles via a tapered capillary. Phys. Fluids **35**(12), 122103 (2023)
10. Li, S.B., Ma, Y.G., Jiang, S.K., et al.: The drag coefficient and the shape for a single bubble rising in viscoelastic fluids. J. Fluids Eng. Trans. Asme **134**(8), 084501 (2012)
11. Li, X.K.: Viscoelastic effects on lubricant thin-film flows. J. Cent. South Univ. Technol. **14**, 68–72 (2007)
12. Ma, X., Zhong, M., He, Y., Liu, Z., Li, Z.: Fingering instability in Marangoni spreading on a deep layer of polymer solution. Phys. Fluids **32**(11), 112112 (2020)
13. Lindner, A., Bonn, D., Poiré, E.C., et al.: Viscous fingering in non-newtonian fluids. J. Fluid Mech. **469**, 237–256 (2002)

Author Index

J. Wang and I. Marusic (Eds.): IUTAM-TNTI 2024, IUTAM Bookseries 45, p. 247, 2025.
https://doi.org/10.1007/978-3-031-78151-3